Ph.D. in Design, Manufacturing and Operations Engineering

XXXVI Cycle

Computational Methods for the Analysis of Ascending Aortic Aneurysms

Antonio Martínez Pascual

A.Y. 2023/2024

Tutor:
Prof. Marco Evangelos Biancolini

Advisor:
Ph.D. Michel Rochette

Coordinator:
Prof. Francesco Vivio

Abstract

Thoracic aortic aneurysm is a disease which affects 5.3 per 100,000 individuals per year. Degenerative processes cause a weakening of the aortic wall and a dilatation of the vessel. Under the standard clinical practice, the severity of an aneurysms is evaluated considering its dimensions exclusively. However, this procedure is not able to capture the patient-specific condition. In order to shed some light on the state and integrity of the blood vessels under physiological conditions prior to performing a surgery, computational tools can be used. This thesis presents a series of computational solutions for the assessment of both the hemodynamic and structural condition of ascending thoracic aneurysms. In first instance, an analysis of the optimal computational strategy for the modelling of hemodynamic flows is presented. In particular, the effect of different turbulence and viscosity models on wall shear stress biomarkers is assessed. In second instance, after having defined the optimal computational strategy for computational fluid dynamics (CFD) analyses, the correlation between CFD derived biomarkers and aneurysm growth rate is examined. Lastly, in order to provide a more complete picture of the aneurysm condition by including the structural domain, a methodology for the creation of high-fidelity fluid-structure interaction aorta models is presented.

The work has received funding from the European Union's Horizon 2020 research and innovation programme under the Marie Sklodowska-Curie grant agreement No 859836, MeDiTATe: "The Medical Digital Twin for Aneurysm Prevention and Treatment".

Acknowledgements

The journey that has led to this thesis has been demanding and full of challenges. Without the people that have supported me along the way, it would have never been possible.

I express my profound gratitude to my supervisors Marco E. Biancolini and Michel Rochette for their continuous support and encouragement to pursue higher goals. I have great memories of the countless pizzas at Vito's with Marco having both scientific and daily life discussions, many of which have been a source of inspiration. I am thankful to Michel for the warm welcome I received after arriving in France, with good food and wine, and for sharing his energy and passion, which has helped to sustain my motivation during this research.

Special thanks to all the clinicians and researchers from Rennes, Dijon and Toulouse, as they shared the passion and motivations of this project. Without the discussions we shared and the help they provided, this work would have never been possible.

My deep gratitude to María Ángeles Pérez Ansón and Frans van de Vosse, for having taken the time to review my thesis. Their works and research have been an example to follow.

I am extremely grateful to my MeDiTATe colleagues, which have made this journey extremely amusing and enriching, sharing thoughts, pains and joys. I am so thankful for the travels we had, the beers we shared and for the time we spent together.

I would like to thank all my colleagues from Ansys, which are too many to name, for their continuous support, the relaxing coffee breaks and laughs during working hours, the amusing evenings and, essentially, making my life in Lyon extraordinary.

Lastly, I thank with all my heart my family and friends, which have always been there, supporting from the very beginning.

Thank you all. You are all truly wonderful people.

Contents

Glossary of acronyms

Ascending thoracic aorta	ATA
Ascending thoracic aortic aneurysm	ATAA
Bicuspid aortic valve	BAV
Brachiocephalic trunk	BT
Carreau viscosity	CV
Computational Fluid Dynamics	CFD
Computed tomography	CT
Descending aorta	DA
Dynamic Smagorinsky-Lilly	DSL
Extracellular matrix	ECM
Fluid-structure interaction	FSI
Laminar flow model	LFM
Large Eddy Simulation	LES
Left common carotid	LCC
Left subclavian	LS
Magnetic resonance imaging	MRI
Newtonian viscosity	NV
Oscillatory shear index	OSI
Peak systole wall shear stress	PSWSS
Shear angle	SA
Smooth muscle cells	SMC
Thoracic aortic aneurysm	TAA
Time averaged wall shear stress	TAWSS
Tricuspic aortic valve	TAV

Chapter 1

Introduction

Thoracic aortic aneurysm is a disease which affects 5.3 per 100,000 individuals per year [1]. Degenerative processes cause a weakening of the aortic wall and a dilatation of the vessel, creating a bulge in the aorta which, if left untreated, can lead to catastrophic complications. It is reported that as much as 22% of individuals with an acute aortic syndrome die before reaching a hospital [2]. Studies have shown that age, sex, history of hypertension, genetic conditions affecting tissues such as Marfan's and Ehlers-Danlos syndromes, aortic stenosis and the presence of bicuspid aortic valve (BAV) can increase the risk of developing an aneurysm and promote faster growth rates [3–6].

Under the standard clinical practice, the severity of an aneurysms is evaluated considering its dimensions exclusively. During the early phases of the aneurysm development, patients are examined using echocardiography and, only when the aneurysm reaches a potentially dangerous size, a computed tomography (CT) angiography or magnetic resonance imaging (MRI) is performed. The diameter of the aneurysm is then assessed and, if the thresholds established by the current guidelines are surpassed, surgery is performed [7]. The guidelines base the risk of rupture on the diameter, since the dilatation of the vessel causes an increase in hoop stress and, thus, leads to an increase of the risk of rupture and dissection [8, 9]. However, this procedure is not able to capture the patient-specific condition. Diameter evaluation alone cannot be used to identify if a section of the aorta has suffered a pronounced degradation or if, on the contrary, the structural integrity of the wall has been preserved during the remodelling process that occurs during the development of the aneurysm. Due to this lack of personalized diagnosis, multiple cases of rupture have been reported when the diameter of the aorta was below the established thresholds [10] and, oppositely, some aneurysms have remained stable while their diameter exceeded the thresholds [11, 12]. This suggests that a better understanding of the pathology is required [13].

To understand the biological processes that occur in the arterial wall during the aneurysm development, various studies have focused on analysing the changes in the arterial wall composition, assessing the changes in elastin and collagen content and smooth muscle cell count [14, 15]. In other studies, aortic tissue extracted during surgery or from autopsies has been used to study the yield strength of arteries and characterize its mechanical properties [16–18], which has aided to understand the normative stress limits for both healthy and diseased arteries. These analyses, however, can be performed only after the diseased tissues have been extracted and, thus, cannot be used to characterize the patients condition during the diagnosis process.

In order to shed some light on the state and integrity of the blood vessels under physiological conditions prior to performing a surgery, computational tools can be used. In-silico models can provide unprecedented insight into the stresses present in the wall and into the hemodynamic conditions of the blood flow. The information provided by these models has the potential to be used to characterize the diseased vessel in a patient-specific manner, opening the door to personalized diagnosis and treatment. Consequently, it enables the identification of patients with an elevated risk of precocious rupture and, simultaneously,

to reduce the number of early interventions on stable aneurysms. In order to facilitate the diagnosis and improve the understanding of cardiovascular pathologies, numerous groups have focused on the development of in-silico models to evaluate the patients condition. Structural models have been developed and used to compute the stresses on the aortic wall and estimate the risk of rupture [19–23]. Other studies have focused on modelling the growth and remodelling phenomena that occurs during the aneurysm development [24–26]. These type of models are capable of predicting the future growth of an aneurysm, enabling for an optimal planning of follow up examinations and surgery. Computational Fluid Dynamics (CFD) models enable to evaluate the hemodynamic conditions inside the vessel. These modes have used to model ascending thoracic aortas (ATA) and compute fluid biomarkers which are suggested to be related to aneurysm [27–30] and dissection [31–33] progression. Altered flow hemodynamics has been suggested to be linked to aneurysm incidence, specially in the presence of BAV [34, 35]. Studies which combined CFD models with histological tissue characterization revealed that high wall shear stress (WSS) was linked to media degeneration and reduced wall thickness, elastin levels and smooth muscle cell count [36, 37].

Fluid–structure interaction (FSI) models provide the most complete picture of the aortic wall condition and can be used to understand the coupled effect of structural and hemodynamic stressors. In a recent work, the heart induced motion on the aortic root was imposed as a boundary condition to accurately capture the wall deformations and stresses [38]. In another work, the risk of rupture of ascending aortic aneurysms was assessed by computing the peak wall stress as function of the wall stiffness and hypertension level [20]. Another research group, which studied the link between aneurysm growth and fluid biomarkers, suggested that WSS angle could be linked to fast vessel dilatation in patients with Marfan syndrome [39]. More elaborate FSI models which account for the anisotropic behaviour of the arterial wall have been used to compute stresses on the arterial wall [30, 40, 41]. A FSI model of the larger vessels from head to foot, coupled to a zero-dimensional lumped-parameter model, was used to study the pressure wave propagation and the effect of arterial stiffening [42].

The predictive capabilities of in-silico models has proven to provide great insight into the patient's condition. This capabilities have been put to use by the healthcare industry and some commercial solutions exist on the market. For example, in-silico modes are used used for endovascular procedure planning using the solution provided by EndoSize® (Therenva SAS, Rennes, France), and for patient-specific eye surgery planning and outcome prediction using Optimeyes™ (Optimo Medical AG, Biel, Switzerland).

Following the works of previous researchers, we present in this work a series of computational solutions for the assessment of both the hemodynamic and structural condition of ascending thoracic aneurysms. In first instance, an analysis of the optimal computational strategy for the modelling of hemodynamic flows is presented. In particular, we assess how WSS biomarkers are affected by the choice of different turbulence and viscosity models. In second instance, after having defined the optimal computational strategy for aorta CFD analyses, we modelled a cohort of 33 patients and assessed if correlations exist

between CFD derived biomarkers and aneurysm growth rate. Lastly, in order to provide a more complete picture of the aneurysm condition by including the structural domain, a methodology for the creation of high-fidelity FSI aorta models is presented. In order to personalize the model and provide a truthful representation of the hemodynamic conditions, a procedure to calibrate the aortic jet using MRI 4D flow data was developed. In the pursuit of accurately modelling the aortic wall, a method to generate a structural model with spatially varying material properties was developed.

Chapter 2

Clinical context

This chapter focuses on presenting the main components of the cardiovascular system, a description of the cardiac cycle, the characteristics of aortic aneurysm and the different types of aortic valve disorders.

2.1 The circulatory system

The cardiovascular system is a complex network in the human body responsible for managing blood circulation. Its primary functions include transporting nutrients to cells, protecting the body, and maintaining homeostasis by regulating temperature and pH levels. This system consists of the heart, blood vessels and blood. Its function is to supply to all tissues in the body with essential proteins, nutrients and oxygen while simultaneously removing waste products such as carbon dioxide, creatinine and urea. In an average human, the cardiovascular system contains around 5 liters of blood. The heart serves as the central pump that keeps the blood flowing throughout the vessels. This system can be divided into two main parts: pulmonary circulation, located within the lungs, and systemic circulation, which transports blood throughout the rest of the body, with the heart serving as the connection between these two circulatory pathways, as depicted in Figure 2.1.

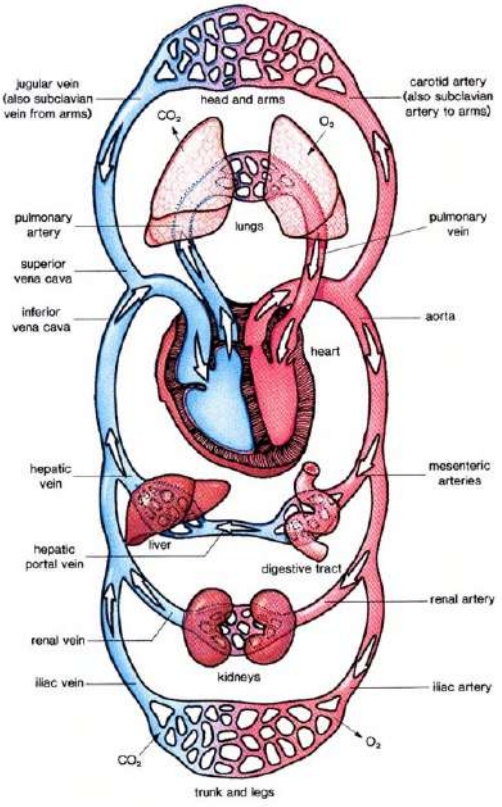

Figure 2.1: Schematic of the cardiovascular system (Source: www.daviddarling.info/encyclopedia, accessed 14/09/2023).

2.1.1 The heart

The heart is the pump responsible for supplying the necessary pressure to make the blood circulate around the body, between the pulmonary and systemic circulations. Its situated in the thoracic cavity between the lungs and it is surrounded by a fibrous membrane known as the pericardium.

2.1.1.1 Anatomy of the heart

The heart consists of four distinct chambers: two atria, which are the upper chambers, and two ventricles, the larger chambers located in the lower portion, as shown in Figure 2.2 . The ventricles are separated by the inter-ventricular septum, while the atria are separated by the inter-auricular septum. The left atrium receives oxygenated blood from the pulmonary veins before transferring it to the left ventricle. The left ventricle ejects the blood into the body through the aorta. In the right heart, the atrium receives deoxygenated blood from the systemic circulation and transfers it to the right ventricle. Subsequently the blood is ejected into the pulmonary circuit where it is oxygenated. Within the heart, we find four valves which ensure that the blood flows in one direction only. Separating the atria and ventricles we find the atrioventricular valves, including the mitral valve and the tricuspid valve, in the left and right heart, respectively. Two semilunar valves separate the arteries and the ventricles, namely the aortic valve in the left heart and the pulmonary heart in the right heart. Pressure gradients regulate the opening and closing of these valves. The cardiac wall is composed by three layers:

- The endocardium: a thin membrane located in the inner wall and which serves to regulate the myocardial contractibility.
- The epicardium: it corresponds to the outer layer of the wall and it is composed by fibrous tissue which protects the heart from damage and friction.
- The myocardium: located between the endocardium and epicardium and made from muscle, it is responsible for producing the contraction action of the heart.

Finally, a fibrous tissue englobes the heart, containing a lubricant and allowing for heart movement within the heart cavity.

2.1.1.2 Heart function

The cardiac cycle is composed of a series of events which lead to a complete heartbeat. It is divided into two main phases: systole and diastole. During systole the heart contraction occurs, commencing with the contraction of the atria, which fills the ventricles. Subsequently the ventricles contract, expelling blood from the heart and elevating blood pressure. During this process, the atrioventricular valves close to prevent backflow of blood into the atria. The systole is followed by the diastole, characterized by the

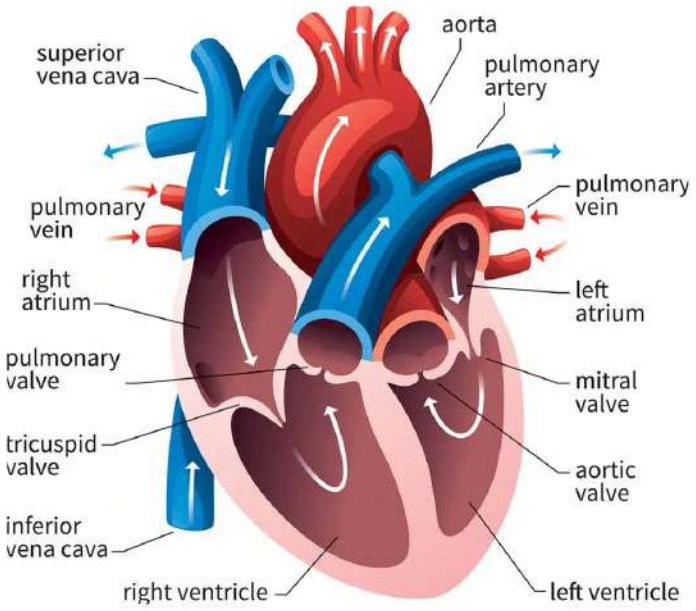

Figure 2.2: Schematic of the heart structure (Source: Queensland Cardiovascular Group).

relaxation and filling of the heart, which is accompanied by a decrease in blood pressure. As ventricular pressure drops, the blood tends to flow backward into the heart, which causes the aortic and pulmonary valves to close. During the cardiac cycle, the left and right heart operate as two parallel pumps. An automatic nervous system is responsible for the synchronization of the different contraction and relaxation phases.

2.1.2 Blood circulation

The pulmonary and systemic circulation are composed of two kinds of vessels: arteries and veins. The inner part of a vessel, where the blood flows, is called the lumen. In the pulmonary circulation, blood with low oxygen levels is ejected from the right ventricle into the pulmonary artery. The blood is oxygenated in the lungs and returned to the heart via the pulmonary vein. In the systemic circulation, the oxygenated blood is pumped by the left ventricle into the aorta through the aortic valve. The blood travels around the systemic vessels exchanging nutrients, oxygen and carbon dioxide with the tissues until it returns to the heart through the superior and inferior vena cava, in order to restart the circulation cycle.

2.1.3 Vessel structure

In this section, we present the main features of the blood vessels. The vessels have three distinct layers in their walls: the intima, media, and adventitia, shown in Figure 2.3. The intima regulates the agents present in the blood and prevents coagulation. It is composed of endothelial cells attached to an internal

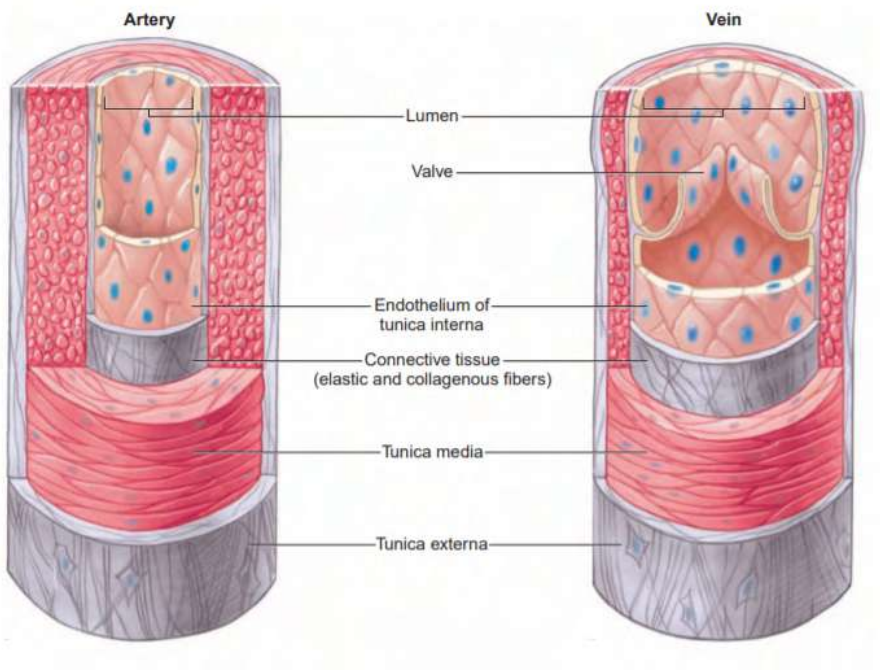

Figure 2.3: Vessel structure (Source: Fox, Stuart Ira., Human physiology, 8th ed., 2004).

elastic membrane. The media is made from smooth muscle tissues and a extra-cellular matrix (composed of elastin and collagen) and is responsible for vessel elasticity. The smooth muscle cells are able to contract or relax in order to modify the vessel diameter. The external layer, named adventitia, contains fibroblasts and collagen, which provides rigidity to the vessel.

Some important differences are present between arteries and veins, due to their distinct function. In the systemic circulation, arteries always carry oxygenated blood, while the contrary occurs in the pulmonary circulation. The arteries originate from the heart and divide into branches, becoming progressively smaller. Arteries and veins are classified according to their size. The largest arteries (pulmonary artery and aorta) have elastic walls that expand and contract to maintain blood pressure. Arterioles, on the other hand, have rigid muscular walls and play a significant role in peripheral resistance. The arterioles then branch into capillaries, which are the vessels where the nutrient and waste exchange is done, thanks to their permeable walls. They are the smallest vessels of the cardiovascular system. Once the exchange is completed, the capillaries merge back into venules, which become progressively larger as they transform into veins. Veins have thinner walls than arteries and possess elastic properties that allow them to accommodate increased blood volume. The veins contain small valves which guarantee that the blood flows back to the heart, even when the driving pressure forces are small and the flow is pushed against gravity. The thickness and composition of arteries and veins differ due to the different conditions they withstand, as described in Figure 2.4. Arteries are exposed to intense and variable pressures, while veins are subject to low and uniform pressures. Arteries receive the pulsatile flow from the heart, which needs to have sufficient pressure to overcome the pressure losses caused by the peripheral resistances in order to return to the atria.

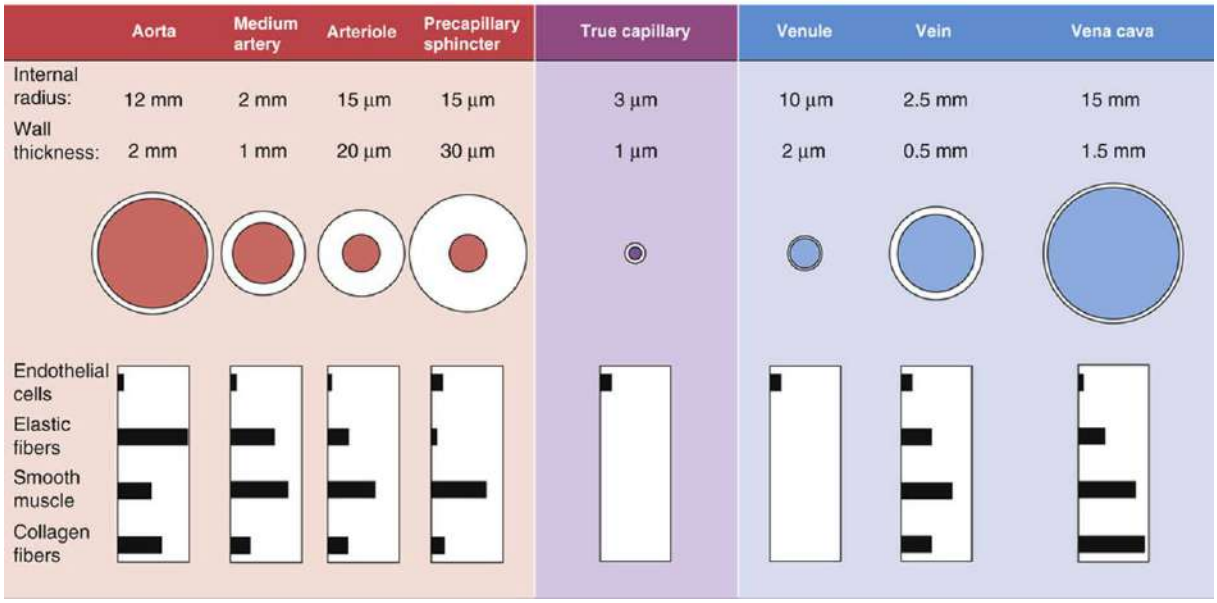

Figure 2.4: Diameter and composition of arteries and veins (Source: Boron, W.F. and Boupaep, E.L., Medical Physiology, 3rd ed., 2016).

The peripheral resistance is caused by the reduction in vessel diameter, the increase of vessel rigidity and the viscous forces. Due to this phenomena, the largest arteries posses compliant walls which enables them to absorb the pressure waves and ensure blood continuity, allowing to maintain blood pressure throughout the cardiac cycle. On the contrary, arterioles posses rigid muscular walls which increase blood pressure, being one of the main contributors to total peripheral resistance.

2.1.4 The aorta

The aorta is the largest artery in the body, which departs from the left ventricle. Its mayor sections are the ascending thoracic aorta (ATA), the aortic arch, the descending aorta (DA) and the abdominal aorta, as shown in Figure 2.5. The first section of the aorta is the ATA, which receives the blood ejected from the heart and has an elevated distensibility. The vessel then curves giving rise to the aortic arch, from which the supra-aortic vessels depart. The supra-aortic vessels transport around 30% of the total blood flow and are composed of the brachiocephalic trunk (BT), the left common carotid (LCC) and the left subclavian (LS) arteries. The BT divides into the right carotid artery and the right subclavian artery. Carotid arteries irrigate the head and brain, while subclavian arteries deliver blood to the upper extremities. Continuing the aorta downstream, we find the DA, which extends to the abdomen where it divides into the iliac arteries. We can subdivide the DA into two sections: the descending thoracic aorta, located above the diaphragm, and the abdominal aorta, located below the diaphragm.

The ATA is connected to the heart through the aortic root, a complex structure which include the sinus of Valsalva, the aortic annulus, the sinotubular junction. The coronary arteries depart from the aortic root. The sinuses are named after coronary arteries branching from them. The left and right

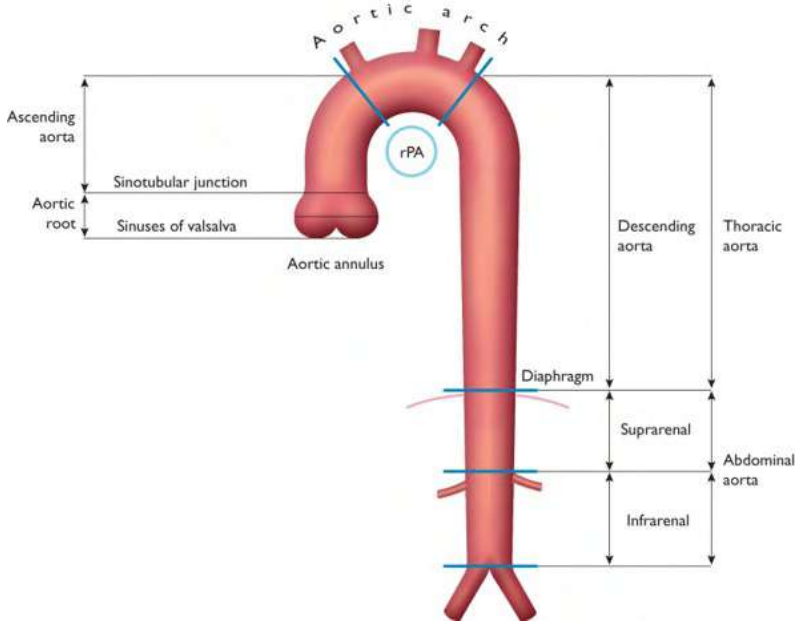

Figure 2.5: Sections of the aorta (Source: Erbel *et al.*, European Heart Journal, 2014 [43]).

coronary sinuses are named after the left and right coronary arteries, respectively, and the remaining sinus is named non-coronary. The structure of the root is detailed in Figure 2.6.

2.1.5 The aortic valve

The aortic valve is situated within the aortic root. It is comprised of a set of leaflets which are attached to the root wall. Pressure gradients control the opening an closing of the valve. During systole, ventricular pressure surpasses the aortic pressure and, thus, the valve opens, whereas, during diastole, as the blood attempts to flow backwards, the valve is closed. A diseased aortic valve will cause a malfunctioning in the flow control and distort the hemodynamic flow, which in turn can have a damaging effect on the aortic wall [45, 46]. Valve stenosis causes a narrowing the area through which the blood can flow and causes an incomplete opening of the valve. This gives rise to increased jet velocities and pressure gradients, which, if left untreated, may lead to heart failure. A depiction of a healthy and a stenotic valve is provided in Figure 2.7.

A healthy aortic valve is comprised of three leaflets which are aligned with the sinuses of the aortic root, hence called tricuspic aortic valve (TAV). However, other phenotypes exist. Genetic mutations in the Notch-1 gene can cause the valve to be formed by only two leaflets [47], which is the most common congenital cardiac malformation. These valves are named bicuspid aortic valves (BAV) and occur in 1-2% of the population [48]. Other phenotypes exists, such as unicuspid and quadricuspid, however they are much less common. Bicuspidity has been related to an incresed risk of aneurysm development and of aortic dissection [49]. Within BAV, we encounter various types. The most common is when the left and right coronary cusps are fused (>70%), followed by the fusion of the right and non-coronary cusps

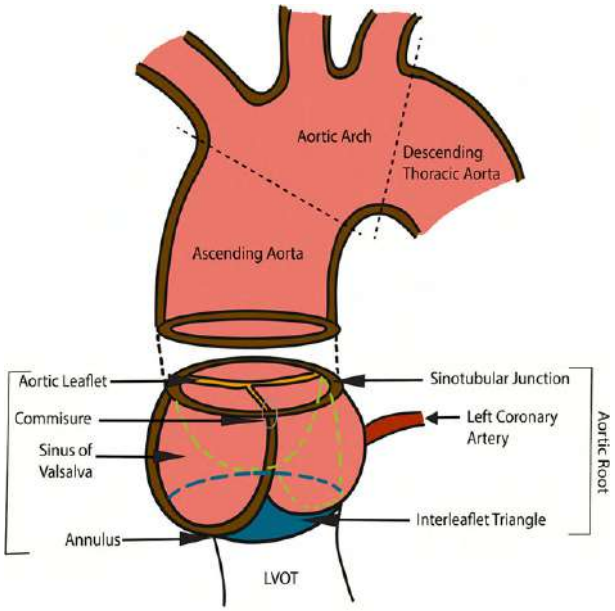

Figure 2.6: Structure of the aortic root (Source: Nagpal *et al.*, Insights into Imaging, 2020 [44].

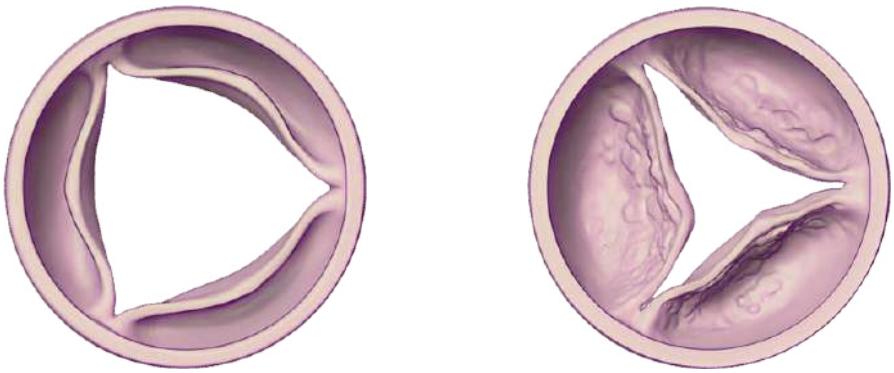

Figure 2.7: Difference between a healthy (left) and a stenosed valve (right) (Source: Boston Medical Center).

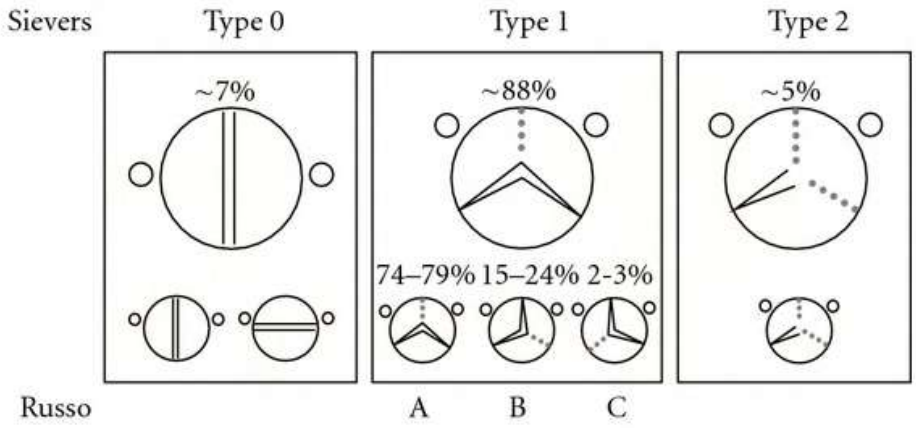

Figure 2.8: Classification of bicuspid aortic valves (Source: Etz *et al.*, 2012 [50]).

(10-20%), being the fusion of the left and non coronary cusps the least common (5-10%). The classification of BAV can be performed according to form of the valve cusps. Type 0 valves contain no raphe, type 1 contains one raphe, and type 2 contain two raphes, as shown in Figure 2.8.

2.2 Aneurysms

An aneurysm is a permanent and progressive dilatation of a vessel wall, causing its diameter to exceed 1.5 times its normal size [51]. Diameters between 1.1 and 1.5 are considered dilated or ectatic [43]. Aneurysms typically have no symptoms but, if left untreated, can lead to dangerous complications like vessel rupture or dissection. A rupture, especially in the aorta, can be fatal, due to massive blood loss. Dissection occurs when the vessel wall tears partially, which causes a bleeding between its layers. If an aneurysm is detected early and prophylactic treatment is performed, elevated prognosis is achievable [52]. In 2005, more than half of the thoracic aneurysms were found in the ascending part of the aorta [53]. The incidence of thoracic aortic aneurysm (TAA) is similar in men and women, however, women tend to be diagnosed at a later age. Studies have established that a link exists between vascular stress and risk of dilatation and rupture [54, 55]. An increase in aortic diameter leads to increased wall tension, due to Laplace's law ($T = P \times r$, where T is circumferential wall tension, P is wall pressure, and r is the average aortic radius). In undilated aortas, the stress is uniformly distributed along the wall, however, aortic dilatation can derive in an uneven distribution of stress in wall, potentially contributing to aneurysm formation.

2.2.1 Classification

Aneurysm can be classified by morphology and location. In terms of their morphology they are classified into two main types: saccular and fusiform. Saccular aneurysms exhibit a spherical shape and typically affect only a specific region of the vessel wall. Fusiform aneurysms cause a uniform dilatation on a segment

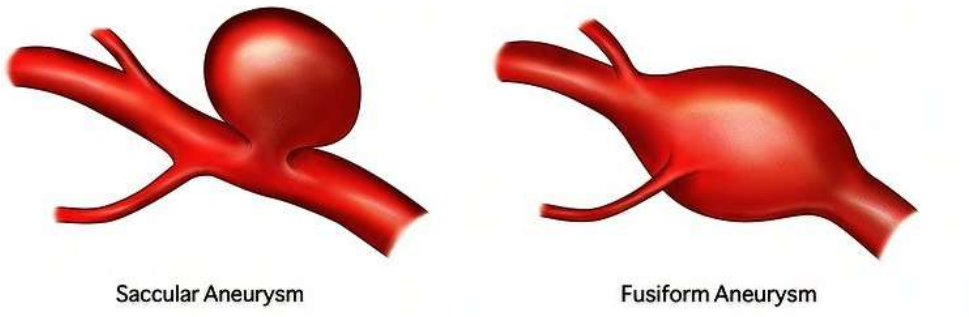

Figure 2.9: Classification of aneurysms according to morphology (Source: UT Health San Antonio).

of the vessel, as shown in Figure 2.9. Aneurysm can appear in nearly all arteries, being more frequently located in the aorta, the brain and the legs. In this work we will focus on aortic aneurysm, more specifically, on thoracic aortic aneurysm (TAA), which can be further subclassified according to its location along the thoracic aorta: root, ascending, arch or descending. This subclassification is depicted in Figure 2.10. The ascending thoracic aortic aneurysm (ATAA) and aortic root aneurysm may lead to a dilatation of the aortic valve and, consequently, impeding a complete valve closure, causing regurgitation [56]. ATAAs are the most common thoracic aneurysm with an incidence of 10 cases per 100,000 person/year [53]. The etiology of most ATAAs is unknown. Descending aortic aneurysm can be treated through an endovascular procedure and thus this pathology presents lower surgical risk.

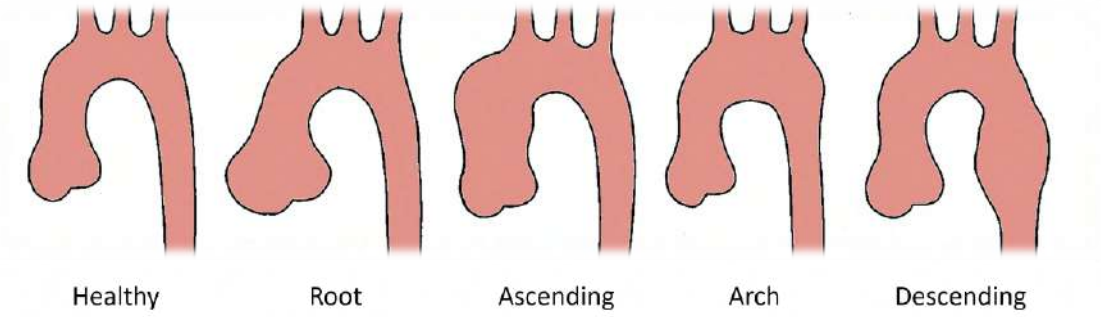

Figure 2.10: Classification of TAA according to location.

2.2.2 Molecular mechanisms of aneurysm formation

The composition of the arterial wall is altered during the development of the aneurysms. In order to understand the underlying causes of aneurysm development, it is essential to decipher the mechanisms that trigger aortic wall remodelling. Within the thoracic aorta, significant differences in terms of elastin-to-collagen ratio are present: as we progress along the aorta, this ratio decreases significantly and thus the vessel rigidity is increased. This is why it is suspected that the etiology of ATAA and DA aneurysm may be different [57].

A degradation of elastin is a commonly observed in ATAAs [58]. It has been found that an increased

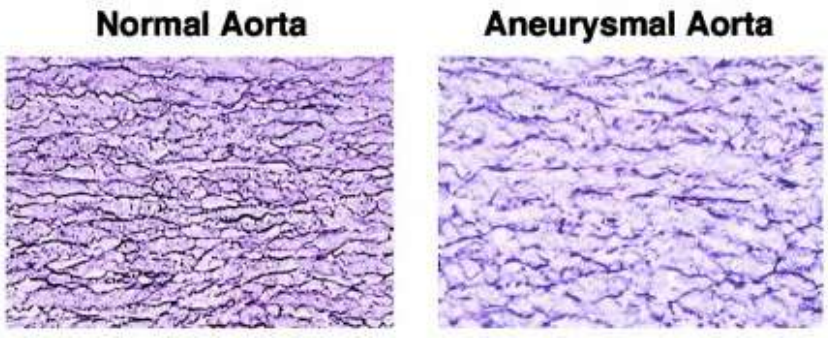

Figure 2.11: Elastin content in healthy and diseased aorta (Source: Absi *et al.*, The Journal of Thoracic and Cardiovascular Surgery, 2003[58]).

abundance and activity of extra-cellular matrix proteolytic systems, such as matrix metalloproteinases (MMPs) can cause such degradation [59]. Augmented MMPs favour the release of inflammatory molecules, causing inflammation in the adjacent tissues. This situation causes a vicious circle, since it causes endothelial an smooth muscle cell dysfunction which activates MMPs. This process then leads to a degradation of the wall which can manifest as an aneurysm. This phenomena can be observed by performing histological analyses on healthy and diseased tissue samples, as shown in Figure 2.11. Within arteries or veins, the extracellular matrix (ECM) makes up more than half of the wall's mass and primarily consists of collagen and elastin. Smooth muscle cells (SMC) are responsible for the majority of collagen and elastin production. The process of wall remodelling is regulated by the transforming growth factor beta one (TGF-β1), which stimulates SMC proliferation and ECM production. This process is a mechanism of adaptation to changes in blood flow and to mechanical or biochemical aggression [60]. This response manifests, for example, when a patient suffers from chronic hypertension. In this scenario, the aortic wall thickens in response to the increase of stress. The process of adaptation seeks to achieve optimal homeostasis in the vessel, however, in some cases, a pathological response can appear and give rise to the formation of aneurysms.

2.2.3 Risk factors and causes of aneurysm development

As previously mentioned, bicuspidity is strongly linked to the incidence of ATAA [5, 61] and to the risk of dissection and rupture [62]. It has been observed that the aneurysm growth rate of BAV patients is larger than that of TAV patients, being 1.9 and 1.3 mm/year, respectively. The estimated annual growth rate on BAV patients is significantly different in other studies, ranging between 0.2 and 1.2 mm/year [63, 64]. It is unclear if the high incidence of aneurysms in BAV patients is due to the genetic disorders that may affect the integrity of the aortic wall [65], or due to the disturbed hemodynamic flow [66], or a combination of both. It is suspected that, due to the increased aortic jet velocity and turbulence levels caused by bicuspidity, some mechanobiological processes can be triggering aneurysm growth.

Other valvular dysfunctions, including atherosclerosis, calcification and stenosis, have also been

associated to aneurysm incidence [67]. Stenosis causes a narrowing of the vessel and a reduction of the effective orifice area, which obliges the heart to eject the flow at a higher speed to preserve the cardiac output. This causes disturbed flow and elevated turbulence levels, together with hemolysis, which, for the same reason as in BAVs, could be triggering the development of aneurysms.

Other factors associated to the risk of developing aortic aneurysm are age, sex and history of hypertension [6]. Genetic conditions affecting tissues such as Marfan's Syndrome, Loeys-Dietz and Ehlers-Danlos augment significantly the risk of developing aneurysms [3, 4]. Marfan syndrome affects the connective tissues and affect the ocular, skeletal and cardiovascular systems due to mutations in fibrilin-1 gene [68]. It has a prevalence between 1.5 to 17.2 per 100,000 people [69]. Marfan syndrome patients have been estimated to have a growth of approximately 0.5 to 1 mm/year, whereas Loeys-Dietz syndrome patients are susceptible to extreme growth rates, above 10 mm/year, which often leads to death at a young age [61, 63].

2.2.4 Diagnosis and risk assessment

Aneurysms are commonly detected during clinical screening of other pathologies, when a patient undertakes a abdominal or chest radiography. When a patient is diagnosed with aneurysm or ectasia, continuous monitoring through echocardiography is performed to evaluate the vessel growth [70]. This imaging procedure is safe, fast and has a low cost. Unfortunately, evaluating aneurysm size using this technique yields only approximate measures, due to the influence of the position and orientation of the probe on the measurement. For this reason, CT or MRI are used when the aneurysm size approaches the thresholds recommended for prophylactic surgery, ensuring accurate diagnosis and appropriate surgical planning [71]. CT has the inconvenient of exposing the patient to ionizing radiation, whereas MRI is completely safe. However, the latter produces lower resolution images. Both angiography modalities enable to examine the entire aorta in three dimensions and evaluate the pathology accurately. The protocol followed during the control of aneurysm growth is detailed by the European Society of Cardiology [72]. If, during the evaluation of the aneurysm it is concluded that the diameter has not reached a critical size, surgery is delayed due to the low risk of rupture and in order to avoid unnecessary post-operatory complications. If needed, medication for hypertension reduction may be recommended in order to reduce aneurysm growth. Under the current guidelines, surgery is performed when the diameter exceeds 5.0 cm in patients without comorbidities [7]. In other situations, lower thresholds are established. A summary of the clinical guidelines is provided in Table 2.1. General risk factors for nonsyndromic heritable TAA or with no identified genetic cause include:

- Family history of aortic dissection at an aortic diameter <5.0 cm
- Family history of unexplained sudden death at age <50 years

- Rapid aortic growth (⩾0.5 cm/y in 1 year or ⩾0.3 cm/y in 2 consecutive years)

Risk factors for BAV include:

- Family history of aortic dissection
- Aortic growth rate > 0.3 cm/y
- Aortic coarctation
- "Root phenotype" aortopathy

In Marfan patients, surgery is performed below thresholds if increased risk of aortic complications are identified, including:

- Family history of aortic dissection
- Rapid aortic growth (>0.3 cm/y)
- Diffuse aortic root and ascending aortic dilation
- Marked vertebral arterial tortuosity

Patient category	Diameter threshold (cm)
General population	⩾5.0
	⩾4.5 + RF
BAV	⩾5.5
	5.0-5.4 + RF
Marfan	⩾5.0
	⩾4.5 + RF
Loeys-Dietz Syndrome	4.0-5.0

Table 2.1: Recommendations for ATAA intervention [7] (RF = Risk Factor).

2.2.5 Treatment

Once an aneurysm has reached a critical size or a rapid growth has been detected, cardiovascular surgeons define an appropriate surgical intervention, either open surgery or endovascular repair, according to the information provided by the angiographies [43]. For ATAA, open-surgery remains the treatment of choice [73]. Open surgery is an invasive procedure which replaces the diseased aorta by prosthetic Dacron graft. It requires a median sternotomy to give access to the thoracic cavity. During the procedure, cardiac arrest is performed, requiring a cardiopulmonary bypass, which allows to connect the patient's systemic circulation to an extra-corporeal circulation system which ensures the oxygenation of the patient's body during the

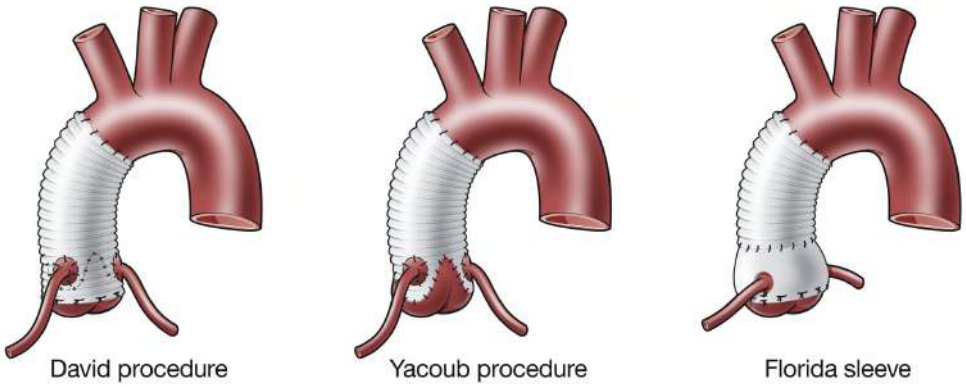

Figure 2.12: Modalities of ascending aorta replacement (Source: Buratto *et al.*, The Journal of Thoracic and Cardiovascular Surgery, 2021 [75]).

intervention. Subsequently, after stopping the heart, the surgeon can proceed to remove the diseased section of the aorta and substitute it for a prosthetic Dacron graft, which is sewn to the remaining healthy tissues. Various modalities of surgical repair are possible (Figure 2.12), depending on the characteristics and extension of the aneurysms: Bentall, Yacoub, David, Florida sleeve and Lansac, just to name a few. Parallel surgeries may be performed if concomitant conditions affecting the aorta or heart functioning are identified, such as aortic valve replacement. It is always preferable to delay intervention if a low risk of rupture is estimated due to the possible post-operatory complications, which include postoperative bleeding, myocardial infarction, stroke, pneumonia and sepsis, amongst others [74].

Chapter 3

Computational methods for accurate turbulence and viscosity modelling

In this chapter, an analysis of the computational methodology required for accurate WSS modelling is presented. Regarding turbulence modelling, the effect of accounting for subgrid viscosity will be evaluated. Regarding viscosity models, a comparison between a Newtonian and a non-Newtonian viscosity model will be performed.

3.1 Introduction

Computational biomarkers are emerging as a tool to aid in the diagnosis process of cardiovascular diseases. Their capability to provide insight into patient-specific hemodynamic and wall conditions position them as a promising tool that will enable clinicians to provide personalized treatment. For decades, numerical models of the cardiovascular system have been developed with varying levels of personalization and complexity [42, 76, 77]. In order to take in-silico model into the healthcare industry, standardized methodologies will be required to obtain approval by the corresponding regulatory agency through a process of validation and verification of the model outputs, ensuring trustworthy and replicable results [78, 79].

CFD and FSI models have been extensively used to evaluate pathological ascending thoracic aortas by quantifying clinically-relevant hemodynamic biomarkers related to aneurysm [27–30] and dissection [31–33] progression. Some studies have been performed considering Newtonian viscosity (NV) and the absence of turbulence models [27, 29], while others have considered a non-Newtonian viscosity and Large Eddy Simulation (LES) turbulence models, which require higher computational effort [80–82]. We also find studies that consider only the non-Newtonian behaviour in the absence of turbulence models [24, 83] or, on the contrary, consider a turbulence subgrid model with constant viscosity [28, 84].

Blood is a non-Newtonian fluid with a shear-thinning behaviour which reaches a Newtonian plateau at high shear rates [85]. The rheological response is primarily modulated hematocrit [86]. It is argued that, under the high shear-rates present in the ascending aorta during the most part of the cardiac cycle, the variations in viscosity are negligible and therefore a NV model can be assumed. A thorough assessment on the influence of viscosity models on aortic valves and ATA simulations have shown otherwise and revealed higher wall shear stress and increased hemolysis when accounting for non-NV [87, 88]. Moreover, shear-thinning has a significant effect on the growth of vortical structures and recirculation zones on idealized curved vessels [89] and has shown to delay turbulent transition on straight pipe flows [90–92].Other studies have analyzed the flow through stenosed arteries considering NV and non-NV [93, 94]. Pathologies such as valve stenosis or the presence of a bicuspid aortic valve favour turbulence generation, as the aortic valve area is reduce and the jet velocity increased [95, 96].

The effect of turbulence model choice has been assessed for various ATA under different scenarios, in order to clarify the computational requirements of different biomarkers. High and low resolution laminar models have been compared against Wall-Adapting Local Eddy-Viscosity (WALE) subgrid-scale model

using constant viscosity and it was shown that high resolution laminar models were capable of capturing accurately shear and turbulence dynamics, but had equal computational cost as LES simulation [97]. Variations in spatially and time averaged WSS have revealed differences below 6% between laminar and WALE considering a Carreau viscosity model [98]. The effect of turbulence modelling on platelet activation was assessed by comparing laminar, RANS, LES and Direct Numerical Simulation (DNS), revealing that predicting blood cell damage required LES or DNS and that RANS, due to its inherent temporal filtering nature, should be avoided as it shortens particle trajectories and alters the shear stress over the platelets [99]. In [80] it was shown that the $k-\omega$ SST model significantly underestimated the turbulent kinetic energy and anisotropy levels when compared to the WALE model under non-Newtonian viscosity. Differences between different LES models and their sensitivity to grid size and convection schemes have been analyzed in [100].

When considering non-NV, we should also emphasise that the shear-thinning behaviour can be described using different models, such as Carreau, Casson and Power-law. The choice made will also influence the flow behaviour, as shown in [101], where an ATA was modeled considering ten viscosity models and the results compared in terms of velocity and WSS.

To our knowledge, only one study [102] has addressed how the combined effect of blood viscosity and turbulence models affects hemodynamic results, in this case by analyzing turbulent-transition at different Reynolds numbers on a backward facing step. This work, however, did not address if WSS was affected and considered an idealized geometry, which greatly differs from a realistic aorta.

To bridge the gap between the studies which have assessed the influence of model choices independently, we present in this work an analysis focused on quantifying the combined effect of turbulence and viscosity models on wall-shear derived biomarkers for ATA using a patient-specific geometry and physiological boundary conditions. Up to date, no study has evaluated how viscosity models influence turbulence models and vice versa. Hence, this work presents a novel analysis of the combined effect of modeling assumptions on aortic flows and provides the optimal modeling strategy to obtain accurate WSS biomarkers. We will assess the effect of considering Newtonian or Carreau fluid models in combination with the absence or presence of a Dynamic Smagorinsky-Lilly (DSL) subgrid-scale turbulence model. The differences between CFD computations considering a healthy and a stenosed aortic valve will be evaluated in terms of time averaged wall shear stress (TAWSS), peak systole wall shear stress (PSWSS), oscillatory shear index (OSI) and shear angle (SA). TAWSS and PSWSS quantify the shear stress magnitude, OSI the fluctuations on the near-wall flow direction and SA the presence of rotating or reversed flow. This work presents the first analysis of the combined effect of turbulence and viscosity model on TAWSS, PSWSS, OSI and SA on ascending aorta simulations.

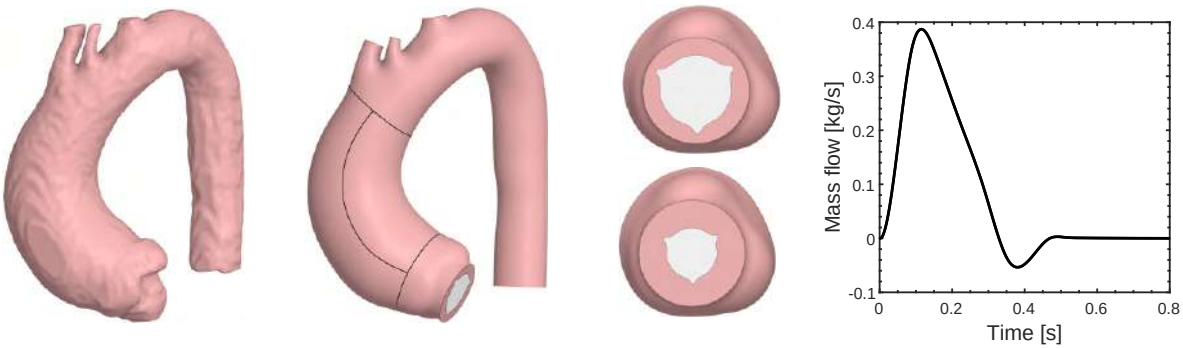

(a) (b) (c) (d)

Figure 3.1: Geometric details of the segmentation (a), processed geometry (b), projections of healthy and stenosed valves (c) and mass flow through the aortic valve (d).

3.2 Method

3.2.1 Geometry

A gated-CT scan with a voxel size of [0.3125, 0.3125, 0.75] mm from a patient suffering from ascending thoracic aortic aneurysm was segmented using a semi-automatic procedure based on local thresholding as described in [103] and manually corrected using 3D Slicer. The procedure was performed complying with the ethical standards. A smoothing and remeshing procedure was performed in order to reduce the triangulation size to a size of 0.2 mm in order to remove any staircase artifacts while preserving the segmentation details, as shown in Figure 3.1.

The centerline of the aorta was then extracted using the Vascular Modelling Toolkit [104]. A cylinder was positioned at the aortic root and aligned with the centerline, providing a planar surface over which an idealized 2-D tricuspid valve shape was projected , as shown in Figure 3.1c. The valve geometry was obtained from a previous work [105]. Two aortic valves are herein investigated: a healthy and a stenosed valve with an orifice area of 300 mm^2 and 150 mm^2 respectively, obtained after scaling the idealized shape. Supra-aortic vessels were extended five equivalent hydraulic diameters to prevent the presence of a recirculation region at the outlets. The ascending aortic wall was identified as the region between the sinotubular junction and the brachiocephalic ostium. We divided the ascending section into external (greater curvature) and internal (lesser curvature) walls by projecting the centerline onto the surface, as depicted in Figure 3.1b.

3.2.2 Computational model and boundary conditions

A polyhedral mesh was used to discretize the resultant geometry, as it enables to obtain good cell-quality and smooth transitions in curved and irregular surfaces as those present in many aneurysms. Both meshing and computing stages were performed using Ansys Fluent 22.1 (ANSYS Inc., Canonsburg, PA, USA).

An idealized mass flow profile was used to impose the inlet condition, considering a cardiac cycle of of duration $T = 0.8$ s, a peak flow of 0.387 kg/s and mean flow of 4.83 l/min, as depicted in Figure 4.4. The spatial velocity-distribution profile imposed through the idealized valve corresponded to a fully developed turbulent flow obeying a $1/7^{\text{th}}$ power-law [106, 107], as it yields a compromise between plug and parabolic profiles. The systolic jet Reynolds was 1.0×10^4 and 7.2×10^3 for the stenosed and healthy valve respectively, corresponding to a jet-center velocity of 3 and 1.5 m/s. In the absence of MRI flow data one cannot justify which profile better represents the patient's flow, as the jet profile is unique to each individual and large variability can be observed across a population, specially in the cases with aortic stenosis [108–110].

A three-element RCR windkessel boundary condition was imposed at the outlets. The parameters were tuned to ensure a predefined pulse pressure, set to 40 mmHg, and a distribution of flow proportional to the outlet areas as described in [111]. The equations for the windkessel components were solved using a second order backward differencing scheme which has been validated against analytical solutions [112].

3.2.3 Turbulence modelling

To capture and assess the effect of turbulence, we included the DSL subgrid-scale model [113] and compared the results with the case where the subgrid model was absent, which, for convenience, will be referred hereafter as laminar flow model (LFM).

On both cases, the Navier-Stokes (N-S) equations for an incompressible fluid are used to resolve the flow dynamics. When considering the LFM, no viscous losses below the grid-resolved flow are considered. However, when considering the DSL model, an additional term is added to the momentum equation in order to model the viscous energy loss associated with the subgrid scale eddies, leading to the filtered N-S for the grid-resolved velocity field ($\bar{u}$). The filtered continuity and momentum equations can thus be rewritten as:

$$\frac{\partial \bar{u}_i}{\partial x_i} = 0\,, \tag{3.1}$$

$$\frac{\partial \bar{u}_i}{\partial t} + \bar{u}_j \frac{\partial \bar{u}_i}{\partial x_j} = -\frac{1}{\rho}\frac{\partial \bar{p}}{\partial x_i} + \nu \frac{\partial}{\partial x_j}\left(\frac{\partial \bar{u}_i}{\partial x_j}\right) - \frac{\partial \tau_{ij}}{\partial x_j}\,, \tag{3.2}$$

where p is the pressure, ρ the density, ν the kinematic viscosity and τ_{ij} the subgrid scale turbulent stress tensor which models the dissipation due to subgrid scale eddies. The subgrid-scale model employs the Boussinesq hypothesis to compute the sub-grid stresses:

$$\tau_{ij} - \frac{1}{3}\tau_{kk}\delta_{ij} = -2\nu_{sgs}\bar{S}_{ij}\,, \tag{3.3}$$

where $\bar{S}_{ij} = \frac{1}{2}\left(\frac{\partial \bar{u}_i}{\partial x_j} + \frac{\partial \bar{u}_j}{\partial x_i}\right)$ is the grid-resolved strain rate and ν_{sgs} the subgrid eddy viscosity, which is

computed considering the Smagorinsky constant C_S and the local grid scale Δ as:

$$\nu_{sgs} = (C_S\Delta)^2|\bar{S}|. \tag{3.4}$$

The choice for using the dynamic subgrid-scale model over the standard Smagorinsky-Lilly or the WALE model, the later being specifically designed to accurately capture the asymptotic behaviour of wall bounded flows, is due to the pulsating nature of the cardiac flow. The large variability of the velocity field makes it difficult to define a static Smagorinski or WALE constant that would accurately model the turbulent viscosity across the spatio-temporal domain. The DSL model allows to update the Smagorinsky constant dynamically by accounting for the instantaneous velocity field to define a second filter for the equations of motion, providing a space and time varying C_S to better model the subgrid eddy viscosity. Moreover, the double-filtering process allows to compute the contribution of the small scale eddies and identify regions of laminar flow, where the subgrid viscosity will be effectively zero, enabling the model to reconstruct laminar to turbulent transition.

On the computations where DSL subgrid-scale model was active, we used SIMPLEC for the pressure-velocity coupling scheme. Second order and bounded central differencing were used to discretize pressure and momentum terms respectively, the latter being chosen due to its low numerical diffusion. For the case where subgrid-scale model was absent, PISO was used for the pressure-velocity coupling and second order differencing for both momentum and pressure terms. In both cases, a second order implicit scheme was used for temporal discretization and a time step of 0.1 ms, ensuring a Courant-Friedrichs-Lewy number below unity. At the inlet, no synthetic turbulence was imposed to ensure equal boundary conditions in all scenarios.

3.2.4 Viscosity

The fluid viscosity was modeled considering both a constant viscosity $\mu_c = 3.5$ mPa·s and a shear-thinning Carreau model [114], commonly used in literature, defined as

$$\mu(\dot{\gamma}) = \mu_\infty + (\mu_0 - \mu_\infty)\left[1 + (\lambda\dot{\gamma})^2\right]^{\frac{n-1}{2}}, \tag{3.5}$$

where the time constant $\lambda = 3.313$ s, Power-Law index $n = 0.3568$, zero shear viscosity $\mu_0 = 56$ mPa·s and infinite shear viscosity $\mu_\infty = 3.5$ mPa·s. The non-NV allows to account for the increased viscosity in low velocity regions, which could in turn affect the wall shear stress (WSS) values and the evolution of the flow structure. Fluid density was set to 1056 kg/m^3.

3.2.5 WSS biomarkers

Numerous hemodynamic indices appear in literature, however, we have limited our study to four wall shear derived biomarkers, namely: timed average WSS (TAWSS), peak systole WSS (PSWSS), oscillating shear index (OSI) and shear angle (SA). TAWSS reveals the averaged magnitude of the wall shear and is described by the following equations:

$$\text{TAWSS} = \frac{1}{T}\int_0^T |\mathbf{WSS}(t)|\, dt, \tag{3.6}$$

where T represents the duration of one cardiac cycle. PSWSS is the magnitude of the WSS field at peak systole, which occurs at 0.12 s. The OSI describes the oscillations on shear direction. When low, the flow over a given node follows a predominant direction and, when high, the flow direction fluctuates during the cardiac cycle. It is defined according to:

$$\text{OSI} = 0.5\left(1 - \frac{\left|\int_0^T \mathbf{WSS}(t)\, dt\right|}{\int_0^T |\mathbf{WSS}(t)|\, dt}\right). \tag{3.7}$$

The SA defines the directionality of the wall shear vector and is used to reveal the the presence of rotating and backward flow. It will be evaluated at peak systole and is defined as:

$$\text{SA} = \frac{2}{\pi}\arctan\left(\frac{\text{WSS}_{\text{Axial}}}{\text{WSS}_{\text{Circ}}}\right), \tag{3.8}$$

where axial and circumferential shear, $\text{WSS}_{\text{Axial}}$ and WSS_{Circ} respectively, are defined by decomposing the WSS according to the centerline direction. $\text{WSS}_{\text{Axial}}$ has a positive sign when the flow progresses along the aorta and a negative in the presence of reversed flow, while WSS_{Circ} takes only positive values as an analysis of clockwise and anticlockwise shear pattern is not considered in this study. For the analysis, nodal positions along the aorta were normalized such that 0 corresponds to the sinotubular junction, and 1 to the brachiocephalic ostium.

3.3 Results

In this section, we first assess the mesh requirements for this study. Secondly, we perform a cycle-convergence analysis to reveal the minimum number of cycles required to guarantee that the results have sufficiently converged to a constant value. Finally, we present the results obtained considering both a healthy and stenotic valve in terms of TAWSS, systolic WSS, systolic SA and OSI.

Mesh parameter	Coarse	Medium	Fine
Face size (mm)	0.50	0.35	0.25
Max. element size (mm)	1.00	0.70	0.50
No. of elements (10^6)	2.23	4.08	7.93

Table 3.1: Mesh parameters.

3.3.1 Mesh convergence

As a first step, a mesh convergence study will be performed considering the stenosed valve and the DSL subgrid model, in order to establish the mesh requirements on the most restrictive case where higher turbulence and velocity is expected. For this analysis the Carreau viscosity (CV) model was chosen as it provides a more faithful description of blood behaviour. For all meshes, the inflation layer is composed of 15 hexagonal prisms and the first layer cell height adjusted to ensure an aspect-ratio of 7. The mesh parameters are summarized in Table 3.1. Orthogonal mesh quality was above 0.9 in 99.5% of the domain on all meshes.

The mesh convergence analysis was performed by evaluating the TAWSS on both the internal and external walls. The TAWSS difference was obtained by subtracting the results from the fine mesh from the results of the coarse and medium meshes, as depicted in Figure 3.2. It was necessary to interpolate the results from the coarse and medium meshes onto the fine mesh in order to enable a node-to-node comparison. We can observe that the medium mesh is capable of resolving the flow structure near the wall with sufficient detail, with a mean error of 0.11 Pa and a maximum node-to-node difference of [-0.89, 0.59] Pa. In the case of the coarse mesh, the mean error was 0.25 Pa and maximum difference [-1.81, 1.01] Pa. The circumferentially averaged values along the centerline for both the internal and external walls are shown in Figure 3.2. We can observe how the difference between fine and medium meshes is negligible, whereas the coarse mesh underestimates significantly the averaged values in the external wall. In view of these results, we consider the medium mesh capable of resolving the flow with sufficient detail for the present study.

3.3.2 Cycle convergence

The cardiac cycle accounts for a systole and a diastole and, in the aorta, this is reflected as a fast accelerating and decelerating phase. Under these conditions, the flow develops a chaotic structure and significant variations can be observed between cycles. The flow structure present at the end of the previous cardiac cycle initializes the flow field for the following cycle and can significantly influence the new eddy structure.

Since this work is focused on performing an accurate and isolated analysis on the turbulence and viscosity models, we must ensure that the cycle averaged results are sufficiently converged. The cycle-to-

cycle variation of the time averaged field variables must be sufficiently small to negligibly affect the model comparison. In this way we ensure a fair analysis in which no uncontrolled phenomena may mask the results.

We assessed the cycle requirements considering the LES-CV model. We performed 41 cardiac cycles and computed the TAWSS_i for the cycles $i \in [2, 40]$ considering the interval $[T, iT]$. The first cycle was excluded from the analysis. The error due to the considered cycles is computed as:

$$\delta_i = \frac{1}{N} \sum_{n=1}^{N} |\text{TAWSS}_{i,n} - \text{TAWSS}_{41,n}|, \tag{3.9}$$

being N the number of nodes on the wall. The evolution of δ_i and spatially-averaged TAWSS are depicted in Figure 3.3, together with the standard deviation (σ) of TAWSS after performing 41 cycles. Mean deviations in the TAWSS field fall below 0.05 Pa after performing 15 cycles. However, spatially-averaged values stabilize faster and lie within 3.29 ± 0.01 Pa of after completing 4 cycles. The highest variability across cycles is observed in the vicinity of the jet impingement region, having a maximum $\sigma = 0.71$ Pa. The deviation field $\Delta\text{TAWSS}_i = \text{TAWSS}_i - \text{TAWSS}_{41}$ is depicted in Figure 3.4. For the present study, after considering both δ and field variations, 20 cycles will be computed to guarantee that the WSS field has stabilized.

3.3.3 Viscosity and turbulence analysis

In order to fully understand the effect of the different viscosity and turbulent models on aorta simulations, we need to analyze the different flow regimes that can be commonly observed in patients. One of the most important factors which influences the flow regime is the stenosis severity, where fusion and stiffening of aortic valve leaflets causes the orifice to deform and reduce. Due to this, two scenarios are explored: a healthy and a stenotic valve.

In favour of clarity and to facilitate the analysis of the differences, the contours for each biomarkers β

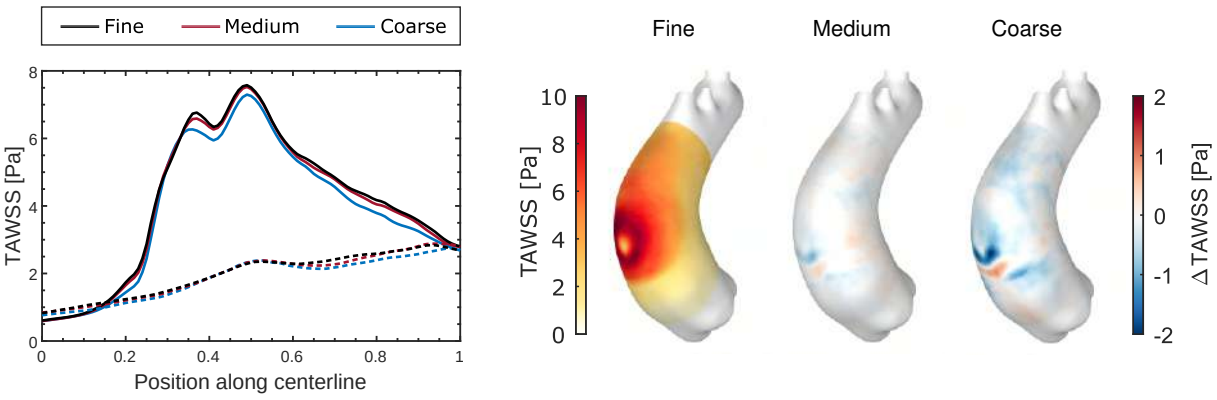

Figure 3.2: Averaged values of TAWSS along centerline for the external (solid) and internal (dashed) walls (left), contours of TAWSS on the fine mesh and contours of TAWSS difference with respect to fine mesh for medium and coarse mesh (right).

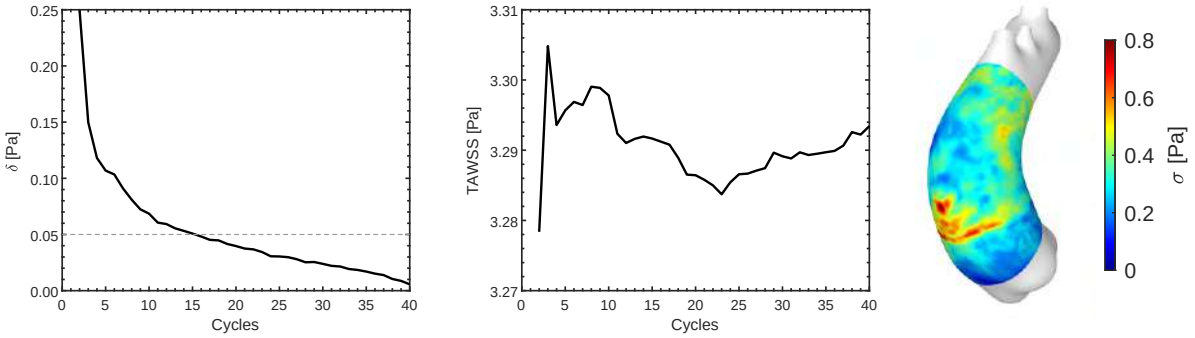

Figure 3.3: Cycle convergence analysis: δ_i (left) and spatially-averaged TAWSS (center) according to number of cycles and contours of the standard deviation of TAWSS after 41 cycles (right).

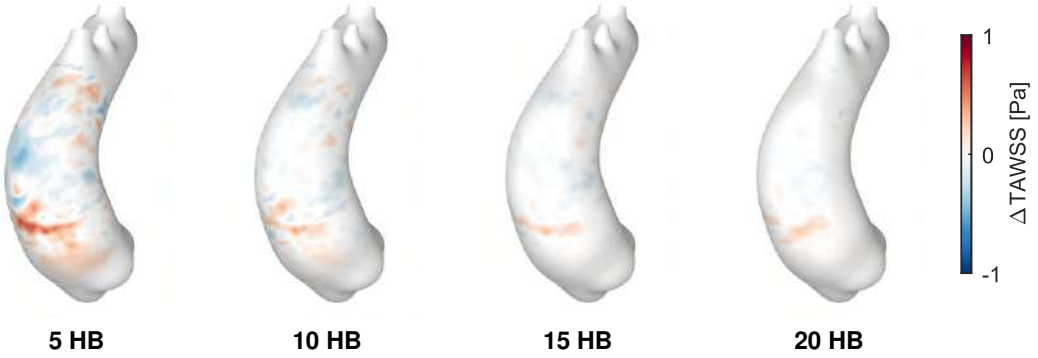

Figure 3.4: Cycle convergence analysis: Contours of local TAWSS error.

will be depicted only for LES-CV, whereas for the remaining cases only the difference with respect to the LES-CV will be depicted as $\Delta\beta_{case} = \beta_{\text{case}} - \beta_{\text{LES-CV}}$. A summary of the mean value and relative difference of the field variables is summarized in Tables 3.2 and 3.3.

Variable	Valve	LES-CV	LES-NV	LFM-CV	LFM-NV
TAWSS	Healthy	1.80	1.71	1.81	1.73
	Stenotic	3.29	3.13	3.27	3.18
PSWSS	Healthy	2.06	1.93	2.08	1.94
	Stenotic	5.09	4.84	5.14	4.96
OSI	Healthy	0.267	0.267	0.270	0.270
	Stenotic	0.247	0.245	0.245	0.252

Table 3.2: Spatially averaged values for the modeled scenarios.

3.3.3.1 Time averaged WSS

The distribution of TAWSS exhibits a similar pattern for both valves, consisting of a circular region with elevated TAWSS on the central part of the external wall, which coincides with the jet impingement region where fast moving flow expands from the collision zone upwards and sideways, creating a region with

Variable	Valve	LES-NV	LFM-CV	LFM-NV
TAWSS	Healthy	-5.04	0.10	-4.37
	Stenotic	-4.65	-0.48	-3.36
PSWSS	Healthy	-6.14	1.19	-5.50
	Stenotic	-5.01	0.94	-2.63
OSI	Healthy	0.19	1.35	1.30
	Stenotic	-0.79	-0.91	2.05

Table 3.3: Relative difference of spatially averaged values for the modeled scenarios with respect to the LES-CV case.

intermediate shear, as depicted in Figure 3.5. Notable differences can be observed between the two valves, as values in the high shear region range between 2 to 4 and 6 to 10 Pa in the healthy and stenotic case respectively. The high shear region is more compact and defined in the stenotic case. For both valve conditions, the differences between the reference LES and the laminar models reveal that the LES achieves a greater dispersion of the high shear region, as on the LFM contours we can observe a negative (blue) band surrounding the inferior border of this high shear region. Considering all the models, the mean TAWSS value for the healthy and stenotic valve was, respectively, 1.762 and 3.22 Pa, with a standard deviation of 0.050 and 0.075 Pa. We observe a larger deviation in the stenotic scenario.

Assessing the viscosity effect reveals that both CV cases develop higher TAWSS with respect to their NV counterparts. Under stenotic conditions, assuming NV causes an underestimation of 4.7% (LES) and 2.9% (LFA). This holds for the healthy condition: underestimation of 5.0% (LES) and 4.5% (LFA). Turbulence model assessment reveals that, under CV, the LFM exhibits differences below 0.5% from its LES counterpart, whereas under NV, the LFM overestimates TAWSS by 0.7-1.4%. This indicates that accounting for non-NV has a greater impact than accounting for a subgrid model. Furthermore, it is revealing to observe the impact of the viscosity model is amplified under a LES turbulence model, since the difference between LES models (4.7-5.0%) is greater than between LFM models (2.9-4.5%). In order to gain further insight into these differences, the circumferentially averaged values along the centerline are plotted for both internal and external walls on Figure 3.6. The best match of LES-CV is obtained when considering a LFM-CV model, which is in agreement with the values given in Table 3.3. To better

Turbulence model	Healthy		Stenosis	
	Systole	TA	Systole	TA
Laminar	1.160	1.277	1.148	1.290
LES	1.165	1.286	1.166	1.297

Table 3.4: Non-Newtonian importance factor under LES and laminar turbulence models for healthy and stenotic valves.

understand viscous phenomena, we define the non-Newtonian importance factor [115] as the ratio between

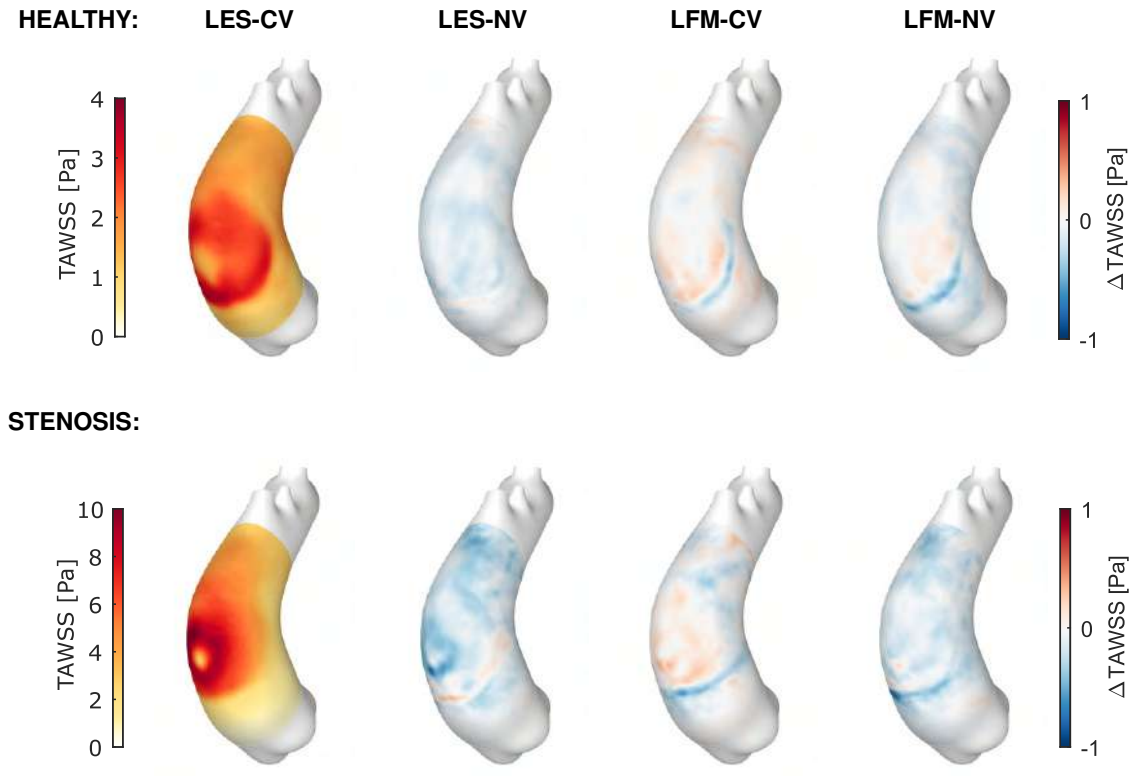

Figure 3.5: TAWSS for healthy (top) and stenotic valve (bottom).

the dynamic viscosity and the Newtonian viscosity: $IF = \mu/\mu_\infty$. The systolic and time averaged IF are given in Table 3.4. The values of IF are higher for LES models under both valve conditions, which shows that the importance of non-NV depends on the turbulence model used. Accounting for subgrid viscosity alters the eddy development and thus the shear rate in the vicinity of the wall, which in turn determines the fluid viscosity and the IF. The contours of IF are depicted in Figure 3.7, where it can observed that the areas of elevated IF are concentrated near the aortic root. For the case of the healthy valve, we can observe that the differences between the two contour plots are significant, since region near the aortic root in the LFM case shows a reduced IF in comparison to the LES case.

3.3.3.2 Peak systole WSS

The systolic WSS depicted in Figure 3.8 reveals distinct patterns between the valve types. In the healthy case, low values are observed along the aortic wall with the exception of the sinotubular junction. This contrasts with the stenosed case, where we can clearly observe the characteristic features that result from the jet impinging on the wall. This can be explained since a healthy valve results in a lower jet velocity and therefore the time required for the jet to develop and arrive to the wall is higher. For the stenotic case, a highly-localized high shear region on the external wall can be observed, with the remaining aorta subject to low shear levels.

A predominant underestimation of shear on both NV cases can be observed, similarly to the observation

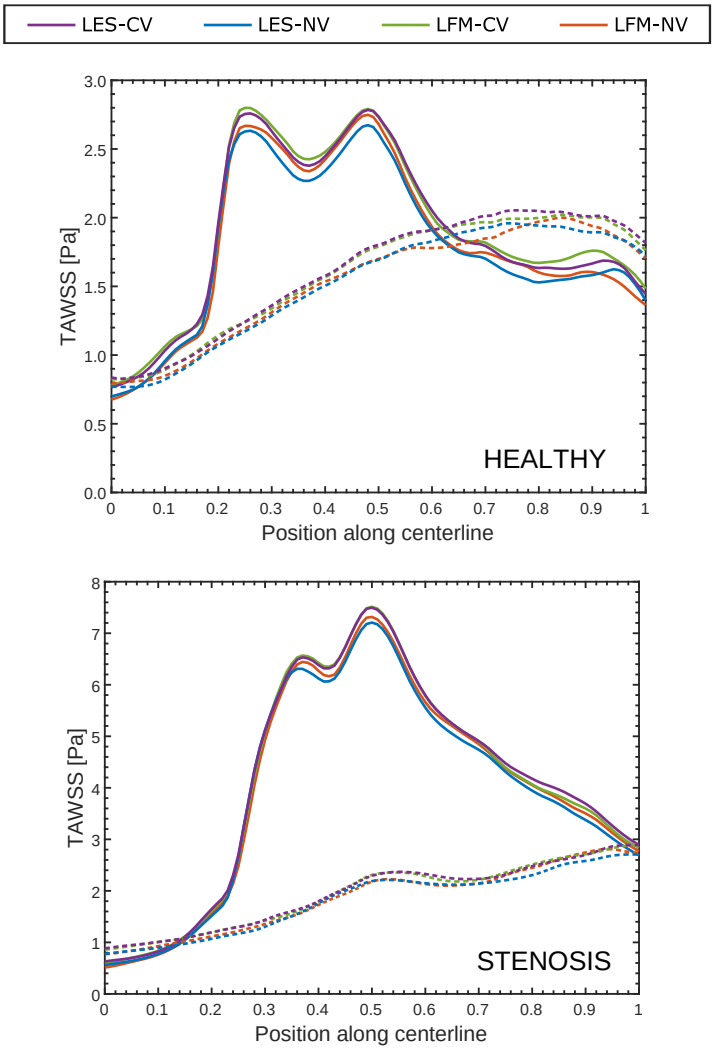

Figure 3.6: Averaged values of TAWSS along centerline for the external (solid) and internal (dashed) walls for the case with healthy (left) and stenotic (right) valve.

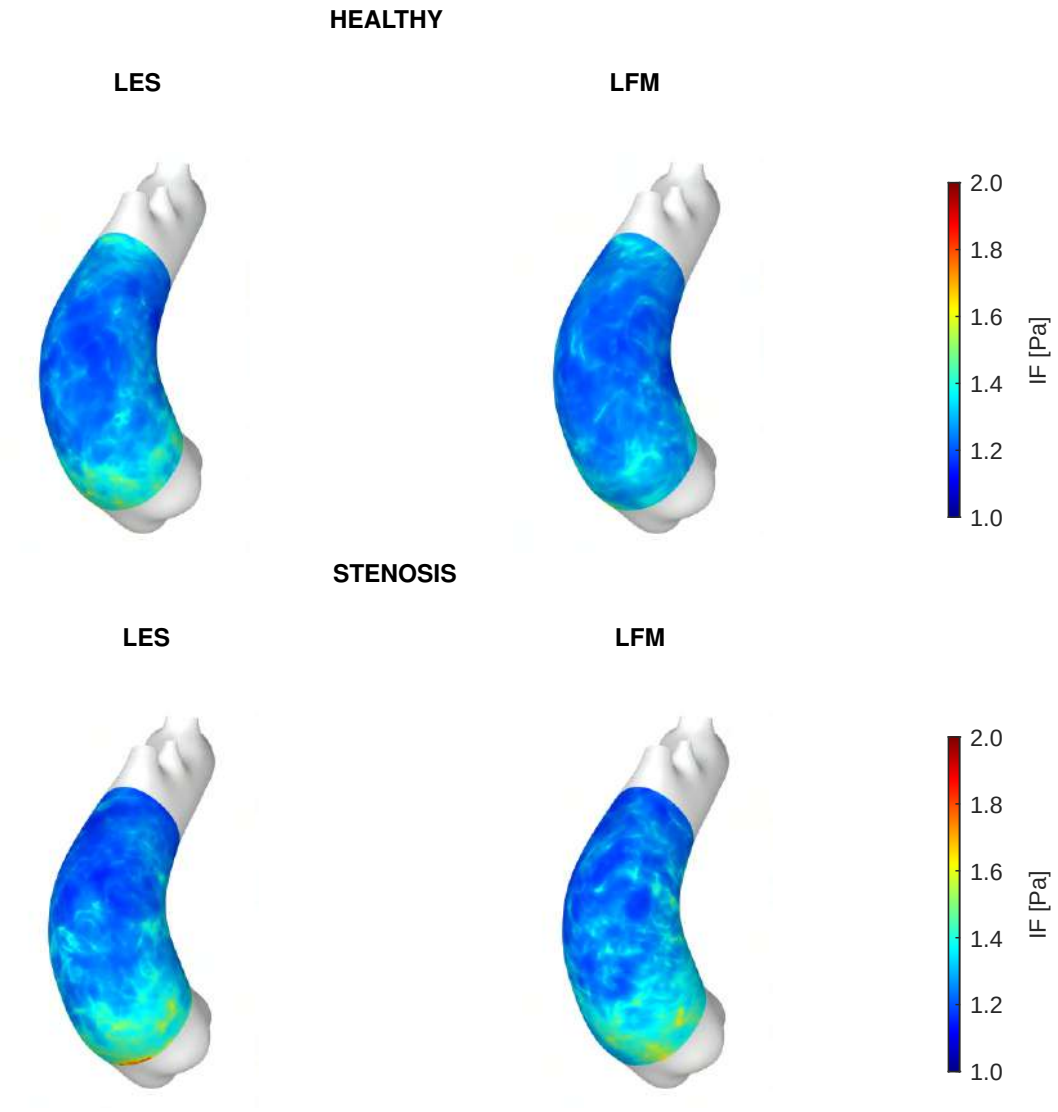

Figure 3.7: Non-newtonian importance factor for the healthy (top) and stenotic cases (bottom).

on TAWSS. The LFM-CV shows smaller differences as confirmed by Table 3.3, with the PSWSS being overestimated by 1.2% and 0.9% for the healthy and stenotic valve conditions respectively. The IF at peak systole, given in Table 3.4, is higher on LES models, as occurred for TAWSS.

3.3.3.3 Shear angle

The SA reveals different patterns for each valve type. Considering the healthy valve, the direction of the systolic WSS reveals a region with reversed flow in the central section of the aorta, as indicated by the negative SA values on Figure 3.9. As can be observed, in all models the shear direction is identical throughout the domain with the exception of a banded region where the reversed flow of the midsection collides with the advancing flow emerging from the sinotubular junction. The banded stripes depicted in

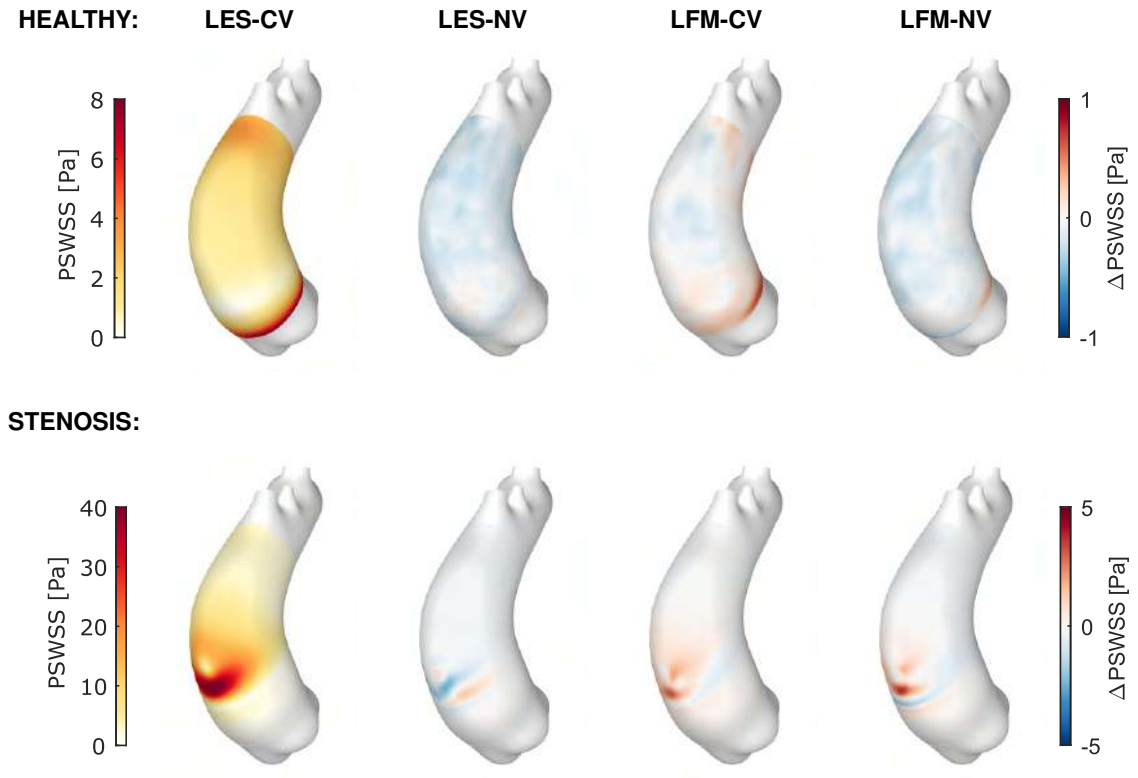

Figure 3.8: PSWSS for healthy (top) and stenotic valve (bottom).

the ΔSA plots indicate that the collision band is minimally distorted. Considering the Lam-New case, which exhibits the largest differences, the maximum width of the band is 2.6 mm. When analyzing the stenotic valve, reversed flow can be observed in the inferior section of the external wall. The rest of the aorta wall has a positive SA close to 1, with the exception of the region where the jet impinges the wall, where the SA ranges between [0, -0.5]. On the LES-NV case the reversed flow region is slightly retreated, approximately 1 mm, whereas on the laminar cases the reversed flow region has advanced 1-2 mm. The results of SA suggest that, although the levels of WSS might be altered by the modelling assumption, the WSS direction at peak systole is preserved.

3.3.3.4 Oscillating shear index

The OSI of the reference LES-CV case reveals similar patterns on both valve scenarios, as depicted in Figure 3.10. The central section of the external wall is exposed to low OSI levels inferior to 0.1, which coincides with the high TAWSS region. This low OSI region is surrounded by high OSI which coincides with the low TAWSS. This can be related to the directional dominance of the impinging jet which produces a well defined flow pattern over the wall directed upstream. On the contrary, the inferior section is subject to reversed flow and the creation of a recirculating region, where the flow pattern is disrupted. The region surrounding the jet impingement is exposed to decaying vortexes which travel along the wall with reduced energy and higher instabilities, leading to a more chaotic flow structure. The combination of low TAWSS

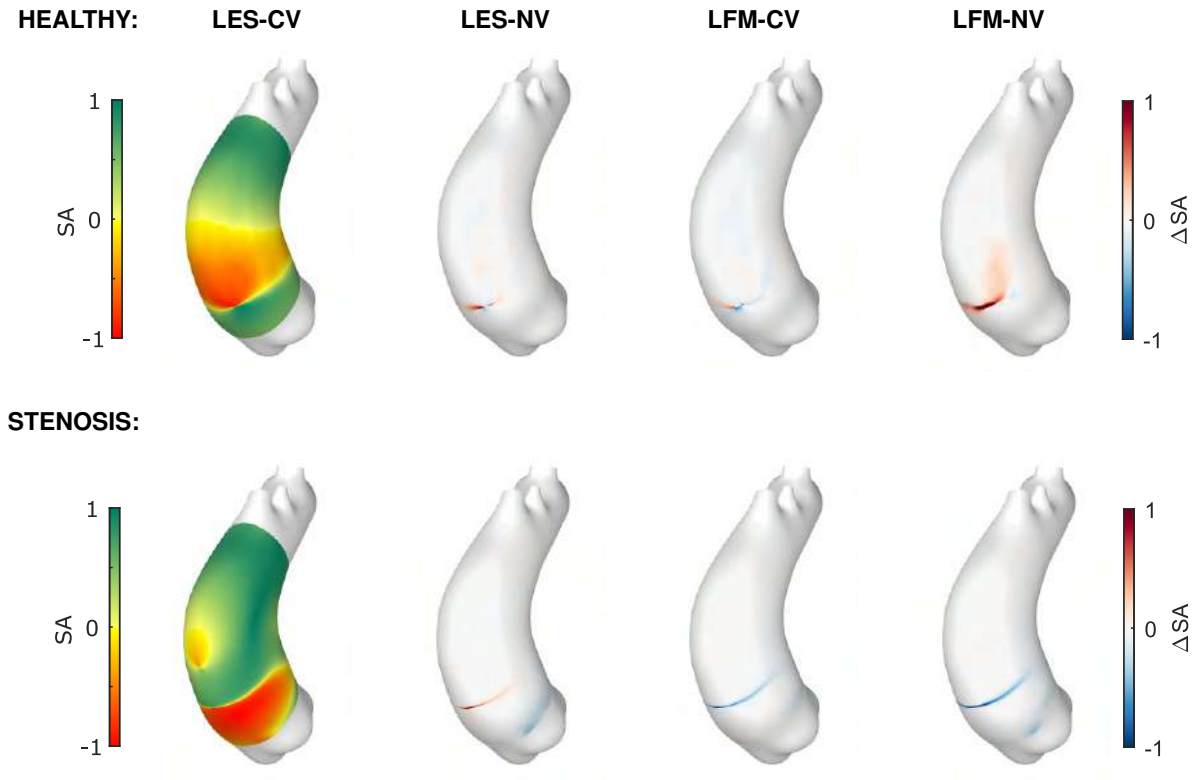

Figure 3.9: SA for healthy (top) and stenotic valve (bottom).

and continuous flow disruption inevitably leads to the creation of a high OSI region.

The comparison between models shows a good agreement on the low OSI central region of the external aortic wall for both valve scenarios. Despite the local differences on the lower section of the aortic wall, all cases exhibit high OSI levels on the inferior section. On the region surrounding the ostium, variations can also be observed. The deviations on Figure 3.10 reveal a complex pattern which impedes further conclusions. The values in Table 3.3 reveal smallest averaged discrepancies when considering the LES-NV (<0.8%) and biggest when considering LFM (0.9-2.1%).

3.4 Discussion

In this work we have quantified the combined effect of LES and non-NV on WSS derived biomarkers and concluded that including non-NV has a greater impact on the results in comparison to the inclusion of the LES subgrid model. We observed a reduction on the TAWSS and PSWSS when considering NV, which agrees with previous studies [87, 116, 117]. Spatially averaged values showed that TAWSS is underestimated by 4.7-5.0% if constant viscosity is assumed under a LES model, although this value drops to 2.9-4.5% when considering a laminar model. The reduction in WSS due to NV could be explained by a nonphysical reduced viscosity in the vicinity of the wall. As we approach the wall the velocity asymptotically decreases to zero thus the non-Newtonian behaviour is magnified. Non-Newtonian effects become more apparent in low velocity regions and it is thus vital to account for this shear dependent

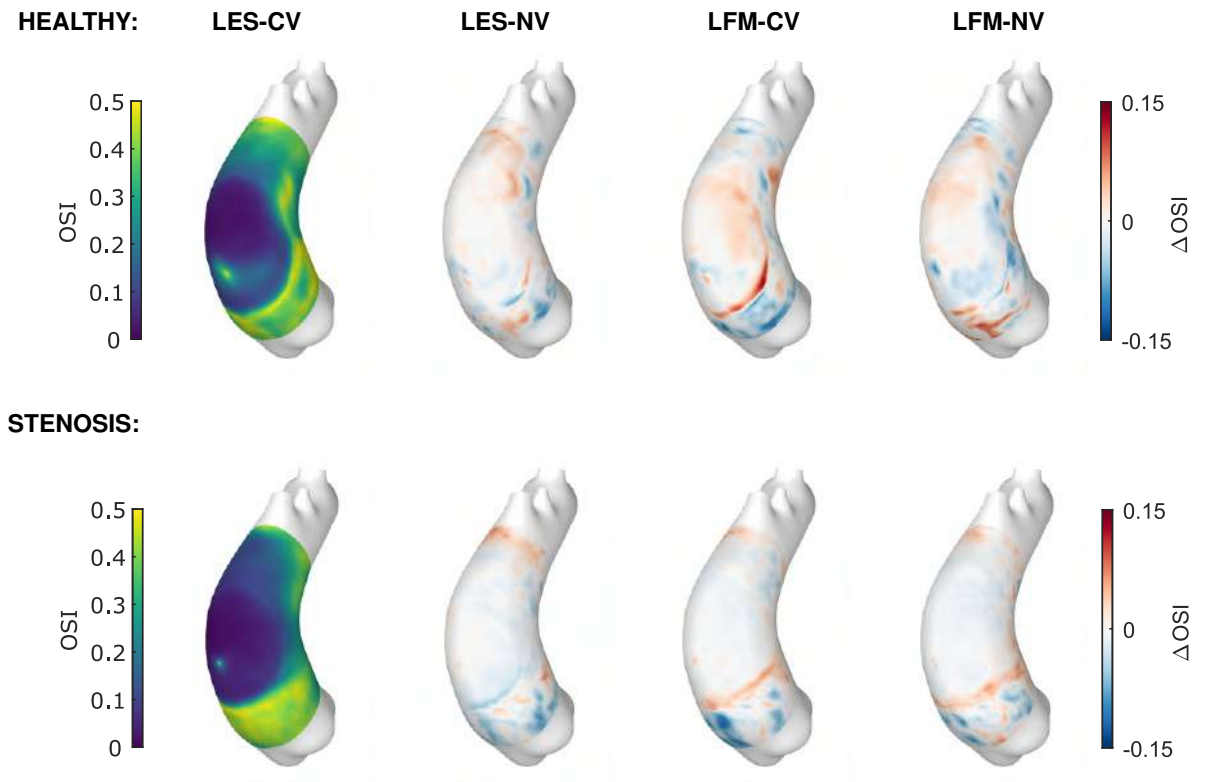

Figure 3.10: OSI for healthy (top) and stenotic valve (bottom).

viscosity when accurately modeling biochemical processes. For example, it has been proven that non-NV should be modeled when analysing lipoprotein deposition in regions with flow recirculation [117], platelet activation potential [87] and monocyte adhesion to endothelian cells on atherosclerotic lesion [116]. The regions where reversed flow and recirculation are expected, as the vicinity of the aortic root, have shown an elevated non-Newtonian IF, as shown in Figure 3.7. This observation provides additional proof which suggest that non-NV should be used when accurate biochemical processes are modeled. Moreover, the IF was greater in the case of stenosis, where higher velocities are expected and, thus, non-Newtonian effects should be diminished. However, the jet is expelled through a smaller opening and thus, instead of having an uniformly distributed flow resembling a Hagen-Poiseuille flow, we observe rather a complex flow structure which generates recirculating and low velocity regions in the vicinity of the sinotubular junction. The IF has revealed a slight increase of non-Newtonian effects when considering the LES model under both valve conditions, which could account for the larger differences in WSS between the LES cases. It is possible that the subgrid viscosity, which contributes to dissipating the eddy structure, leads to a diminished velocity field which amplifies the non-Newtonian phenomena in the LES scenarios.

Differences between turbulence models with an equal viscosity model are surpassed by the differences between viscosity models with an equal turbulence model, as shown in Table 3.3. Two interesting findings regarding the combination of viscosity and turbulence models are worth mentioning. Firstly, the impact of the turbulence model is greater when considering a NV and, secondly, the impact of non-NV is greater

when including a subgrid turbulence model. Despite this, we have observed that the turbulence model has a marginal impact on the results and we conclude that high resolution laminar models are capable of sufficiently resolving the flow dynamics, as the relative difference in TAWSS for LFM-CV is below 0.5%, agreeing with the results of [97]. Although spatially-averaged values show limited discrepancies due to turbulence model choice, we must consider that the additional subgrid viscosity provided by the LES model affects the eddy development and breakdown which consequently alters the WSS pattern along the wall, as shown in Figure 3.5. A final consideration in this regard is that both the laminar and LES computations required equivalent computational resources, hence no clear benefit is gained by considering a laminar model.

At present, no study has examined the discrepancies on SA. Our results have shown that SA exhibits negligible differences amongst the considered models, one possible explanation being that the SA is defined by the bulk flow pattern, which is mainly determined by the jet profile and only marginally by the modelling assumptions.

The results of OSI exhibit significant deviations amongst the studied models. The differences due to the viscosity assumptions agree with [118], however this study focused on abdominal aneurysm where the Re is lower and the flow profile has damped temporal variability. Despite the OSI discrepancies between the herein considered models, the pattern consisting of a low OSI region in the external wall surrounded by high OSI is preserved in all cases. Since OSI quantifies the flow direction fluctuations and regions exposed to vortexes are exposed to chaotic flow disruptions, it is possible that the analysis on high OSI regions would benefit from computing additional cycles in order to obtain a smoother comparison.

The present study exposes the importance of assessing different aortic valve conditions as the flow structure and WSS patterns are severely affected by the jet characteristics. Thus, studies focused on computational strategies should be performed on a wide range of flow conditions.

We have observed that significant differences can appear on the herein analyzed set of fluid biomarkers. However, it is surprising that these differences can be just as important as the cycle-to-cycle variations that occur if insufficient cycles are considered for the time averaging process. This is due to the differences in the flow structure present in the fluid domain before each cardiac cycle begins. The flow of the previous cycle conditions how the flow will develop during the following cycle. Thus, when comparing different models and computational strategies, we must ensure that the time averaged results have sufficiently stabilized in order to not mask the differences caused by the numerical methods alone. This work suggests that studies focused on evaluating the effect of numerical methodologies should be performed considering a minimum of 15 cardiac cycles to ensure errors in TAWSS remain below 0.05 Pa. As much as the difference between models may seem considerable, it is obvious that the differences between the healthy and stenosis valves are much more significant. Since the biomarker distribution pattern is preserved in all cases, the choice of model has minimal impact in comparison to including a spatially and temporally calibrated jet

[119]. However this may be, our results demonstrate the importance of considering appropriate turbulence and viscosity models when developing in-silico hemodynamic analyses for the ATA. The effect of the model combinations has been quantified and could serve to justify modelling assumptions when dealing with ATA simulations and potentially aid in establishing standardized workflows for clinical applications.

3.4.1 Limitations

We did not tackle on this analysis the differences in turbulent kinetic energy in the flow as we decided to exclusively analyse the wall shear derived biomarkers. Previous studies have analyzed turbulence and its dependency on the modelling assumptions including valve shape and jet velocity [106] and different turbulence models [98, 100].

It is fair to criticize the choice of an idealized valve shape for the healthy and, specially, the stenosed case since idealized shapes such as the one herein presented are rarely observed in real patients. However, our work was not intended to precisely characterize a patient specific condition but rather to compare the influence of the modelling assumptions in a rigorous manner. Moreover, we have performed this analysis using a projection of the valve opening and imposing a spatially varying profile, rather than modelling the 3D structure of the valve leaflets. This simplification has a direct effect on the flow structure, specially in terms of turbulence generation [106]. Further analysis is required to correctly understand the effect of modelling choices under patient-specific conditions, such as highly stenosed patients with highly irregular valve opening. Furthermore, the effect of the modelling assumptions would differ if we accounted for wall and valve motion, as it has been proven that the FSI effect significantly alters WSS [120].

It is clear that numerous improvements can be incorporated in a pursuit of fidelity. However, we must consider that not all biomarkers require an equal modelling complexity to provide the necessary insight to aid clinicians during the diagnosis. By understanding the influence which modelling assumptions have on the results, one is capable of establishing a justified balance between accuracy requirements and modelling complexity. Achieving this balance is of vital importance as higher complexity implies increased computational cost, an issue which is currently limiting the expansion of computational tools for clinical use.

3.5 Conclusions

In this work, a thorough analysis of the combined effect of viscosity and turbulence models on WSS biomarkers has been performed. Firstly, it has revealed that non-NV have a greater impact on WSS than LES subgrid model. In addition, NV has shown to cause an underestimation of shear levels: 4.7-5.0% considering LES, 2.9-4.5% considering LFM. We thus encourage the use of non-NV for ATA simulations as it will prevent underestimation of WSS. It is noteworthy that the contribution of a non-NV

is amplified when combined with a subgrid model, as can be concluded from the larger differences in TAWSS exhibited between LES models than between laminar models. This finding indicates that the LES model is augmenting the non-Newtonian behaviour of the fluid. Overall, in all scenarios the biomarkers followed a similar distribution along the aortic wall, where the main differences were due to a distinct expansion and decay of the jet along the wall. Lastly, it is revealing to observe that the cycle-to-cycle variability has a significant impact if insufficient cycles are assessed and consequently can mask the differences between the numerical models. Be that as it may, a precise knowledge of the impact of the chosen modelling assumptions is mandatory if we pursue to develop a new generation of tools certified for clinical use, where the requirements of trustworthiness and reproducibility of results are of paramount importance.

Chapter 4

CFD biomarkers for aneurysm growth prediction

After having assessed the influence of the computational methodologies on WSS derived biomarkers and having determined that LES turbulence modelling combined with a non-Newtonian viscosity provides the most trustworthy CFD results, we are in a position to perform a study on a set of both stable and dilating aneurysm in order to determine the relationship between aneurysm growth and CFD derived biomarkers. In this chapter, in addition to the WSS derived biomarkers presented in Chapter 3, we will also assess a set of flow derived biomarkers obtained from the fluid velocity field.

4.1 Introduction

Aneurysm growth rate is one of the two measurements which determine if surgical procedure is required. However, accurately measuring growth rate is challenging and requires at least one follow up angiography. Therefore, the development of predictive tools capable of estimating growth rate from an unique acquisition would provide unprecedented insight into the aneurysm's condition, which would facilitate the diagnosis process. This tools could be used to identify patients with a potentially fast growing aneurysm and aid in the planning of follow-up exams, diminishing the risk of early aneurysm rupture.

As explained in Chapter 1, dilatation of the aorta causes an increase in hoop stress and, thus, leads to an increase of risk of rupture and dissection [8, 9]. This is why it is mandatory to continuously monitor patients in order to perform prophylactic surgery repair when the aortic diameter reaches the threshold (45-50 mm) or when growth rate surpasses 3 mm/year, as indicated by current clinical practice guidelines [7]. A fast growing aneurysm has the risk of reaching a critical size before the follow-up exam is performed. Additionally, a fast growing aneurysm may indicate that the aortic wall has rapidly weakened and deteriorated and thus the rupture may occur in the presence of lower stresses, or, in other words, with a smaller diameter and under lower aortic pressure. Due to these two reasons, patients with high growth rates are eligible for surgery even when the aneurysm size is below the diameter threshold.

The risk of developing aortic aneurysm depends on age, sex, history of hypertension, genetic conditions affecting tissues such as Marfan's Syndrome and Ehlers-Danlos, aortic stenosis and the presence bicuspid aortic valve (BAV) [3–6]. These factors do not only affect the triggering of the aneurysm, but also the growth rate. Analyses on ascending thoracic aortic aneurysm (ATAA) growth rate patterns have suggested that unsurveyed aneurysm follow an exponential growth [121, 122]. However, availability aneurysm follow-ups with at least three angiographies sufficiently spaced in time are scarce, thus limiting the possibilities to perform these kind of studies. This is why aneurysm development has usually been assessed by considering a linear growth rate, since only two angiographies are required. A recent study following 332 patients over an averaged period of 6.7 years reported averaged growth rates of 0.3 and 0.2 mm/year for women and men respectively [123]. Previous studies, performed on smaller populations or with shorter screening periods, measured averaged growth rates ranging from 0.14 to 1.4 mm/year and

reported patients which exceeded 2 mm/year [4, 5, 124–126].

Despite the current guidelines, multiple cases of rupture have been reported below thresholds and, oppositely, some aneurysms have remained stable while their diameter exceeded the thresholds. This suggests that a better understanding of the pathology is required [13]. For this purpose, various researchers have focused on analysing how the aortic wall properties change during the dilatation process and the factors which cause certain components of the wall to degrade. Various studies focused on the analysing aortic wall degradation using histology and revealed that aneurysmal tissue presented disorders in elastin, collagen and smooth muscle cells [14, 15]. Others studies have focused on the mechanobiology of the aortic wall analysing risk factors which affected the aortic wall properties [17] and assessing how increased stiffness and reduced thickness are related to risk of rupture [21, 127, 128].

However, in order to understand the underlying mechanisms which promote aneurysm growth, it is necessary to investigate the long term effect of different stressor agents originated from the hemodynamic flow and wall conditions. It is suggested that disrupted hemodynamic flow is associated with aneurysms incidence, specially in BAV patients [34, 35]. Endothelial cells are exposed to different conditions depending on the patient specific hemodynamics and this can trigger different biological processes such as cell alignment and elongation [129], endothelial damage and the release of biochemical messengers, which can affect the cellular response and thus the aneurysm evolution [130, 131]. Post-operatory samples of aneurysmal tissues have revealed marked difference when compared to healthy tissue. A study combined imaged-based computational models with tissue mechanical and microstructural characterization revealed that high WSS was linked to media degeneration and reduced wall thickness, elastin levels and smooth muscle cell count [36, 37]. On BAV patients, histology analysis and 4D MRI flow data revealed that extra cellular matrix dysregulation and elastin degeneration were associated with regions of increased WSS [132].

Following these lines of research, various works have assessed the relationship between fluid biomarkers and aneurysm size using 4D MRI flow imaging and CFD modelling. Increased flow jet angle with respect to aortic axis has been shown to be related to aortic diameter, indicating that misaligned blood flow could promote aneurysm growth [133]. Elevated vortical and helical flow has been observed on dilated aortas when compared to controls [134]. The WSS topological skeleton has shown marked differences between aneurysmal and control aortas, making it a potential indicator for risk stratification [135]. Patient-specific valve pathologies greatly influence WSS and oscillatory shear index (OSI), being aortic stenosis a mayor cause for increased WSS [136].

Despite the great insight on patient-specific conditions that these studies provide, limited consensus has been achieved regarding the role played by hemodynamics on aneurysms development, since it is challenging to decipher, whether, hemodynamic variables promotes aneurysm growth, or if geometric changes are causing flow disruption. To bring some light to this subject, some authors, using 4D MRI

flow measurements, have focused their efforts on quantifying the relationships between patient specific hemodynamics and aneurysm growth rate instead of aneurysm diameter. A longitudinal study including 30 ATA patients who underwent MRI angiography at baseline and after a one-year follow-up period showed that elevated flow eccentricity and reduced WSS in the inner aortic curvature were correlated with growth rate [137]. Another study used three-year spaced CT angiographies for evaluating growth and concluded that WSS angle correlated with aortic growth on BAV patients [138]. Similar finding have been observed when assessing growth on ATAA patients with Marfan's syndrome [39].

Longitudinal studies have the potential to unveil the long term effect of different biomarkers on the evolving aneurysms. However, few works of this kind are currently available in literature. This is a consequence of the limited availability of longitudinal clinical data, since current clinical protocols do not consider CT or MRI angiography until an aneurysm has reached a significant size with potential for rupture. Moreover, the growth of typical aneurysms has been recently reported to be 0.2-0.3 mm/year, thus a large time span between acquisitions is required to observe significant changes. To add further complexity to the subject, in order to make patient-specific hemodynamic analyses, the angiographies need to be accompanied by flow measures, further limiting the availability of eligible patients. Considering the need to unveil the long-term effects of hemodynamics on aneurysm development, we present an analysis of the relationship between CFD-derived biomarkers and ATAA growth on a heterogeneous cohort of patients, including tricuspid and bicuspid aortic valves.

4.2 Clinical data

A data-base 33 patients with double CT scans with voxel size [0.3125, 0.3125, 0.75] mm provided by the University Hospitals of Rennes, Dijon and Toulouse (France) was considered in this study. Patients with genetic tissue disorder such as Marfan's or Ehlers-Danlos syndrome were excluded. The patients had a mean age of 57.3 years when the first CT scan was acquired, with a minimum 27.2 and a maximum 78.1 years. The average height was 1.71 m. The cohort was divided in 25 males and 8 females. The cohort consisted of sixteen tricuspid aortic valves, fifteen bicuspid type 1 valves with left-right coronary cusp fusion and two patients with type 0 bicuspid valve, the later consisting of one patient with left-right cusps and another with anterior-posterior cusp. The acquisitions had a minimum spacing of 11 months. The average spacing was 42.2 and 39.8 months for tricuspid and bicuspid valve patients, respectively. The data acquisition was performed following the ethical standard and complying with the national regulation.

4.2.1 Aortic valve area and jet velocity

Echocardiographic measurements of valve area and peak velocity were available for 20 patients, thus a direct calibration of valve area and inlet velocity was possible. MRI 4D flow acquisitions were available

No.	Age (years)	Height (m)	Sex	Scan interval (months)	Valve type
1	78.1	1.68	M	53.2	T
2	62.2	1.60	M	47.7	T
3	60.5	1.76	M	47.6	T
4	47.5	1.69	M	36.1	T
5	73.9	1.57	F	11.9	T
6	55.9	1.70	F	13.0	T
7	63.6	1.66	M	51.6	T
8	57.2	1.75	M	27.8	T
9	58.9	1.61	F	19.2	T
10	51.6	1.68	M	23.5	T
11	49.8	1.75	F	63.9	T
12	60.2	1.94	M	52.9	T
13	59.4	1.81	M	67.6	T
14	65.0	1.75	M	18.6	T
15	66.0	1.75	M	89.6	T
16	63.0	1.60	F	51.2	T
17	51.7	1.72	M	48.0	B_1
18	47.5	1.75	M	18.6	B_1
19	76.9	1.68	M	17.2	B_1
20	53.7	1.82	M	18.3	B_1
21	60.1	1.65	F	13.9	B_1
22	51.1	1.78	M	22.7	B_1
23	66.9	1.83	M	47.9	B_1
24	58.1	1.69	M	16.7	B_1
25	27.2	1.74	M	16.3	B_1
26	72.8	1.80	M	11.0	B_1
27	64.1	1.66	M	101.0	B_1
28	50.0	1.74	M	42.4	B_1
29	68.0	1.75	M	28.3	B_1
30	49.0	1.60	F	80.0	B_1
31	38.6	1.70	M	46.6	B_1
32	53.2	1.63	F	25.1	B_0
33	29.1	1.62	M	85.2	B_0

Table 4.1: Clinical data of the patient dataset.

Parameter	Men		Women	
Age	<65	>65	<65	>65
A_{Nor}/Height (cm^2/m)	1.9	1.75	1.6	1.56
V_{Nor} (m/s)	1.19	1.22	1.23	1.25

Table 4.2: Aortic valve normative values for peak velocity valve area-to-height.

for 5 patients and were used to measure the peak velocity of the aortic jet. For the remaining 8 patients, no velocimetry measurements were available in the register. In order to calibrate the aortic valve on these subjects, normative values for peak velocity and normalized valve area-to-height were imposed according to [139]. The normative values according to age range and sex are summarised in Table 4.2. When MRI 4D velocimetry was available, the calibration of the aortic valve area (A_{MRI}) was performed by scaling the normative area (A_{Nor}) by the ratio between the the normative V_{Nor} and measured (V_{MRI}) velocity as:

$$A_{\mathrm{MRI}} = A_{\mathrm{Nor}} \frac{V_{\mathrm{Nor}}}{V_{\mathrm{MRI}}}. \tag{4.1}$$

The cohort's measured and estimated aortic jet velocities are given in Table 4.3.

4.3 Methods

4.3.1 Geometry

The angiographies were segmented using 3D Slicer [140] by means of a semi-automatic procedure based on local thresholding, as described in [103], and posteriorly underwent manual correction. Segmented geometries were processed in a computer-aided design software. Smoothing and remeshing techniques were used to remove staircase artifacts and irregularities on the surface while preserving segmentation details, making the geometry suitable for CFD analyses, as shown in Figure 4.1. The centerline of the resultant geometries were extracted using the Vascular Modelling Toolkit [104]. A planar surface perpendicular to the centerline was created on the aortic root where an idealized valve geometry was projected. The idealized valve geometry was calibrated with patient data according to the valve morphology and valve area. In this study, three different aortic valve morphologies were considered: tricuspid and bicuspid types one and zero. A depiction of the valve geometries is shown in Figures 4.2a-c. The ascending aortic wall, spanning from the sinotubular junction up to the brachiocephalic ostium, was divided into two regions: the external and the internal walls, were the former contains the greater curvature and the later the lesser curvature, as depicted in Figure 4.2d. This enables to independently assess the fluid biomarkers on each region.

No	Valve type	Acquisition modality	Measured velocity (m/s)	Measured valve area (cm^2)	Estimated velocity (m/s)	Estimated area (cm^2)
1	T	-	-	-	1.22	2.94
2	T	ED	1.66	3.30	-	-
3	T	ED	1.48	3.13	-	-
4	T	ED	4.51	1.05	-	-
5	T	-	-	-	1.25	2.45
6	T	ED	1.54	3.51	-	-
7	T	ED	1.40	2.47	-	-
8	T	-	-	-	1.19	3.33
9	T	ED	1.33	3.45	-	-
10	T	ED	1.00	3.80	-	-
11	T	ED	1.50	2.30	-	-
12	T	-	-	-	1.19	3.69
13	T	ED	1.90	2.50	-	-
14	T	MRI 4D	1.41	-	-	3.06
15	T	MRI 4D	0.98	-	-	3.06
16	T	MRI 4D	1.42	-	-	2.56
17	B_1	-	-	-	1.19	3.27
18	B_1	ED	1.40	3.00	-	-
19	B_1	ED	2.51	1.92	-	-
20	B_1	ED	2.40	1.40	-	-
21	B_1	-	-	-	1.23	2.64
22	B_1	ED	3.99	0.81	-	-
23	B_1	ED	4.02	0.95	-	-
24	B_1	ED	2.18	2.20	-	-
25	B_1	-	-	-	1.19	3.31
26	B_1	ED	2.12	1.95	-	-
27	B_1	ED	3.70	1.40	-	-
28	B_1	ED	4.01	0.70	-	-
29	B_1	MRI 4D	1.53	-	-	3.06
30	B_1	MRI 4D	1.66	-	-	2.56
31	B_1	-	-	-	1.19	3.23
32	B_0	ED	2.32	1.52	-	-
33	B_0	ED	4.00	1.30	-	-

Table 4.3: Measured and estimated peak velocities (ED = Echo-Doppler velocimetry).

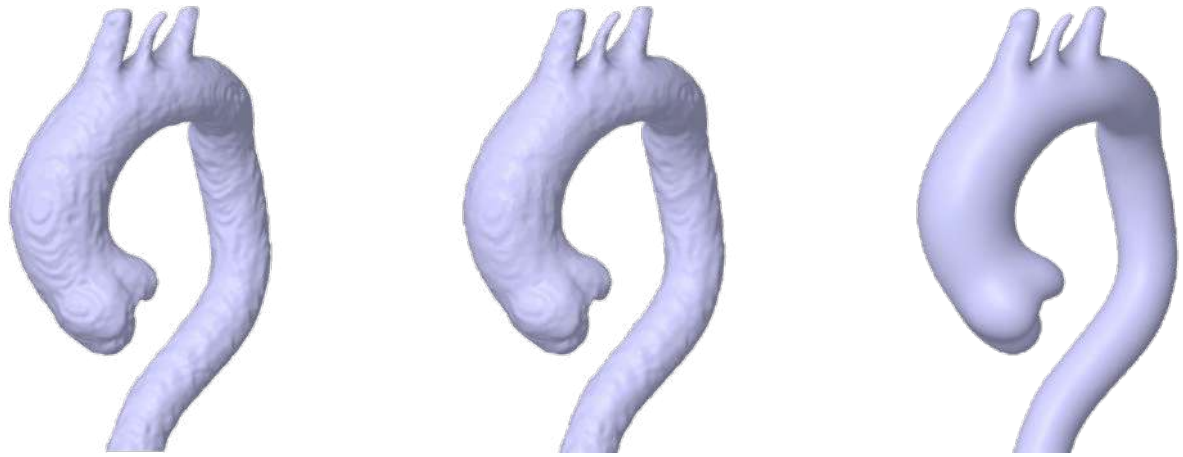

Figure 4.1: Smoothing procedure performed on all models.

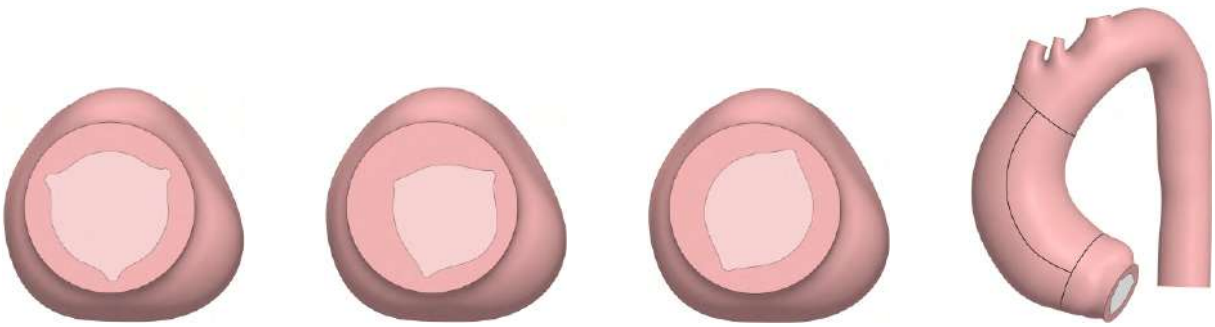

(a) Tricuspid (b) Bicuspid type 1 (c) Bicuspid type 0 (d) 3D model

Figure 4.2: Geometric details of the valve geometry and final 3D model.

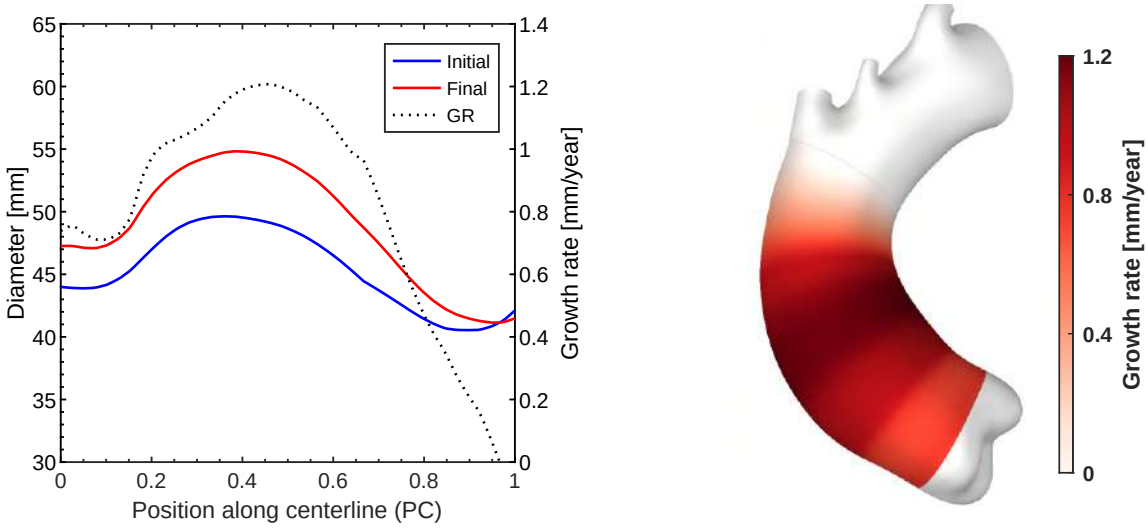

(a) Profiles of initial and final diameter and growth rate.

(b) Contours of GR_L.

Figure 4.3: Diameter and growth rate analysis.

4.3.2 Growth assessment

The target of this work is to understand the relationship between fluid biomarkers and aneurysm growth rate, hence, an accurate analysis of the geometric changes of the aorta is required. Under current clinical guidelines, only maximum diameter (D_{max}) measurements are considered during the diagnosis and eligibility for surgery is determined when the D_{max} surpasses established thresholds or when growth rate based on maximum diameter change (GR_D) surpasses 3-5 mm/year. However, we consider this metric insufficient to correctly characterize the aneurysm growth, as different regions of the aorta could grow at different rates, as they are exposed to different conditions and stresses. For this purpose, we employed an automatic method to accurately acquire the diameter along the ascending aorta. The method is based on measuring the maximum diameter on set of cross-sections of the aorta, which are constructed from the intersection of a plane perpendicular to the centerline and the segmented geometry. By sweeping the plane from the sinotublar junction up to the brachiocephalic ostium we are able to obtain the diameter profile depicted in Figure 4.3a, where the position along the centerline (PC) is normalized from 0, which corresponds to the sinotubular junction, to 1, which corresponds to the brachiocephalic ostium. By comparing diameter measurements from the first and last CT scans, we are able to define the maximum diameter growth rate (GR_D) and, more importantly, the local diameter changes ΔD_L and local growth rate (GR_L), shown in Figure 4.3a-b. When GR_L below zero was detected we assumed a null growth, since the aortic wall has no mechanism to restore its original shape and thus we assume that negative GR_L is caused by either an acquisition or segmentation error or from drug therapy to reduce blood pressure, or a combination of both factors.

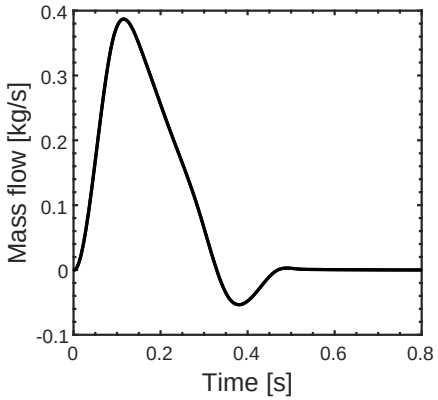

Figure 4.4: Mass flow through the aortic valve.

4.3.3 Boundary conditions

Due to the lack of personalized flow profiles derived from MRI flow acquisitions for most of the cohort, an idealized mass flow profile was used to impose the flow through the aortic valve, with cardiac cycle duration $T = 0.8$ s, as depicted in Figure 4.4. The spatial distribution of the inlet profile corresponds to a fully developed turbulent flow profile following the $1/7^{\text{th}}$ power-law [106, 107], as done in Chapter 3.

On the supra-aortic vessels and descending aorta a three-element RCR windkessel boundary condition was imposed. Assuming a pulse pressure of 40 mmHg and a distribution of flow proportional to the outlet areas, a tuning of the parameters was performed as described in [111]. To ensure accuracy and numerical convergence, the supra-aortic vessels were extended five equivalent hydraulic diameters, preventing the build up of a recirculating region at the outlet boundary. The equations modelling windkessel components were solved using a second order backward differencing scheme which has been validated against analytical solutions [112].

4.3.4 Numerical set-up

The segmented geometries were discretized using a polyhedral mesh, capable of capturing the small geometrical details with smooth cell size transition and preserving optimal cell quality. The meshing process and the computations were performed using Ansys Fluent 22.1 (ANSYS Inc., Canonsburg, PA, USA). The mesh was defined by surface elements with a maximum face size of 0.35 mm, a boundary layer composed of 15 hexagonal prisms and the first layer cell height of 0.05 mm, ensuring an aspect-ratio of 7 suitable for LES, and a maximum cell size of 0.7 mm on the internal domain, as determined in Section 3.3.1. In sight of the results obtained in Chapter 3, the Dynamic Smagorinsky-Lilly subgrid-scale model [113] was used to model turbulence in combination with a non-Newtonian Carreau viscosity model [114]. The coefficients of the Carreau viscosity model are provided in in Section 3.2.4. The DSL subgrid-scale model enables to capture the laminar to turbulent transition and prevents an underestimation of the WSS, while accounting for the shear-thinning behaviour of blood enables for a faithful description of the flow

field on low velocity regions and an accurate estimations of WSS derived biomarkers. The density of blood was set to 1056 kg/m^3. Pressure-velocity coupling was solved via the SIMPLEC algorithm. Pressure and momentum terms were solved using second order and bounded central differencing respectively. A second order implicit scheme was used to compute time dependent terms. Six cardiac cycles were computed using a time-step of 0.2 ms.

4.3.5 CFD Biomarkers

Since the role of hemodynamic variables on aneurysm development is yet poorly understood, a comprehensive set of fluid biomarkers is considered in this study in order to assess their relevance as aneurysm growth predictors. We will consider in this study both wall shear stress and flow derived biomarkers.

4.3.5.1 Wall shear stress derived biomarkers

The first category of biomarkers include timed average WSS (TAWSS), peak systole WSS (PSWSS), oscillatory shear index (OSI), shear angle (SA) and reversed flow ratio (RFR). These variables have been presented in Section 3.2.5, however, a brief description is provided for convenience of the reader.

The TAWSS quatifies the averaged magnitude of the wall shear stress an is computed as follows:

$$\text{TAWSS} = \frac{1}{T}\int_0^T |\mathbf{WSS}(t)|\, dt, \tag{4.2}$$

being T the duration of one cardiac cycle. PSWSS represents instantaneous WSS magnitude at peak systole, which occurs 0.12 s after a cardiac cycle begins. Variations in shear direction are described by the OSI. Low OSI values indicate that the flow follows a predominant direction thought the cardiac cycle while high OSI values indicate large fluctuations on the shear direction. It is defined according to:

$$\text{OSI} = 0.5\left(1 - \frac{\left|\int_0^T \mathbf{WSS}(t)\, dt\right|}{\int_0^T |\mathbf{WSS}(t)|\, dt}\right). \tag{4.3}$$

The SA is used to describe the direction of shear and it is used to identify the presence of rotating and backward flow. The SA is defined as

$$\text{SA} = \frac{2}{\pi}\arctan\left(\frac{\text{WSS}_{\text{Axial}}}{\text{WSS}_{\text{Circ}}}\right), \tag{4.4}$$

which is obtained by decomposing the WSS vector into axial and circumferential shear, $\text{WSS}_{\text{Axial}}$ and WSS_{Circ}, respectively. $\text{WSS}_{\text{Axial}}$ is positive when the flow progresses along the ascending aorta towards the aortic arch and a negative in the presence of reversed flow. WSS_{Circ} takes only positive values, as the sign is used to indicate either clockwise or anticlockwise shear, which is beyond the scope of this work. Depending on whether the TAWSS or peak systole WSS field are considered, we can compute the

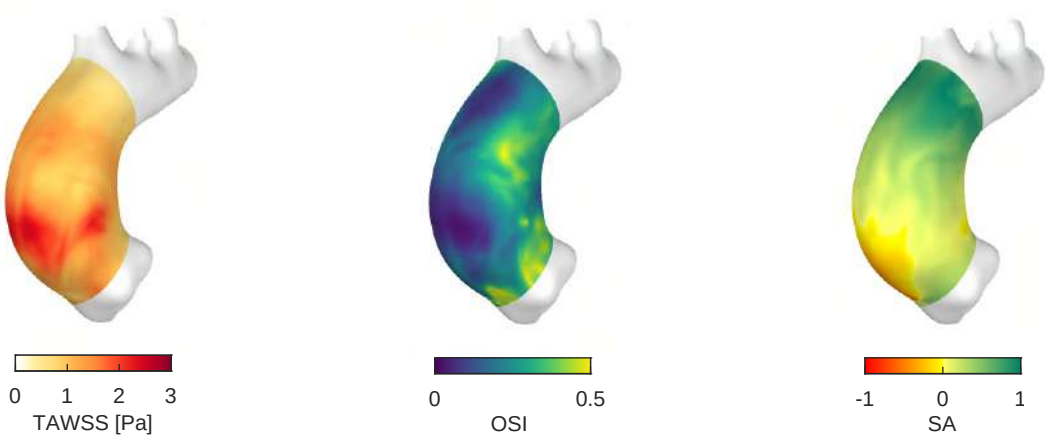

Figure 4.5: Countours of WSS derived biomarkers.

time-averaged shear angle (TASA) or the peak systole shear angle (PSSA). Finally, considering the total ATA wall area (A_{wall}) and the field defined by the SA, we compute the area of regions with reversed flow (A_{RF}) to define the reversed flow ratio as

$$\text{RFR} = \frac{A_{RF}}{A_{wall}} \tag{4.5}$$

A depiction of the contours of WSS derived biomarkers is shown in Figure 4.5.

4.3.5.2 Wall shear stress topological skeleton

On the luminal surface, the TAWSS vector field can be used to identify the WSS topological skeleton by applying the Eulerian method [141]. The topological skeleton can be used to identify fixed points, located where the WSS vanishes, and manifolds, which correspond to regions where contraction and expansions occurs. The method proposed in [141] and used in subsequent studies [135, 142, 143] is based on the Volume Contraction Theory and uses the WSS vector field divergence to define the topological skeleton. The analysis is performed on the normalized WSS vector field and, thus, the divergence (DIV_W)is defined as follows:

$$\text{DIV}_W = \nabla \cdot (\boldsymbol{\tau_u}) = \nabla \cdot \frac{\mathbf{WSS}}{\|\mathbf{WSS}\|}, \tag{4.6}$$

where $\boldsymbol{\tau_u}$ is the normalized WSS vector field. We can identify the topological skeleton patterns according to the divergence field sign, since the contraction and expansion regions are located where DIV_W is, respectively, negative and positive. The analysis of the topological skeleton can be further extended by considering the Poincaré index, the Topological Shear Variation Index and the fixed point weighted residence time, however, these elaborate analysis will not be performed in this study and only the divergence field will be assessed.

To obtain the WSS topological skeleton from a CFD computation, the divergence operator was applied following the procedure described in [141]. First, the CFD results, obtained on a polyhedral mesh, where

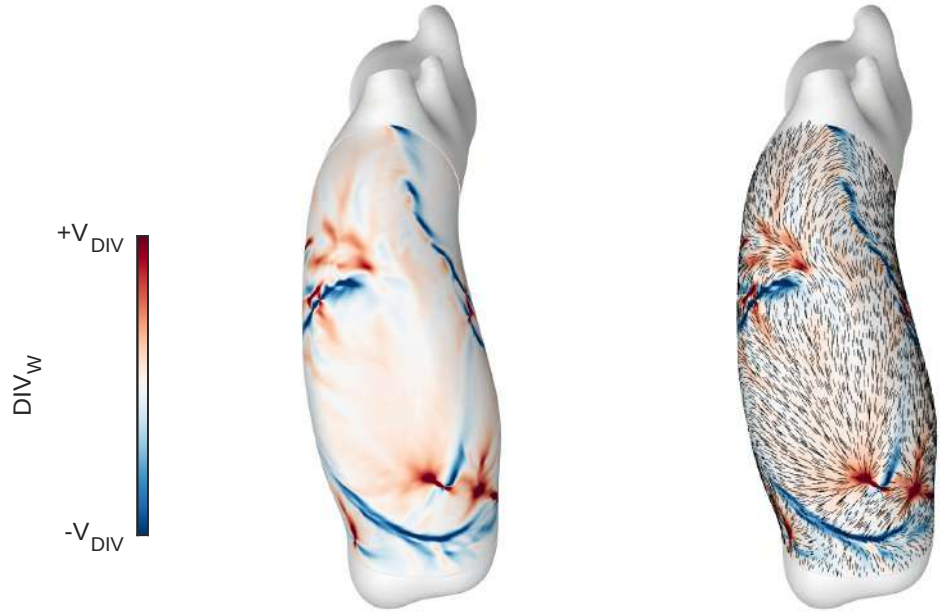

Figure 4.6: Contours (left) and quiver plot (right) of the WSS topological skeleton. The limits of the colorbar has been adjusted for visualization purposes.

mapped onto a triangular mesh constructed from the luminal cell face centres. Then, for any triangle T_n (n=1,...,N, being N the total number of mesh triangles), we consider the values of WSS on the vertices η ($\eta = i, j, k$). Each component of the vector field is then discretized by a piecewise constant vector per mesh triangle by interpolating the WSS field into a generic position inside the mesh triangle T_n using barycentric coordinates and piecewise linear basis functions $\boldsymbol{B_i}$:

$$\tau_\zeta(\mathbf{p}) = (\tau_\zeta)_i B_i(\mathbf{p}) + (\tau_\zeta)_j B_j(\mathbf{p}) + (\tau_\zeta)_k B_k(\mathbf{p}), \tag{4.7}$$

being ζ the spatial directions (x, y, z) and $\mathbf{p} = (\mathbf{x}, \mathbf{y}, \mathbf{z}) \subset \mathbf{T_n}$. The gradient of each WSS component can be obtained as

$$\nabla\tau_\zeta(\mathbf{p}) = (\tau_\zeta)_i \nabla B_i(\mathbf{p}) + (\tau_\zeta)_j \nabla B_j(\mathbf{p}) + (\tau_\zeta)_k \nabla B_k(\mathbf{p}), \tag{4.8}$$

where $\nabla B_\eta(\mathbf{p})$ represents the steepest ascent direction perpendicular to the opposite edge, which is expressed as:

$$\begin{aligned} \nabla B_i(\mathbf{p}) &= \frac{\mathbf{n}_{T_n} \times \mathbf{e_{jk}}}{2A_T}, \\ \nabla B_j(\mathbf{p}) &= \frac{\mathbf{n}_{T_n} \times \mathbf{e_{ki}}}{2A_T}, \\ \nabla B_k(\mathbf{p}) &= \frac{\mathbf{n}_{T_n} \times \mathbf{e_{ij}}}{2A_T}, \end{aligned} \tag{4.9}$$

being A_T the surface area of the triangle T_n, $\mathbf{n}_{T_n}$ the normal unit vector of the triangle T_n, and $\mathbf{e_{jk}}, \mathbf{e_{ki}}$

and $\mathbf{e_{ij}}$ the edge opposite to vertex i, j, k, respectively. In this way, we can define the divergence of the WSS field on any point $\mathbf{p} \subset T_n$ as:

$$\nabla \cdot \boldsymbol{\tau}(\mathbf{p}) = \nabla \boldsymbol{\tau_x}(\mathbf{p}) \cdot \vec{x} + \nabla \boldsymbol{\tau_y}(\mathbf{p}) \cdot \vec{y} + \nabla \boldsymbol{\tau_z}(\mathbf{p}) \cdot \vec{z}. \tag{4.10}$$

Then, for each vertex η of the mesh, the value of $\nabla \cdot \boldsymbol{\tau}_\eta$ is computed as the averaged value of $\nabla \cdot \boldsymbol{\tau}$ on all the triangles to which η belongs to. An example of the resultant topological WSS skeleton is depicted in Figure 4.6, together with the quiver plot of the WSS field which facilitate the comprehension of the WSS pattern.

4.3.5.3 Flow field derived biomarkers

The flow derived biomarkers used to characterize the behaviour of the full flow field inside the aorta and identify disrupted or anomalous flow behaviour. The set of biomarkers herein presented have been measured evaluating the velocity field at different cross-sections of the aorta. For each patient, a set of forty planes perpendicular the centerline were used to construct the set of cross-sections. To evaluate the flow field characteristics we measured the flow eccentricity (FE), the bounded flow eccentricity ($\mathrm{FE}_{80\%}$), the flow dispersion ($\mathrm{FD}_{80\%}$) and the flow angle (α).

The flow eccentricity was used to measure the flux mass-center offset and it was defined as

$$\mathrm{FE} = \frac{||\mathbf{C}_\mathrm{G} - \mathbf{C}_\mathrm{F}||}{R}, \tag{4.11}$$

were $\mathbf{C}_\mathrm{G}$ and $\mathbf{C}_\mathrm{F}$ represent the geometric and flux centroids respectively and R the equivalent hydraulic radius. Elaborating on this metric, by considering only the cells with a velocity higher than 80% of the maximum velocity through the given plane to compute the bounded flux centroid $\mathbf{C}_{\mathrm{F}_{80\%}}$, which enables us to define the bounded flow eccentricity $\mathrm{FE}_{80\%}$ as:

$$\mathrm{FE}_{80\%} = \frac{||\mathbf{C}_\mathrm{G} - \mathbf{C}_{\mathrm{F}_{80\%}}||}{R}. \tag{4.12}$$

The total area of the cells used in the computation of $\mathbf{C}_{\mathrm{F}_{80\%}}$ allow us to define the bounded area $A_{80\%}$, which can in turn be used compute the flow dispersion $\mathrm{FD}_{80\%}$ as the fraction between the bounded area and the total surface A_T on a given cross-section as:

$$\mathrm{FD}_{80\%} = \frac{A_{80\%}}{A_T}. \tag{4.13}$$

Finally, we can compute the averaged velocity on the plane to define the mean flow direction $\mathbf{n}_\mathrm{F}$ and

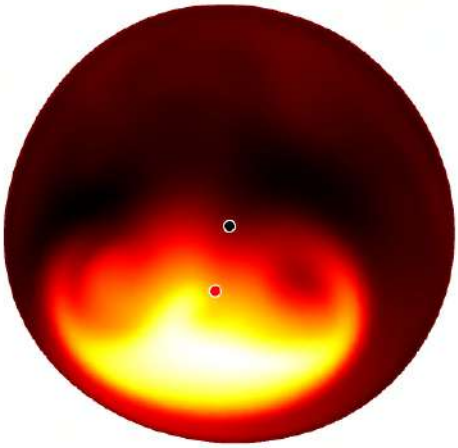

(a) Position of the geometric (black) and flux (red) centroids used to compute FE.

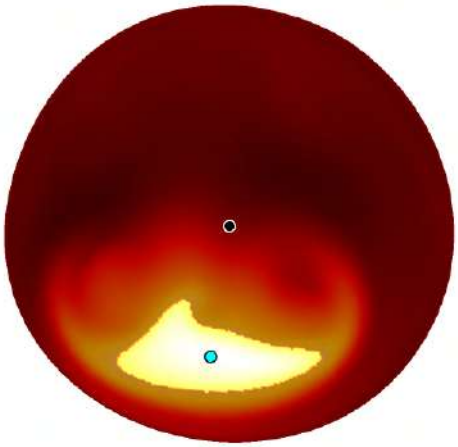

(b) Position of the geometric (black) and bounded flux (blue) centroids used to compute $FE_{80\%}$. The bounded area $A_{80\%}$ used to compute the flow dispersion is highlighted.

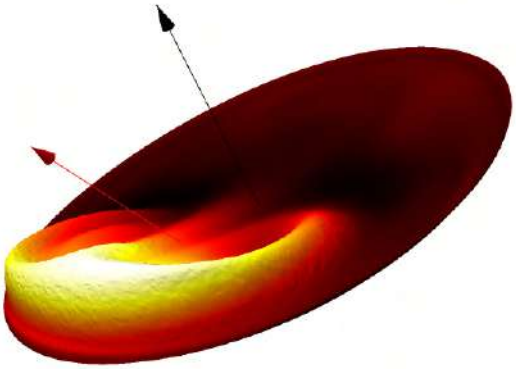

(c) Normal vector $\mathbf{n}_P$ (black) and flow direction $\mathbf{n}_F$ (red) together with the 3D velocity contours.

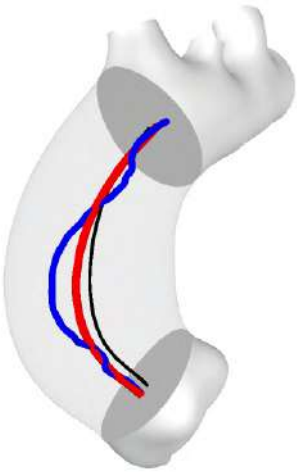

(d) Plot of the centerline (black), flux centroid (red) and bounded flux centroid (blue) along the ascending aorta.

Figure 4.7: Flow field derived biomarkers for a patient from the cohort.

compute the deviation α from the plane normal $\mathbf{n}_\mathrm{P}$:

$$\alpha = \arccos\left(\frac{\mathbf{n}_\mathrm{F} \cdot \mathbf{n}_\mathrm{P}}{|\mathbf{n}_\mathrm{F}|\,|\mathbf{n}_\mathrm{P}|}\right). \tag{4.14}$$

A depiction of the flow derived biomarkers is shown in Figure 4.7

4.4 Results

This section includes the resultant measurements of aortic growth rate for the patient cohort, the CFD computations and biomarkers results and the correlation between growth and biomarkers according to aortic valve type.

4.4.1 Growth

The first objective was obtaining growth measurements for the cohort. The initial and final D accounting for the acquisition interval is depicted in Figure 4.8a, differentiated according to aortic valve type. The location of the aneurysm is patient specific. Figure 4.8b depicts the location of maximum diameter. We can observe that the majority (61%) of the aneurysms where located in the mid section of the ATA, in range PC $\in$ [0.3, 0.5], and none where located beyond NP $>$ 0.54. It can be observed that the majority of the tricuspic valve patients have an aneurysm located closer to the sinotubular junction with respect to bicuspid valve patients. The maximum diameter was located, on average, on PC = 0.25 for TAV and on PC = 0.40 for BAV. It is significant that the average diameter on the first acquisition was 49.6 and 46.3 mm for tricuspid and bicuspid aortic valve patients, respectively. The relationship between GR_L and GR_D is depicted in Figure 4.8c, having some patients significant differences between the two measures. On average, GR_L was 0.81 mm higher than GR_D. The maximum difference between GR_L and GR_D was 3.8 mm. Finally, measures of D_0 against GR_D are plotted on Figure 4.8d. The correlation coefficient between these variables is 0.04, thus this result highlights that, in the current cohort, the initial diameter does not correlate with GR_D. Substantial differences were observed on the patient cohort regarding the diameter and local growth profiles. Five patients showed null maximum diameter growth. Two BAV patients (P19 and P21) had growth exceeding 4 mm/year, for which, the segmentations and growth rate are highlighted in Figure 4.9. The geometries of both patient are clearly different. Patient 19 haa standard cylindrical shape, whereas patient 21 shows a highly tortuous geometry. It can be observed that high growth in patient 19 is present on two segments: in the vicinity of PC = 0.2 and the brachiocephalic ostium (PC = 1). Patient 21 shows a different profile, with the growth being concentrated around PC = 0.7. The diameter and growth rate profiles for the full cohort are depicted in Figure 4.10. We can observe some cases in which D_{max} is located closely to the sinotubular junction (PC = 0), which could indicated that an aortic root aneurysm is present. This is the case for patients 3, 6, 7, 9 10, 13, 27 and 30.

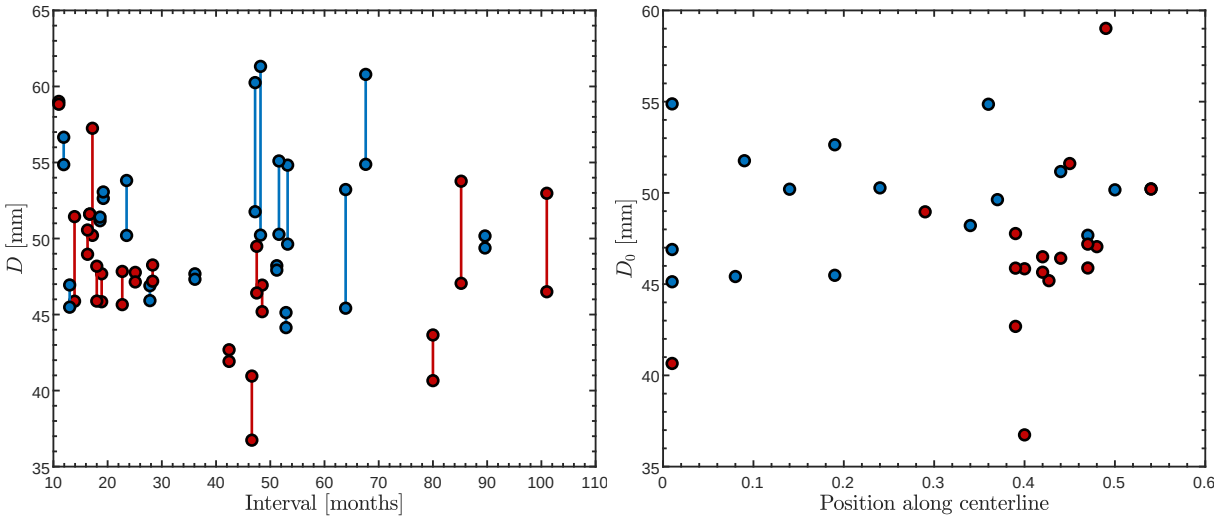

(a) Initial and final diameters ploted againts scan interval. (b) Maximum diameter ploted against its position along the centerline.

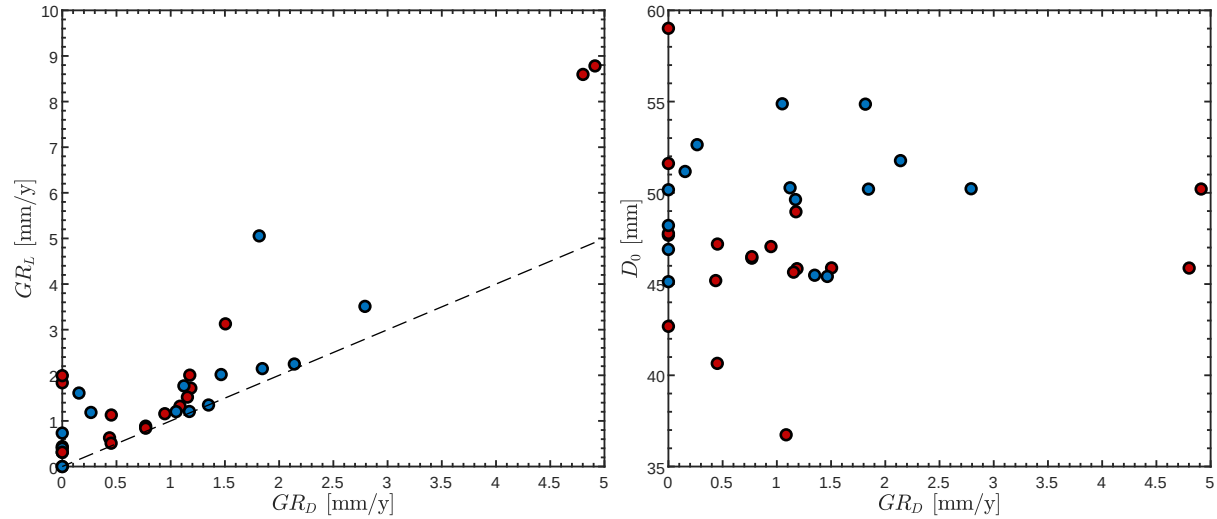

(c) Maximum local growth rate against maximum diameter growth rate. (d) Initial diameter against maximum diameter growth rate.

Figure 4.8: Growth analysis. Results differentiated by color (Tricuspid = blue, bicuspid = red).

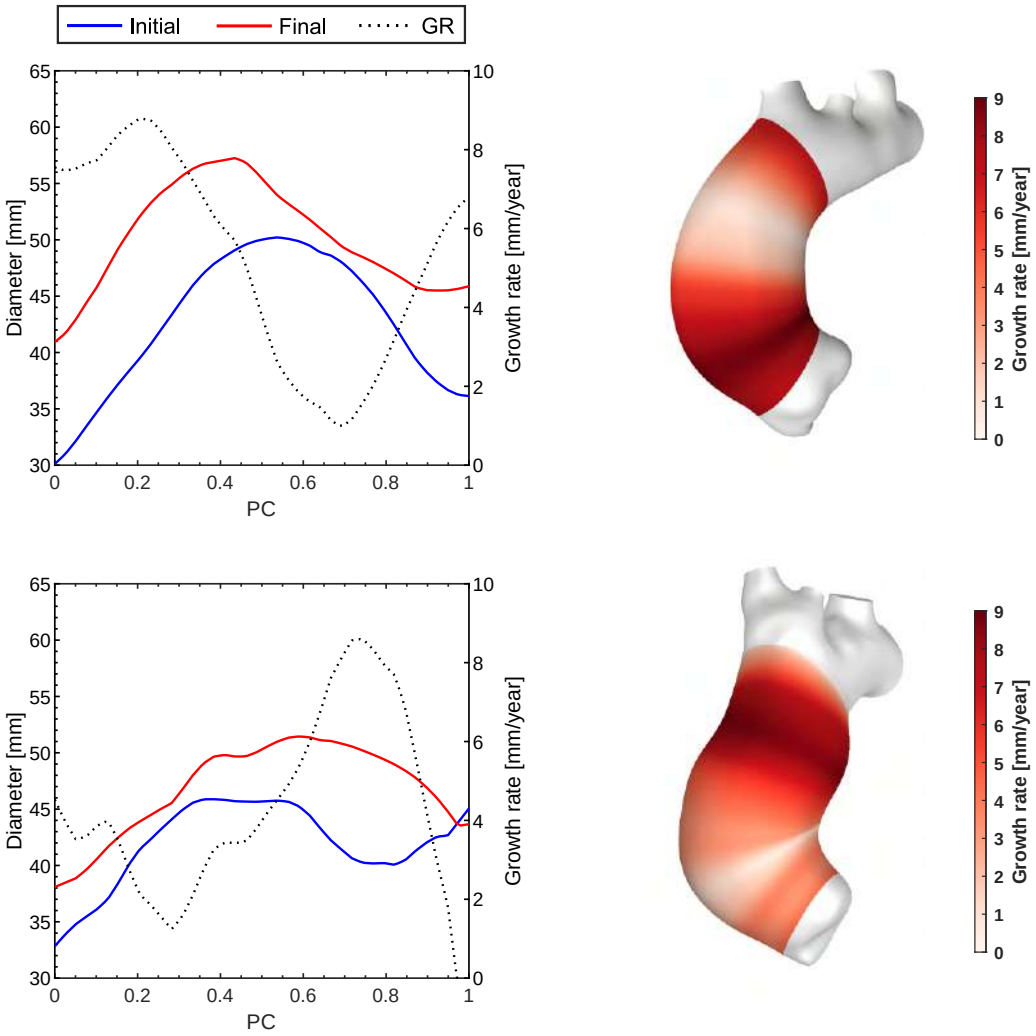

Figure 4.9: Growth rate analysis for patients 19 and 21, which have a GR_L surpassing 8 mm/y.

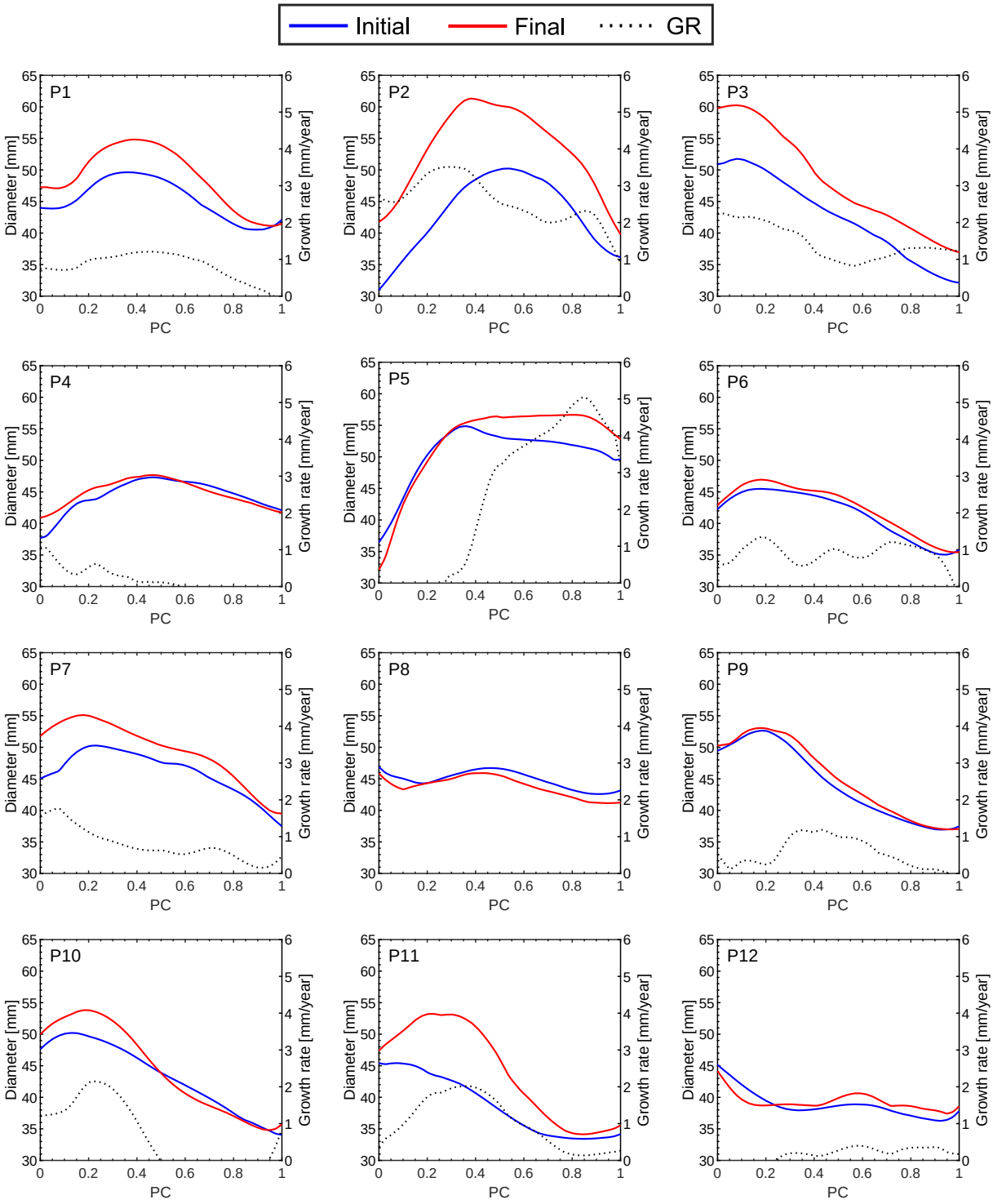

Figure 4.10: Diameter and growth rate for the patient cohort.

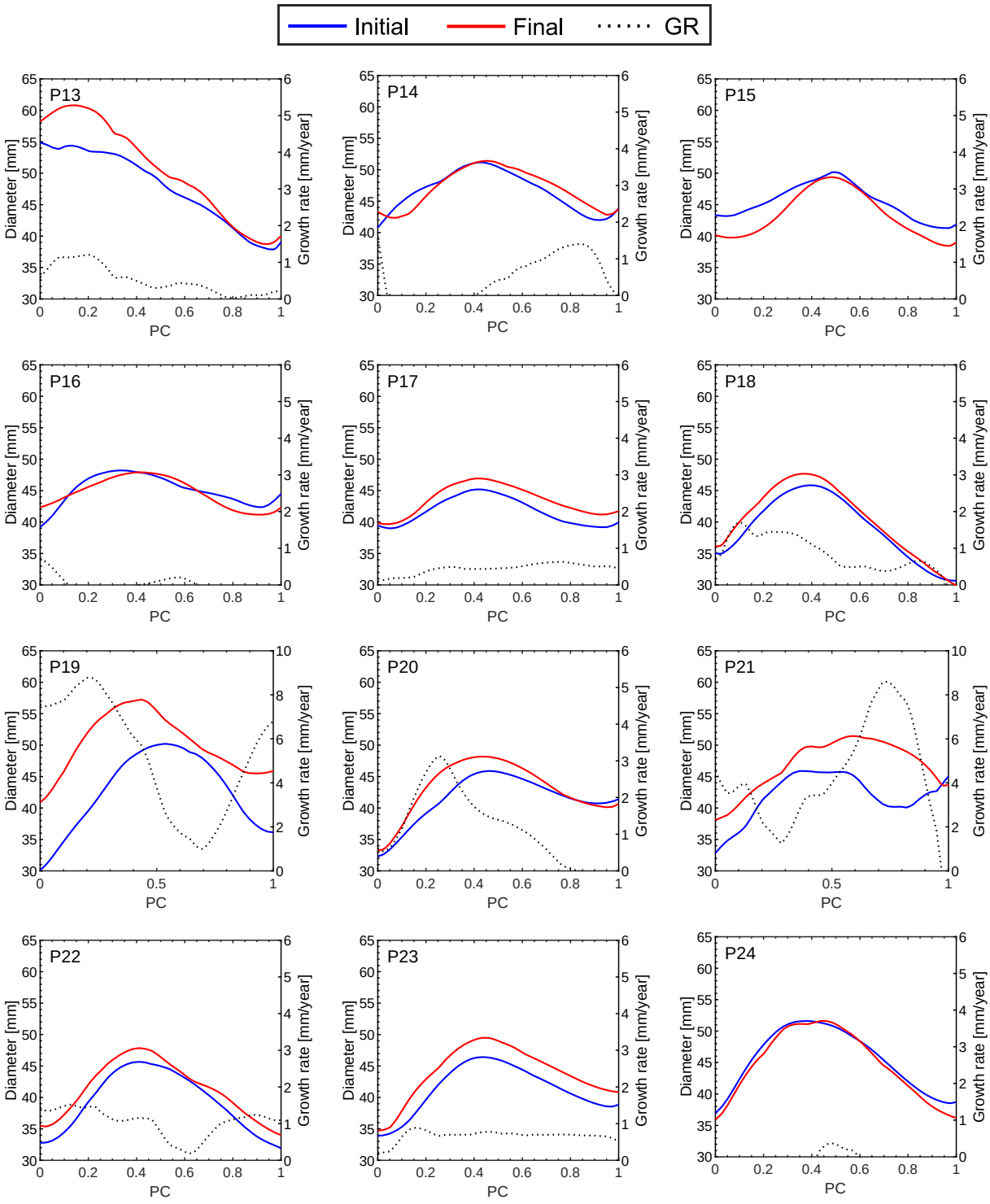

Figure 4.10: Diameter and growth rate for the patient cohort (continued).

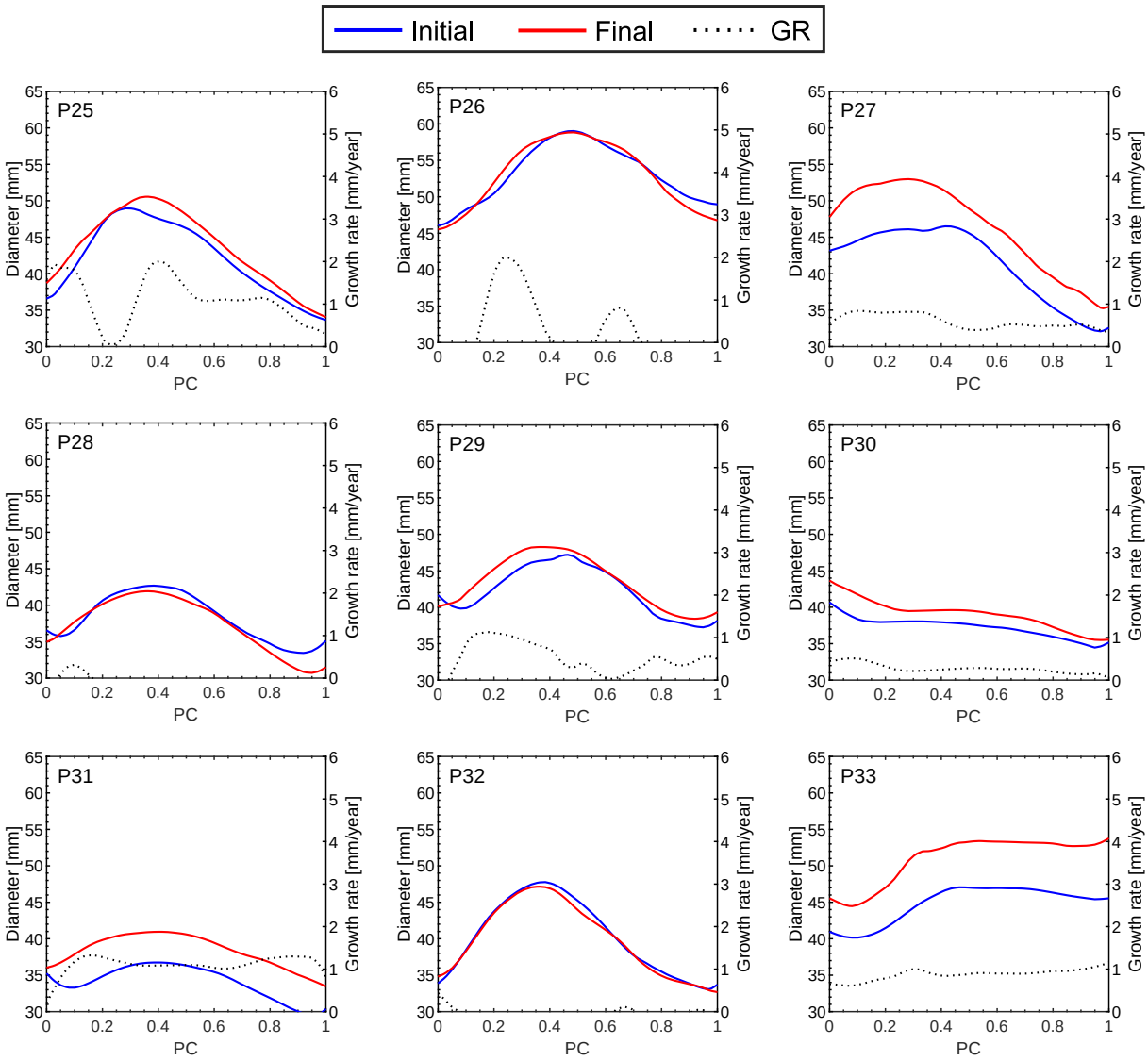

Figure 4.10: Diameter and growth rate for the patient cohort (continued).

4.4.2 CFD results

In this section we present the results of CFD biomarkers on the patient cohort.

4.4.2.1 WSS biomarkers

A depiction of WSS-derived and WSS topological skeleton contour plots for the patients cohort is provided at the end of the Chapter, in Figures 4.22-4.25, showing marked differences between patients. In order to provide further insight, the WSS derived biomarkers where measured on the internal and external wall independently, since different flow conditions affect these regions due to the jet impinging on the external wall.

From hereinafter, the averaged value of a biomarker β is obtained by computing, for each patient, the spatially averaged value and performing an average across the considered patient set.

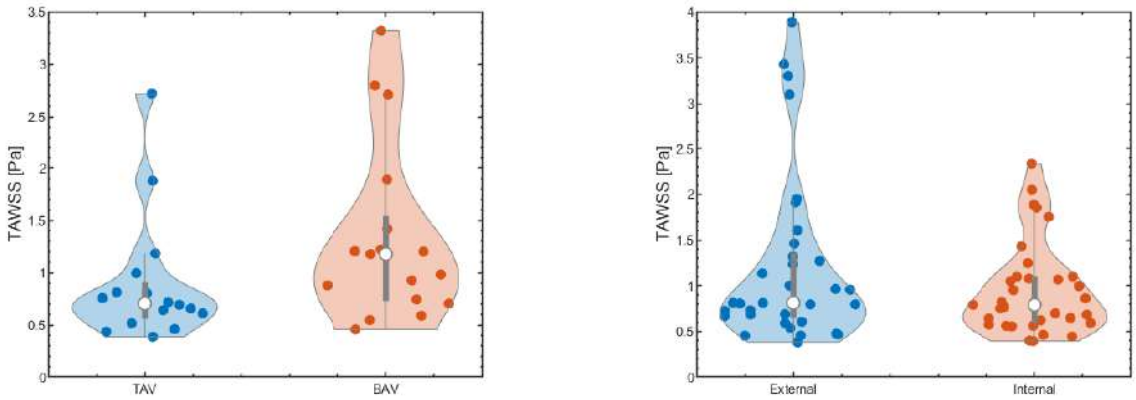

Figure 4.11: Violin plots of TAWSS for the TAV and BAV groups (left) and for external and internal walls (right).

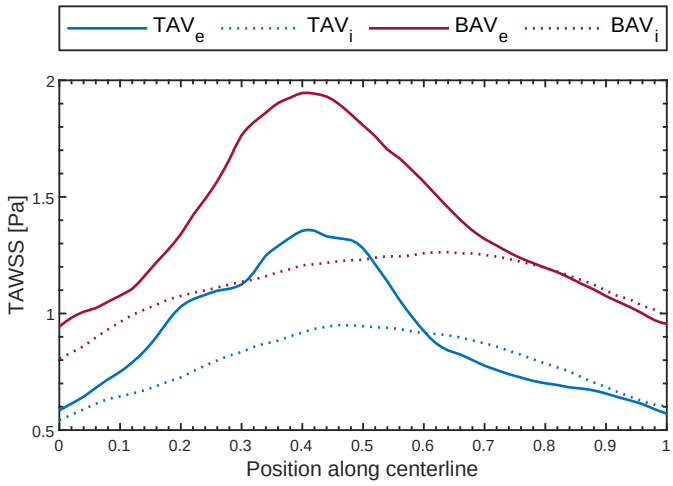

Figure 4.12: Plot of averaged TAWSS for the TAV and BAV according to wall region.

The mean TAWSS was 0.89 Pa for tricuspid and 1.33 Pa for bicuspid aortic valve patients. The spatially-averaged TAWSS was strongly correlated with inlet velocity, having a correlation coefficient R = 0.82 (p = 4.1×10^{-8}). Some patients present elevated TAWSS in both valve groups, having averaged TAWSS above 2.5 Pa, as can be observed in Figure 4.11. These patients correspond to the severely stenosed cases. Regarding the external and internal walls, we observe that the external wall is, on average, subject to 26% higher TAWSS in comparison to the internal wall, having a mean value of 1.21 and 0.96 Pa, respectively. This difference is present since the aortic jet impacts on the external wall, generating high WSS on the impact region. The difference between the external and internal walls is more pronounced on the patients suffering from stenosis. The averaged values along the centerline are plotted in Figure 4.16, where the difference between TAV and BAV can be clearly observed. Both valve types present a peak of TAWSS at PC $\in$ [0.4, 0.5], which corresponds to the jet impact region of most patients, and follow a similar pattern on both walls.

The OSI showed minimal difference between tricuspid and bicuspid patients, having a mean equal to

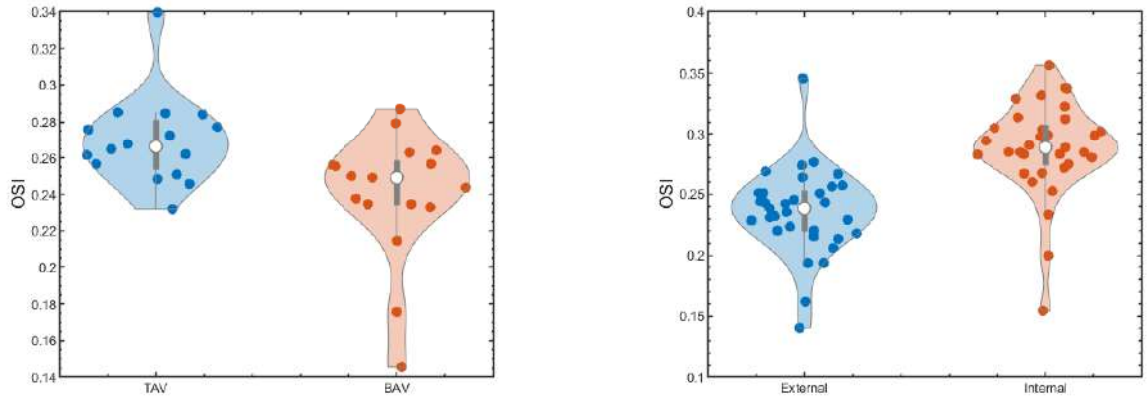

Figure 4.13: Violin plots of OSI for the TAV and BAV groups (left) and for external and internal walls (right).

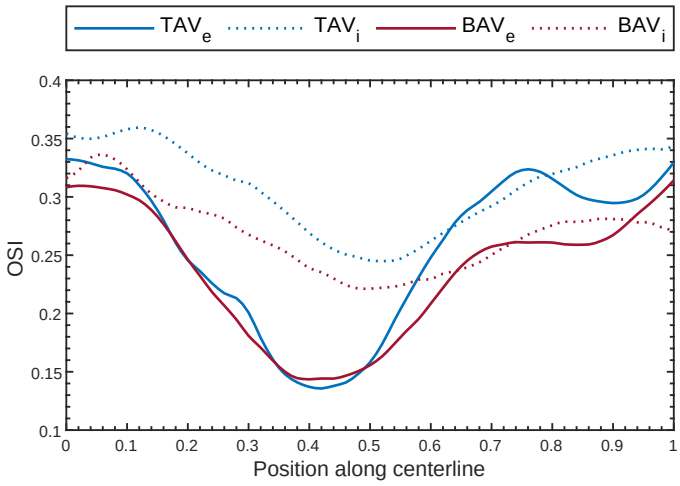

Figure 4.14: Plot of averaged OSI for the TAV and BAV groups according to wall region.

0.269 and 0.239, respectively. We can observe, however, that the outliers differ, since the TAV group has a patient with an OSI of 0.34 and the BAV group two patients with an OSI below 0.18, as can be seen in Figure 4.13. The OSI is negatively correlated with inlet velocity, having a correlation coefficient R = -0.71 ($p = 3.3\times10^{-6}$). The OSI is lower on the external wall than in the internal wall, having a mean value of 0.235 and 0.287, respectively. This can be observed in Figure 4.16.

The TASA difference between TAV and BAV groups is negligible, as the mean is 0.113 and 0.114, respectively. We can observe in Figure 4.15 that the TASA has a larger spread in the BAV group, having an interquartile range (IQR) of 0.177, in comparison to the TAV, which has an IQR of 0.059. The TASA is also negatively correlated with the aortic jet velocity, having a correlation coefficient of R = -0.53 (p = 0.0014). The TASA shows marked differences between the external and internal walls. On the external wall, the flow is predominantly flowing in the downstream direction, with a mean TASA of 0.33. On the contrary, the flow is predominantly reversed in the internal wall, having a mean value of -0.274. Observing Figure 4.16, we can deduce that the flow in the vicinity of the aortic root has a strong

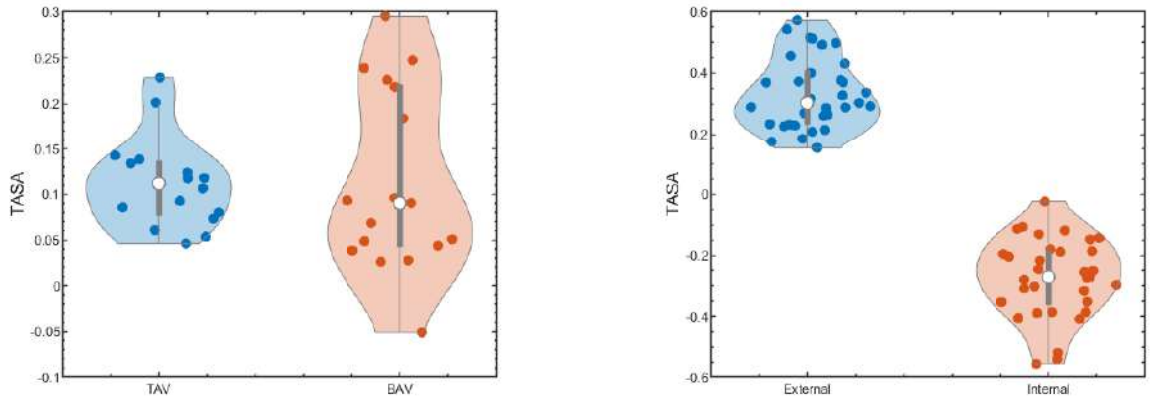

Figure 4.15: Violin plots of TASA for the TAV and BAV groups (left) and for external and internal walls (right).

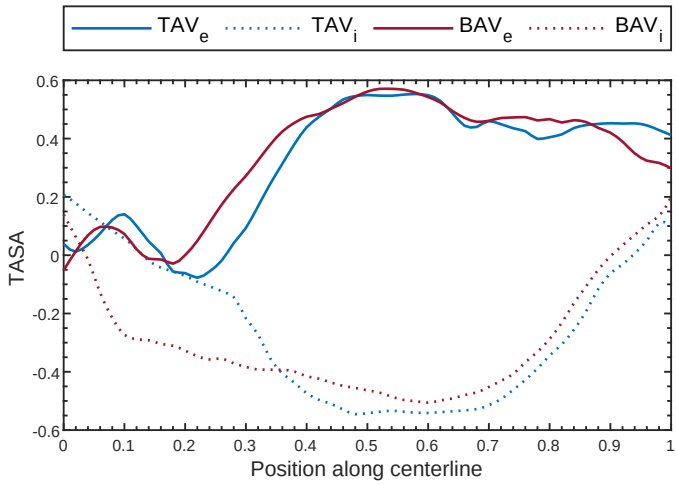

Figure 4.16: Plot of averaged TASA for the TAV and BAV groups according to wall region.

circumferential component, since TASA values range between -0.1 and 0.2. On the external wall, we observe a similar pattern for both valve types, except in PC $\in$ [0.2, 0.3] where the BAV show a higher TASA. Concerning the internal wall, we observe a predominant reversed flow, which is maximal in PC $\in$ [0.4, 0.7]. A marked difference can be observed in PC $\in$ [0, 0.3] between valve types, since the BAV has a significantly lower TASA in this range, indicating a higher presence of rotating and reversed flow in this region.

4.4.2.2 WSS biomarkerstopological skeleton

The WSS topological skeleton show a diverse range of patterns, as can be seen in Figure 4.25. In some patients, the location of the jet impingement region is clearly visible, as a marked red spot in the central part of the ascending aorta. In this cases, the jet is colliding against the wall with an elevated angle, causing a spot of positive WSS divergence. Although this occurs in some scenarios, the geometry of the aorta and the angle at which the jet impacts the wall on the other cases creates a complex pattern.

The topological skeleton will be assessed along the centerline by differentiating between the regions of positive (DIV_W^+) and negative (DIV_W^-) divergence. The averaged positive and negative divergence values against the centerline position are plotted in Figure 4.17. We can observe some differences between the valve groups. The TAV shows near the sinotubular junction (PC $\in$ [0, 0.1]) a more marked expansion and contraction pattern, since the absolute values of DIV_W are greater in both the positive and negative regions. Some local differences can be observed along the aorta, for example at PC = 0.3, however the overall pattern is similar in both valve groups.

4.4.2.3 Flow biomarkers

The second set of biomarkers is related to the internal flow structure. Due to the geometric variations, the angle at which the inlet jet is positioned and the inlet velocity, differences in the internal flow structure appear within the cohort. The averaged values of systolic FE, $\mathrm{FE}_{80\%}$, $\mathrm{FD}_{80\%}$ and α along the centerline for TAV and BAV patients are depicted in Figures 4.18-4.21. A clear difference between valve types can be observed with respect to FE, being the averaged values 0.078 and 0.128 for TAV and BAV patients, respectively. On both valve groups the peak is located around PC = 0.45, which coincides with the jet impingement region. The initial difference at PC = 0 is due to the off-set with respect to the centerline of the aortic valve, as can be seen in Figure 4.2. The difference between the to valve groups decreases after PC = 0.5.

The differences in $\mathrm{FE}_{80\%}$ are less apparent. Again, as occurs with FE, the BAV group has a higher $\mathrm{FE}_{80\%}$ due to the valve off-set. Some differences can be seen in PC $\in$ [0.6, 1]. On average, the $\mathrm{FE}_{80\%}$ was 0.389 and 0.431 for TAV and BAV patients.

The flow dispersion $\mathrm{FD}_{80\%}$ follows similar trends on both patients, although some differences can be observed. The TAV surpasses the BAV $\mathrm{FE}_{80\%}$ in the interval PC $\in$ [0.1, 0.4], while the opposite occurs in the interval PC $\in$ [0.5, 0.9]. The averaged values where nearly identical, being 0.107 for the TAV group and 0.110 for the BAV group.

Considering the flow angle, defined as the angle between the centerline and the averaged velocity vector on a cross-section, significant differences are present between the valve groups. The TAV shows low values of α across the full lumen, ranging between 6 and 10°. On the contrary, BAV patients show an higher α in the vicinity of the sinotubular junction, reaching 21°at PC = 0.20. This elevated α tends to decrease as the flow progresses along the aorta.

4.4.3 Correlation between growth and biomarkers

After modelling the patient cohort, an analysis of the correlation between growth and averaged biomarker values was performed in order to identify which could potentially aid in the diagnosis process. WSS derived biomarkers $\beta_{i,t}^W$ are defined on the nodes i of the aortic wall at an instance t while the flow-derived

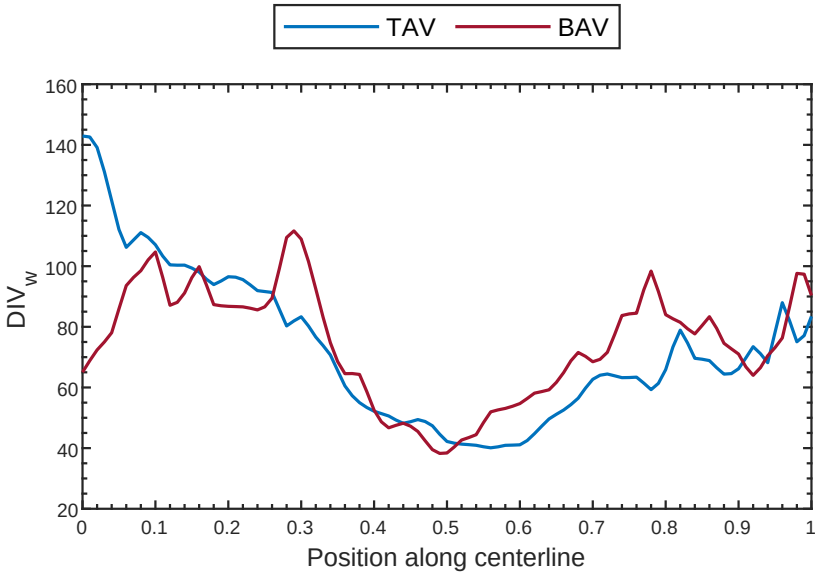

(a) Averaged values of positive DIV_W

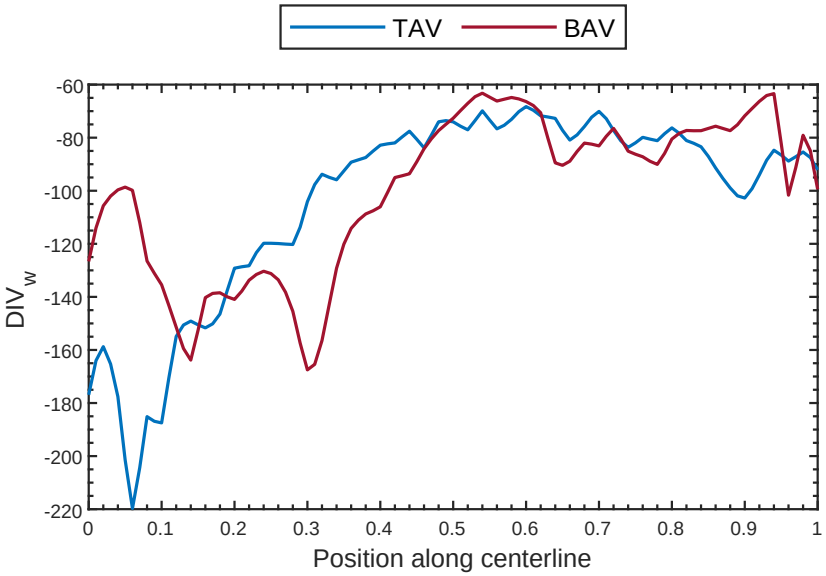

(b) Averaged values of negative DIV_W

Figure 4.17: Plot of averaged DIV_W for the TAV and BAV groups.

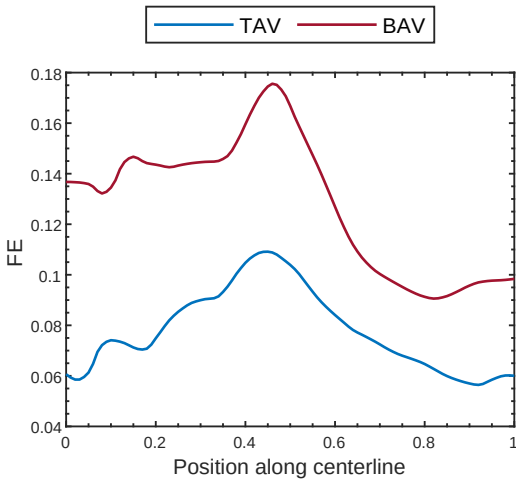

Figure 4.18: Plot of averaged systolic FE.

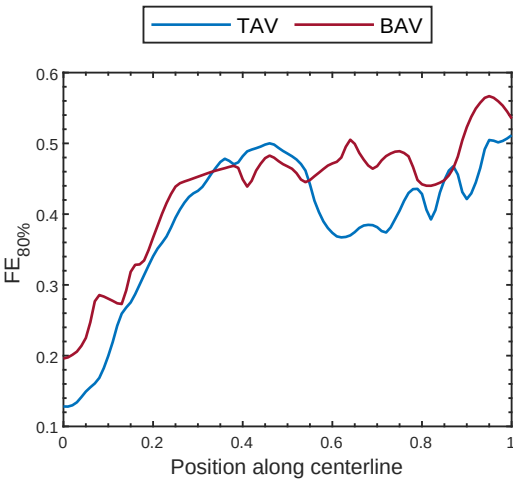

Figure 4.19: Plot of averaged systolic $FE_{80\%}$.

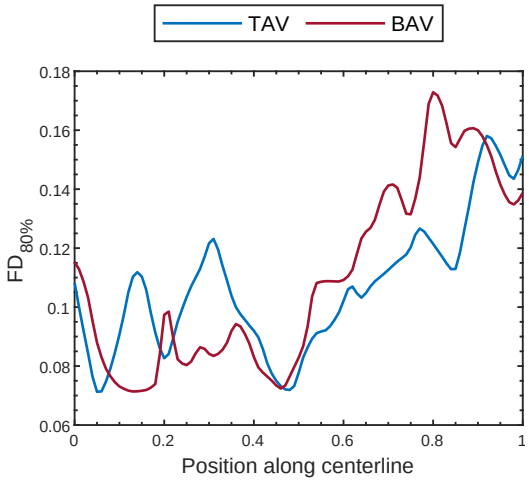

Figure 4.20: Plot of averaged systolic $FD_{80\%}$.

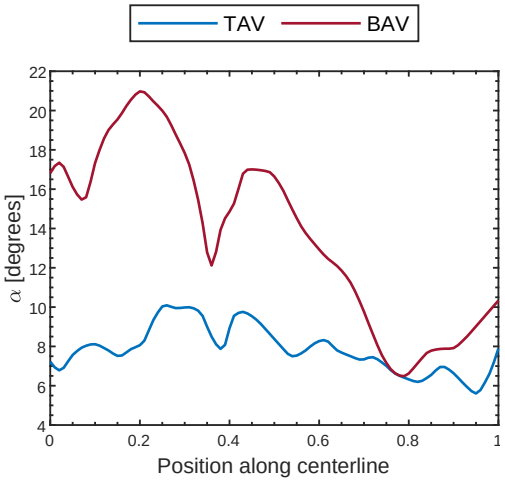

Figure 4.21: Plot of averaged systolic α.

		TAV				BAV			
Biomarker	Measure	GR_D		GR_L		GR_D		GR_L	
		R	p	R	p	R	p	R	p
TAWSS	Max	-0.151	0.577	-0.243	0.365	-0.141	0.589	-0.236	0.362
	Mean	0.016	0.954	-0.164	0.545	-0.128	0.625	-0.204	0.432
PSWSS	Max	-0.073	0.789	-0.126	0.641	-0.034	0.897	-0.130	0.620
	Mean	-0.064	0.815	-0.248	0.355	-0.103	0.695	-0.224	0.387
OSI	Mean	-0.044	0.871	-0.017	0.950	-0.166	0.523	-0.081	0.759
SA	TA-Mean	0.556	0.025	0.334	0.207	0.173	0.507	0.158	0.545
	PS-Mean	0.093	0.733	-0.009	0.975	-0.347	0.173	-0.354	0.163
RFR	TA	-0.369	0.159	-0.193	0.475	-0.201	0.439	-0.230	0.375
	PS	0.011	0.969	0.073	0.788	0.114	0.663	0.144	0.580

Table 4.4: Correlation coefficients and P-values between WSS derived biomarkers and growth rate on the aorta surface.

biomarkers $\beta^F_{j,t}$ are defined along the aorta cross-sections j, thus a compression is required in order to obtain scalar values which can, in turn, be correlated with growth rates. Depending on the considered biomarker, we will account for time averaged (TA), peak systole (PS) or flux averaged (FA) values regarding the temporal domain and for maximum and mean values regarding the spatial domain. This enables us to compute the correlation coefficients between the biomarkers and the growth rate. The results for WSS derived biomarkers are summarized in Tables 4.4-4.6. For the flow derived biomarkers, the correlations are summarized in Table 4.7. The results show that the majority of the biomarkers are not correlated to neither GR_D or GR_L. Statistically significant correlations are observed between GR_D and TASA when considering the full luminal surface of TAV patients, with R = 0.556 and p = 0.025. However, this biomarker does not seem to have a correlation when assessing the external and internal walls independently or when considering GR_L. On BAV patients, when considering the external wall only, a negative correlation can be observed for the peak systole SA (PSSA). The correlation coefficients are similar considering either GR_D or GR_L. For the former, R = -0.482 and p = 0.050, and for the later, R = -0.482 and p = 0.050. Regarding flow derived biomarkers, only the maximum flux averaged $FD_{80\%}$ on TAV patients shows a correlation with GR_D, being R = 0.554 and p = 0.032. This could indicate that patients having a high velocity region concentrated on a reduced area are prone to faster aneurysm growth. However, the GR_L does not show a correlation with this biomarker.

4.4.4 Profile correlation of WSS derived biomarkers and growth rate

In this section a different approach is taken in order to eliminate the patient-specific susceptibility to aneurysm growth. Many factors are involved in the mechanobiological processes affecting the aneurysm

		TAV				BAV			
Biomarker	Measure	GR_D		GR_L		GR_D		GR_L	
		R	p	R	p	R	p	R	p
TAWSS	Max	-0.223	0.407	-0.274	0.304	-0.160	0.541	-0.256	0.321
	Mean	-0.054	0.843	-0.190	0.480	-0.128	0.623	-0.209	0.421
PSWSS	Max	-0.132	0.626	-0.162	0.549	-0.053	0.841	-0.148	0.570
	Mean	-0.178	0.510	-0.282	0.291	-0.095	0.717	-0.213	0.411
OSI	Mean	-0.030	0.911	0.108	0.692	-0.089	0.734	0.002	0.995
SA	TA-Mean	0.061	0.823	-0.048	0.860	0.255	0.324	0.274	0.287
	PS-Mean	0.004	0.987	-0.048	0.859	-0.482	0.050	-0.481	0.051
RFR	TA	0.034	0.899	0.073	0.787	-0.266	0.303	-0.306	0.232
	PS	0.048	0.859	0.072	0.792	0.243	0.347	0.275	0.286

Table 4.5: Correlation coefficients and P-values between WSS derived biomarkers and growth rate on the external wall.

		TAV				BAV			
Biomarker	Measure	GR_D		GR_L		GR_D		GR_L	
		R	p	R	p	R	p	R	p
TAWSS	Max	0.377	0.150	0.047	0.863	-0.021	0.935	-0.094	0.718
	Mean	0.273	0.305	-0.040	0.884	-0.121	0.642	-0.180	0.489
PSWSS	Max	0.472	0.065	0.229	0.394	0.028	0.916	-0.044	0.866
	Mean	0.357	0.175	0.001	1.000	-0.122	0.642	-0.239	0.356
OSI	Mean	-0.063	0.816	-0.324	0.221	-0.251	0.331	-0.175	0.501
SA	TA-Mean	0.419	0.106	0.233	0.386	-0.077	0.768	-0.187	0.473
	PS-Mean	0.215	0.424	0.047	0.863	-0.052	0.842	-0.078	0.766
RFR	TA	-0.384	0.142	-0.150	0.580	-0.049	0.850	-0.001	0.997
	PS	-0.040	0.884	0.080	0.768	-0.080	0.761	-0.053	0.840

Table 4.6: Correlation coefficients and P-values between WSS derived biomarkers and growth rate on the internal wall.

		TAV				BAV			
Biomarker	Measure	GR_D		GR_L		GR_D		GR_L	
		R	p	R	p	R	p	R	p
FE	FA-Mean	-0.031	0.914	0.028	0.922	-0.147	0.617	-0.166	0.570
	FA-Max	-0.332	0.227	-0.256	0.357	-0.176	0.547	-0.210	0.472
	PS-Mean	-0.127	0.652	0.257	0.356	-0.057	0.846	-0.067	0.820
	PS-Max	-0.278	0.317	-0.036	0.899	-0.04	0.892	-0.057	0.846
$FE_{80\%}$	FA-Mean	-0.310	0.260	-0.134	0.633	0.092	0.755	0.087	0.768
	FA-Max	-0.279	0.314	-0.182	0.516	0.058	0.843	0.067	0.819
	PS-Mean	0.215	0.443	0.274	0.322	0.196	0.502	0.155	0.596
	PS-Max	-0.047	0.869	0.004	0.988	0.315	0.273	0.329	0.251
$FD_{80\%}$	FA-Mean	0.370	0.175	0.010	0.971	-0.104	0.723	-0.19	0.516
	FA-Max	0.554	0.032	0.273	0.325	-0.007	0.980	-0.095	0.746
	PS-Mean	0.184	0.513	-0.103	0.715	-0.291	0.312	-0.399	0.158
	PS-Max	0.115	0.684	-0.035	0.903	-0.189	0.517	-0.343	0.230
α	FA-Mean	0.030	0.916	0.252	0.364	-0.014	0.962	0.047	0.873
	FA-Max	-0.026	0.928	0.079	0.779	-0.128	0.662	-0.067	0.820

Table 4.7: Correlation coefficients and P-values between flow derived biomarkers and growth rate.

development, such as age, wall stiffness, drug therapy, blood pressure, genetical factors, amongst others. Due to this multifactorial influence, in order to identify the relationship between growth profiles and biomarker profiles, we will compute the correlation coefficient between the position of the center of mass of the biomarkers (PC_β) along the centerline and the center of mass of growth rate ($\mathrm{PC}_{\mathrm{GR}}$) as follows:

$$\mathrm{PC}_\beta = \frac{\int_0^1 \beta(\mathrm{PC})\,\mathrm{PC}\,d\mathrm{PC}}{\int_0^1 \beta(\mathrm{PC})d\mathrm{PC}}, \tag{4.15}$$

$$\mathrm{PC}_{\mathrm{GR}} = \frac{\int_0^1 GR(\mathrm{PC})\,\mathrm{PC}\,d\mathrm{PC}}{\int_0^1 GR(\mathrm{PC})d\mathrm{PC}}. \tag{4.16}$$

We will also compute the correlation between PC_β and the location of maximum growth ($\mathrm{PC}_{\mathrm{GR}}^{\mathrm{max}}$). For this analysis, only patients with a fast growing aneurysm with a minimum $GR_L > 0.5$ mm/year, will be considered. The analysis will be performed on the internal and external walls for TAWSS, TASA and OSI and considering the full arterial wall for DIV_W^+ and DIV_W^-. The results are summarized in Tables 4.8-4.10. We can observe that only DIV_W^- on TAV patients has a statistically significant correlation with the location of maximum growth rate, being R = 0.645 and p = 0.023. This could indicate that the location where the aneurysm develops is located in the vicinity of regions of negative divergence.

PC_β	TAV				BAV			
	PC_{GR}		PC_{GR}^{max}		PC_{GR}		PC_{GR}^{max}	
	R	p	R	p	R	p	R	p
TAWSS	-0.334	0.289	-0.294	0.354	-0.108	0.701	-0.004	0.988
OSI	-0.449	0.143	0.043	0.895	0.107	0.705	-0.081	0.774
TASA	0.242	0.449	0.006	0.984	0.074	0.792	-0.004	0.990

Table 4.8: Correlation coefficients and P-values between PC_β and $PC_{\mathbf{GR}}$ on the external wall.

PC_β	TAV				BAV			
	PC_{GR}		PC_{GR}^{max}		PC_{GR}		PC_{GR}^{max}	
	R	p	R	p	R	p	R	p
TAWSS	-0.619	0.032	-0.493	0.104	-0.432	0.108	-0.361	0.186
OSI	-0.005	0.988	0.424	0.170	0.240	0.388	-0.020	0.944
TASA	-0.473	0.121	-0.344	0.274	-0.331	0.228	0.061	0.828

Table 4.9: Correlation coefficients and P-values between PC_β and $PC_{\mathbf{GR}}$ on the internal wall.

PC_β	TAV				BAV			
	PC_{GR}		PC_{GR}^{max}		PC_{GR}		PC_{GR}^{max}	
	R	p	R	p	R	p	R	p
DIV_W^+	-0.389	0.211	0.393	0.206	0.113	0.689	0.135	0.630
DIV_W^-	-0.055	0.865	0.645	0.023	0.347	0.205	0.317	0.249

Table 4.10: Correlation coefficients and P-values between PC_{DIV} and $PC_{\mathbf{GR}}$.

4.5 Discussion

In the present work, an analysis of the growth rate and fluid biomarkers on a cohort of patients has been performed and consequently the correlation between them has been evaluated. The diameter and growth rate analysis revealed some interesting findings with respect to the location of maximum diameter, difference between local and absolute growth rate and the correlation between initial diameter and growth rate. The average growth rate based on diameter was 0.94 and 1.15 mm/year for TAV and BAV patients, respectively, which is slightly higher than the values reported in previous studies: 0.47 mm/year in [5] and 0.2 mm/year [123]. With regard to the location of D_0, a significant difference was observed between TAVs (PC = 0.25) and BAVs (PC = 0.40). This indicates that TAV patients are more prone to aneurysm near the sinotubular junction where as the BAV patients are prone to developing aneurysms in the mid-ascending section of the arta. It can also be observed that the dispersion of TAV patients is significantly larger than in BAV patients, being the standard deviation of maximum diameter location equal to 0.18 and 0.11, respectively. For TAVs, the aneurysms are uniformly distributed in the range PC $\in$ [0, 0.5], whereas, for BAVs, the aneurysms are concentrated in the range PC $\in$ [0.4, 0.5]. This could be due to the altered jet flow caused by the BAV shape, which could be distorting the flow in a similar manner in all patients, or, alternatively, because of the genetic disorder of the aortic wall cells, which could be manifesting more intensely in this location. Concerning the differences between growth rate measures, the local growth rate was, on average, 63% higher than the global growth rate. This suggest that evaluating the growth based on maximum diameter could lead to an underestimation of risk of rupture on certain patients, since the current guidelines for surgery eligibility are based on GR_D [7]. This is specially true for patients with GR_D close to zero, but which show a significant GR_L. With respect to the link between initial diameter and growth rate, it is surprising to observe that no correlation exists, since the growth rate is expected to be exponential [121, 122] and thus, bigger diameters should be linked to bigger growth rates. A possible explanation for this may be that patients which develop a large aneurysm are given medication to lower blood pressure and thus reduce the aneurysm growth rate and risk of rupture. On the other hand, it may be possible that, since patients are surveyed by echography during the initial phase of the aneurysm, when exponential growth was detected surgery was performed after a first angiography acquisition and, thus, these patients with exponential growth rate are not present in our study, as they require a double acquisition. A final remark with respect to growth rate should be made: in our study, two patients had a GR_D exceeding 4.8 mm/year, which surpasses by an order of magnitude the threshold for surgery eligibility. In a previous study with 90 subjects, only 15.6% of subjects exceeded a growth rate of 1 mm/year and the maximum growth rate was 2.3 mm/year [5]. This could suggest that, either an error was made during the acquisition of the angiographies or during the segmentation procedure, leading to an overestimated growth rate, or, simply, that these two BAV patients had entered a phase of

accelerated growth and were at high risk of rupture before the surgery.

The CFD results have shown some marked differences between TAVs and BAVs. This is specially the case for TAWSS and TASA. The TAWSS was, on average, 50% higher in BAV patients, which agrees with previous studies [144]. This can be explained as there exist a direct link between aortic jet velocity and TAWSS (R = 0.82) and, at the same time, BAV patients have, on average, 56% higher jet velocity than TAV patients. When assessing the external and internal wall independently, we observe an that the former is subject to 26% higher TAWSS, gue to the fact that the jet impingement region is located in this region. The TASA shows similar averaged values between TAV and BAV groups, however a significant difference is observed when assessing the dispersion of the data, as the interquartile range is 0.06 and 0.18, respectively. This which could be due to the stenosis caused by the bicuspidity which is causing a more chaotic flow structure [136]. The most relevant finding regarding TASA is the larger difference between the external and internal walls. It has been shown that the external wall is subject to a predominant forward flow whereas the internal wall is subject to a predominant reversed flow. This can be explained due to the fact that the impinging jet gets deflected by the aortic wall towards the aortic arch creating a region of forward flow on the external wall, while, on the internal wall, recirculation and reverse flow regions are present throughout the cardiac cycle as the aortic jet does not occupy the full cross-section of the aorta. It would be interesting to assess if in healthy aortas, which have a smaller diameter and where the aortic jet occupies a larger proportion of the cross-section, different results are obtained. Concerning the OSI, we observed a higher value on the internal wall which can be explained by the predominantly reversed flow present, linking the elevated OSI levels with low values of TASA. Where reverse flow is present, a more chaotic flow structure is present and thus higher OSI is expected.

The majority of the fluid biomarkers has not shown a correlation with growth rate, with the exception of TASA, $FD_{80\%}$ and DIV_W^- on TAV patients and PSSA on BAV patients. It is remarkable that TAWSS has not shown any correlation with aneurysm development, since it has been suggested that regions subject to elevated WSS suffer from extra cellular matrix dysregulation and have reduced thickness, elastin levels and smooth muscle cell count [36, 37, 132]. Regarding the OSI, our results have shown no correlation. Up to date, no study has provided evidence suggesting that OSI levels are related to aneurysm growth. Contrary to TAWSS and OSI, some correlations have been found when evaluating the SA. When considering the full luminal surface of TAV valve patients, a correlation coefficient of 0.556 (p = 0.025) was obtained between TASA and GR_D. However, prudence must be taken before assuring that a relationship exists, since no correlation was found when the external and internal walls were assessed independently and, moreover, no correlation was found in any of the three considered zones (full surface, external and internal wall) when considering GR_L. Additionally, this correlation suggest that a predominant forward flow (SA = 1) promotes aneurysm growth, which is contrary to the current findings that suggest that SA close to zero promote aneurysm growth [138]. We hypothesise that if a strong relationship was present

between TASA and growth on TAV patients, we would observe significant correlation when considering a specific region (external or internal wall) and also when evaluating GR_L. Oppositely to TAV patients, BAV patients showed a negative correlation between SA and growth rate when evaluating the external wall, suggesting that reversed and rotating flow are linked to wall degeneration, which agrees with previous studies [39, 138]. Specifically, the PSSA showed a correlation coefficient R = -0.482 and -0.481 with GR_D and GR_L, respectively. The fact that both GR_D and GR_L show a nearly identical correlation further supports the hypothesis of PSSA being linked to growth rate. Finally, we conclude that further studies on a larger cohort are required in order to clarify if SA and growth rate are related, since the current cohort consists of only 16 TAVs and 17 BAVs, in order to ensure that the statistically significant correlations remain on a larger set of patients. Additionally, a more elaborate analysis of the SA distribution should be performed in order to understand the flow patterns that promote aneurysm growth since. In this analysis, no distinction is made between a patient which has a predominating rotating flow, with SA $\approx$ 0 along the majority of the luminal surface, and a patient which has regions of both forward and reversed flow, with SA $\approx$ 1 and -1, respectively. This is because we have assessed averaged values across the surfaces and, thus, both scenarios will yield an averaged TASA close to zero. To add further complexity to the subject, an analysis distinguishing between clockwise and anticlockwise circumferential WSS would enrich the understanding of the SA distribution, although a more elaborate formulation of SA would be required for this purpose.

The WSS topological skeleton has shown that a correlation exists between the location of negative DIV_W regions and the location of maximum growth on TAV patients, being the correlation coefficient R= 0.645 (p = 0.023). The negative divergence of the WSS field means that the local shear forces are exerting a contraction on the endothelium. Since the WSS topological skeleton can be used to identify near-wall mass transport and decipher biomechemical concentration patterns along the aortic wall [143], the regions subject to a predominant DIV_W^- are also subject to accumulation of biochemical molecules, which could be a accelerating the aneurysm development. Further analysis of the WSS topological skeleton is required in order to decipherer the full picture of the near wall flow dynamics. In this regard, an analysis of the fixed points residence time should be used to quantify the risk of biochemical accumulation [141, 145] and an assessment of the variation of the contraction and expansion action over the endothelium, namely the topological shear variation index [135], should be performed, as it has been shown to be linked to endothelial cell dysfunction and apoptosis [146, 147].

The flow biomakers have shown no relationship with growth rate, with the exception of maximum flux averaged $\mathrm{FD}_{80\%}$ on TAV patients (R = 0.554, p = 0.032) and GR_D. As occurred with TASA on TAV patients, only GR_D showed a correlation while GR_L showed no correlation (R = 0.273, p = 0.325). Thus, again, care should be taken when drawing definite conclusion on this regard. However this may be, the correlation with GR_D could indicate that patients having the flux contained over a reduced area of

the aorta cross section are prone to faster aneurysm development. This biomarker is an indicator of the dispersion and uniformity of the velocity field and, hence, it suggests that a non-uniformly distributed flow with pronounced regions of high velocity may be causing a disruption of the flow and triggering a biomechanical response on the aortic surface. In previous studies, some flow biomarkers have been related to aneurysm growth. It has been suggested that flow angle could be related to aneurysm development [133], since a correlation was found between the deviation of the aortic jet and the aortic diameter. However, this link could be a consequence of the aneurysm development and not a cause, as occurs with flow eccentricity, which has been shown to be directly linked to the bulge size [148].

As a final remark, in this work it has been shown that some fluid biomarkers have a potential to predict the aneurysm growth rate. By assessing the flow dynamics through a set of biomarkers, the future diagnosis procedures could be improved by enriching the clinical data with a full understanding of the fluid stressors that act on the wall and by quantifying the biochemical processes that occur in the vicinity of the wall. To provide strong evidence of the veracity of these results and the correlations found herein, a multi-centric study over a large population should be performed.

4.5.1 Limitation

Independently of the strength of the correlations found in this work, some critical limitations prevents drawing definite conclusions and thus the herein computed correlations should be taken with care. A series of limitations concerning the acquisitions are present. Firstly, since the first acquisitions are taken when the aneurysm has already developed, we only analyse in this study the later phase of the aneurysm progression and not the initial phase which triggers aneurysms development. We thus analyse the effect of hemodynamics on the aneurysm once the wall has already weakened and deformed and we are therefore unable to draw conclusions on how hemodynamics are related to the kick-off of aneurysm growth on a healthy, undeformed aorta. Secondly, the time window between acquisitions was, in some cases, low, as 40% of the cohort has a spacing under 24 months. Assuming standard growth rates reported in literature, between 0.2 and 0.5 mm/year [5, 123], the expected average growth is of the order of magnitude of the angiography resolution: [0.312, 0.312, 0.75] mm. Due to this fact, the growth rate measurements are prone to having a large error. In order to reduce this error, either a CT scan with a higher resolution is required, or a larger time window should be used. Lastly, diastolic pressure readings where not taken during the angiography acquisition and, thus, one cannot distinguish between geometric changes caused by the aneurysm development or due to changes in the arterial pressure. In other words, if the patient has a higher arterial pressure during the second acquisition, the aorta will appear larger, however, this increase in size might be due to the pressure only and not to a degeneration of the wall and a dilatation of the vessel. Thus, in order to quantify the influence of the aortic pressure on the aneurysm size and differentiate between aneurysm growth and pressure deformation, pressure reading should accompany the

angiographies.

Doppler and MRI measurements were available for 25 patients which where used to calibrate the inlet velocity and valve area. For the remaining 8 patients the velocity and area where calibrated with normative values according to [139]. This has introduced an uncertainty as we cannot guarantee that these 8 patients have a healthy valve condition, thus, the biomarkers obtained for this set of patients may be erroneous. More over, the jet direction was assumed parallel to the centerline, and it is know that, specially in cases of stenosis, this is not the case [110, 133]. Therefore, the region where the jet impacts the wall is highly affected by this assumption and the overall flow structure is severely affected by this parameter. Lastly, the geometry of the valves was assumed using idealized shapes and a fully-developed turbulent profile was imposed on all patients. However, aortic jets characteristics differ and stenosis develops differently amongst patients, giving rise to different jet shapes and flow structures, as shown in [119]. Due to the simplification made on the aortic jet, the imposed boundary condition is not personalized and, therefore, we cannot ensure that our results have accurately capture the patient-specific conditions. We expect to obtain different biomarker values if a patient-specific flow profile had been used on the aortic valve.

Finally, we must emphasise that the aortic wall movement has been neglected. It has been shown that WSS is affected by the wall dynamics [29, 39, 149] and, hence, the WSS derived biomarkers computed in this study would be expected to differ if FSI effects would have been included.

4.6 Conclusions

Limited evidence of correlation between aneurysm growth and fluid biomarkers has been obtained in this study. Only TASA, $FD_{80\%}$ and DIV^{-}_{W} on TAV patients and PSSA on BAV patients showed a statistically significant correlation. Due to the numerous limitations of this study, we conclude that the analysis should be repeated on a cohort of patients which has been followed during a larger time window, in order to reduce the error in the growth rate measurements, and which have undergone an MRI 4D exam in order to accurately calibrate the aortic jet. The spatio-temporal velocity profile of the aortic jet will severely determine the flow structure throughout the cardiac cycle, hence, for accurate CFD biomarker analysis, patient-specific models including aortic jet calibration are mandatory.

However this may be, the availability of clinical data remains a bottleneck for investigating the role of computational biomarkers on cardiovascular pathologies. Although the technology required to acquire the necessary data for performing this type of in-silico analyses has been developed, their use is limited as it is not part of the standard clinical protocols. Therefore, it is challenging to obtain a large cohort of patients which have two sufficiently spaced angiographies and a MRI 4D flow acquisition.

4.7 Contour plots of WSS biomarkers

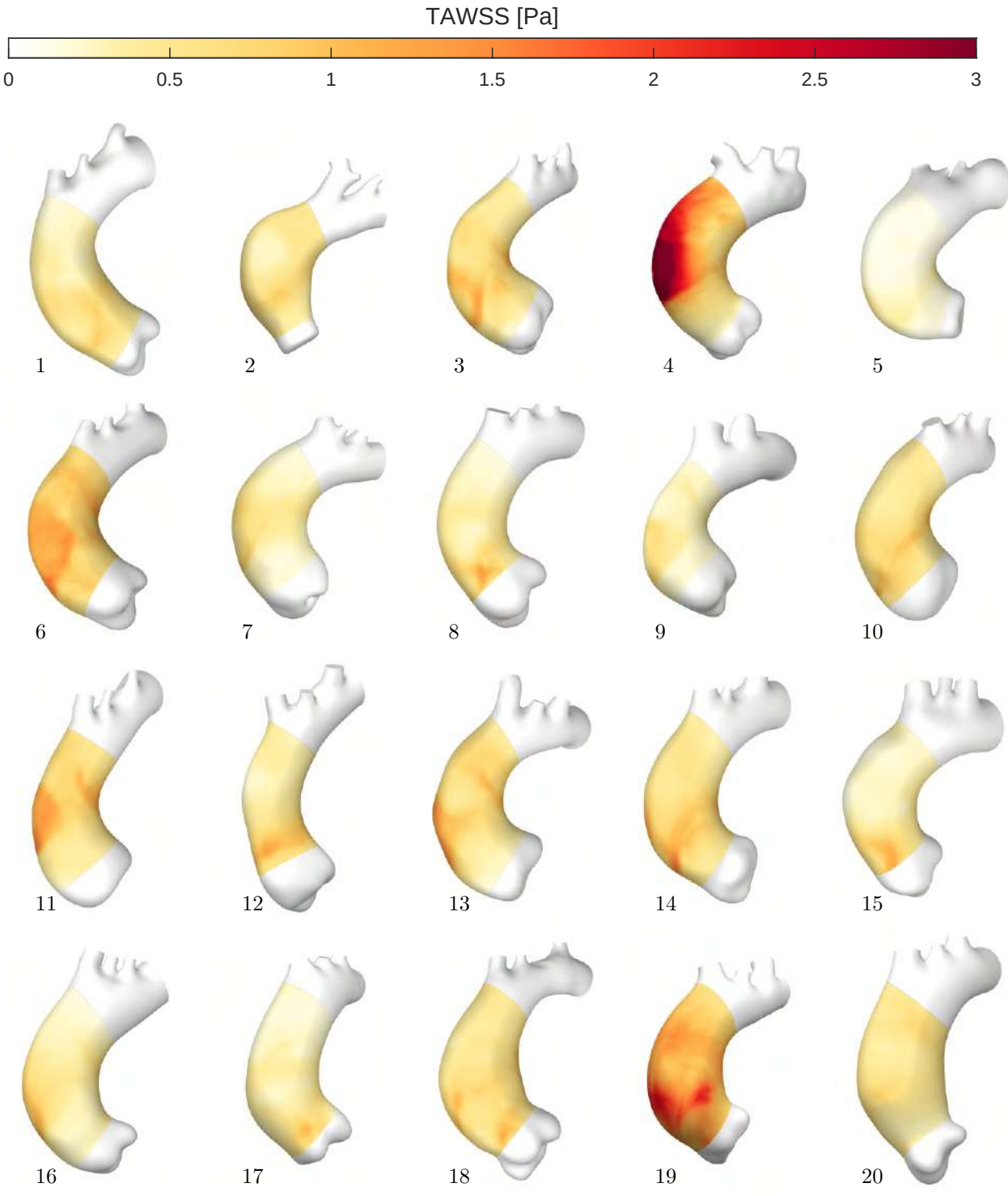

Figure 4.22: TAWSS for the patient cohort.

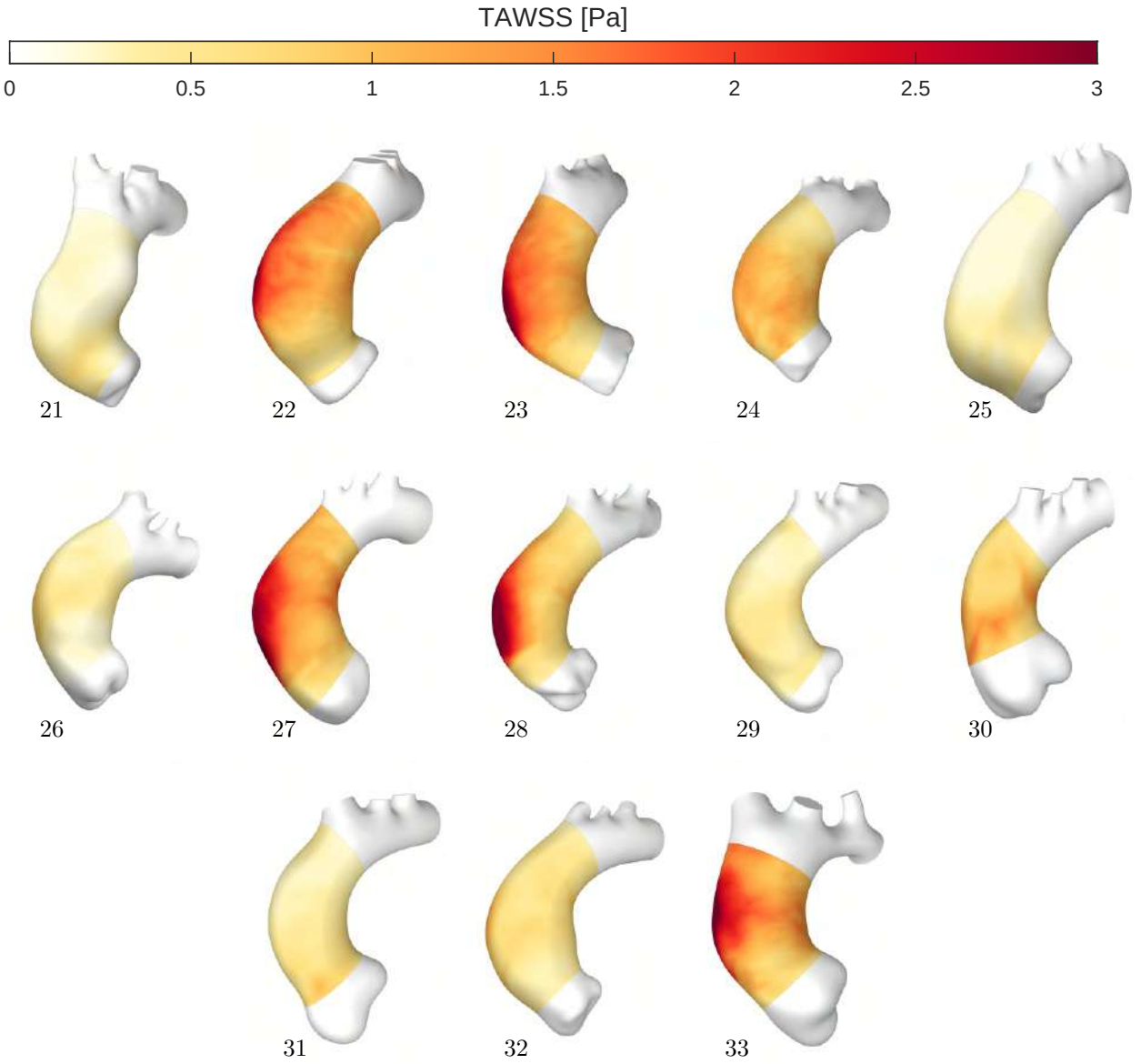

Figure 4.22: TAWSS for the patient cohort (continued).

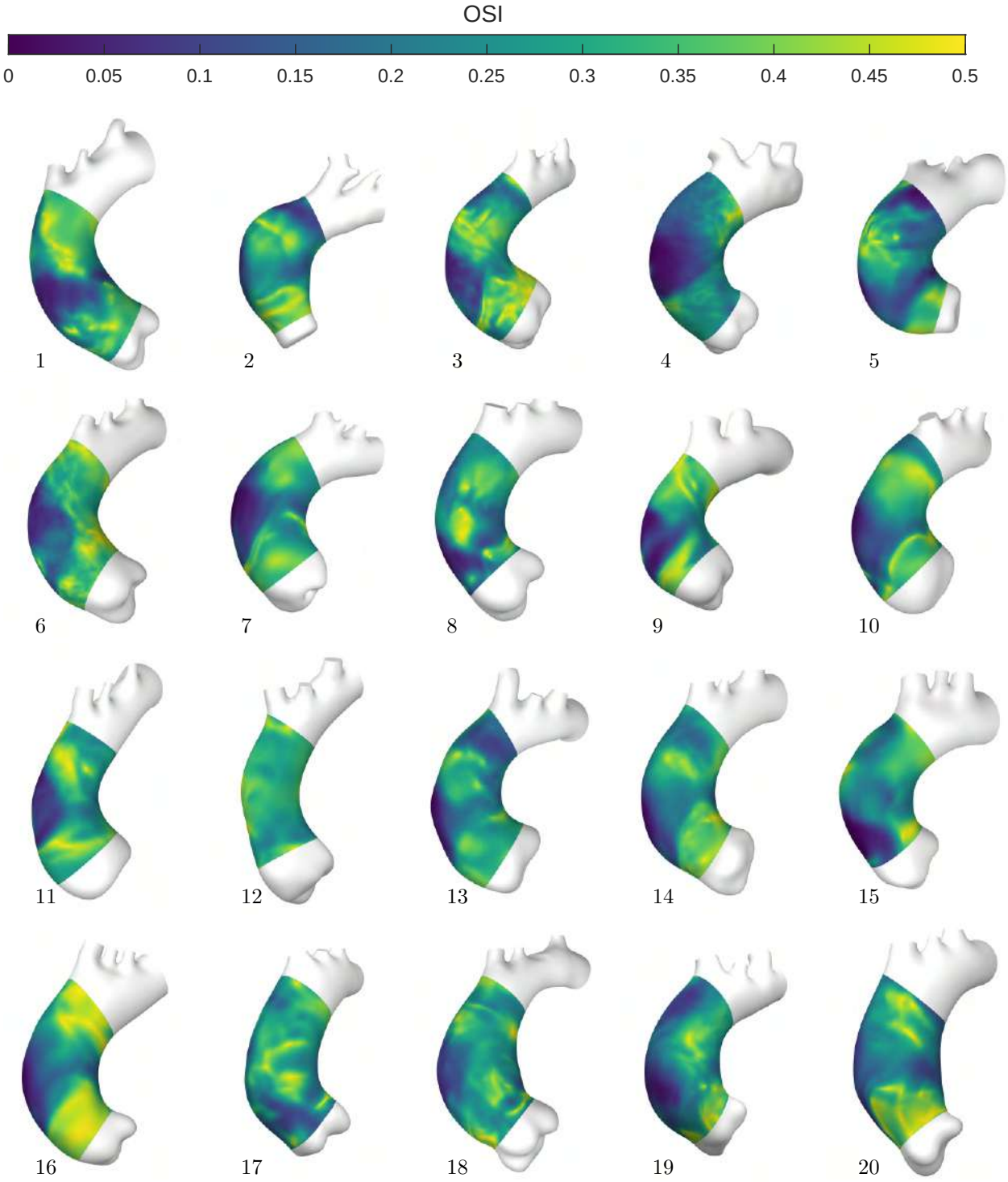

Figure 4.23: OSI for the patient cohort.

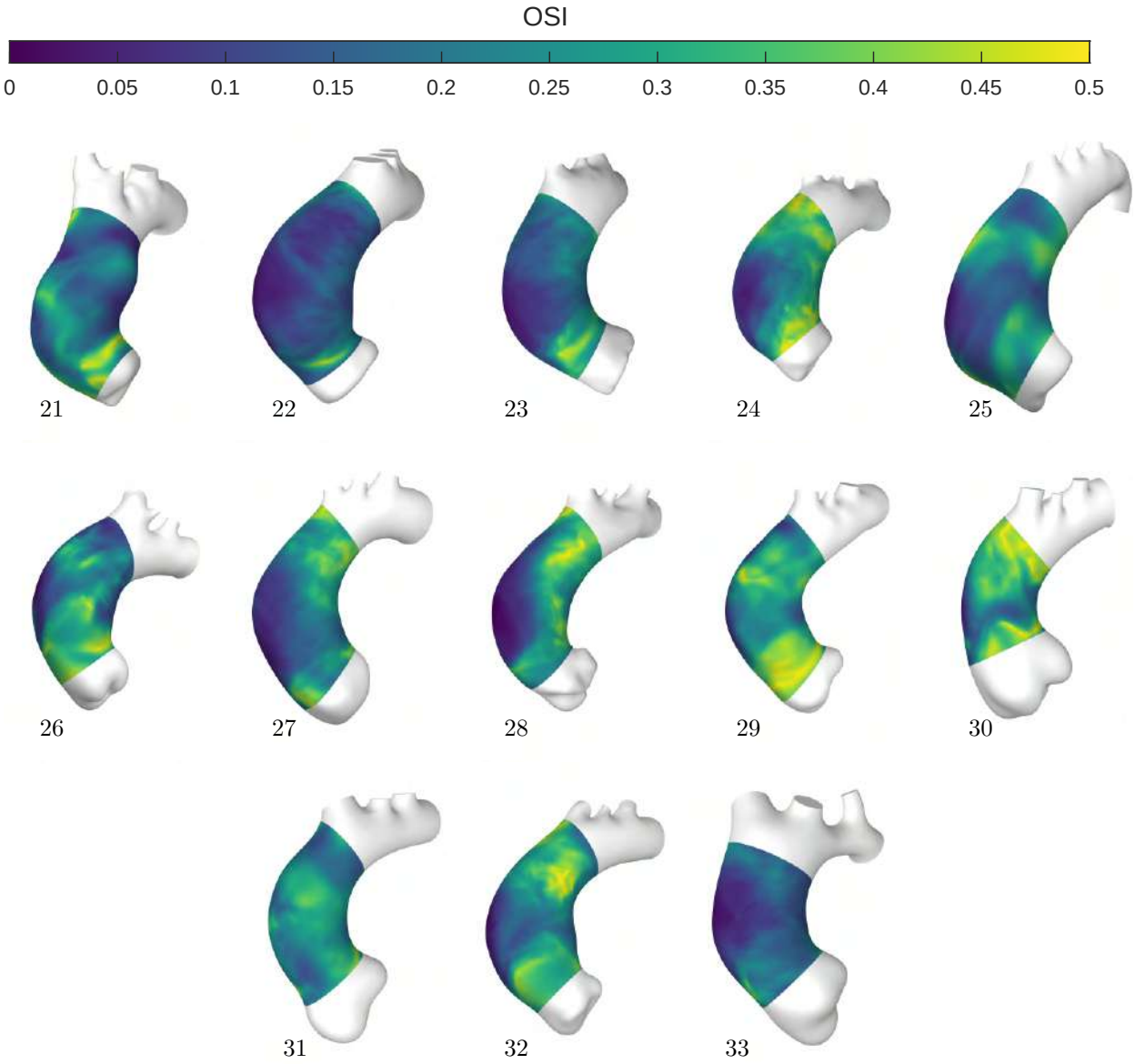

Figure 4.23: OSI for the patient cohort (continued).

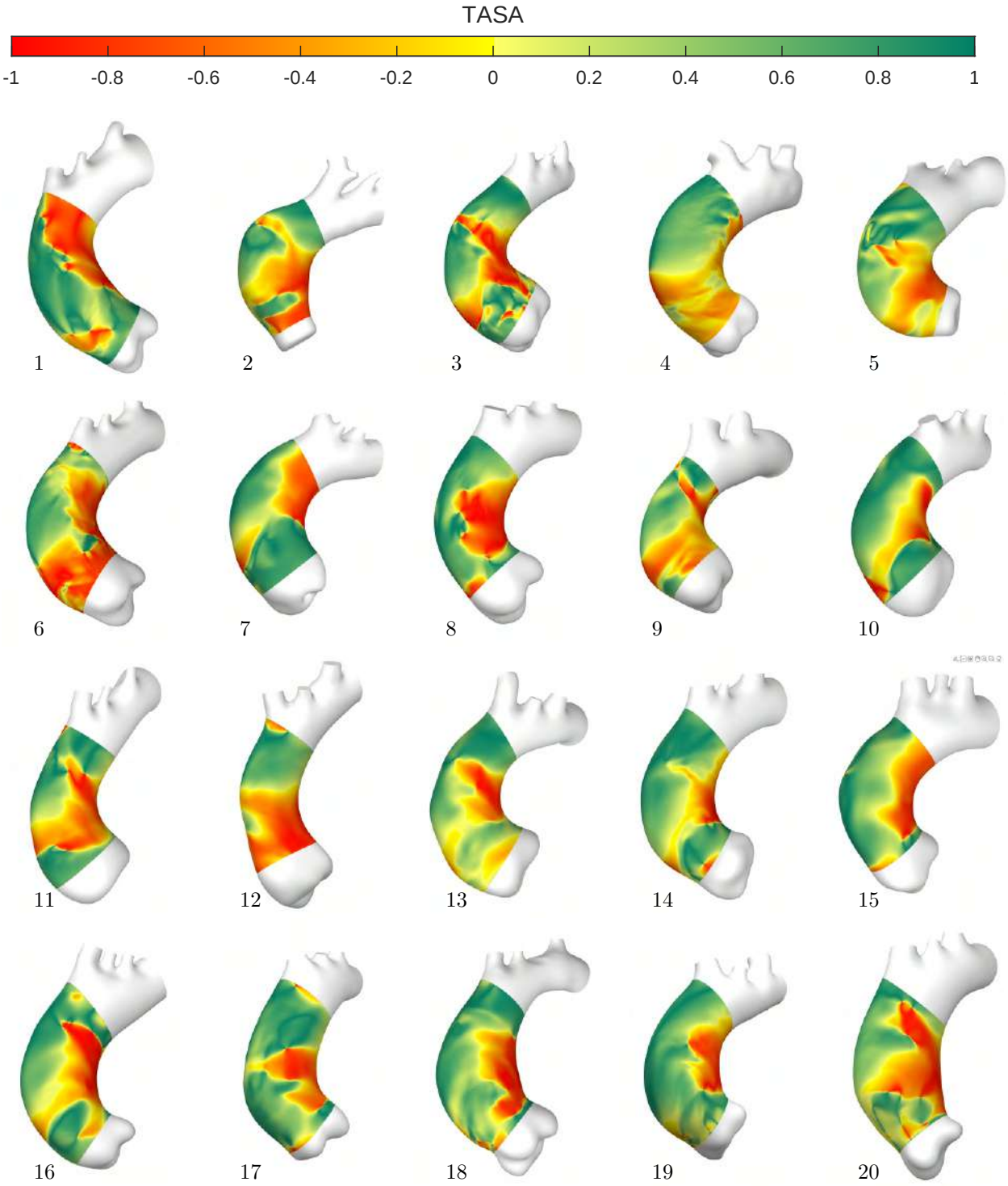

Figure 4.24: TASA for the patient cohort.

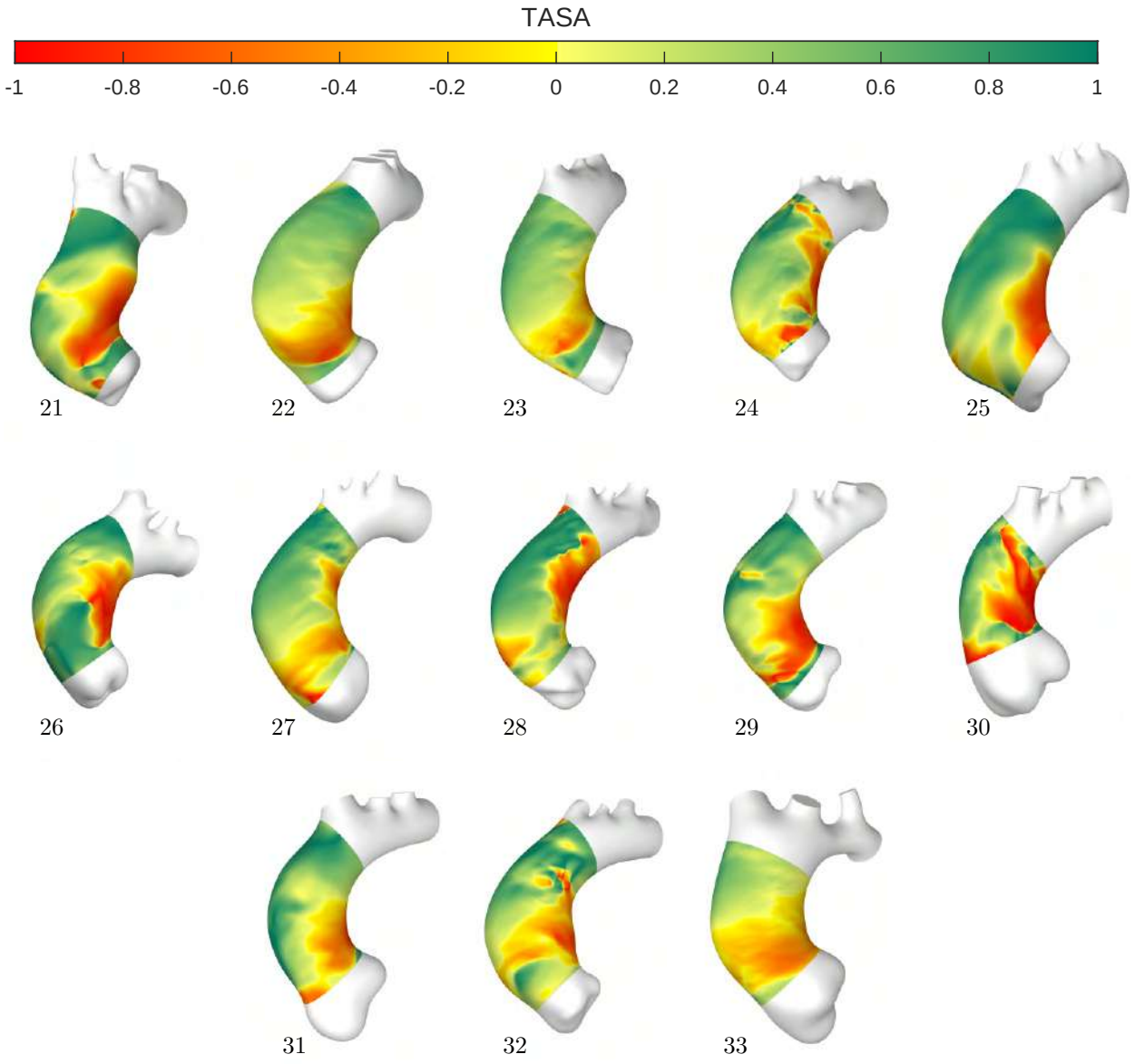

Figure 4.24: TASA for the patient cohort (continued).

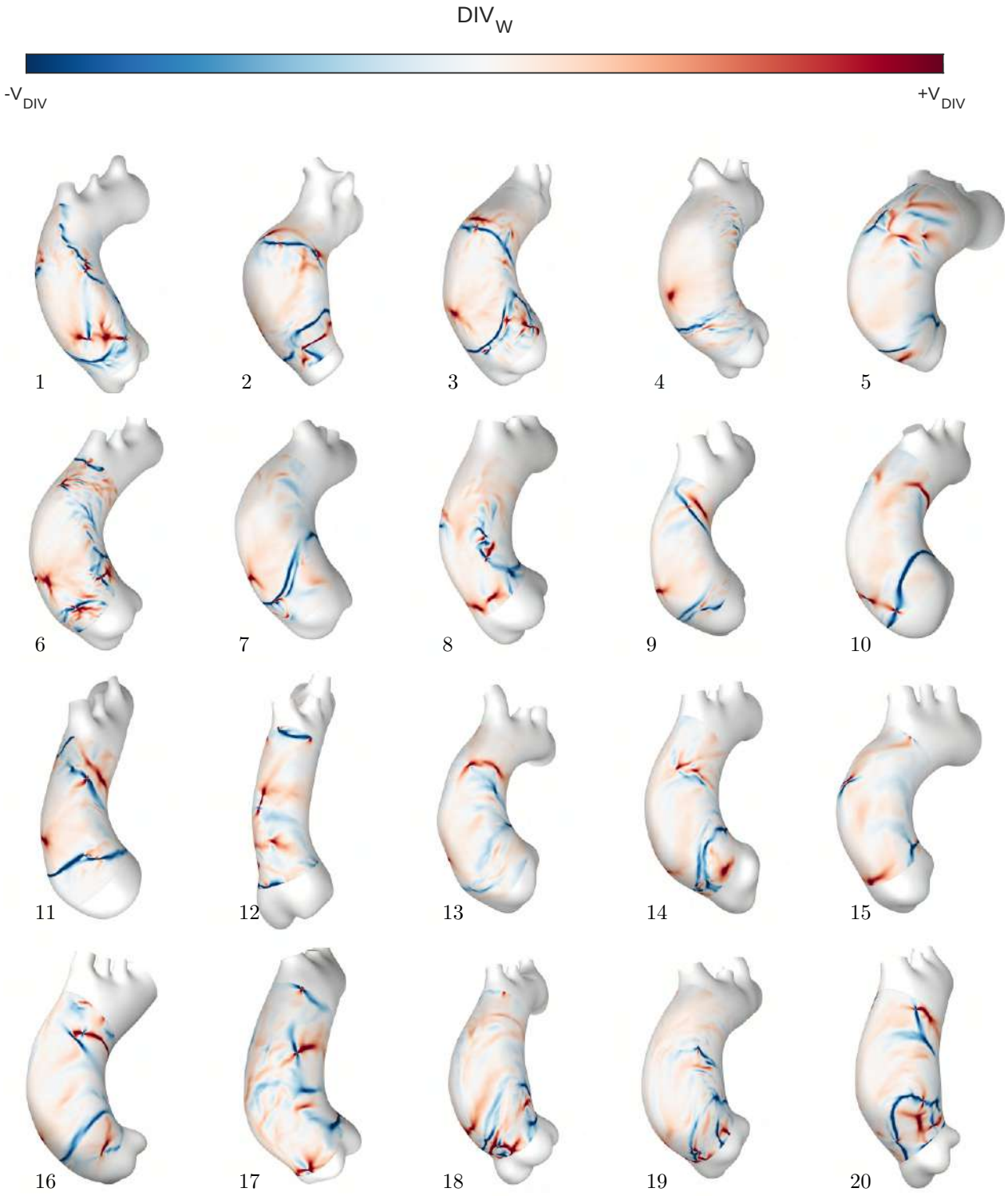

Figure 4.25: WSS topological skeleton for the patient cohort.

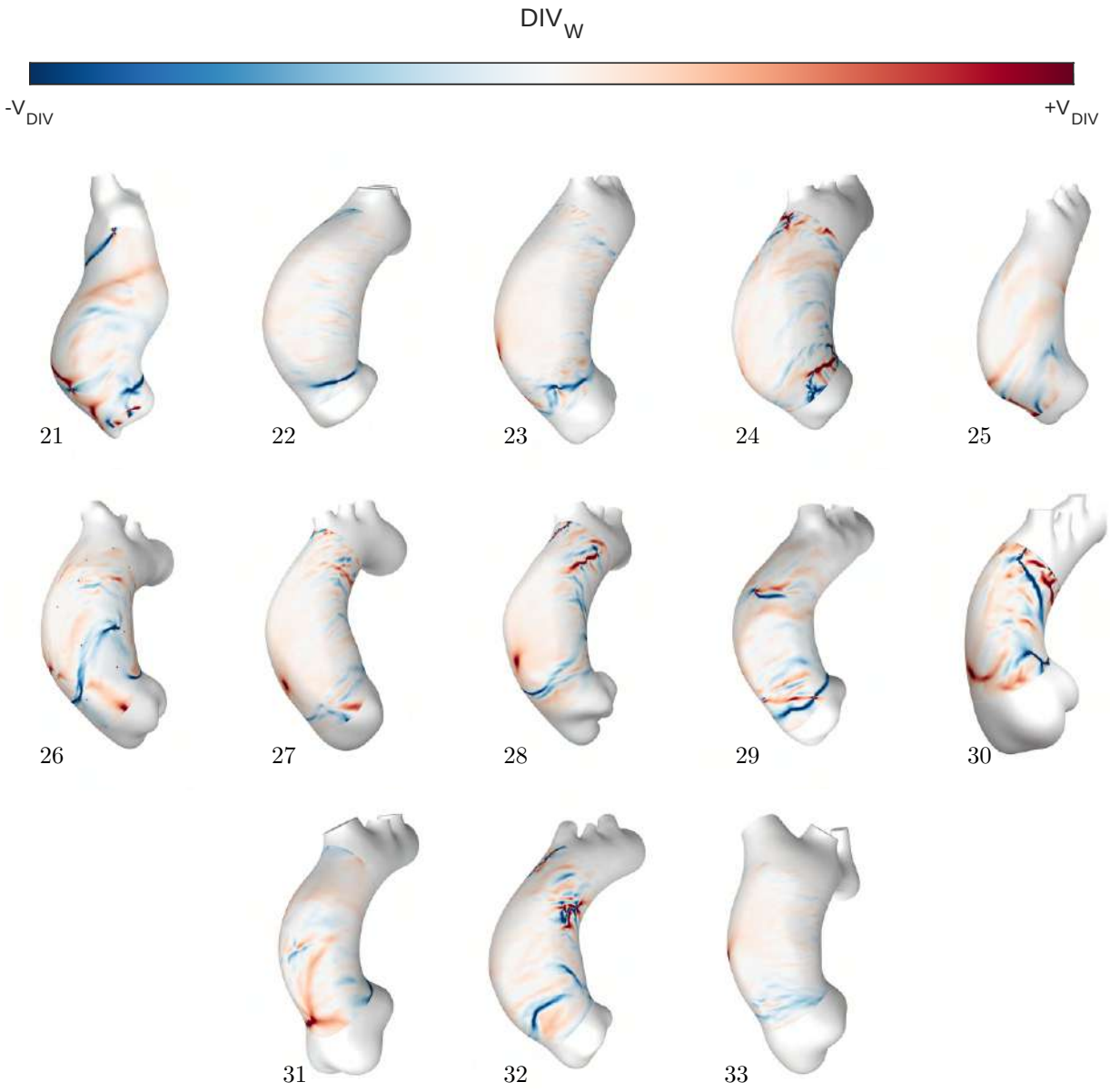

Figure 4.25: WSS topological skeleton for the patient cohort (continued).

Chapter 5

Patient-specific FSI models

The development of an aortic aneurysm is a multi-factorial process in which it is suspected that the contributions of both hemodynamic and structural stresses play a role in the aortic wall dysregulation and degeneration. In sight of the complex nature of the factors involved in the pathology progression, an adequate model capable of capturing both stressors is required for a comprehensive understanding of the patient's condition. For this purpose, FSI models are used, since they combine a CFD and a FEM solver to capture the phenomena of both physics and the interaction between them. The development of such models is challenging, since numerous clinical measurements are required to generate the numerical data used to personalize the model. Additionally, the complexity of FSI models is greater than that of CFD or FEM alone, thus a larger uncertainty in the model maybe introduced and therefore additional precautions should be taken when analysing the results.

In this chapter, we address this challenge by developing the techniques required to accurately represent the hemodynamic flow, performing a spatio-temporal calibration of the aortic jet from data provided by 4D MRI flow acquisitions. Additionally, a personalization of the structural model of the aorta wall is performed by accounting for spatial variability of material properties. The workflow is used to model a single patient suffering from ascending aortic aneurysm. In this way, a high-fidelity workflow capable of capturing the patient-specific conditions is presented.

5.1 State of the art

Due to the great insight that numerical simulation can provide to the understanding of patient's arterial condition, numerous works have been done to develop the techniques required for the accurate modelling of arteries. In Chapter 3 we described the computational methodologies which have been used to model the hemodynamic flow, while in Chapter 4 we described the current state of the art regarding the influence of fluid biomarkers on aneurysm development. In this Chapter, we summarize the latests works which have focused on the characterization of the aortic wall and the risk of rupture, together with the state of the art FSI models, which have been used to understand the interaction between the flow and arterial wall deformations.

The effect of considering the wall displacement has a direct impact on the flow behaviour and thus differences appear in the WSS field when accounting for transient deformations. In a recent work [83], the displacement of the arterial wall has been modelled using a 1-way coupling approach to perform an hemodynamic analysis of a compliant vessel. To do so, a registration of the aorta deformation throughout the cardiac cycle was performed by using a multiphase CT scan. Subsequently, the simulation was performed and compared against a rigid wall model, concluding that the wall displacement affected the distribution of OSI and reduced the WSS. In this line of research, a 2-way FSI model considering a uniform, linear elastic wall was used and also showed a reduction in WSS levels in compliant models [149].

In another study [29], a 2-way FSI model was compared to a CFD and a FEA model, in terms of WSS and intramural stress, respectively. In the FEA, the motion caused by the cardiac motion was considered and used to distinguish the stresses caused by the fluid pressure and valve motion separately. Further readings regarding this line of research are available in literature focusing on the ascending [150, 151] and abdominal aorta [152–155] and aortic dissection [156, 157]. One additional phenomena which cannot be captured using CFD models is the behaviour of the aortic valve. For this reason, a FSI model of a pulsatile flow and a deformable aortic valve was developed to assess the effect of such deformations on the turbulence generation [158].

The aorta is located within the thorax and surrounded by diverse organs and tissues. Various works have assessed the influence of these tissues on the deformations, both for the ascending and descending thoracic aorta [159] and for the abdominal aorta and iliac arteries [160, 161]. It has been shown that the proximity to the spine has a direct influence on the stiffness of the supports and that it is important to consider it in order to compute accurate deformations on the aorta. In a more recent study, the displacement of the aortic valve was tracked using high resolution CINE MRI and used to calibrate the viscoelastic support surrounding the aorta [38]. The aortic root motion has also been used to quantify the proximal aorta axial stretch and its influence on the estimation of wall distensibility by evaluating the deformations both in-silico and in-vivo [162].

It has been shown that aortic wall thickness varies within the vessel segments, specially in damaged regions prone to aneurysm development [163]. With the aim of evaluating the risk of rupture of ascending aortic aneurysms, FSI computations where used to assess the variations in peak wall stress as function of the wall stiffness and hypertension level [20]. Other works accounted for the variation of wall thickness, measured using microCT scan, in order to accurately compute risk of rupture on arterial segments [21, 22]. These improvements on the material characterization enable for a more truthful representation of the wall stress.

It is well known that the aortic wall is composed of three distinct layers which have an anisotropic behaviour [17, 18]. In the pursuit of better modelling the aortic wall properties, the anisotropy has been included in structural models to perform FSI simulations of the ascending aorta [30] and abdominal aneurysms [40, 41].

Due to the the fact that the aorta is just a part of the cardiovascular system, some authors have attempted to model the FSI phenomena while coupling the outlet boundaries to zero-dimensional models representing the downstream vasculature. Within this line of research, a model of the primary large arteries of the human body, which extend from the heart up to the head, legs and arms, was used to model the pressure and flow waveforms through the arterial network [42]. This work included a variable thickness and elastic properties of the arterial walls according to vessel diameter. Additionally, they evaluated the impact of age related arterial stiffness on the flow dynamics, revealing that the modelled

pressure amplification and increase in pulse wave velocity was in agreement with clinical measures.

We conclude this summary of the current state of the art by highlighting that only one work has currently addressed the relationship between numerical biomarkers and growth rate using FSI models [39]. In this work, they used pulse wave velocity measures to personalize the wall stiffness and used MRI 4D data to calibrate the aortic jet. It was shown that the shear angle (defined in Equation 4.4), is linked to aneurysm growth in Marfan syndrome patients. However, no assessment of the structural stress was performed.

5.2 Clinical data

Patients suffering from ascending aortic aneurysm which underwent ascending aorta replacement in the University Hospital of Dijon were considered in this study. The patients participated in a study approved by the French national ethic committee (Project 2018-A02010-55, approved by the French "Comite de Protection des Personnes") which was registered on ClinicalTrials.gov with the number NCT03817008XX. The patients followed the MECATHOR protocol and informed consent was given in order to use clinical data for research purposes. The first angiography did not require MRI 4D flow measurements as it was only used for the computation of the aortic diameter growth. On the second acquisition, both CT and MRI angiographies and MRI 4D flow were acquired. Patients underwent MRI in the days prior to the surgical procedure. This is as standard practice and part of the hospital's protocol in order to correctly assess the patients condition and understand if additional procedures are required during the intervention, such as aortic valve replacement.

The aortic flow was measured using MRI 4D flow acquisitions using a Siemens Magnet, 3T, Skyra. To generate the 4D flow data, a combination of 3D spatial encoding, 3D velocity encoding and cine acquisition is required. The resultant image consists of one magnitude and three phase volumes, corresponding to the three directions of space. As the sequence requires to fill line by line the Fourier plane, the acquisition was performed under ECG and respiratory gating. It is vital to perform the acquisition at a constant instant of the breathing cycle as otherwise the image would be distorted since the heart rests on the diaphragm, which commands the respiratory motion and displaces the full thoracic cavity. To trigger the acquisition, an echography navigator was used to track the diaphragm motion and synchronize the acquisitions. The same applies for the ECG gating, as the heart motion and instance of the cardiac cycle needs to synchronize on each frame. For the ECG measurement, 3 electrodes were placed on the patient and triggered the acquisition with the R-wave. The sequence was composed of 25 frames per cardiac cycle. The resolution was [2.00, 2.00, 2.00] mm. The velocity encoding was set after performing a 2D flow measure in order to avoid aliasing in the 4D flow.

To calibrate the fluid outlet boundary conditions, information on blood pressure is required. Two

procedures can be performed to obtain blood pressure reading: invasive and non-invasive. The patient considered in this study had pressure readings acquired by arm cuff during the MRI acquisition. A minimum of 6 readings were performed through out the duration of the procedure and the average value was recorded.

The patients underwent surgery days after the MRI acquisition. During surgery the ascending aorta was removed and replaced by a stent graph. The removed tissue was then taken to a biomedical laboratory to perform an exhaustive study of its mechanical properties. Thickness measurements and equi-biaxial tensile testing were performed. The experimental study followed a strict protocol in order to ensure the quality of the harvested sample and guarantee a standardized and reproducible procedure as described in [164]. A maximum of eight hours passed between the surgical extraction and the completion of the experiment. The following steps were followed: (1) Tissue sample was preserved in saline water for transportation from the operating room to the laboratory, (2) the tissue was stored and frozen at -80°C, (3) histological fixation was made, (4) biaxial test was performed. The tissue samples were prepared for the mechanical testing by removing the fat attached to the aortic wall in order to accurately measure the wall thickness, which has an important impact on the stress calculation. The aorta was then cut into four quadrants: anterior (ANT), posterior (POST), lateral (LAT) and medial (MED). From each quadrant, square samples of size 15 mm × 15 mm were extracted. The circumferential and longitudinal directions were noted. A depiction of the sample preparation is presented in Figure 5.1. For each sample, the thickness was measured five times in different locations and the averaged value was taken. This measurement was performed using an electronic micrometer (Litematic 12 VL-50, Mitutoyo, Japan) providing a constant force thickness ($\pm 0.01 \mu$m). The mechanical test was performed using a equi-biaxial tensile test machine (LM1,14 TA Instruments, ElectroForce System Group, USA) by positioning four hooks on each edge. The sample remained in saline water at 37°C during the experiment, which consisted of a preconditioning of 10% stretch with ten loading and unloading repetitions followed by a stretch until rupture at a rate of 10 mm/min. The biaxial test setup is shown in Figure 5.2. An example of the results obtained is depicted in Figure 5.3.

5.3 Geometry and meshing

The angiographies obtained were segmented using a semi-automatic algorithm based on semi-automatic procedure based on local thresholding as described in [103] and manually corrected using 3D Slicer. Once the STL geometries were obtained, they were imported into Spaceclaim 22.1 (Ansys Inc, Canonsburg, PA, USA) to perform CAD manipulation and preparation for the meshing stage. A similar procedure was used as in Chapter 4, as a set of smoothing and remeshing iterations were performed to ensure a smooth final surface. The geometry was then separated into the following sections: inlet, annulus, aortic root,

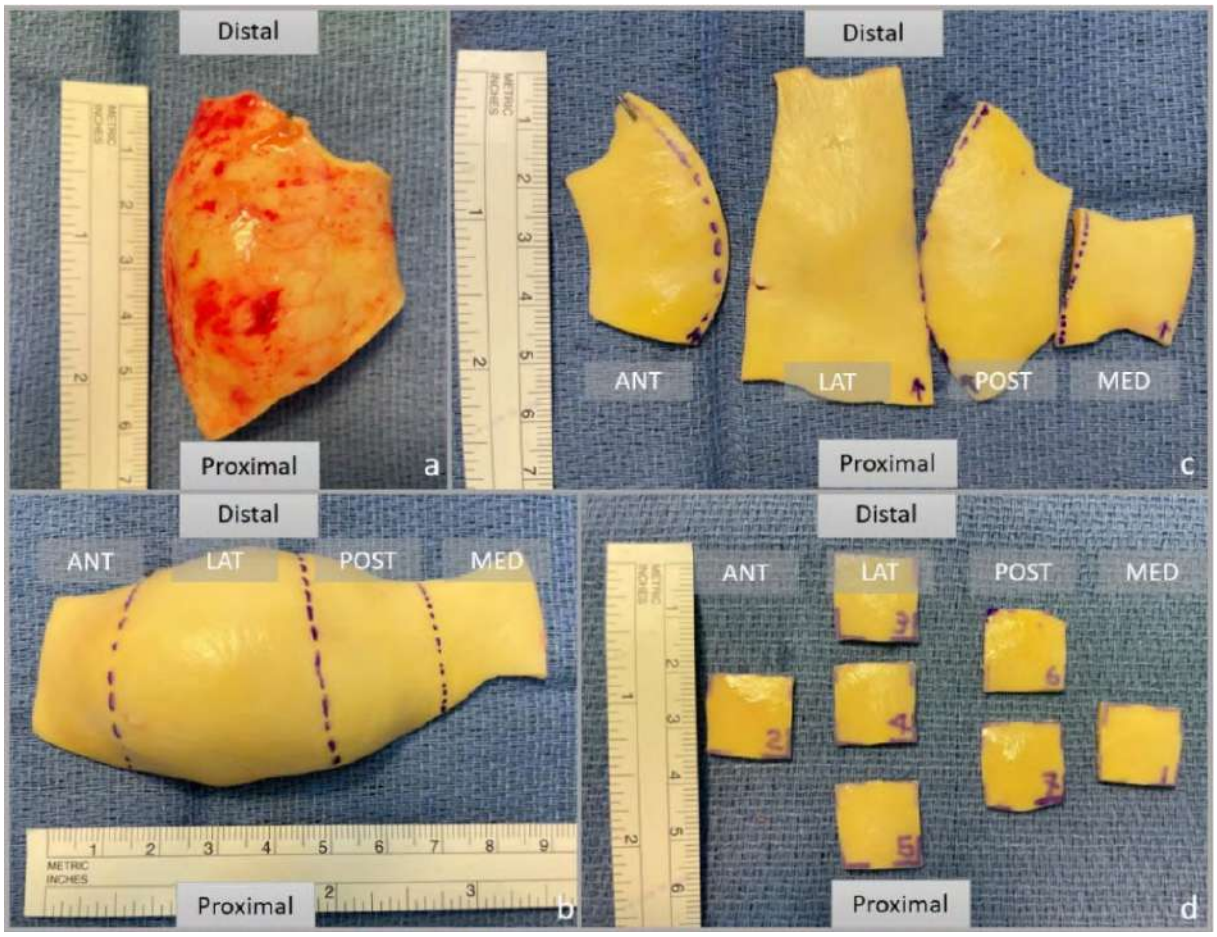

Figure 5.1: Tissue sample preparation: (a) aorta after fat removal, (b) division into four quadrants, (c) separated quadrants and (d) sample ready for mechanical test. (From: S. Lin, "Biomechanics of human ascending aorta and aneurysm rupture risk assessment", PhD Thesis, 2021 [16]).

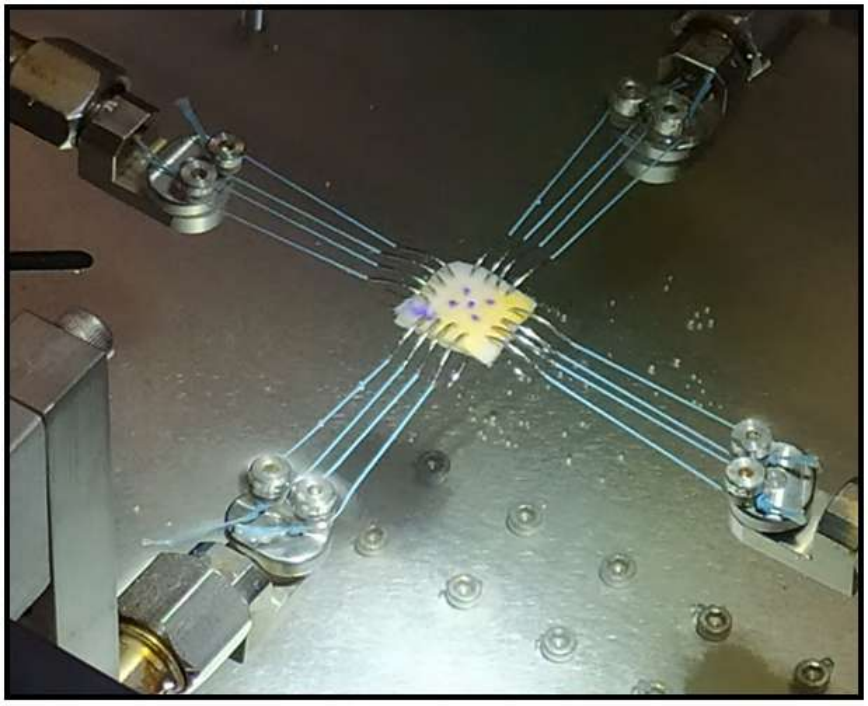

Figure 5.2: Equi-biaxial tensile test performed in the University Hospital of Dijon.

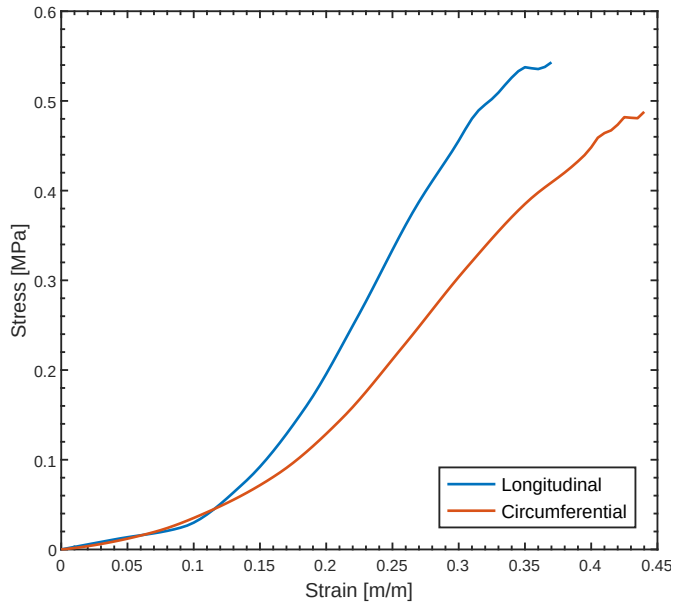

Figure 5.3: Strain-stress results obtained for the longitudinal and circumferential directions after performing an equi-biaxial tensile test on the anterior quadrant.

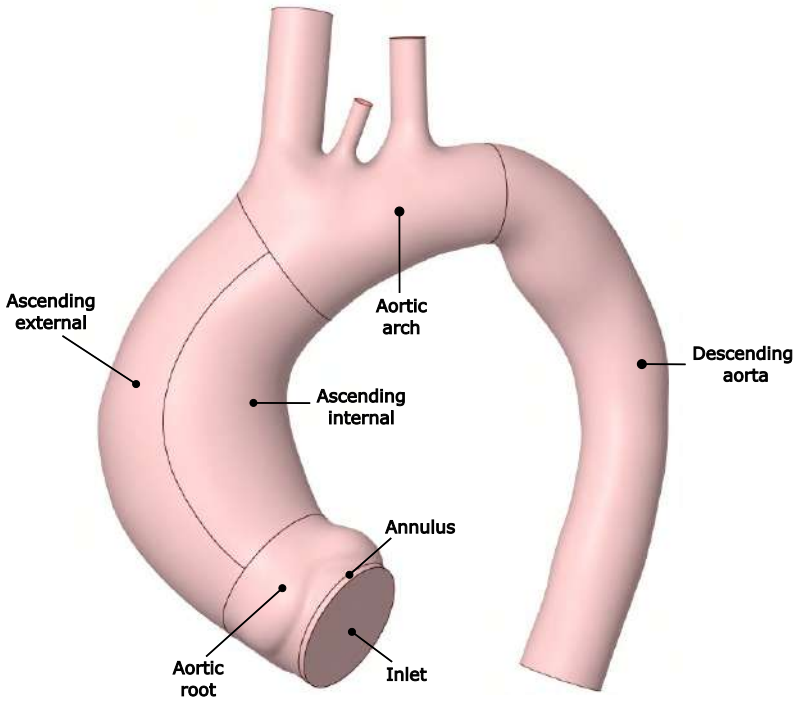

Figure 5.4: Aorta geometry with differentiated surfaces.

ascending aorta (internal and external), aortic arch and descending aorta, as can be seen in Figure 5.4. In this case the valve shape was not imprinted on the inlet face as MRI flow data will be used to define a velocity field across this surface.

The geometry was then imported into Ansys Fluent 22.1 (Ansys Inc, Canonsburg, PA, USA) in order to create a triangular surface mesh. As opposed to the methodology followed on Chapters 3-4, a coarser mesh was adopted due to the computational requirements of FSI studies. The mesh controls are summarized in Table 5.1. The surface mesh was then exported to ICEM 22.1 (Ansys Inc, Canonsburg, PA, USA) in order to transform the initial Fluent mesh into a LSDYNA compatible mesh. The initial surface mesh was used to create the fluid and structural meshes, which were saved separately. Fluid and structural meshes were conformal. The structural mesh was identical to the fluid mesh but had the outlet and inlet faces removed in order to produce an open shell. The volumetric mesh was generated in LSDYNA using tetrahedral elements and three inflation layers on the walls.

Mesh parameter	Value
Face size (mm)	1.0
Max. element size (mm)	1.5
Max. curvature normal angle	16°
No. of elements Fluid (10^5)	8.72
No. of elements Structure (10^4)	4.62

Table 5.1: Mesh parameters.

5.4 Personalized hemodynamic boundary conditions

In order to accurately model the behaviour of the hemodynamic flow, it is of prime importance to calibrate the hemodynamic boundary conditions according to patient-specific data. In this respect, the limiting factor is the availability of velocity and pressure measurements. With out adequate clinical data, approximations using averaged population values are required in order to create the boundary conditions.

5.4.1 Preliminary considerations

Despite clinical data being available, it is important to consider how this information can be feed into the numerical model. For example, some readings might have an acquisition speed lower than what is required for the numerical model and an interpolation ensuring continuity and smoothness is required in order to guarantee a stable computation. On another side, it may happen that it is not possible to impose certain measurements directly as boundary conditions, for example, LSDYNA lacks the capability of defining a mass-flow profile boundary condition and a workaround is required in order to impose the

desired behaviour. In this subsection we discuss the considerations that must be accounted for and the existing limitations concerning the fluid boundary condition setup.

5.4.1.1 Pressure considerations

Pressure measurements are vital to calibrate the outlet boundary conditions. In this regards, we are able to setup our model by either imposing pressure profiles measured from invasive pressure recorders or by calibrating multiscale models. Despite the fact that pressure profiles lead to an accurate imposition of pressure on the model, this procedure poses three main drawbacks. Firstly, we encounter the practical limitation of measuring pressure simultaneously on all the locations required for our model, namely in the descending aorta and the brachiocephalic, left common carotid and left subclavian arteries. Small pressure variations occur amongst the aforementioned locations and an incorrect correspondence between the four pressure profiles would lead to an unphysical flow behaviour in the numerical model. Due to this fact, in the absence of four simultaneous reading, imposing equal pressure profiles on all outlets would lead to an erroneous behaviour. Secondly, the mismatch between the patient specific and the modelled mechanical properties leads inevitably to an incorrect flow through the boundary. This is phenomena occurs since, although the pressure is close to in-vivo values, the dilatation of the vessel may be over or under estimated due to the mechanical modelling assumptions and, thus, the outlet boundary area will be incorrectly calculated. Given a preestablished outlet pressure, the flow through the boundary will be determined by the pressure drop and the opening area. Modelling of the supra-aortic vessels is challenging in this respect due to the lack of patient-specific measurements, since mechanical characterization was only performed on the ascending aorta. Moreover, the ramification of smaller vessels from a main artery implies a rapid change in the wall properties, both regarding thickness and elasticity, and modelling this transition is extremely challenging. Lastly, the stability of the flow on the computational model is compromised as there is a mismatch between the imposed pressure and a numerically stable pressure profile. The FSI model requires a set of coupling iterations in order to converge the deformation and pressure fields. At each fluid sub-iteration cycle the pressure and flow are computed by an iterative algorithm in order to satisfy the Navier-Stokes equations while accounting for the deformation field. If a pressure profile is imposed, the flow will have to drastically adapt at each time step to satisfy the fluid equations and may lead to oscillatory flux patterns.

On the other side, an alternative approach using multi-scale models allows to predefine an approximate behaviour of the system without directly imposing the pressure profiles. Within this alternative, an extensive range of models exist with a myriad of complexity levels. These models are based on modelling the outlet boundary conditions by mimicking the behaviour of the downstream cardiovascular system by using 1-D and 0-D components and allowing the algorithm to automatically compute the boundary conditions, which mimic physiological behaviour and produce a numerically stable profiles for flow and

pressure. This procedure, however, requires an additional modelling effort, since the multi-scale model needs to be calibrated in order to respond as desired and match the patient-specific model.

5.4.1.2 Velocity and flow considerations

To accurately impose the desired patient-specific velocity profiles on both inlets and outlets, high-quality 4D velocity data is required. It is possible approximate the flow profile by using 2D MRI-data (2D + time) since the mass flow traversing the considered plane is unaffected by the in-plane velocity. However, the 3D velocity vector field is lost and only velocity perpendicular to the MRI plane may be computed, leading to a lost of truthfulness in the velocity field. Despite this, MRI 2D flow data represents an optimal technology to obtain mass-flow measures since the spatio-temporal resolution is higher with respect to MRI 4D flow and, thus, it is specially beneficial when extracting flow profiles on small arteries such as the supra-aortic vessels, whose diameter tends to by on the order of a few millimeters and where MRI 4D acquisitions fail to accurately measure the velocity field with sufficient resolution.

Valvular pathologies severely distort the aortic jet [119] and lead to an off-set of the flow. Aortic stenosis caused by a stiffening or fusion of the valve leaflets cause the valve opening to be reduced and distorted in shape. This irregular opening obstructs the blood flow and leads to an asymmetric jet profile with elevated peak velocity, which severely impacts the overall flow structure on the ascending aorta. Additionally, the geometry of tortuous aortas or large aneurysms differ greatly from the idealized geometry of a healthy subject, making it difficult in these cases to accurately orient and align an idealized aortic jet. It is therefore mandatory to use patient-specific data to extract the velocity profiles required for the calibration of an accurate computation. To achieve this aim, MRI 4D flow acquisition currently represents the most comprehensive and detailed measurement available under the current clinical practice.

A novel procedure to acquired velocity readings is 4D Doppler ultrasound velocimetry, which has reached maturity and solutions have been deployed on the market. This technology benefits from a high temporal acquisition rate, although the spatial resolution is similar to that of MRI. However this may be, these technologies have not been yet integrated in the standard clinical practice and, thus, the availability and access to patient-specific data presents a limiting constraint for developing computational workflows based on these technologies.

Depending on the data available, we encounter three possible scenarios to personalize the velocity boundary conditions. In increasing level of exactitude and complexity: idealized spatially defined profile scaled according to velocity flow measurements, as was done in Chapter 4, where the aortic valve shape and jet profiles and not available; through-plane spatial and temporal velocity profiles obtained form an MRI 2D acquisition, which increase the realism of the aortic jet as the effect of the aortic valve opening is accounted for on the setup; and three-dimensional spatial velocity vector field defined in along time on the boundary, obtained from MRI 4D, which yields and unmatched level of personalization and exactitude.

While the approach used on outlet boundary conditions remains a critical pillar to ensure the stability of the solution, defining the inlet boundary using an imposed velocity field has a minimal effect on the numerical convergence as long as the input data is interpolated using a continuous C^2 function. In this way the acceleration term required on each fluid element on the boundary faces will be C^1 continuous, leading to smooth pressure variations on the inlet boundary.

5.4.2 Aortic jet

In this work, the aortic valve jet was calibrated using MRI 4D flow data. The flow data was imported into QIR 4D version 1.03 (CASIS, Quetigny, France), a MRI 4D processing software. This software allowed to perform an offset correction by applying the algorithm proposed in [165], where static tissues are used to perform a fitting of the velocity field. This can be observed in Figure 5.5. Once the MRI flow

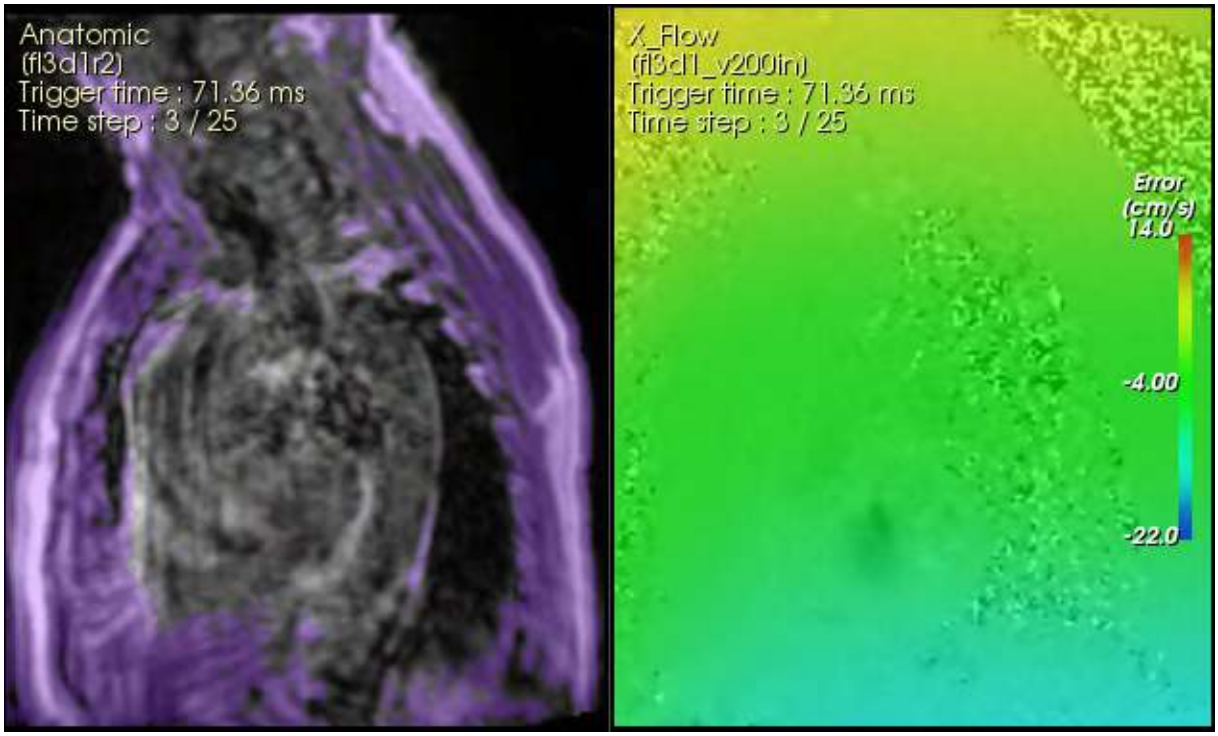

Figure 5.5: Details of the offset correction step. Left image highlights the location of static tissue (purple). The correction applied on the X-velocity component is shown on the right image.

data was corrected, an automatic segmentation algorithm which used mean voxel grey level was used to segment the aortic volume by detecting discontinuities in the velocity field using the level set method as described in [166, 167]. The automatic segmentation required manual correction, as the boundaries of the aorta where poorly captured and fusion with the pulmonary artery was present, as shown in Figure 5.6. Once the segmentation was performed, the centerline of the vessel was computed using Voronoi diagrams. After completing these steps, a plane was placed proximal to the aortic valve. The resolution of the MRI prevented an accurate positioning of the plane, although we ensured that the plane was positioned as close as possible to the sinotubular junction. A planar view of the through plane velocity was available on the

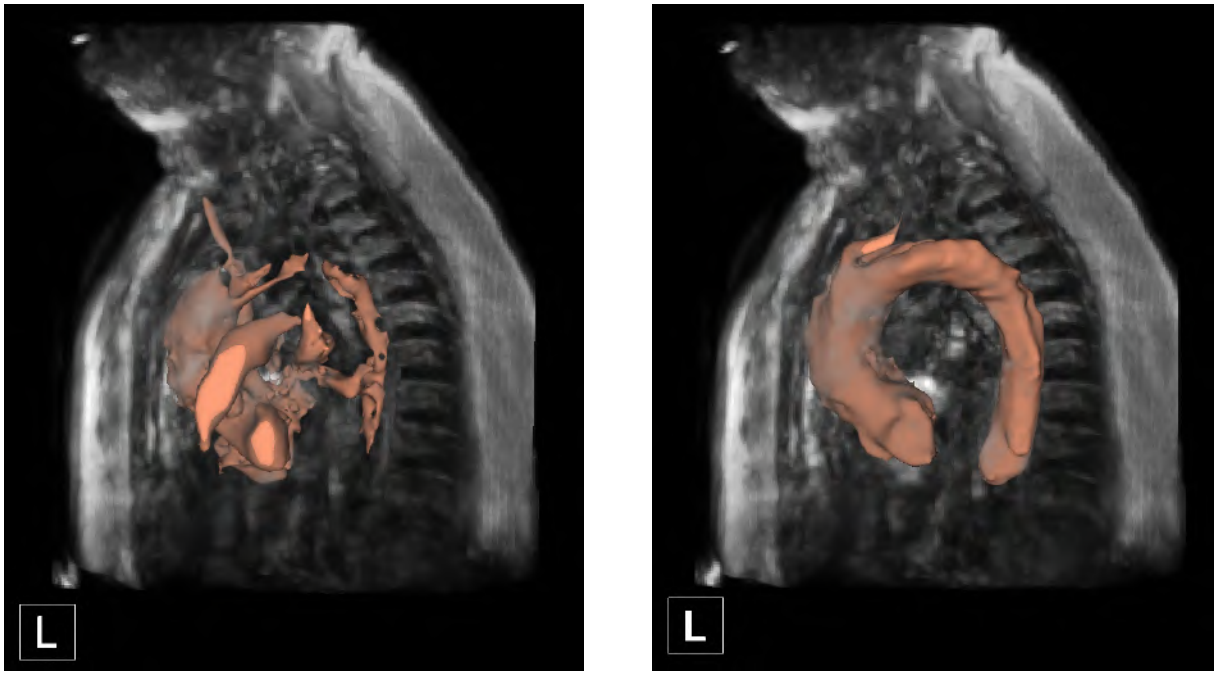

(a) Automatic segmentation (b) Manual segmentation

Figure 5.6: Segmentation obtained after the automatic procedure (a) and after the manual correction (b).

software and used to aid during the positioning (Figure 5.7). The velocity field across the given plane was then exported in order to provide the input data for the boundary condition design process. The velocity

(a) Velocity field and plane position (b) Velocity magnitude on the plane

Figure 5.7: Velocity extraction procedure: Position of the plane used for velocity extraction (a) and velocity magnitude on the plane (b).

field exported from QIR 4D was composed of a set of files containing pixel positions and the velocity vector field. A set of scripts were developed in Matlab and Python to import the measurements, perform

a spatial and temporal interpolation onto the CFD mesh and generate the files required to define the velocity field as an LSDYNA boundary condition. The first phase simply consisted on importing the data into Matlab. The MRI velocity field $\mathbf{V}_{\mathrm{MRI}}$ was defined on $n_P \times n_P$ pixels, where $n_P = 49$, and $n_{T_{\mathrm{MRI}}} = 25$ time frames. Firstly, a filtering stage was performed in order to eliminate noise, smooth the velocity field and eliminate voxels with unphysically high velocity values. For this purpose, the velocity field was resampled onto a finer grid with three-times higher resolution using a modified Akima interpolation, which is a cubic interpolation producing piecewise polynomials with continuous first-order derivatives and which results in reduced local undulations when compared to spline interpolation. This step was performed in order to prevent the filter from over-flattening the velocity field, since applying the filter on the original low-resolution velocity field results in a reduction of the velocity values around the aortic jet region. Once the velocity field was resampled, a Gaussian 2-D filter was applied to smooth each of the three velocity components. A smoothing kernel with standard deviation 2.5 was used. The comparison between the resampled (V_{R}) and the filtered (V_{F}) velocity magnitude is depicted in Figure 5.8. The effect of the Gaussian filter, or in other words, the difference between these velocity fields $\Delta V = V_{\mathrm{R}} - V_{\mathrm{F}}$, is depicted in Figure 5.9.

After performing the filtering, the velocity field was copied and concatenated in order to have a repeating flow field during 3 cardiac cycles. Subsequently, we performed an interpolation based on splines to produce a smooth signal with 10^4 points per cardiac cycle, ensuring in this way that the local acceleration terms on each inlet face are C^1 continuous. An example of the resultant x, y and z velocity components on a sample pixel is provided in Figure 5.10. The following step consisted on interpolating the MRI flow data onto the fluid mesh faces. To this aim, we first constructed a 3D scattered interpolant, which makes use of Delaunay triangulation of scattered sample points in order to construct the interpolation function [168]. To perform such an operation, the velocity field was replicated onto two parallel planes (P^+ and P^-) separated by 6 mm on both sides of the initial plane, in order to construct a three dimensional scattered sample. This procedure was necessary in order to compensate for the fact that the MRI plane and inlet face where not perfectly aligned. By creating this 3D interpolant, the data of the MRI plane can be interpolated comfortably onto a non-parallel plane which is contained within the bounds of [P^+, P^-], as shown in Figure 5.11. The initial MRI velocity field and the mesh-interpolated LSDYNA velocity field are shown in Figure 5.12. Once the velocity field on the mesh faces was obtained, they were exported to a .csv file. A Python script was then used to construct the LSDYNA input files by defining the x, y and z velocity profiles at each inlet face. The flow profile is depicted in in Figure 5.13

5.4.3 Outlets

The configuration chosen for the outlet boundary conditions will have a significant impact on the model's response. In this study, due to the reasons explained in Section 5.4.1, each outlet will be coupled to a

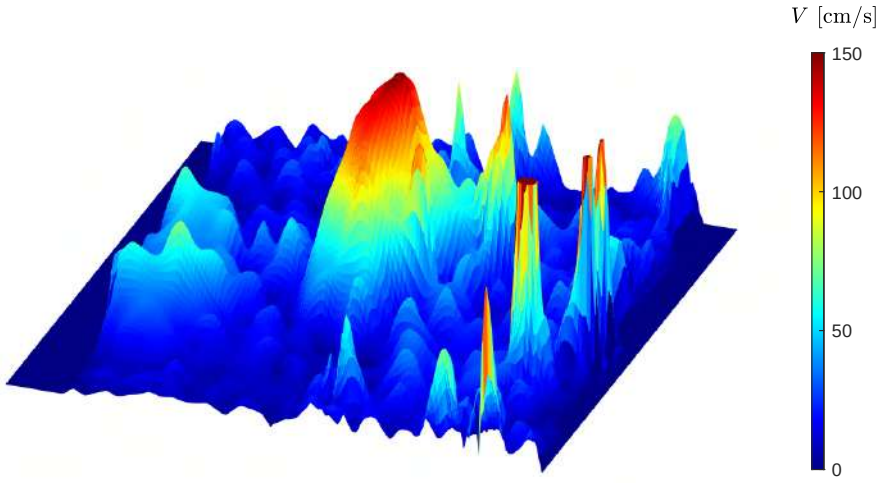

(a) Resampled velocity field

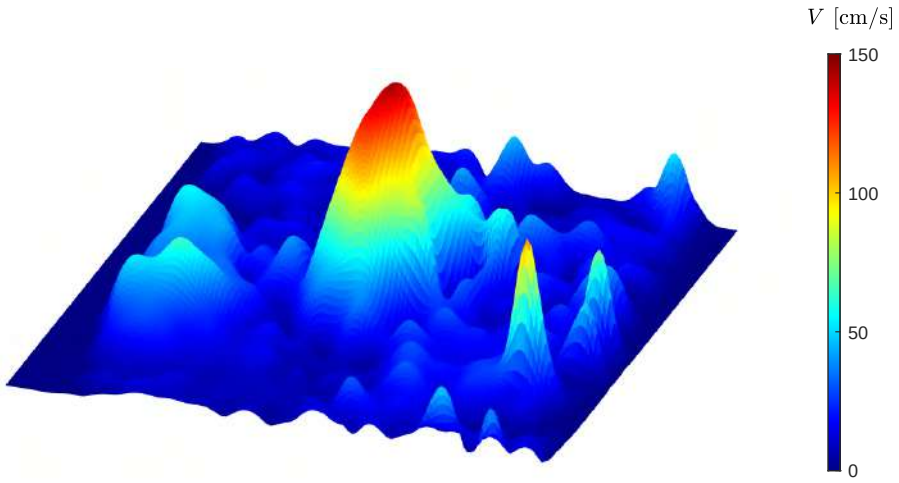

(c) Filtered velocity field

Figure 5.8: Velocity field extracted directly from MRI and resampled on a finer grid (a) and velocity field after performing filtering operation (b).

three-element windkessel model consisting of a proximal and distal resistance, R_p and R_d respectively, and a distal capacitance (C_d). The procedure used to calibrate the windkessel components is similar to the one detailed in Chapter 4, although some modifications have been made in order to incorporate further personalization thanks to the availability of mass flow data and pressure reading. The procedure used to calibrate the windkessel components is performed as follows. Firstly, the total equivalent peripheral resistance (R_T) is computed according to:

$$R_T = \frac{P_{mean}}{Q_{mean}}, \tag{5.1}$$

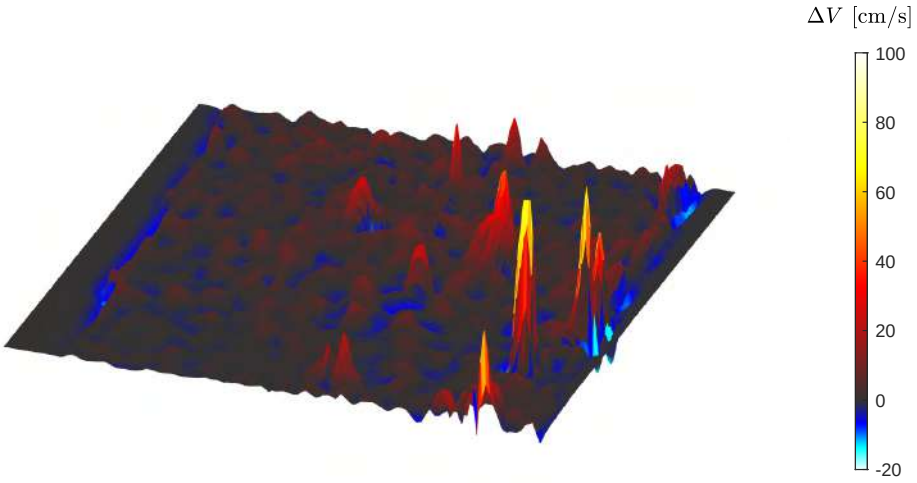

Figure 5.9: Difference between the non-filtered and filtered velocity.

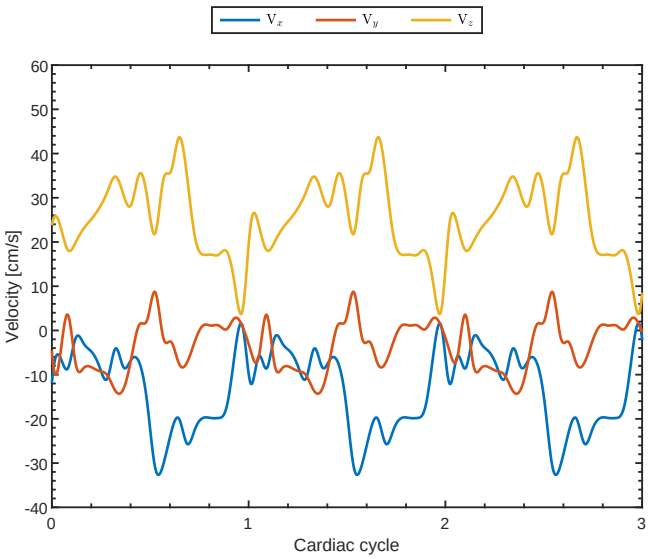

Figure 5.10: X, Y and Z velocity components on a sample pixel.

the mean pressure is defined as

$$P_{mean} = P_{Dias} + \frac{P_{Sys} - P_{Dias}}{3}. \tag{5.2}$$

At each outlet i, the individual resistance (R_i) is defined as the sum of R_{p_i} and R_{d_i}, being $R_T = (\sum_i 1/R_i)^{-1}$. The individual resistances are computed according to the distribution of flow using the following relationship:

$$R_i = R_T/f_i\,, \tag{5.3}$$

where f_i represents the flow fraction and is defined as $f_i = \frac{\dot{m}_i}{\dot{m}_{As}}$, being $\dot{m}_i$ and $\dot{m}_{As}$ the mass flow flowing through the outlet and the ascending aorta, respectively. After obtaining the individual resistances, the proximal and distal resistances were computed as $R_p = c_p R_T$ and $R_d = c_d R_T$, being c_p and c_d equal to 0.056 and 0.944, respectively, as described in [169]. The calibration of the components was performed

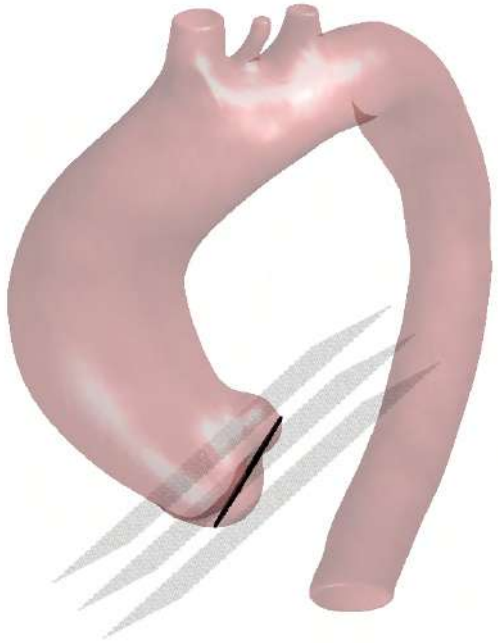

Figure 5.11: Position of the scattered interpolant points (grey) and inlet nodes (black).

considering a distribution flow proportional to the outlet areas (A_i). For this analysis, since MRI 4D data is available, the mass flow of the ascending and descending aorta, $\dot{m}_{As}$ and $\dot{m}_{DA}$ respectively, where measured and used to compute the descending aorta flow fraction as:

$$f_{DA} = \frac{\dot{m}_{DA}}{\dot{m}_{As}}. \tag{5.4}$$

The remaining flow fraction was then distributed on each supra-aortic vessel j, according to outlet area.

$$f_j = (1 - f_{DA}) \frac{A_j}{A_{T_{sa}}}, \tag{5.5}$$

being $A_{T_{sa}}$ the total area of the supra-aortic vessels.

The total compliance (C_T) can be expressed as the change of total volume ($V(t)$) contained in the systemic arteries with respect to pressure as $C_T = \frac{\mathrm{dV}}{\mathrm{dP}}$. As detailed in [170], this relationship can be approximated as

$$C_T = \frac{Q_{max} - Q_{min}}{P_{Sys} - P_{Dias}} \Delta t\,, \tag{5.6}$$

where Q_{max} and Q_{min} represent the maximum and minimum flow rates measured at the aortic valve using the MRI 4D flow data and Δt the time-difference between the occurrence of Q_{max} and Q_{min}. It is necessary to consider the, when modelling an aorta using FSI, the 3D model has a compliance that needs to be accounted for. Thus, when calibrating the windkessel parameters under an FSI model C_T is

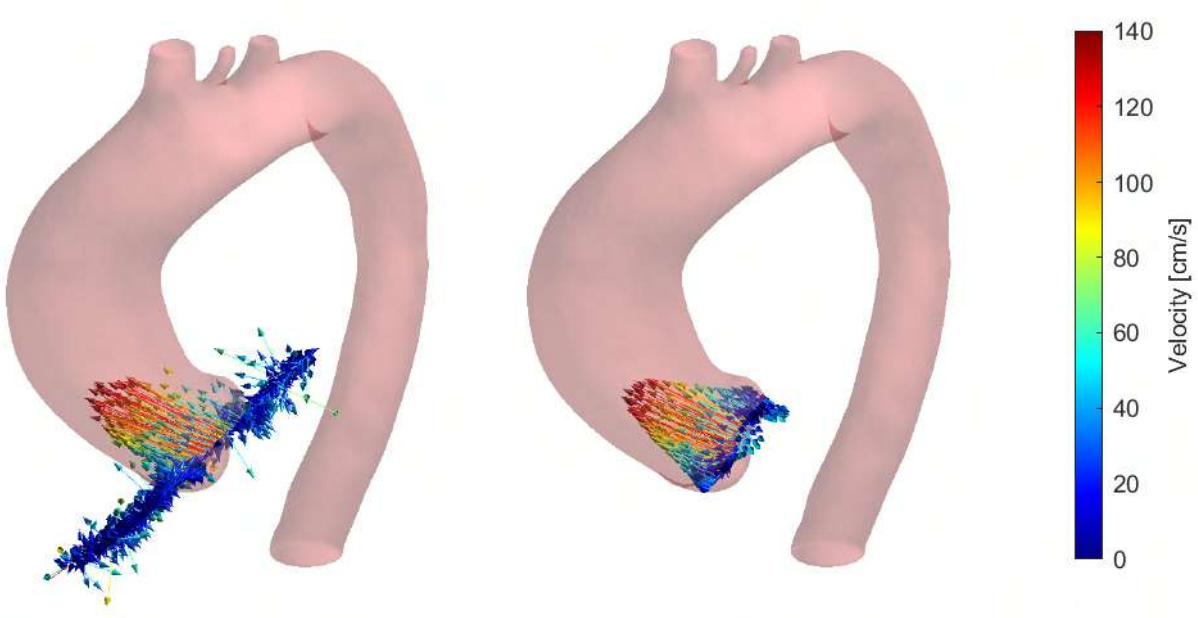

(a) (b)

Figure 5.12: Velocity field extracted directly from MRI (a) and after performing the interpolation onto the CFD mesh (b).

corrected as:

$$C_T^* = C_T - C_{As}^{3D}, \tag{5.7}$$

where C_{As}^{3D} is the estimated compliance of the ascending aorta which is subtracted from the total compliance. For any 3D section, the estimated compliance is computed as:

$$C^{3D} = \frac{3\pi r^3 L}{2E_{inc}T}, \tag{5.8}$$

where r is the hydraulic radius, L the length of the segment, E_{inc} the incremental young modulus at physiological pressure and T the wall thickness. Once the correction is made, we can compute the compliance associated to each vessel. As described by Stergiopulos *et al.* [171], the compliance of the outlets branches can also by distributed according to mass flow fraction. By accounting for the correction proposed by Xiao *et al.* [172], the compliance of the outlet branches (C_i) is computed as

$$C_i = f_i\, C_T^* \frac{R_i}{R_{d_i}} = C_T^* \frac{R_T}{R_{d_i}}. \tag{5.9}$$

On the supra-aortic vessels, since the length of the outlet is minimal and the compliance of the segment small, no correction will be made to account for the proximal compliance. However, we should consider that the 3D segment of the descending aorta provides a significant compliance that should be accounted

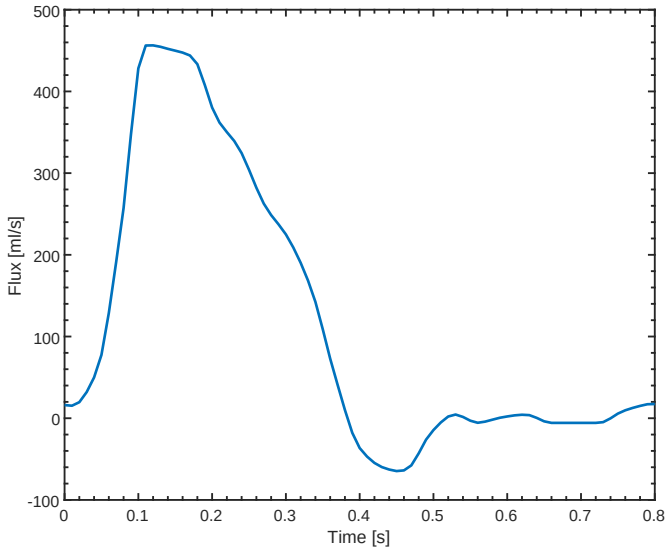

Figure 5.13: Flow rate through the aortic valve for patient considered in the study.

for, therefore the distal compliance of the DA is corrected, as was done for C_T, as:

$$C^*_{DA} = C_{DA} - C^{3D}_{DA}. \tag{5.10}$$

For the patient considered in this study, the clinical measurements required for the windkessel calibration are summarized in Table 5.2. Note that P_{Sys} and P_{Dias} have been set to 60 and 0 mmHg respectively, since the FSI computation is initiated after the inflation from zero-pressure to 80 mmHg in order to avoid modelling inflation stage in the FSI simulation. The measurements required to compute C^{3D} are given in Table 5.3. The radius of the ascending section was computed as the averaged radius from the valve to the BT ostium, the thickness as the mean value of the four quadrants, and E_{inc} was taken from [173], where E_{inc} in given for the circumferential direction at the physiological pressure range 80-120 mmHg. The values of elasticity and thickness of the DA are obtained after the material definition procedure described in Section 5.5.2. The resultant windkessel parameters obtained after the calibration procedure are detailed in Table 5.4.

Measure	Value	Unit
Q_{max}	456.2	ml/s
Q_{min}	15.3	ml/s
Q_{mean}	6.89	l/min
Q_{DA}	3.48	l/min
P_{Sys}	60	mmHg
P_{Dias}	0.0	mmHg
Δt	0.1	s
A_{BT}	185.2	mm^2
A_{LCC}	20.4	mm^2
A_{LS}	67.3	mm^2

Table 5.2: Measurements used in the windkessel calibration.

Measure	AsAo	DA	Unit
r	21.1	10.5	mm
L	140	167	mm
E_{inc}	2.61	0.598	MPa
T	2.72	1.06	mm

Table 5.3: Measurements of the ascending and descending aorta used for the computation of C^{3D}.

Component	Value
$R_{p_{BT}}$	3.858×10^{6}
$R_{d_{BT}}$	6.504×10^{7}
C_{BT}	1.587×10^{-9}
$R_{p_{LCC}}$	3.569×10^{7}
$R_{d_{LCC}}$	6.016×10^{8}
C_{LCC}	1.715×10^{-10}
$R_{p_{LS}}$	1.065×10^{7}
$R_{d_{LS}}$	1.796×10^{8}
C_{LS}	5.746×10^{-10}
$R_{p_{DA}}$	2.575×10^{6}
$R_{d_{DA}}$	4.340×10^{7}
C^{*}_{DA}	9.407×10^{-10}

Table 5.4: Windkessel components obtained after a patient specific calibration. R_d and R_p given in Pa·s/m^3 and C in m^2/Pa.

5.5 Personalized aortic wall model

Modelling of patient specific human aortas considering both the hemodynamic and aortic wall requires an accurate tuning of the both the fluid and structural models. For the later, it is of vital importance to characterize the geometry, thickness and elastic properties of the wall with sufficient detail in order to capture the local peak stress regions and identify potential regions suffering from damage and degradation.

5.5.1 Geometry

Considerations regarding the geometric set up has been detailed in Section 5.3, as they are common to both the fluid and structural models. When it comes to the structural geometry, care should be taken in order to prevent abrupt curvatures inherited from the segmentation procedure. Rapid curvature changes result in concentrations of stress which may not correspond to the physiological ones, as cardiovascular vessels are smooth and their shape transitions in a gentle manner. Artificial sharp geometric changes may therefore cause overestimations of stress in some regions, masking the true high stress regions and misleading the assessment of stress. The intima layer is responsible for this smoothness on healthy subjects, however, it is true that atherosclerotic plaques deposition and local damage may influence the aorta's inner roughness. Unfortunately, the resolution of the imaging acquisition is insufficient to accurately these details unless they reach a significant size.

5.5.2 Material properties

The aorta wall structural model can be defined using a wide range of models and considering numerous assumptions and simplifications. The degree of accuracy and fidelity will strongly depend on the modelling choices, although care must be taken as the personalized calibration of the model parameters is crucial to ensure a truthful result. Elevating the degree of complexity of the model may unfortunately not be possible beyond a certain limit due to the lack of clinical and experimental data necessary to accurately calibrate the model. The modelling choices require a thorough and critical assessment in order to understand and have awareness of their influence on the model results. It has been shown, for example, how the assumption of uniform wall thickness may lead to an unrealistic distribution of stress on the wall [22, 163].

To calibrate the structural models used in this study, experimental measurements on ascending aortas where performed by the University Hospital of Dijon. The results of thickness and elastic response where used to define a non-uniform aorta wall model.

5.5.2.1 Thickness

The experimental measures of the ascending aorta were performed on four quadrants: the posterior, lateral, medial and anterior walls. The descending aorta was modelled using constant thickness derived

from the measurements from a healthy aorta retrieved after autopsy. Patient-specific descending aorta measurements where not available since only the ascending section was replaced during surgery. The aortic arch was defined as a continuation of the ascending aorta, following the four segments of the ascending aorta. Supra-aortic vessel thickness (T_v) was defined as 10% of the vessel radius (r_v), as described in [174]. However, this approach may lead to vessel thickness of extremely low values, since r_v is occasionally low (< 2.5 mm), especially in the left common carotid artery. In order prevent extreme changes in wall thickness, the vessel thickness was therefore limited as $T_v = \max(r_v/10\,,\, 0.75\,\text{mm})$.

In order to benefit of the richness of data available and generate a high-fidelity aorta wall model, a procedure to define the wall thickness on a node-by-node basis was developed in Python. The procedure is based on defining the material thickness on certain predefined set of nodes, called hereafter seed nodes (n_s), and posteriorly interpolate the thickness onto the remaining wall nodes (n_n) by considering the node-to-seed distance (D_n^s). The interpolation procedure varied depending on the position of the node. In the ascending aorta, only the two most proximal seed nodes were considered for the interpolation, where as, in the aortic arch, the distance to the four most proximal points was considered, since the influence of the supra-aortic vessels augmented the complexity of the interpolation procedure and additional seed nodes where required in order to ensure a smooth thickness transition. The detailed steps of the procedure are the following:

1. Seed definition: Once the structural mesh is generated, it is loaded into a visualizer that enables to identify specific nodes, which will construct the set of seed nodes. Since the method relies on interpolation based on distance, a sufficient number of nodes on each quadrant of the ascending aorta need to be defined in order to ensure that longitudinal uniformity is achieved. The interpolation in the ascending section is intended to account only for circumferential variations. To this aim, we defined seven seed points for each of the four quadrants of the ascending aorta. In this way the seed points are sufficiently close along the longitudinal direction and thus longitudinal variations are minimized. It may be possible to define a higher number of seed points on each quadrant, although, since the the manual and computational effort required increases proportionally to the number of seed points and the improvement obtained by augmenting the number of seeds is negligible, we limited the set to seven seed nodes per quadrant. On the aortic arch, three sets of nodes per regions (considering same nomenclature as for the ascending aorta), where positioned. The first of the three set of nodes was positioned before the brachiocephalic trunk, the second between the brachiocephalic trunk and left common carotid and the last between the left common carotid and the left subclavian artery. The material properties of the three aortic arch sets were defined as a weighted average of the ascending and descending aorta properties. The material ratio for sets 1, 2 and 3 was defined as 75%-25%, 50%-50% and 25%-75% for the ascending and descending aorta, respectively. On each supra-aortic vessel, two nodes where considered. Finally, 7 nodes on the edge which separates the

aortic arch and descending aorta were identified. The distribution of seed nodes is depicted on Figure 5.14.

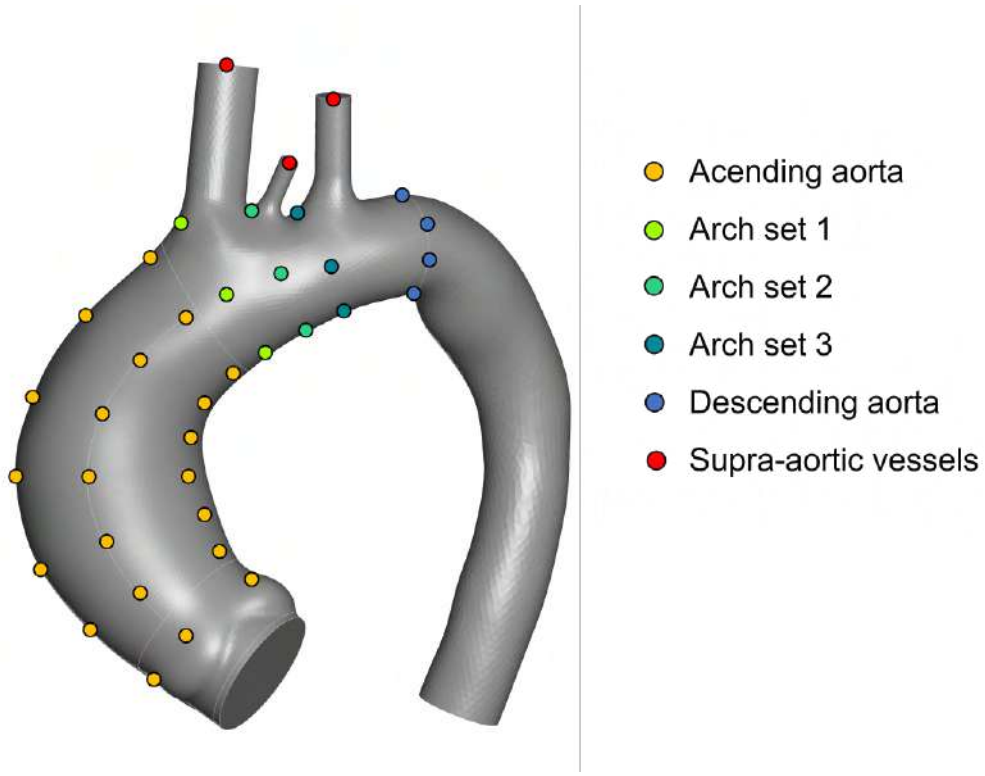

Figure 5.14: Distribution of seed points along the aortic wall.

2. Node to seed distance: having the seed nodes and structural mesh defined, their identifiers and coordinates are imported onto the structural model generator algorithm. The objective is to compute the distance of each node to the seed set ($D_{n,s}$) by computing the path distance from one node to another though the mesh structure through an iterative procedure. Considering a seed node n_s, on the first iteration $j = 1$ we obtain its connectivity by identifying the nodes n_w^1 which share an element with n_s. The following step is to compute the distance between the former and later. Once the first iteration is completed, we have a set of nodes n_w^1 and the corresponding distance $D_{n,s}^1$ to the seed node n_s. During the second iteration, the connectivity n_w^{2*} of each node of the set n_w^1 is extracted. By excluding the nodes contained in n_w^1, we obtain the set n_w^2. Now, for each node on the set n_w^2, we compute the minimum distance ($D_n^{1,2}$) to the set n_w^1. Finally, we obtain the distance between the second set and the seed node as $D_n^2 = D_n^1 + D_n^{1,2}$. The iterations proceed until the distance on all mesh nodes is obtained. Thus, for a generic iteration j, we perform the following operation:

$$n_w^j = n_w^{j*} \setminus n_w^{j-1}, \tag{5.11}$$

$$D_{n,s}^j = D_n^{j-1,j} + D_{n,s}^{j-1}. \tag{5.12}$$

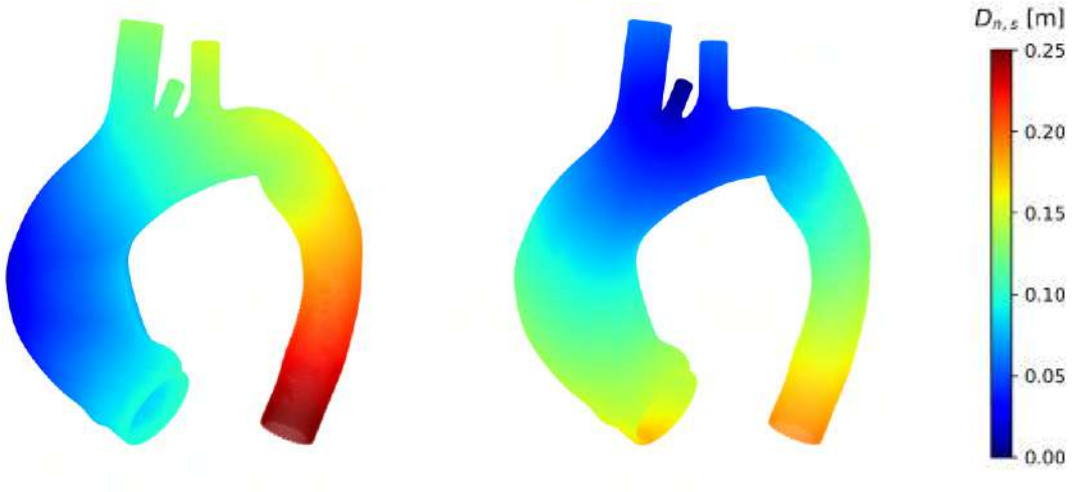

(a) Lateral seed (b) LCC seed

Figure 5.15: Distance across the mesh nodes to different seeds

By repeating the process for all seed nodes, we obtain the distance of every node to every seed. An example of the seed distance is depicted on Figure 5.15 for a node on the ascending aorta and in the left common carotid artery.

3. Node thickness: Considering if a given node n_w falls in the ascending aorta or the aortic arch, a different procedure will be employed to interpolate the seed thickness onto the given node. For nodes belonging to the ascending aorta, the procedure to establish which seed nodes will be considered is straight forward: we identify the two quadrants which have a minimum distance to the given node, namely n_{s1} and n_{s2}. By simple interpolation, the thickness T_n on node n_w is defined as:

$$T_n = T_{s1}\frac{D_{n,s1}}{D_{n,s1}+D_{n,s2}} + T_{s2}\frac{D_{n,s2}}{D_{n,s1}+D_{n,s2}}\,. \tag{5.13}$$

When the node belongs to the aortic arch, the procedure is modified since a greater number of seed nodes needs to be considered. In a first step, the distance to the set of nodes N_{As}, N_{Arch_j} and N_{DA} are computed to identify the longitudinal position of the node along the main aorta vessel. Considering the distance to the two closest sets, we compute an an initial thickness T_n^* in a similar manner as for the ascending aorta using Equation 5.13. The minimum distance to the closest aortic arch seed point ($D_{n,s}^{\text{Min}}$) is registered. After, the distance $D_{n,v}$ to the closest supra-aortic vessel is obtained. In order to limit the influence of the supra-aortic nodes, the contribution of these nodes is limited to a distance (D_{Lim}) equal to 4 cm. Then a modifier is introduced to compute the modified distance ($D_{n,v}^{\text{mod}}$) in order to obtain a smooth and asymptotic influence of the supra-aortic vessels as:

$$D_{n,v}^{*} = \min\left\{D_{n,v}, D_{\text{Lim}}\right\}, \tag{5.14}$$

$$D_{n,v}^{\text{mod}} = D_{n,v}^{*} \frac{D_{\text{Lim}}}{D_{\text{Lim}} - D_{n,v}^{*}}. \tag{5.15}$$

The modified distance thus behaves as depicted in Figure 5.16. Finally, the thickness of the aortic arch nodes is computed as:

$$T_n = T_n^{*} \frac{D_{n,s}^{\text{Min}}}{D_{n,s}^{\text{Min}} + D_{n,v}^{\text{mod}}} + T_v \frac{D_{n,v}^{\text{mod}}}{D_{n,s}^{\text{Min}} + D_{n,v}^{\text{mod}}}\,. \tag{5.16}$$

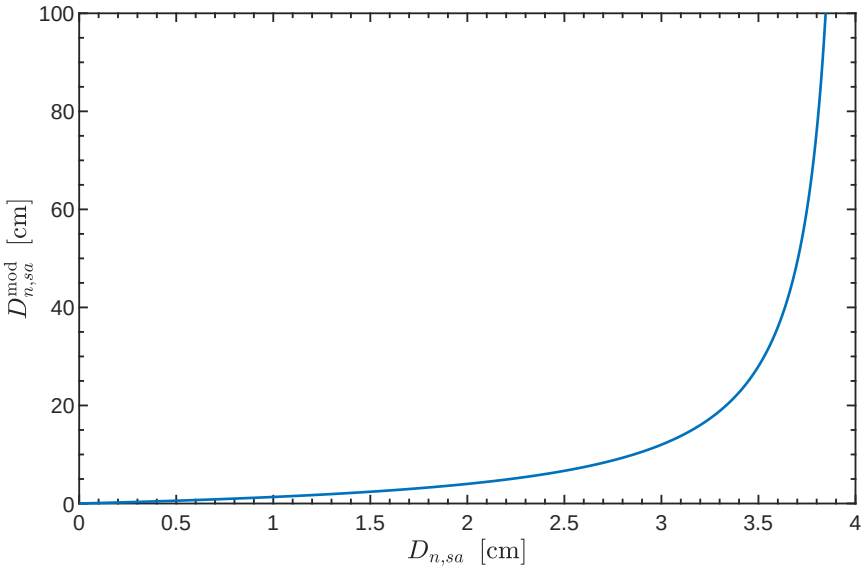

Figure 5.16: Modified distance against measured supra-aortic node distance.

4. Final smoothing: Due to the procedure used to compute the thickness interpolation, some discontinuities can appear on the borders where the set of seed nodes used for the interpolation changes. In order to ensure a smooth transition of thickness through out the structural domain, we perform and iterative procedure to reduce the thickness change across shells. To do so, we defined the maximum allowed thickness difference on on a shell ΔT_{max} as 1% of the maximum wall thickness. The smoothing algorithm then evaluated the thickness change on each shell of the structural mesh as the maximum thickness difference between the 3 nodes belonging to each shell, ΔT_s. If the shell thickness difference surpassed ΔT_{max}, the node thickness of the three nodes was reset to the mean shell thickness as:

$$\tilde{T}_n = \frac{1}{3} \sum_{i=1}^{3} T_i. \tag{5.17}$$

The procedure was performed until no shell had $\Delta T_s > \Delta T_{max}$ and was limited to 20 iterations. The result of the procedure is illustrated in Figure 5.17, where the evolution of ΔT_s is depicted, and in Figure 5.18, where the evolution of T_n is shown. We can observe that the thickness jump has been strongly reduced and that the thickness distribution exhibits a smooth character, as the

abrupt changes that can be observed in Figure 5.18a are no longer appreciable in Figure 5.18d.

(a) Initial (b) Iteration 1 (c) Iteration 2 (d) Iteration 3

Figure 5.17: Maximum thickness difference across shells.

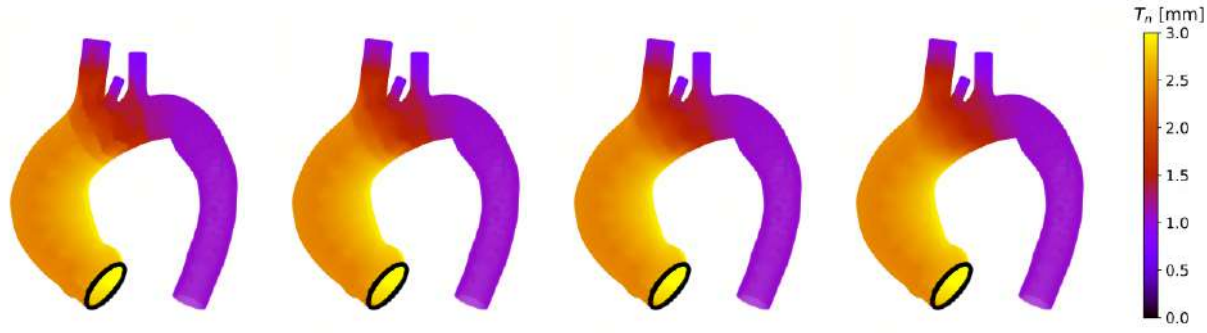

(a) Initial (b) Iteration 1 (c) Iteration 2 (d) Iteration 3

Figure 5.18: Nodal thickness on the structural mesh.

5.5.2.2 Material model: Element choice and hyperelasticy model

In this work, in order to accurately model the wall stress, an hyperelastic material model was used. This enables to accurately capture the strain-stress evolution throughout the inflation stage and obtain a realistic response during the cardiac cycles. The aortic wall is composed of three main layers, namely: intima, media and adventitia. Each of the layers has unique mechanical properties and thickness. It is well known that these layers exhibit an anisotropic behaviour due to the internal fibre orientation, as it can be observed on the biaxial testing results shown in Figure 5.19. Despite the complexity of the structure which composes the aortic wall, in this work we will assume an isotropic model defined on shell elements. Thus, the hyperelastic model will be defined considering only the circumferential strain-stress curve and the three-layer wall will be reduced to a simple triangular shell element without distinction between layers. The reason for the later is the lack of separate experimental data of the different layers. It is possible to model the aortic wall using 3D elements (prisms or cubes) which could provide a better representation of the true wall. However, the extrusion of the CAD geometry along the normal direction

poses some difficulties and an increment in modeling complexity, specially on high-curvature regions, such as near the ostiums of supra-aortic vessels, where the curvature radius and separation between branches maybe inferior to the wall thickness, making the extrusion process non-trivial. Thus, the marginal benefit of considering 3D elements does justify their use due to the augmented modelling complexity and added geometric uncertainty.

The hyperelastic response of the ascending aorta was modelled using a third order Yeoh material model [175], which has been used to model aortic aneurysm previously [176, 177]. This model is based on Ronald Rivlin's model for incompressible, nonlinear elastic materials which are described using a strain energy density function. To model the strain-strain relationship, a reduced polynomial form of strain-energy potential W is used by considering the first deviatoric strain invariant I_1 from the Cauchy-Green deformation tensor. The form of the strain energy function is defined as:

$$W = \sum_{i=1}^{3} C_{i0}(\bar{I}_1 - 3)^i. \tag{5.18}$$

The model coefficients for each quadrant where obtained after performing a curve fitting via minimization of normalized error of the circumferential strain-stress curves. For this procedure, Ansys Workbench 23.1 (Ansys Inc, Canonsburg, PA, USA) was used. The experimental and modelled strain-stress curves of the four ascending aorta quadrants are depicted on Figure 5.19. We can observe that a third-order Yeoh model is capable of capturing the hyperelastic behaviour of the aortic tissue. Minimal discrepancy is observed between the experimental data and the modelled response. It is worth pointing that the anterior and medial walls possess the highest and lowest stiffness respectively. For the case of the supra-aortic vessels and descending aorta elasticity, we assumed a linear strain-stress relationship, i.e: elastic behaviour. This choice was made due to the absence of both experimental data and normalized literature data. It is true that hyperelastic model coefficients are available in literature, however, these coefficients do not correspond to those of the patient herein modelled and cannot be scaled or tuned to our needs. In sight of this limitation for defining the hyperelastic response of the outlet vessels, a personalization of the elastic response based on estimated pulse-wave velocity (PWV) was performed using the empirical formula derived by Reymond et al. [178] and which establishes the relationship between vessel radius (r_v) and PWV as:

$$\mathrm{PWV} = \frac{\alpha}{(2\times 10^3\, r_v)^\beta}, \tag{5.19}$$

where $\alpha = 13.3$ and $\beta = 0.3$. Once the PWV has been estimated, we can compute the incremental elastic modulus (E_{inc}) of the arterial wall as:

$$E_{\mathrm{inc}} = \frac{2 r_v \rho}{T_v} \mathrm{PWV}^2\,, \tag{5.20}$$

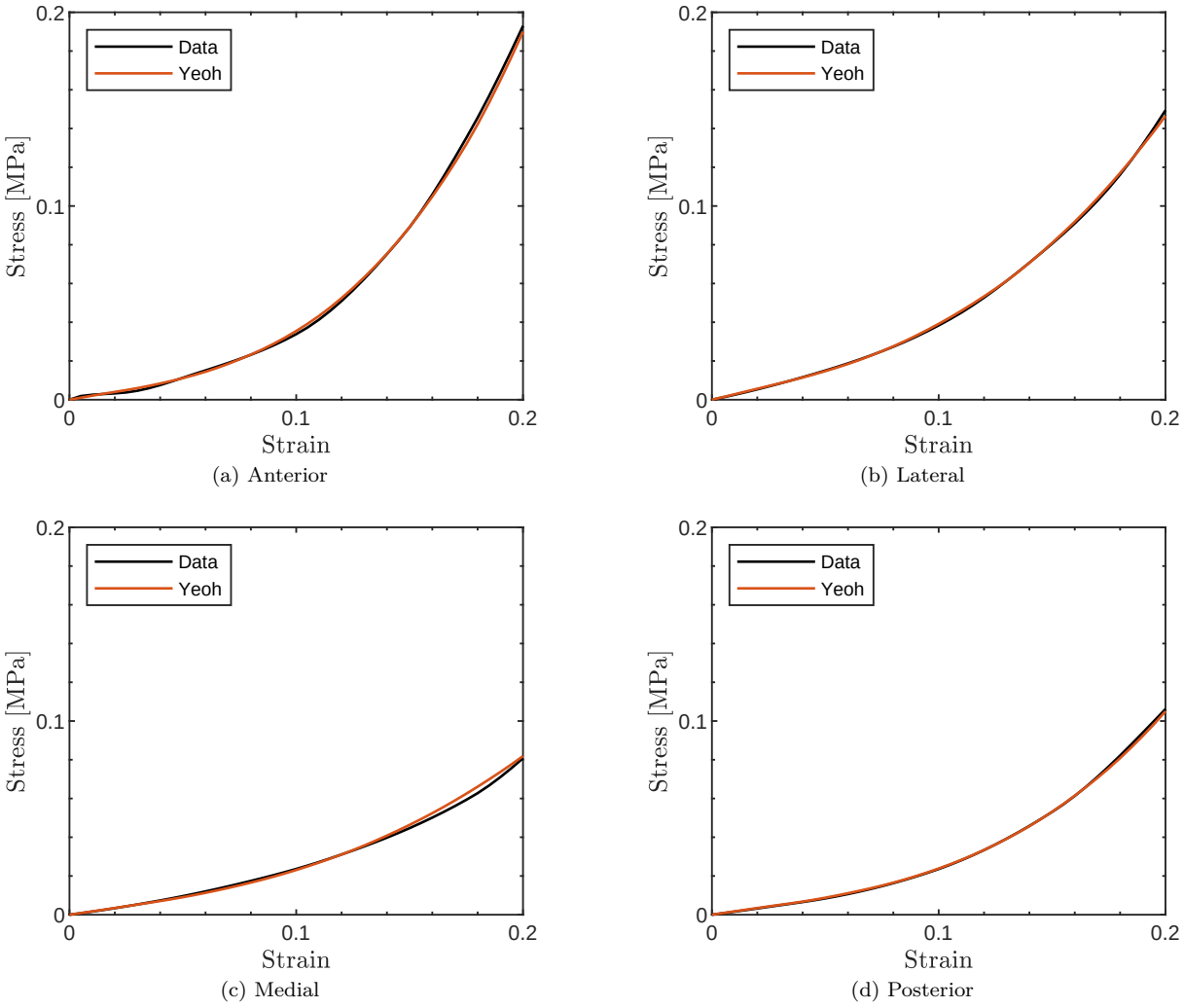

(a) Anterior (b) Lateral

(c) Medial (d) Posterior

Figure 5.19: Biaxial strain-stress model versus experimental data on the four ascending aorta quadrants.

being ρ the blood density. This equation was proposed by Adriaan I. Moens [179] and Diederik Korteweg [180] independently in 1878 and derives from Newton's second law of motion assuming isotropic behaviour and isovolumetric change with pulse pressure. Once E_{inc} was obtained, we performed the curve fitting for a second-order Yeoh model on the uniaxial stress-strain line defined by a constant elastic modulus. This enabled to model the elastic behaviour of the vessels using an hyperelastic material model. The results of the curve-fitting for outlet vessels is shown in Figure 5.20. We can observe that a quasi linear response is obtained up to a strain of 0.4, with minimal deviation in the strain interval 0-0.4. This demonstrates the capability of this procedure to approximate the elastic response with sufficient accuracy. Once the hyperelastic coefficients where computed, an algorithm was required to interpolate the material definition throughout the structural model. The workflow is identical to the one used to define T_n, adjusted to manage hyperelastic coefficients instead of thickness:

1. Seed definition: Identical step as for thickness definition, as same seed nodes where used.

2. Node to seed distance: Identical methodology as for thickness definition.

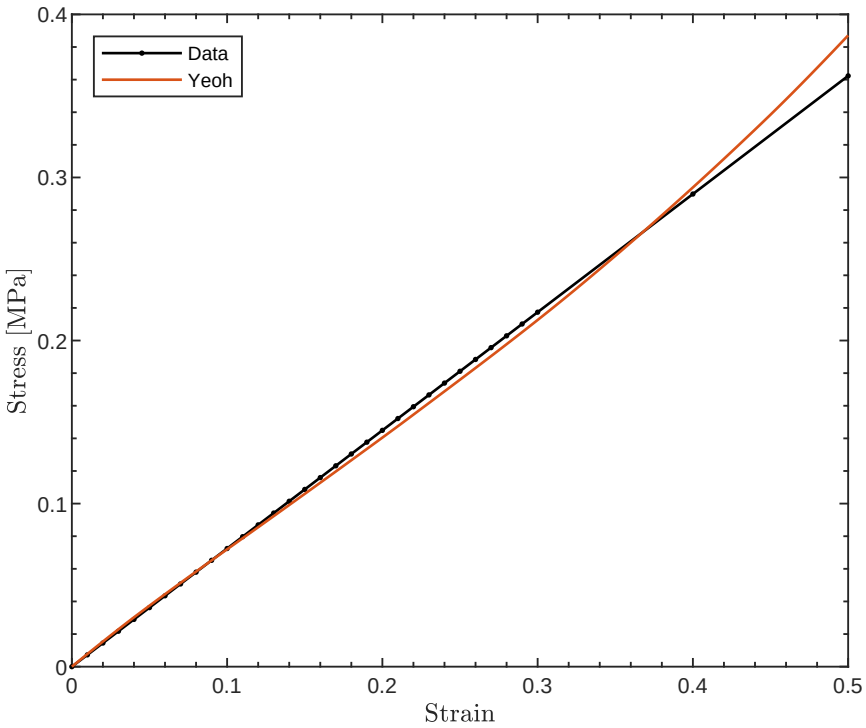

Figure 5.20: Second-order Yeoh model uniaxial strain-stress response versus elastic response for the brachicephalic trunk with $E_{\text{inc}} = 0.725$ MPa.

3. Nodal hyperelastic coefficients: Although this step follows the same principle as the thickness definition, some minor adjustments where required. Each shell is defined using a third-order Yeoh model. Thus, for any node along the ascending aorta, the coefficient $C_{\phi,n}$, where $\phi = \{10, 20, 30\}$, was computed as:

$$C_{\phi,n} = C_{\phi,s1}\frac{D_{n,s1}}{D_{n,s1} + D_{n,s2}} + C_{\phi,s2}\frac{D_{n,s2}}{D_{n,s1} + D_{n,s2}}\,. \tag{5.21}$$

For the case of the aortic arch, we define, as explained in the thickness definition section, an initial coefficient $C^{*}_{\phi,n}$ using Equation 5.21. In the case of the outlet vessels seed nodes, where a second-order model was used, $C_{\phi,v}$ where defined and C_{30} was to zero. The final value of the $C_{\phi,n}$ was then obtained as:

$$C_{\phi,n} = C^{*}_{\phi,n}\frac{D^{\text{Min}}_{n,s}}{D^{\text{Min}}_{n,s} + D^{\text{mod}}_{n,v}} + C_{\phi,v}\frac{D^{\text{mod}}_{n,v}}{D^{\text{Min}}_{n,s} + D^{\text{mod}}_{n,v}}\,. \tag{5.22}$$

It is worth justifying that the interpolation of hyperelastic coefficients works as expected and that the final structural model recreates this smooth elastic transition. Considering an elastic material M_1 and an hyperelastic material M_2, who's coefficients have been derived using curve-fitting as detailed above, we create three sample materials $M_{25\%}$, $M_{50\%}$, $M_{75\%}$, where the subscript indicates the proportion of M_1 on the material, being the rest constituted by M_2. In Figure 5.21 we can observe how the sample materials recreate the expected response and thus demonstrate that interpolating hyperelastic coefficients provides an appropriate method to produce smoothly-changing material

definition.

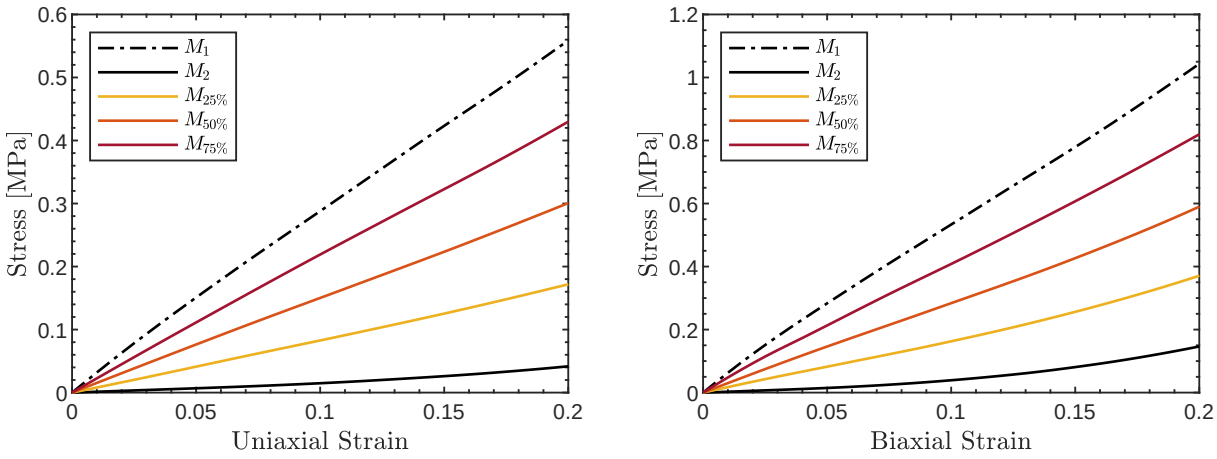

(a) Uniaxial stress-strain (b) Biaxial stress-strain

Figure 5.21: Hyperelastic response for an interpolated elements and the two seed points considered.

4. Smoothing: During the procedure performed for thickness smoothing, when a shell was identified as having an abrupt thickness change, its hyperelastic coefficients where also adjusted considering the mean values of the three nodes defining the shell as:

$$\tilde{C}_{\phi,n_s} = \frac{1}{3}\sum_{i=1}^{3} C_{\phi,i} \tag{5.23}$$

Having performed a node-by-node definition of both the thickness and the hyperelastic coefficients, we are now capable of representing the patient-specific aorta with a cutting-edge methodology capable of capturing the local variations the properties of the arterial wall in a flexible and automatized manner. The method allows to define additional seed nodes if further data is available to personalize the model, such as measurements along the descending aorta, to better describe the true nature of the aorta. For the current analysis, the aforementioned number of seed nodes provides sufficient detail for the study of ascending aortic aneurysm.

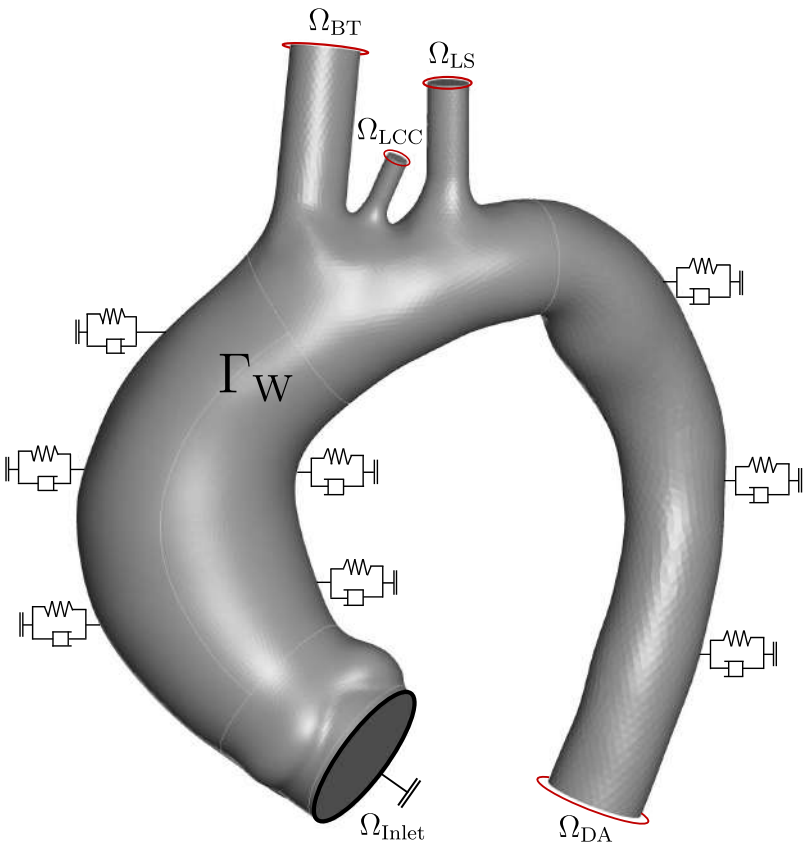

Figure 5.22: Boundary condition imposed on the structural model.

5.5.3 Boundary conditions

The ascending aorta is attached to the heart and the distal arteries and surrounded by anatomic structures such as the heart, lungs, spine and soft tissues. This environment influences and limits the displacements due to the cardiac motion and the pressure variations. In order to represent the effect of the surrounding tissues, boundary conditions need to be appropriately defined. Within this subsection, we describe the supports used to model this interactions along the aorta wall and the conditions imposed on the outlet and inlet edges. A overview of the boundary conditions setup is depicted in Figure 5.22. An important phenomena influencing the ascending aorta deformation is the motion transmitted from the heart, which causes the aortic annulus to displace in a cyclic pattern during each heartbeat. The effect of the heart induced motion has been previously studied, [29, 38] and it has shown to have a significant impact on the stress distribution. However this may be, in this work we will suppress the heart induced motion in order to simplify the structural setup and due to the lack of high-quality imaging with sufficient spatial and temporal resolution. Therefore, the nodes on the aortic annulus (Ω_{Inlet}) where given a fixed support. On the outlet vessels, namely supra-aortic vessels (Ω_{BT}, Ω_{LCC} and Ω_{LS}) and descending aorta (Ω_{DA}), in order to represent that the vessel continues downstream, nodes where allowed to displace in the radial direction only. This provided a limited support to the structure, preventing large displacements during

the zero-pressure computation while representing accurately the behaviour of the downstream vessels. In order to define this boundary condition, the nodes on along the edge defining the outlets and the shells containing these nodes were identified. Once this was registered, we computed the node normal (N_n) computing the mean vector from the normals of the s shells sharing the node:

$$N_n = \frac{1}{s} \sum_{j=1}^{s} N_j. \tag{5.24}$$

The vector N_n was used to define the axes in LS-DYNA along which the nodes where allowed to move, providing the radial boundary condition.

In order to mimic the effect of surrounding tissues, an visco-elastic support was added to every node of the structure (Γ_{W}). This support is constituted by three springs, one for each direction of the coordinate system: x, y, z. Some works regarding the tuning of this parameters are available in literature [159–161]. A more recent study [38] focused on the calibration of boundary conditions of the ascending aorta for an accurate modelling of the heart-induced motion, accounting for the effect of the transient patient-specific hemodynamic pressure and for the extra support provided by the spine. From cine-MRI acquisitions, the valve motion was tracked and the motion imposed on the structural model. An optimization algorithm was then used to adjust the spring constants in order to minimize the displacement differences on the aorta wall between the cine-MRI images and the model. The results from this work will, therefore, be used to calibrate our structural supports, since it is based on a novel and accurate methodology for spring calibration. To model the visco-elastic support, a Robin boundary condition was imposed on the structure as:

$$\sigma_{Tissue} = -\mathbf{K}\mathbf{x} - \boldsymbol{\eta}\dot{\mathbf{x}}, \tag{5.25}$$

being σ_{Tissue} the pressure exerted on along the structure's surface, $\mathbf{K}$ and $\boldsymbol{\eta}$ the elastic and viscous coefficients defining the external tissue support, $\mathbf{x}$ and $\dot{\mathbf{x}}$ the surface displacement and velocity vectors. The viscoelastic coefficient vectors where decomposed on along the three anatomical directions: x-coronal, y-transverse and z-sagital. To translate this support definition to the model, each node $n \in \Gamma_{\mathrm{W}}$ was connected to three springs and three dampers for each anatomical direction j. For each spring, the stiffness was tuned as:

$$K_{n_j} = \left(K_{\mathrm{Soft}} + W_d W_j K_{\mathrm{Spine}}\right) A_n \, e_{n_j}, \tag{5.26}$$

being K_{Soft} the component representing the soft tissues surrounding the aorta, which was identical in the three spatial directions. W_j represents the optimized coefficient along each direction of space, K_{Spine} a constant coefficient representing the stiffness due to the spine proximity, and W_d the scaling factor which considers the aorta-to-spine distance. W_d will be assumed constant and its value is derived from the averaged spine-to-aorta distance computed on a node-by-node basis in [38]. A_i represents the area of the

node, obtained as

$$A_n = \frac{1}{3}\sum_{r=1}^{s} A_r, \tag{5.27}$$

being A_r the area of the s shells connected to the node n. The supports are assumed to be oriented and acting normally to the surface, thus, to correctly calibrate the spring constant along each direction, we make use of the surface unitary normal vector $\hat{n} = \{e_x, e_y, e_z\}$ to adjust Equation 5.26. The coefficient values used in this work are provided in Table 5.5. The viscous support was modelled equally along the

Coefficient	Value
K_{Soft}	1.5×10^4 Pa/m
K_{Spine}	10^6 Pa/m
W_d	0.53
W_x	0.60
W_y	0.02
W_z	0.04

Table 5.5: Coefficients used to calibrate the spring supports.

three-spatial directions as:

$$\eta_{n_j} = \eta_c \, A_n \, e_{n_j}, \tag{5.28}$$

where the constant term η_c is equal to 10^3 Pa·s/m, taken from [159] where and optimization of the viscous coefficient was performed.

The herein described set-up enables to model the environment within which the aorta is embedded, providing a faithful description of the interactions between the aorta wall and the surrounding tissues. It is true that further complexity can be added to model the surrounding environment, for example by accounting for the proximity of pulmonary arteries, lungs and, as mentioned earlier, spine. However, this is beyond the scope of this research and, as much as the accuracy of the model may be increased, so does the modelling uncertainty due to the modelling assumptions one should perform to account for surrounding tissues, such as material properties, geometry and contact formulation. The current procedure is thus considered to be sufficiently detailed for the current scope of this work.

5.5.4 Numerical setup

An implicit algorithm was used to resolve the structural model. Shell element formulation was a fully integrated shell element where, in order to mitigate locking and enhance the in-plane bending behaviour, assumed strain interpolants are used [181, 182]. Three through shell thickness integration points are used on each shell. A non-linear BFGS quasi-Newton solver was employed, which is robust and requires fewer iteration than the modified Newton method.

5.5.5 Zero pressure geometry

The 3D segmentations obtained from angiographies provide an accurate representation of the aorta under in-vivo physiological conditions. This implies that the vessel is subject to an internal pressure and thus it is in a deformed configuration with an initial stress condition [183]. If the geometry obtained was used directly on the model, the initial stress-strain conditions would be omitted and the final stress provided by the simulation would not coincide with the true state. Additionally, since the material is hyperelastic, the deformations would be overestimated since the material is less rigid on the low strain region (see Figure 5.19). In sight of these problematic, it is mandatory to compute an approximation of the zero-stress state in order to recreate the true behaviour of the arterial wall. By computing the zero-stress state we can obtain the initial undeformed geometry and inflate it up to diastolic pressure in order to obtain the diastolic stress state and an accurate rigidity on each element. Alternatively, it is possible to consider the model as linear elastic by approximating the young modulus by the incremental stress-strain behaviour between the diastolic and systolic pressures. This procedure, although it will rely on a linearization of the hyperelastic behaviour, would result in reasonable deformations. However, it would omit the stress due to the inflation process, between zero and diastolic pressure, and only the partial stress due to pulse pressure would be modelled, therefore it could not be used to identify potential rupture locations.

The zero-stress geometry requires solving an inverse problem, where the loads and final deformation are known and the initial geometry is to be computed. The zero-stress state will be approximated by the zero-pressure state. It must be noted that the zero-pressure state may not account for residual internal stresses and does not guarantee that the true stress-free state is obtained [184, 185], however it provides a sufficiently accurate result for the needs of this study. The zero-pressure state will be computed using the Augmented Sellier's Inverse Method [186], an iterative method based on correcting the initial geometry by displacing the nodes in the opposite direction of the deformations obtained after applying the loads until the deformed configuration matches the reference geometry. More precisely, we define the loads as the measured in-vivo tractions, in this case a uniform pressure field equal to the diastolic aortic pressure. This load is then applied to the initial configuration $\boldsymbol{\Phi_0}$ with coordinates $\boldsymbol{X_0}$, which is identical to the in-vivo measured configuration $\boldsymbol{\Phi^*}$ with coordinates $\boldsymbol{X^*}$, in order to obtain the initial deformed configuration $\boldsymbol{\Phi_0^D}$ with coordinates $\boldsymbol{x_0}$. Then, the geometry is updated in order to obtain $\boldsymbol{\Phi_1}$ by applying a displacement field $\boldsymbol{R_0}$ on the nodes, which is defined as the difference between the updated deformed geometry and the target geometry. Thus, for a generic iteration k, $\boldsymbol{R_k} = \boldsymbol{x_k} - \boldsymbol{X^*}$ and $\boldsymbol{X_{k+1}} = \boldsymbol{X_k} - \alpha \boldsymbol{R_k}$. The addition of α enables to control the geometric update for acceleration or stabilization purposes. The case α=1 is equal to the standard Sellier's Method. In this case, α was updated according to:

$$\alpha_{k+1} = -\alpha_k \frac{\boldsymbol{R_{k-1}} \cdot [\boldsymbol{R_k} - \boldsymbol{R_{k-1}}]}{[\boldsymbol{R_k} - \boldsymbol{R_{k-1}}] \cdot [\boldsymbol{R_k} - \boldsymbol{R_{k-1}}]}. \tag{5.29}$$

The iterative procedure is executed until one of the convergence criteria is met, which are as follows: (1) the max error ($e_{\max}$) between the deformed configuration $\boldsymbol{\Phi_k}$ and the reference falls below a certain threshold ϵ =0.1 mm or (2) the mean error ($\bar{e}$) begin to increase. In the original algorithm [186], only the first convergence criteria was included, however, by adding the second criteria we prevent the algorithm from proceeding in case of an increase of average error. Once the procedure was completed, we defined the zero-pressure configuration as $\boldsymbol{X_{ZP}} = \boldsymbol{X_k}$. In order to apply this method to our workflow, a Python script was used to automatically launch the numerical computations, import the deformed configuration, compute the vector $\boldsymbol{R_k}$ and update the geometry for the following iteration until the convergence criteria were met. The algorithm is summarized as follows:

Algorithm: Augmented Sellier's Inverse Method [186]

initialize $\boldsymbol{X_0} \leftarrow \boldsymbol{X}^*$

initialize $\boldsymbol{R_0} \leftarrow \boldsymbol{x_0} - \boldsymbol{X}^*$

k=0

while $e_{\max} > \epsilon$ **or** $\bar{e}_k < \bar{e}_{k-1}$:

    $k \leftarrow k + 1$

    solve forward problem, $\boldsymbol{x_k} = \phi(\boldsymbol{X_k})$

    compute error, $\boldsymbol{R_k} = \boldsymbol{x_k} - \boldsymbol{X}^*$

    if $k > 1$:

        update alpha, $\alpha_{k+1} = -\alpha_k \dfrac{\boldsymbol{R_{k-1}} \cdot [\boldsymbol{R_k} - \boldsymbol{R_{k-1}}]}{[\boldsymbol{R_k} - \boldsymbol{R_{k-1}}] \cdot [\boldsymbol{R_k} - \boldsymbol{R_{k-1}}]}$

    end if

    update configuration, $\boldsymbol{X_{k+1}} = \boldsymbol{X_k} - \alpha \boldsymbol{R_k}$

end while

$\boldsymbol{X_{ZP}} = \boldsymbol{X_k}$

The algorithm was applied to the configurations derived from medical images. In this way, we obtained the zero-pressure geometry, as shown in Figure 5.23, where we can observe the effect of the deflation. The algorithm stopped due to an increase in $\bar{e}$, thus the error threshold was not achieved. The evolution of $\bar{e}$ and $e_{\max}$ is plotted in Figure 5.24. The final $e_{\max}$= 1.54 mm and $\bar{e}$ = 0.31 mm. The error contours along the aorta are depicted in Figure 5.25. We can observe a localized spot of high error in the superior part of the ascending aorta where the maximum error is located. This region, as observed in Figure 5.23, coincides with the location of a dimple on the deflated geometry. Due to these dimples and corrugations, when correcting the geometry using the present algorithm, we obtain an augmented dimple, which results in an increased bulge in the deformed configuration, as there is an inversion on the surface curvature during the inflation. An schematic of this phenomena is depicted in Figure 5.26, where we can observe how the error has increased as $\boldsymbol{R_{k+1}} > \boldsymbol{R_k}$, demonstrating a limitation of the algorithm.

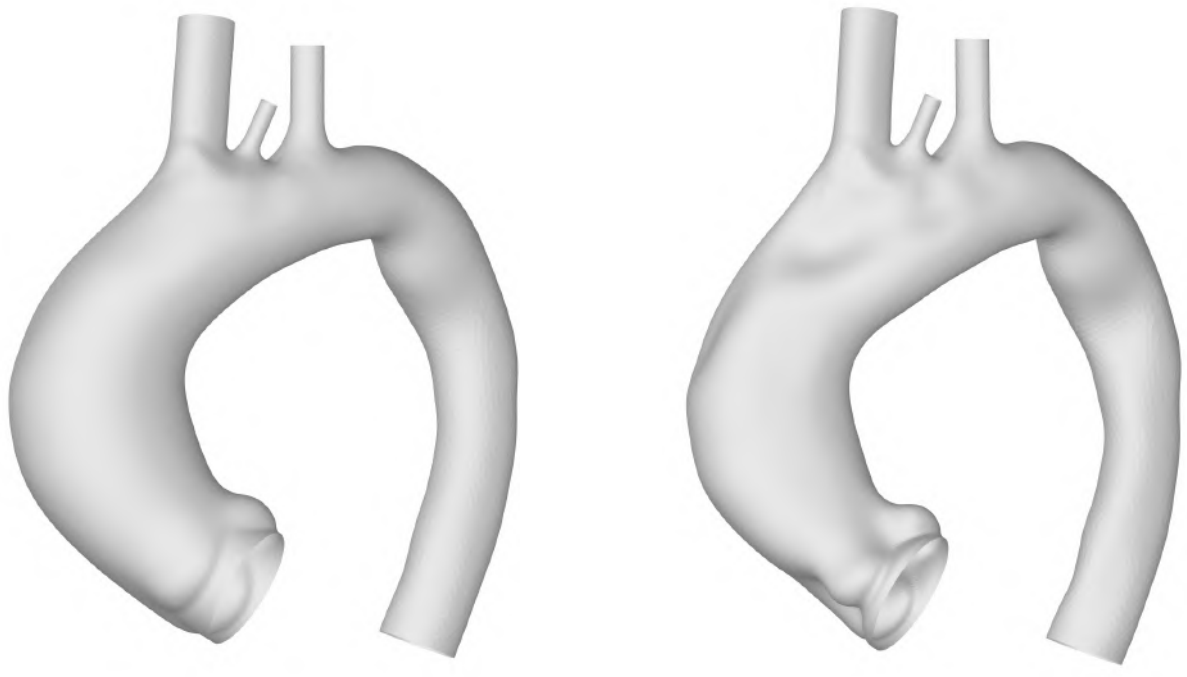

Figure 5.23: Reference configuration $\boldsymbol{X}^*$ (left) and zero-pressure configuration $\boldsymbol{X}_{\mathbf{ZP}}$ (right).

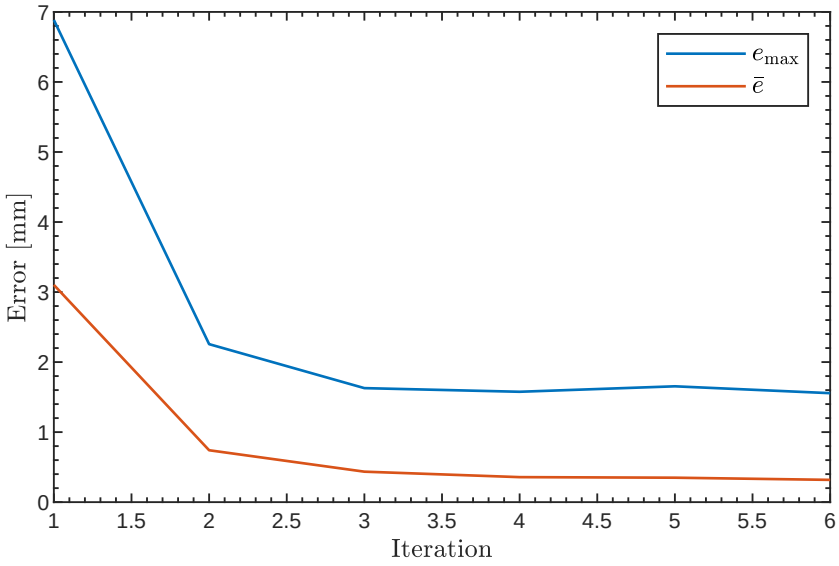

Figure 5.24: Mean and maximum errors obtained through the iterations of the algorithm.

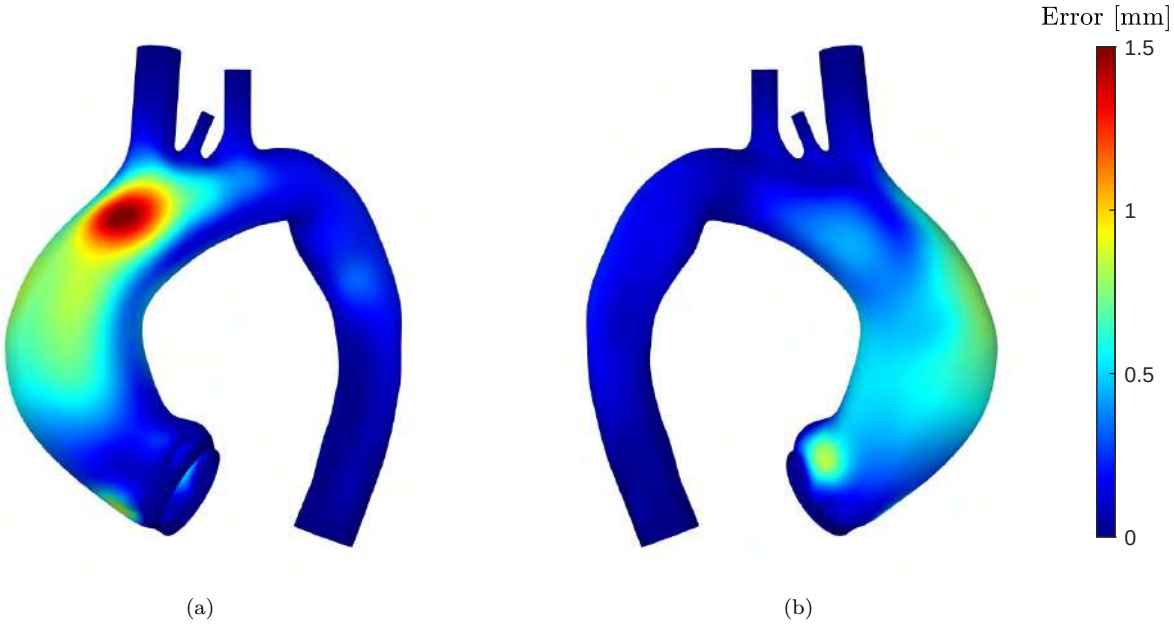

Figure 5.25: Error $\boldsymbol{R_6}$ between the final deformed configuration $\boldsymbol{\Phi_6}$ and the reference configuration $\boldsymbol{\Phi}^*$.

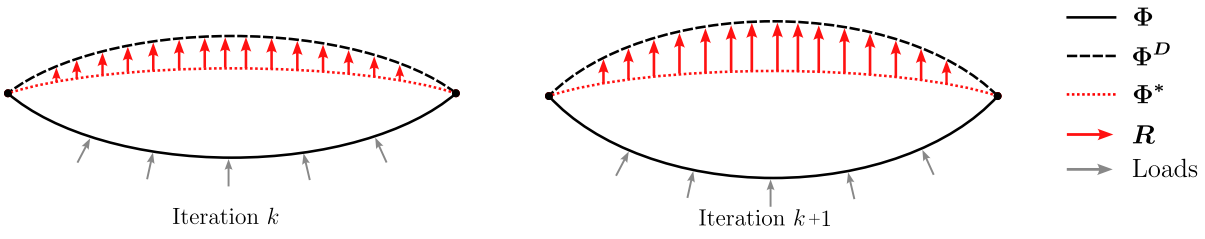

Figure 5.26: Problematic with the Augmented Sellier's Inverse Method when the update in the configuration augments the error.

5.5.6 Results - Idealized vs Personalized

The effect of modelling the aorta using an heterogeneous material model has a great impact on the final stress state. In order to provide an approximate quantification of the difference between an heterogeneous and homogeneous model, a zero-pressure geometry for the later was also computed. In this case the material thickness was chosen to be uniform in all the model, equal to the mean thickness of the four ascending aorta quadrants, $T_{\mathrm{C}} = 2.72$ mm. The material was assumed hyperelastic, again with the mean Yeoh material coefficients of the four quadrants computed for heterogeneous case: $C_{10} = 1.637 \times 10^4$, $C_{20} = 6.64 \times 10^4$ and $C_{30} = 4.431 \times 10^4$. Once both zero-pressure configurations where obtained, a computation was launched to inflate them up to the diastolic pressure and derive the von Mises equivalent stress for the homogeneous ($\sigma^{\mathrm{C}}_{\mathrm{VM}}$) and heterogeneous ($\sigma^{+}_{\mathrm{VM}}$) cases, as depicted in Figure 5.27. In order to better visualize the results, the stress difference $\Delta\sigma_{\mathrm{VM}} = \sigma^{\mathrm{C}}_{\mathrm{VM}} - \sigma^{+}_{\mathrm{VM}}$ is depicted in Figure 5.28. It can be clearly observed how the homogeneous model overestimates the stress on the ascending section and, oppositely, underestimates it on the arch and descending aorta. Since ascending aorta properties were used to define the homogeneous model, it is not surprising that the stresses on the arch and descending sections are lower, since in the heterogeneous case the thickness is significantly lower. On the other hand, it is interesting to note the big differences in the ascending section alone. By considering a homogeneous material defined by the averaged properties of the ascending aorta, the resultant stress is significantly higher. In the ascending section, the stress σ_{VM} was, on average, 7.52 kPa (20 %) higher. The maximum difference was 25.12 KPa, located on the interior curvature of the aorta. The result of this analysis highlights the importance of accounting for an accurate definition of the aorta wall properties, as significant stress differences appear when considering an homogeneous model.

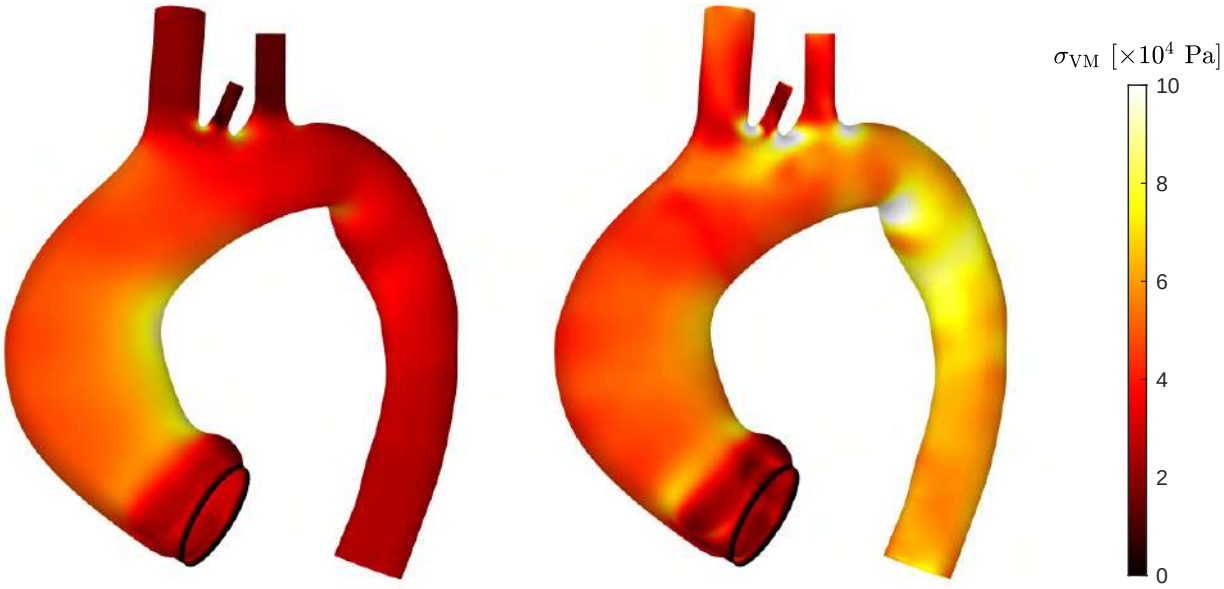

(a) (b)

Figure 5.27: Von Mises stress for the case of a homogeneous (a) and heterogeneous (b) material model.

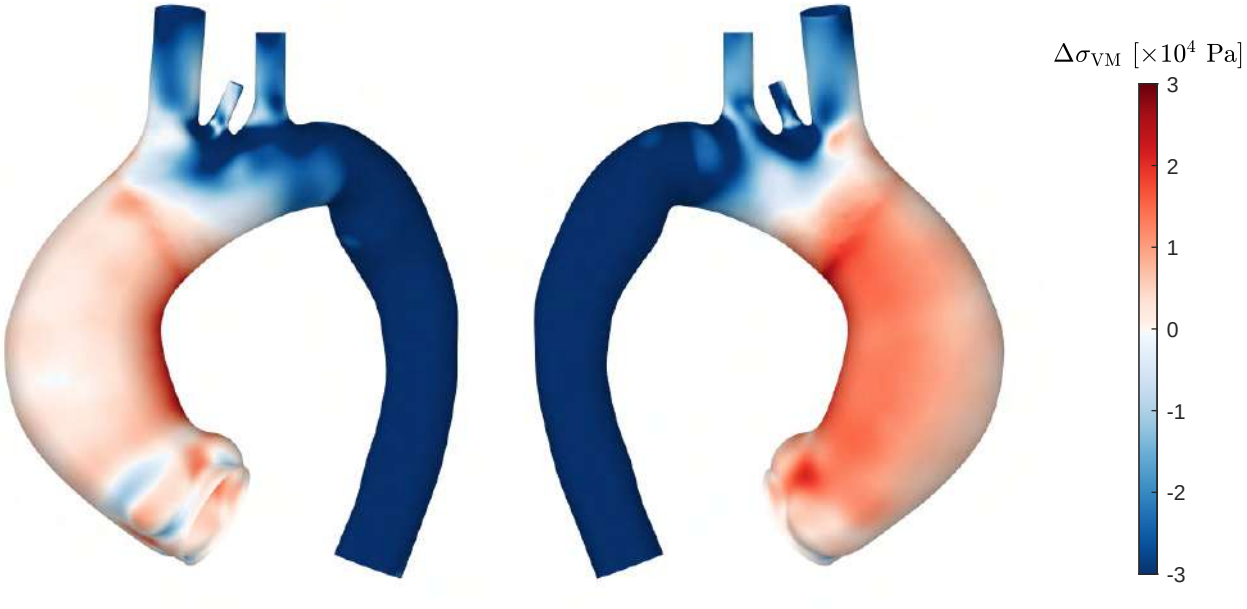

Figure 5.28: Von Mises stress difference ($\Delta\sigma_{\mathbf{VM}}$) between homogeneous and heterogeneous material model.

5.6 FSI solver and numerical setup

After constructing the fluid and structural models, a solver capable of performing FSI is required to model the multi-physics simulation. For this purpose LSDYNA R14.1 (ANSYS Inc., Canonsburg, PA, USA) was used, which allows to model both the fluid and structural problem using the FEM. The computational strategy used in the structural solver was described in Section 5.5.4.

The fluid problem is solved using the Fractional Step method (FSM) for incompressible flows [187] and a second-order time scheme. In the FSM, the velocity and pressure equations are decoupled and thus four equations need to be solved: three for the momentum equation and one to guarantee the incompressibility constraint. The FSM consists of three main steps: Firstly, a predictor velocity u_i^* is calculated, which does not satisfy the incompressibility constraint. The second step consist on projecting the velocity field into a divergence free field in order to obtain a Poisson equation for pressure. Lastly, the computed pressure field is used to correct the velocity field to obtain a divergence free velocity u_i.

To solve the interaction between the two physics, two approaches are available: the monolithic and the partitioned approach. It is possible to use a monolithic approach where the equations of the fluid and structure are considered as a single domain and solved simultaneously. This procedure enables to capture the FSI interaction accurately, however, it has an extremely elevated computational cost since the non-linear system is large and ill-conditioned, making this approach infeasible for many practical applications. The partitioned (or staggered) method [188–190] uncouples the fluid and solid equations and enables to use specific algorithms to solve each problem, boosting the efficiency of the computations by solving two separate, smaller and better conditioned problems. In this later approach, two schemes are available: the weakly and strongly coupled. In the former, only one solution per time step is computed for each problem (fluid and structure) and it is thus viable for simple problems, for example, with small deformations or large solid-to-fluid density ratio. This scheme becomes unstable when the added-mass effect is important [191]. Cardiovascular simulations involves modelling blood and arterial tissue, which have a density ratio near unity, and thus the weak scheme is not an option. The strongly coupled scheme performs numerous coupling iterations, solving the fluid and structural problem numerous times until convergence between solvers is achieved, namely convergence between displacements and forces. This enables to model complex phenomena, with density ratios near unity and large deformations. In the present solver, the strong scheme relies on approximating the tangent operator on the FSI interface, as described in [192].

In this study, a time step of 0.2 ms was used. A maximum of 25 coupling iterations per time step were allowed, however, this limit was never reached, as can the maximum coupling iterations required was 13. The averaged coupling iterations required per time step was 4.84.

5.7 Results and Discussion

The structural and hemodynamic behaviour of the patient was computed for three cardiac cycles using the personalized model described in this chapter. For reference, an additional simulation of the hemodynamic problem alone was performed in order to assess the windkessel behaviour. In this section, we first analyse the resultant hemodynamic boundary conditions by assessing the flux and pressure profiles, followed by an analysis of the structural stress.

5.7.1 Flux and pressure

First, we will analyse the results on the outlet boundary conditions. The results for flux and pressure on the four outlets are plotted in Figures 5.29 and 5.30, both for CFD and FSI simulations. Regarding the CFD fluxes and pressures we can observe that the model achieves rapid cycle convergence, as all three cycles show an identical behaviour. This in not the case for the FSI model, as we observe significant differences between the three cardiac cycles. During the first two cycles oscillations in both flux and pressure during diastole are more significant. The differences in fluxes between the second and third cycle show that cyclic convergence has not been achieved. However, when analysing the pressure plots we can observe that the peak pressure on all outlets have similar values on the last two cycles. For example, on the descending aorta, the peak pressure reaches 129.15 and 129.24 mmHg during the second and third cycle, respectively. We can observe that the target systolic pressure, set to 140 mmHg, was not achieved on either the CFD or FSI simulations. For the case of CFD, the systolic pressure reached 129.2 mmHg, leading to an error of 10.8 mmHg. For the FSI, this error augmented to 30.8 mmHg, since the obtained pressure was 109.2 mmHg. The calibration of the windkessel parameters gives an initial guess for the component values, however an optimization of the components is needed in order to achieve the desired behaviour. This is of greater importance in the case of the FSI, where the compliance of the 3D model leads to reduced pressure profiles on all boundaries, which consequently causes an underestimation of the stress on the wall, since a lower load is acting on the wall. It significant that, although having accounted for the compliance of the 3D model during the windkessel tuning, the achieved pressure had a considerable error much larger than in the case of CFD. On the other hand, the distribution of flow achieved the desired target on the FSI case. The target flow distribution was set to [0.337, 0.036, 0.112, 0.5048] for the BT, LCC, LS and DA respectively, and the achieved distribution was [0.335, 0.036 0.112 0.506].

5.7.2 Structural stress

The simulation of the FSI model enables to capture the stress suffered by the wall. This variable is of great importance as it is assumed to be a driving factor of aortic wall degeneration and it determines when aortic wall rupture will occur. The resultant Von Misses stress (σ_{VM}) at peak systole for the third

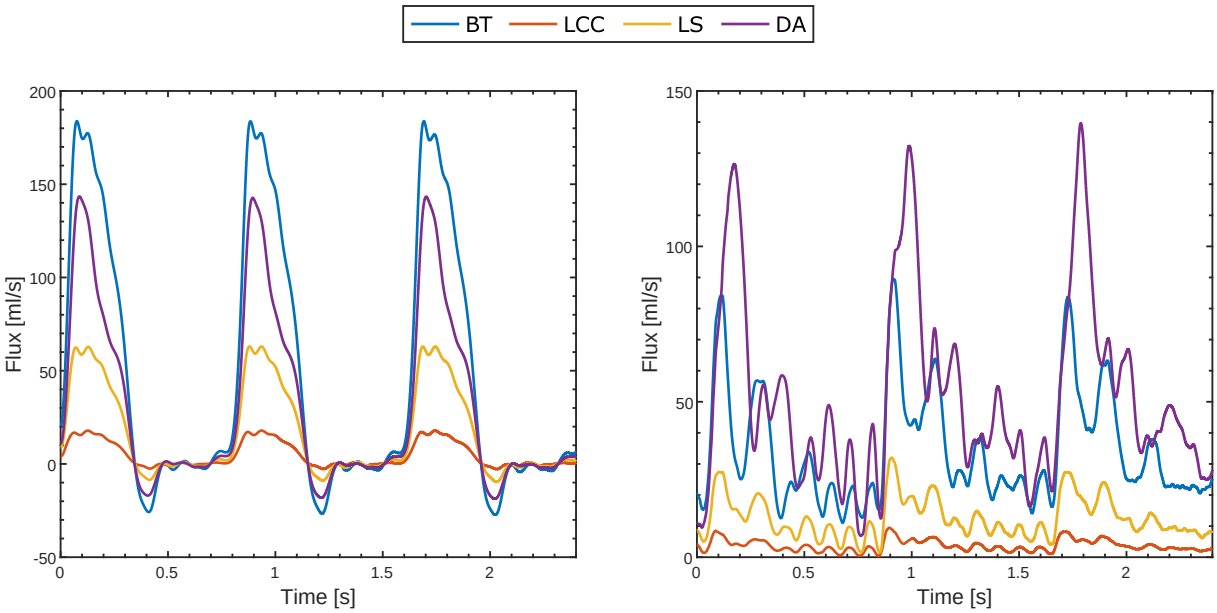

Figure 5.29: Flux through the four outlets for the CFD (left) and FSI (right) computations.

cardiac cycle is depicted in Figure 5.31. We can observe that the stress on the descending aorta and the supra-aortic vessel insertions is significantly higher than in the ascending aorta. The peak stress is located between the BT and LCC carotid insertions, reaching 345 kPa. The ascending section has two peak stress regions, both located along the internal curvature (medial quadrant), reaching 106 kPa at the level of the sinotubular junction and 102 kPa on the central section. The values on the external curvature (lateral quadrant) are lower and remain in range 50-80 kPa. The aortic root has low stress values (<50 kPa). As a reference, the initial and final diameter of the patient, together with the growth rate contours, has been depicted in Figure 5.32, where we can observe that the maximum growth rate is located above the sinotubular junction. To better analyse the relation between stress and growth, the profiles of growth rate together with the circumferentially averaged ($\bar{\sigma}_{\mathrm{VM}}$) and maximum Von Misses stress ($\sigma_{\mathrm{VM}}^{\mathrm{Max}}$) are depicted in Figure 5.33. The highest stress (106 kPa) is located on the sinotubular junction (PC = 0), having this location a null growth rate. However, in the vicinity of this region we find the location of maximum growth rate, GR = 1.12 mm/year, located at PC = 0.2, having an averaged and maximum σ_{VM} equal to 70 and 86 kPa, respectively. The second region with an elevated stress concentration, with $\bar{\sigma}_{\mathrm{VM}}$ = 70 kPa and $\sigma_{\mathrm{VM}}^{\mathrm{Max}}$ = 102 kPa respectively, is located in the central section of the ascending aorta (PC = 0.62) and shows also a near-null growth rate.

5.7.2.1 Discussion

The present analysis has not shown clear evidence of a correlation between stress and aneurysm growth. Moreover, the locations with highest stress concentration show null growth, which is counter intuitive considering that stress is a cause of damage and fatigue. However, the location of maximum stress near the sinotubular junction is in accordance to previous studies [29] and matches the location where type A

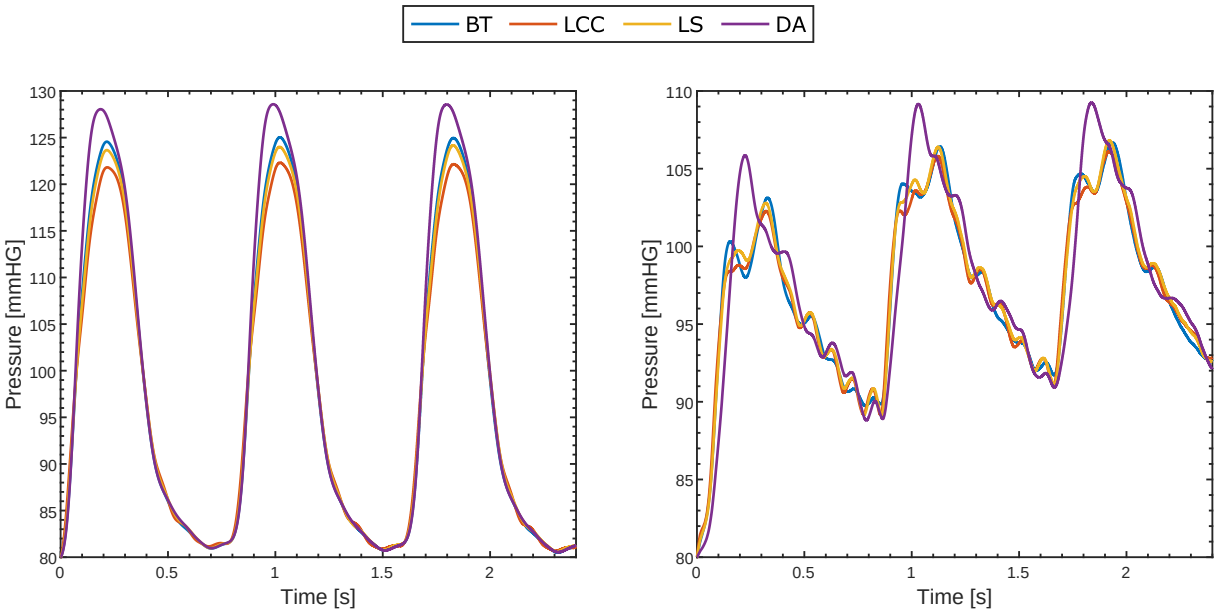

Figure 5.30: Pressure on the four outlets for the CFD (left) and FSI (right) computations.

aortic dissection usually occurs. The ultimate yield strength was 310, 250,470 and 260 kPa for the lateral, medial, anterior and posterior quadrants, respectively. This results in having the maximum stress in the quadrant with minimum ultimate yield strength. This could be a consequence of the wall degradation caused by elevated stress although material characterization of healthy aortas would be required to confirm this. Since the resultant peak stress on the internal curvature was 106 kPa, the aortic wall was at 42% of its maximum yield strength. Considering that the windkessel calibration did not achieve the target systolic pressure of 140 mmHg, the risk factor under the patient specific pressure conditions would be higher. The patient was therefore, prior to the surgery, at a high risk of rupture, since a sudden peak of pressure caused by intense effort could have increased the maximum stress and detonated the wall rupture.

These results could potentially be used to determine the locations of risk of rupture and aneurysm growth. The current results suggest the patient has higher risk of rupture on the aortic arch and descending aorta, however, these sections have not been correctly calibrated since no patient data was available. The elevated stress could be due to the linear elastic behaviour imposed on the descending aorta and the supra-aortic vessels and different results would be obtained if an appropriate patient-specific hyperelastic model had been used. Unfortunately, this measurements where not available. Moreover, the elevated curvature around the supra-aortic vessel insertion causes a rise of stress that maybe non realistic since, on the one hand, the angiography resolution is insufficient to capture the geometrical details in these regions and, therefore, the curvature is constructed artificially during the CAD editing stage. On the other hand, thickness variations around high curvature regions will cause a redistribution of stress but, again, the angiography lacks the resolution to perform these measurements. Thickness variations are to be expected since the curvature radius in these regions is smaller than the imposed wall thickness. From a numerical point of view, modelling such regions with shell elements is not optimal and 3D elements should be used

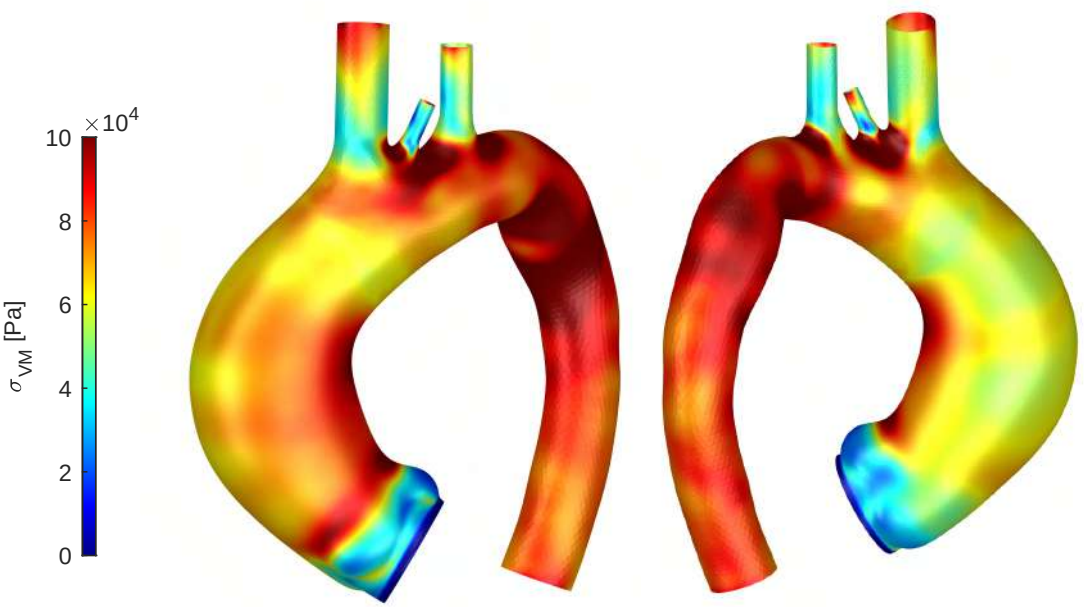

Figure 5.31: Von Misses stress for the analysed patient.

ideally to accurately capture the stress distribution. The material definition also affects the aortic root, as it has different material properties to those imposed on the model. As for the case of the descending aorta and supra-aortic vessels, an accurate definition of the root properties would lead to stress differences. Moreover, a fixed boundary condition was imposed on the annulus nodes, restricting the deformations in the vicinity of the annulus and diminishing the stress.

5.7.3 Limitations

It should be noted that various simplifications have been made due to the lack of the clinical data required and this has a significant impact on the results. Regarding the structural set-up we encounter the following limitations: Firstly, the motion transmitted from the heart to the aorta during the cardiac cycle has been neglected. It has been shown that this motion has a significant impact on the strain and stress distribution [29, 38], as the cardiac motion derived stresses are of the same order of magnitude as those caused by the fluid forces alone, being concentrated around the aortic root and sinotubular junction. Secondly, numerous assumptions have been made when defining the spatially-varying material properties (thickness and elasticity) due to the lack of experimental data. The supra-aortic vessels and descending aorta have been modelled using linear elasticity and, thus, the behaviour of these regions greatly differs from the ascending section. The elasticity of these branches was derived from estimated pulse wave velocity which, although it has been tuned according to patient's data, provides only an approximate characterization of the vessel properties. A similar issue occurs when defining the aortic root. In this case the material was

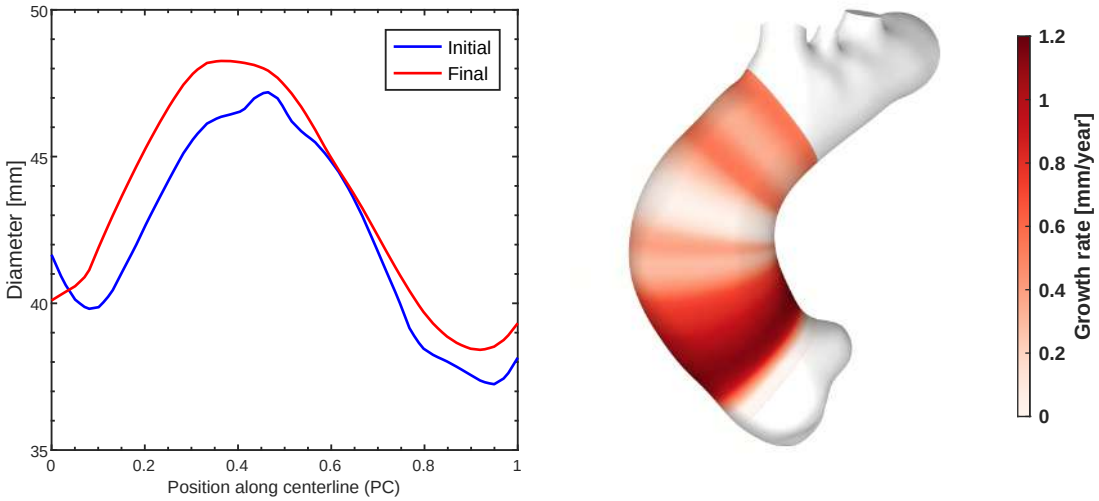

Figure 5.32: Initial and final diameter (left) and growth rate contours (right).

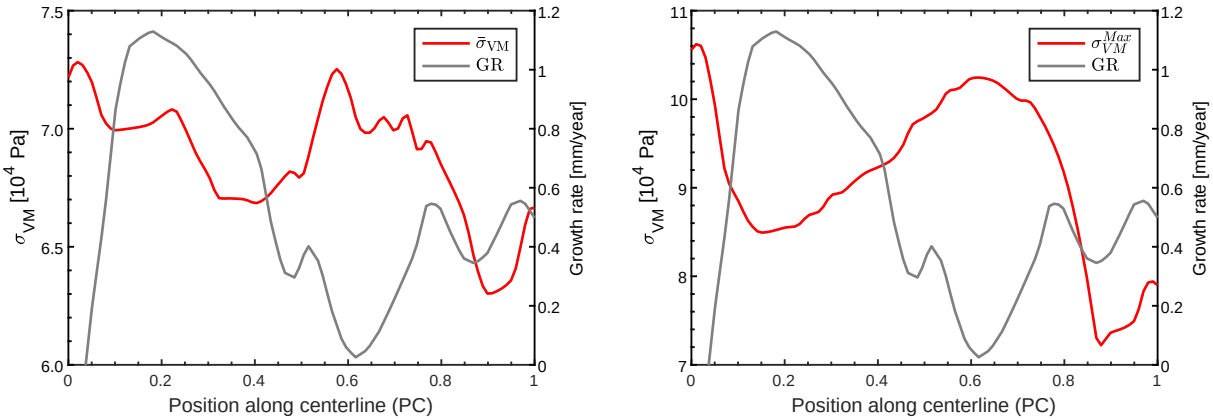

Figure 5.33: Plot of the growth rate along the centerline together with the circumferentially averaged Von Misses stress (left) and maximum Von Misses stress (right).

modelled identically to the ascending aorta. Thirdly, the viscoelastic supports have not been personalized and the spring and viscous constants have been taken from literature. An improvement of the model's fidelity would be achieved if a tuning of the supports was made.

Concerning the fluid set-up, it has been shown that an optimization of the windkessel components is mandatory to accurately capture the patient-specific pressure conditions. The values obtained from the current state of the arts workflows [169–172] provide only an approximation and not an accurate tuning. Alternatively, pressure profiles could be used on the outlets to guarantee that the target pressure is reached, although this configuration requires precise invasive measurements of the patient's aortic pressure. An additional issue concerning the fluid set-up is the lack of MRI 2D flow measurements on the supra-aortic branches and thus an assumption of flow distribution based on outlet area was required. The tuning of the windkessel components could be improved if such measurements were available.

Regarding the numerical set-up, a coarse mesh was used. As it was shown in Chapter 3, the mesh convergence on the fluid domain is achieved when the surface mesh is generated with a face size below 0.35 mm and the internal domain discretised with elements smaller than 0.7 mm. In this case, the surface mesh was created with 1 mm triangular faces and the internal domain with 1.5 mm tetrahedrons, due to the computational requirements of FSI simulations. A mesh convergence analysis of the structural domain was not performed, but it would enable to define the minimum mesh requirements for accurate stress modelling.

With regard to the clinical outcomes of this study, due to having modelled one patient only, it is not possible to hypothesise on the relationship between growth and stress. A large cohort should be modelled and assessed, considering both healthy, stable and dilating aneurysms followed up during a long period of time ($>$ 2 years).

5.8 Conclusion

A procedure to create personalized high-fidelity FSI aorta models has been presented and has shown to improve the accuracy of the model outputs. Combining both patient-specific hemodynamic boundary conditions and material definition allows for an accurate estimation of the stress suffered by the aortic wall and can provide insight on the risk of rupture of the aortic wall. However, our results also show that, in order to create an accurate model, numerous clinical and experimental measurements are required which, unfortunately, are not acquired during standard clinical routines.

Our results have also shown that in order to accurately capture the patient's systolic and diastolic pressures, an estimation of the windkessel parameters is not sufficient. It is necessary to perform an optimization of the windkessel parameters in order to compensate for the compliance and flow dynamics of the 3D model.

Chapter 6

Final remarks

6.1 Final conclusions

In this work, a study of the methodology required for performing accurate CFD analyses of ascending aortic aneurysms has been presented. We concluded that accounting for the shear thinning behaviour is of prime importance when computing WSS biomarkers, since, otherwise, the WSS maybe underestimated by $\sim$5%. Non-Newtonian behaviour is accentuated in regions of low velocity and, hence, it is important to account for it in the near-wall region. Accounting for subgrid scale viscosity has revealed to be less important, since its impact on WSS values has been estimated to be $\sim$0.5%. Be that as it may, including the Dynamic Smagorinsky-Lilly subgrid-scale model had no impact on the computational resources required for the simulations, therefore, we concluded that subgrid-scale models should be included in aortic aneurysm simulations.

The second part of this work consisted on evaluating if a relationship exists between CFD biomarkers and aneurysm growth rate. The results show that certain biomarkers could be related to aneurysm growth rate, such as the time-averaged shear angle, the flux dispersion and the location of negative divergence of the WSS field for TAV patients and peak systole shear angle for BAV patients. This results should, however, be handled with care, since the cohort was limited to 16 TAVs and 17 BAVs and, moreover, the aortic jet was not calibrated using MRI flow data. Without neglecting these limitations, it must be highlighted that this work has presented the first analysis of the relationship between CFD biomarkers and aneurysm growth rate on a large cohort of patients.

Lastly, after having identified the limitations of the herein presented CFD analyses, a methodology for generating high-fidelity personalized FSI aorta models was developed. This work included a procedure to calibrate the aortic jet by imposing the spatially-varying patient-specific velocity profile to personalize the fluid model. It was made clear that the patient-specific jet largely differs from and idealized profile. Concerning the structural model, a method for personalizing the material properties of the aortic wall was developed. The method was based on calibrating the spatially-varying thickness and elastic properties in order to capture the variability of the material properties of the different quadrants of the ascending section and the downstream vessels. Considerable differences were found between structural stress of a varying material model and uniform material model. Once the methodology for creating personalized FSI models was completed, a test case was performed in order to demonstrate the capability of these models to estimate the stress along the aorta and identify potential regions prone to aneurysm growth. This work has highlighted the importance of accounting for the patient-specific conditions when using computational tools for aiding the diagnosis process of ascending aortic aneurysms.

6.2 Future works

The work herein presented contains some novel developments which position these models in the state of the art of ascending aortic simulation. However, we are aware that, concerning certain aspects of the modelization and analysis, numerous improvements could be made. On the one hand, more advanced methods have been proposed by other research groups and, on the other hand, additional clinical measures could be incorporated for the personalization of the model.

Concerning the analysis of CFD computational methodologies, it would be interesting to assess whether or not significant differences appear if other subgrid scale models are used. In previous works, the WALE model has been used to evaluate the WSS [80, 97, 98], since it was specifically designed to accurately capture the asymptotic behaviour of wall bounded flows. Thus, extending this work by assessing the effect of the WALE model would enrich the understanding of the requirements for turbulence modelling. With regard to the viscosity model, the same applies. Numerous alternatives to the Carreau model exist and should be examined in order to understand the influence of the viscosity model. A previous study was performed with this aim [101], however it did not account for an LES model. An assessment between the different combinations of non-Newtonian models and LES models could provide further insight of the importance of the modelling choices on WSS estimation.

The study on the relationship between CFD biomarkers and growth rate could incorporate numerous improvements. As mentioned in 4.5.1, the most critical simplification done in this analysis was the assumption of an idealized aortic jet profile. It has been shown that the CFD biomarkers are highly influenced by the jet shape [119] and, therefore, it is vital to incorporate this improvement if we seek to achieve an accurate quantification of the CFD biomarkers. Having identified this flaw, in Chapter 5 we developed the techniques required to incorporate such boundary conditions to our model. However, due to the lack of MRI 4D data on the patient cohort, it was not possible to repeat this study while incorporating this improvement. With regard to the growth measurements, we must emphasise that the measurements are susceptible to having a large error. This was due to the limited time window between some acquisitions, and due to the resolution of the angiography. In order to perform an accurate assessment of the relationship between biomarkers and growth, a larger cohort of patients with a larger time window should be considered. Furthermore, healthy subjects and aneurysms in an early stage of development should be included in the study in order to fully understand the role of the fluid biomarkers on aneurysm development. This improved study should, unquestionably, include personalized jet profiles derived from MRI flow acquisitions. Another improvement that should be incorporated is the personalization of the viscosity. The rheological response of blood is primarily modulated haematocrit [86] and, since haematocrit levels vary across the population and due to the intake of drugs, variations in blood viscosity across a population could be important. It is important to account for this variability since it would have a direct

impact on the WSS values, as shown in [193]. Lastly, the analysis of the WSS topological skeleton should be extended and used to compute the fixed points residence time and the topological shear variation indexes, two biomarkers which have been related to arterial stiffness and which can be used to identify regions prone adverse biological events [141–143].

In the last chapter, we have presented a high-fidelity FSI model capable of capturing the structural stresses. However, this workflow was not used to model a large cohort of patients and thus no conclusions between the stress and growth could be made. A future study using this methodology, but performed on a large cohort, could shed light into the relationship between stress and growth. Furthermore, evaluating simultaneously the structural and fluid biomarkers would provide addition insight on the patient's condition. Concerning the accuracy of our model, it is mandatory to improve the calibration technique of the windkessel components, as it was shown that the pressure profiles did not reach the target pressures. For this purpose, an optimization of the FSI model coupled to the windkessel should be performed, however, this is computationally prohibitive and an alternative procedure should be used. The solution is constructing a Dynamic ROM of the FSI model and couple it to the windkessel circuit, and optimize the components in using this compressed, coupled model, as was done in [31] for CFD models. Concerning the material properties, a better calibration of the supra-aortic vessels and the descending aorta would improve the accuracy of the simulation. Finally, we should incorporate the valve movement and perform a calibration of the viscoelastic supports, as was done in [38], in order accurately capture the stresses on the aorta wall and the full phenomena of the FSI interaction.

In sight of the numerous improvements which can be incorporated to our work, we conclude that various lines of research can be continued in the pursuit of high-fidelity cardiovascular in-silico models. It has been shown that it is of prime importance to calibrate the models with high quality clinical measurements in order to accurately capture the patient-specific conditions and, consequently, be able to deliver clinically-relevant information which could aid in the diagnosis.

Bibliography

[1] R. Gouveia e Melo, G. Silva Duarte, A. Lopes, M. Alves, D. Caldeira, R. Fernandes e Fernandes, and L. Mendes Pedro, "Incidence and prevalence of thoracic aortic aneurysms: A systematic review and meta-analysis of population-based studies," *Seminars in Thoracic and Cardiovascular Surgery*, vol. 34, pp. 1–16, Mar 2022.

[2] C. Olsson, S. Thelin, E. Ståhle, A. Ekbom, and F. Granath, "Thoracic aortic aneurysm and dissection," *Circulation*, vol. 114, no. 24, pp. 2611–2618, 2006.

[3] C. Harris, B. Croce, and C. Cao, "Thoracic aortic aneurysm," *Annals of Cardiothoracic Surgery*, vol. 5, no. 4, 2016.

[4] K. Cheung, M. Boodhwani, K. Chan, L. Beauchesne, A. Dick, and T. Coutinho, "Thoracic aortic aneurysm growth: Role of sex and aneurysm etiology," *Journal of the American Heart Association*, vol. 6, no. 2, p. e003792, 2017.

[5] S. A. Avadhani, W. Martin-Doyle, A. Y. Shaikh, and L. A. Pape, "Predictors of ascending aortic dilation in bicuspid aortic valve disease: A five-year prospective study," *The American Journal of Medicine*, vol. 128, no. 6, pp. 647–652, 2015.

[6] K. Kato, M. Oguri, N. Kato, T. Hibino, K. Yajima, T. Yoshida, N. Metoki, H. Yoshida, K. Satoh, S. Watanabe, K. Yokoi, T. Murohara, and Y. Yamada, "Assessment of Genetic Risk Factors for Thoracic Aortic Aneurysm in Hypertensive Patients," *American Journal of Hypertension*, vol. 21, pp. 1023–1027, 09 2008.

[7] E. M. Isselbacher, O. Preventza, J. Hamilton Black III, J. G. Augoustides, A. W. Beck, M. A. Bolen, A. C. Braverman, B. E. Bray, M. M. Brown-Zimmerman, E. P. Chen, T. J. Collins, A. DeAnda, C. L. Fanola, L. N. Girardi, C. W. Hicks, D. S. Hui, W. S. Jones, V. Kalahasti, K. M. Kim, D. M. Milewicz, G. S. Oderich, L. Ogbechie, S. B. Promes, E. G. Ross, M. L. Schermerhorn, S. S. Times, E. E. Tseng, G. J. Wang, and Y. J. Woo, "2022 ACC/AHA Guideline for the Diagnosis and Management of Aortic Disease," *Journal of the American College of Cardiology*, vol. 80, pp. e223–e393, Dec. 2022.

[8] D. A. Vorp, M. Raghavan, and M. W. Webster, "Mechanical wall stress in abdominal aortic aneurysm: Influence of diameter and asymmetry," *Journal of Vascular Surgery*, vol. 27, no. 4, pp. 632–639, 1998.

[9] W. R. Mower, L. J. Baraff, and J. Sneyd, "Stress distributions in vascular aneurysms: Factors affecting risk of aneurysm rupture," *Journal of Surgical Research*, vol. 55, no. 2, pp. 155–161, 1993.

[10] E. L. George, J. A. Smith, B. Colvard, J. T. Lee, and J. R. Stern, "Precocious rupture of abdominal aortic aneurysms below size criteria for repair: Risk factors and outcomes," *Annals of Vascular Surgery*, 2023.

[11] R. J. Soler, D. Fabre, A. C. Watkins, E. Fadel, O. Mercier, and S. Haulon, "Hybrid treatment of a giant thoracic aneurysm in a 38 year-old woman," *Journal of Vascular Surgery*, vol. 69, pp. 1591–1595, May 2019.

[12] M. Bicer, A. Yuksel, and I. I. Kan, "The largest reported giant ascending aortic aneurysm presented with superior vena cava syndrome," *Braz J Cardiovasc Surg*, vol. 35, pp. 834–837, Oct. 2020.

[13] K. H. Chau and J. A. Elefteriades, "Natural history of thoracic aortic aneurysms: Size matters, plus moving beyond size," *Progress in Cardiovascular Diseases*, vol. 56, no. 1, pp. 74–80, 2013. Aneurysms.

[14] D. M. Pierce, F. Maier, H. Weisbecker, C. Viertler, P. Verbrugghe, N. Famaey, I. Fourneau, P. Herijgers, and G. A. Holzapfel, "Human thoracic and abdominal aortic aneurysmal tissues: Damage experiments, statistical analysis and constitutive modeling," *Journal of the Mechanical Behavior of Biomedical Materials*, vol. 41, pp. 92–107, Jan. 2015.

[15] T. L. Surman, J. M. Abrahams, J. Manavis, J. Finnie, D. O'Rourke, K. J. Reynolds, J. Edwards, M. G. Worthington, and J. Beltrame, "Histological regional analysis of the aortic root and thoracic ascending aorta: a complete analysis of aneurysms from root to arch," *Journal of Cardiothoracic Surgery*, vol. 16, p. 255, Sep 2021.

[16] S. Lin, *Biomechanics of human ascending aorta and aneurysm rupture risk assessment.* PhD thesis, 2021. Thèse de doctorat dirigée par Bouchot, Olivier Instrumentation et informatique de l'image Bourgogne Franche-Comté 2021.

[17] S. Lin, M. C. Morgant, D. M. Marín-Castrillón, P. M. Walker, L. S. Aho Glélé, A. Boucher, B. Presles, O. Bouchot, and A. Lalande, "Aortic local biomechanical properties in ascending aortic aneurysms," *Acta Biomaterialia*, vol. 149, pp. 40–50, 2022.

[18] M. Liu, L. Liang, F. Sulejmani, X. Lou, G. Iannucci, E. Chen, B. Leshnower, and W. Sun, "Identification of in vivo nonlinear anisotropic mechanical properties of ascending thoracic aortic aneurysm from patient-specific ct scans," *Scientific Reports*, vol. 9, p. 12983, Sep 2019.

[19] O. Trabelsi, F. M. Davis, J. F. Rodriguez-Matas, A. Duprey, and S. Avril, "Patient specific stress and rupture analysis of ascending thoracic aneurysms," *Journal of Biomechanics*, vol. 48, no. 10, pp. 1836–1843, 2015.

[20] R. Campobasso, F. Condemi, M. Viallon, P. Croisille, S. Campisi, and S. Avril, "Evaluation of peak wall stress in an ascending thoracic aortic aneurysm using fsi simulations: Effects of aortic stiffness and peripheral resistance," *Cardiovascular Engineering and Technology*, vol. 9, pp. 707–722, Dec 2018.

[21] V. Y. Dolgov, K. Y. Klyshnikov, E. A. Ovcharenko, T. V. Glushkova, A. V. Batranin, A. S. Agienko, Y. A. Kudryavtseva, A. E. Yuzhalin, and A. G. Kutikhin, "Finite Element Analysis-Based Approach for Prediction of Aneurysm-Prone Arterial Segments," *Journal of Medical and Biological Engineering*, vol. 39, pp. 102–108, Feb. 2019.

[22] E. K. Shang, D. P. Nathan, E. Y. Woo, R. M. Fairman, G. J. Wang, R. C. Gorman, J. H. Gorman, and B. M. Jackson, "Local wall thickness in finite element models improves prediction of abdominal aortic aneurysm growth," *Journal of Vascular Surgery*, vol. 61, no. 1, pp. 217–223, 2015.

[23] M. Breeuwer, S. de Putter, U. Kose, L. Speelman, K. Visser, F. Gerritsen, R. Hoogeveen, R. Krams, H. van den Bosch, J. Buth, T. Gunther, B. Wolters, E. van Dam, and F. van de Vosse, "Towards patient-specific risk assessment of abdominal aortic aneurysm," *Medical & Biological Engineering & Computing*, vol. 46, pp. 1085–1095, Nov 2008.

[24] S. Jamaleddin Mousavi, R. Jayendiran, S. Farzaneh, S. Campisi, M. Viallon, P. Croisille, and S. Avril, "Coupling hemodynamics with mechanobiology in patient-specific computational models of ascending thoracic aortic aneurysms," *Computer Methods and Programs in Biomedicine*, vol. 205, p. 106107, June 2021.

[25] W. Hao, S. Gong, S. Wu, J. Xu, M. R. Go, A. Friedman, and D. Zhu, "A mathematical model of aortic aneurysm formation," *PLOS ONE*, vol. 12, pp. 1–22, 02 2017.

[26] K. Volokh, "Modeling aneurysm growth and failure," *Procedia IUTAM*, vol. 12, pp. 204–210, 2015. IUTAM Symposium on Mechanics of Soft Active Materials.

[27] K. Capellini, E. Vignali, E. Costa, E. Gasparotti, M. E. Biancolini, L. Landini, V. Positano, and S. Celi, "Computational Fluid Dynamic Study for aTAA Hemodynamics: An Integrated Image-Based and Radial Basis Functions Mesh Morphing Approach," *Journal of Biomechanical Engineering*, vol. 140, 08 2018. 111007.

[28] E. L. Manchester, S. Pirola, M. Y. Salmasi, D. P. O'Regan, T. Athanasiou, and X. Y. Xu, "Analysis of Turbulence Effects in a Patient-Specific Aorta with Aortic Valve Stenosis," *Cardiovascular Engineering and Technology*, vol. 12, pp. 438–453, Aug. 2021.

[29] V. Mendez, M. Di Giuseppe, and S. Pasta, "Comparison of hemodynamic and structural indices of ascending thoracic aortic aneurysm as predicted by 2-way FSI, CFD rigid wall simulation and patient-specific displacement-based FEA," *Computers in Biology and Medicine*, vol. 100, pp. 221–229, 2018.

[30] E. Vignali, E. Gasparotti, S. Celi, and S. Avril, "Fully-coupled FSI computational analyses in the ascending thoracic aorta using patient-specific conditions and anisotropic material properties," *Frontiers in Physiology*, vol. 12, 2021.

[31] J. Tomasi, F. Le Bars, C. Shao, A. Lucas, M. Lederlin, P. Haigron, and J. Verhoye, "Patient-specific and real-time model of numerical simulation of the hemodynamics of type B aortic dissections," *Medical Hypotheses*, vol. 135, p. 109477, 2020.

[32] M. Bonfanti, S. Balabani, J. P. Greenwood, S. Puppala, S. Homer-Vanniasinkam, and V. Díaz-Zuccarini, "Computational tools for clinical support: a multi-scale compliant model for haemodynamic simulations in an aortic dissection based on multi-modal imaging data," *Journal of The Royal Society Interface*, vol. 14, no. 136, p. 20170632, 2017.

[33] H. Xu, M. Piccinelli, B. G. Leshnower, A. Lefieux, W. R. Taylor, and A. Veneziani, "Coupled Morphological–Hemodynamic Computational Analysis of Type B Aortic Dissection: A Longitudinal Study," *Annals of Biomedical Engineering*, vol. 46, pp. 927–939, July 2018.

[34] T. Liu, M. Xie, Q. Lv, Y. Li, L. Fang, L. Zhang, W. Deng, and J. Wang, "Bicuspid aortic valve: An update in morphology, genetics, biomarker, complications, imaging diagnosis and treatment," *Frontiers in Physiology*, vol. 9, 2019.

[35] A. Aydin, N. Desai, A. M. Bernhardt, H. Treede, C. Detter, S. Sheikhzadeh, M. Rybczynski, M. Hillebrand, V. Lorenzen, K. Mortensen, P. N. Robinson, J. Berger, H. Reichenspurner, T. Meinertz, S. Willems, and Y. von Kodolitsch, "Ascending aortic aneurysm and aortic valve dysfunction in bicuspid aortic valve disease," *International Journal of Cardiology*, vol. 164, pp. 301–305, Apr 2013.

[36] M. Y. Salmasi, S. Pirola, S. Sasidharan, S. M. Fisichella, A. Redaelli, O. A. Jarral, D. P. O'Regan, A. Y. Oo, J. E. Moore, X. Y. Xu, and T. Athanasiou, "High wall shear stress can predict wall degradation in ascending aortic aneurysms: An integrated biomechanics study," *Frontiers in Bioengineering and Biotechnology*, vol. 9, 2021.

[37] M. Kiema, J. K. Sarin, S. P. Kauhanen, J. Torniainen, H. Matikka, E.-S. Luoto, P. Jaakkola, P. Saari, T. Liimatainen, R. Vanninen, S. Ylä-Herttuala, M. Hedman, and J. P. Laakkonen, "Wall shear stress predicts media degeneration and biomechanical changes in thoracic aorta," *Frontiers in Physiology*, vol. 13, 2022.

[38] L. Geronzi, A. Bel-Brunon, A. Martinez, M. Rochette, M. Sensale, O. Bouchot, A. Lalande, S. Lin, P. P. Valentini, and M. E. Biancolini, "Calibration of the mechanical boundary conditions for a patient-specific thoracic aorta model including the heart motion effect," *IEEE Transactions on Biomedical Engineering*, pp. 1–12, 2023.

[39] R. Pons, A. Guala, J. F. Rodríguez-Palomares, J. C. Cajas, L. Dux-Santoy, G. Teixidó-Tura, J. J. Molins, M. Vázquez, A. Evangelista, and J. Martorell, "Fluid–structure interaction simulations outperform computational fluid dynamics in the description of thoracic aorta haemodynamics and in the differentiation of progressive dilation in marfan syndrome patients," *Royal Society Open Science*, vol. 7, no. 2, p. 191752, 2020.

[40] P. Rissland, Y. Alemu, S. Einav, J. Ricotta, and D. Bluestein, "Abdominal Aortic Aneurysm Risk of Rupture: Patient-Specific FSI Simulations Using Anisotropic Model," *Journal of Biomechanical Engineering*, vol. 131, p. 031001, 12 2008.

[41] S. Lin, X. Han, Y. Bi, S. Ju, and L. Gu, "Fluid-structure interaction in abdominal aortic aneurysm: Effect of modeling techniques," *BioMed Research International*, vol. 2017, p. 7023078, Feb 2017.

[42] N. Xiao, J. D. Humphrey, and C. A. Figueroa, "Multi-scale computational model of three-dimensional hemodynamics within a deformable full-body arterial network," *Journal of Computational Physics*, vol. 244, pp. 22–40, July 2013.

[43] R. Erbel, V. Aboyans, C. Boileau, and E. Bossone, "2014 esc guidelines on the diagnosis and treatment of aortic diseases: Document covering acute and chronic aortic diseases of the thoracic and abdominal aorta of the adultthe task force for the diagnosis and treatment of aortic diseases of the european society of cardiology (esc)," *European Heart Journal*, vol. 35, pp. 2873–2926, 08 2014.

[44] P. Nagpal, M. D. Agrawal, S. S. Saboo, S. Hedgire, S. Priya, and M. L. Steigner, "Imaging of the aortic root on high-pitch non-gated and ecg-gated ct: awareness is the key!," *Insights into Imaging*, vol. 11, p. 51, Mar 2020.

[45] R. T. Hahn, M. J. Roman, A. H. Mogtadek, and R. B. Devereux, "Association of aortic dilation with regurgitant, stenotic and functionally normal bicuspid aortic valves," *Journal of the American College of Cardiology*, vol. 19, no. 2, pp. 283–288, 1992.

[46] J. B. Kim, M. Spotnitz, M. E. Lindsay, T. E. MacGillivray, E. M. Isselbacher, and T. M. Sundt, "Risk of aortic dissection in the moderately dilated ascending aorta," *Journal of the American College of Cardiology*, vol. 68, no. 11, pp. 1209–1219, 2016.

[47] V. Garg, A. N. Muth, J. F. Ransom, M. K. Schluterman, R. Barnes, I. N. King, P. D. Grossfeld, and D. Srivastava, "Mutations in notch1 cause aortic valve disease," *Nature*, vol. 437, pp. 270–274, Sep 2005.

[48] J. I. Hoffman and S. Kaplan, "The incidence of congenital heart disease," *Journal of the American College of Cardiology*, vol. 39, no. 12, pp. 1890–1900, 2002.

[49] E. W. Larson and W. D. Edwards, "Risk factors for aortic dissection: A necropsy study of 161 cases," *The American Journal of Cardiology*, vol. 53, no. 6, pp. 849–855, 1984.

[50] C. D. Etz, M. Misfeld, M. A. Borger, M. Luehr, E. Strotdrees, and F.-W. Mohr, "Current indications for surgical repair in patients with bicuspid aortic valve and ascending aortic ectasia," *Cardiology Research and Practice*, vol. 2012, p. 313879, Sep 2012.

[51] E. Saliba, Y. Sia, A. Dore, and I. El Hamamsy, "The ascending aortic aneurysm: When to intervene," *IJC Heart and Vasculature*, vol. 6, pp. 91–100, 2015.

[52] W. D. Clouse, J. W. Hallett, Jr, H. V. Schaff, M. M. Gayari, D. M. Ilstrup, and L. J. Melton III, "Improved Prognosis of Thoracic Aortic AneurysmsA Population-Based Study," *JAMA*, vol. 280, pp. 1926–1929, 12 1998.

[53] B. S. Brooke, J. P. Habashi, D. P. Judge, N. Patel, B. Loeys, and H. C. Dietz, "Angiotensin ii blockade and aortic-root dilation in marfan's syndrome," *New England Journal of Medicine*, vol. 358, no. 26, pp. 2787–2795, 2008. PMID: 18579813.

[54] S. J. Smart and C. T. Kroodsma, "Potential relevance of laplace's law to the vascular permeability induced by vasodilators such as histamine and bradykinin.," *Journal of Allergy and Clinical Immunology*, vol. 123, p. S258, Feb 2009.

[55] A. J. Hall, E. F. Busse, D. J. McCarville, and J. J. Burgess, "Aortic wall tension as a predictive factor for abdominal aortic aneurysm rupture: Improving the selection of patients for abdominal aortic aneurysm repair," *Annals of Vascular Surgery*, vol. 14, pp. 152–157, Mar 2000.

[56] H. B. BURCHELL, "Aortic dissection (dissecting hematoma; dissecting aneurysm of the aorta)," *Circulation*, vol. 12, no. 6, pp. 1068–1079, 1955.

[57] I. El-Hamamsy and M. H. Yacoub, "Cellular and molecular mechanisms of thoracic aortic aneurysms," *Nature Reviews Cardiology*, vol. 6, pp. 771–786, Dec 2009.

[58] T. S. Absi, T. M. Sundt III, W. S. Tung, M. Moon, J. K. Lee, R. R. Damiano Jr., and R. W. Thompson, "Altered patterns of gene expression distinguishing ascending aortic aneurysms from abdominal aortic aneurysms: complementary dna expression profiling in the molecular characterization of aortic disease," *The Journal of Thoracic and Cardiovascular Surgery*, vol. 126, pp. 344–357, Aug 2003.

[59] J. R. Barbour, F. G. Spinale, and J. S. Ikonomidis, "Proteinase systems and thoracic aortic aneurysm progression," *Journal of Surgical Research*, vol. 139, pp. 292–307, May 2007.

[60] J. Xu and G.-P. Shi, "Vascular wall extracellular matrix proteins and vascular diseases," *Biochimica et Biophysica Acta (BBA) - Molecular Basis of Disease*, vol. 1842, no. 11, pp. 2106–2119, 2014.

[61] B. M. Schaefer, M. B. Lewin, K. K. Stout, E. Gill, A. Prueitt, P. H. Byers, and C. M. Otto, "The bicuspid aortic valve: an integrated phenotypic classification of leaflet morphology and aortic root shape," *Heart*, vol. 94, no. 12, pp. 1634–1638, 2008.

[62] S. S. Fazel, H. R. Mallidi, R. S. Lee, M. P. Sheehan, D. Liang, D. Fleischman, R. Herfkens, R. S. Mitchell, and D. C. Miller, "The aortopathy of bicuspid aortic valve disease has distinctive patterns and usually involves the transverse aortic arch," *The Journal of Thoracic and Cardiovascular Surgery*, vol. 135, pp. 901–907.e2, Apr 2008.

[63] D. Detaint, H. I. Michelena, V. T. Nkomo, A. Vahanian, G. Jondeau, and M. E. Sarano, "Aortic dilatation patterns and rates in adults with bicuspid aortic valves: a comparative study with marfan syndrome and degenerative aortopathy," *Heart*, vol. 100, no. 2, pp. 126–134, 2014.

[64] S. C. Siu and C. K. Silversides, "Bicuspid aortic valve disease," *Journal of the American College of Cardiology*, vol. 55, no. 25, pp. 2789–2800, 2010.

[65] M. L. Loscalzo, D. L. Goh, B. Loeys, K. C. Kent, P. J. Spevak, and H. C. Dietz, "Familial thoracic aortic dilation and bicommissural aortic valve: A prospective analysis of natural history and inheritance," *American Journal of Medical Genetics Part A*, vol. 143A, no. 17, pp. 1960–1967, 2007.

[66] E. Girdauskas, M. A. Borger, M.-A. Secknus, G. Girdauskas, and T. Kuntze, "Is aortopathy in bicuspid aortic valve disease a congenital defect or a result of abnormal hemodynamics? A critical reappraisal of a one-sided argument," *European Journal of Cardio-Thoracic Surgery*, vol. 39, pp. 809–814, 06 2011.

[67] G. G. Hartnell, "Imaging of aortic aneurysms and dissection: Ct and mri," *Journal of Thoracic Imaging*, vol. 16, no. 1, 2001.

[68] S. Hoffjan, "Genetic Dissection of Marfan Syndrome and Related Connective Tissue Disorders: An Update 2012," *Molecular Syndromology*, vol. 3, pp. 47–58, 06 2012.

[69] B. L. Loeys, H. C. Dietz, A. C. Braverman, B. L. Callewaert, J. D. Backer, R. B. Devereux, Y. Hilhorst-Hofstee, G. Jondeau, L. Faivre, D. M. Milewicz, R. E. Pyeritz, P. D. Sponseller, P. Wordsworth, and A. M. D. Paepe, "The revised ghent nosology for the marfan syndrome," *Journal of Medical Genetics*, vol. 47, no. 7, pp. 476–485, 2010.

[70] A. Evangelista, F. A. Flachskampf, R. Erbel, F. Antonini-Canterin, C. Vlachopoulos, G. Rocchi, R. Sicari, P. Nihoyannopoulos, J. Zamorano, D. Reviewers:, M. Pepi, O.-A. Breithardt, and o. b. o. t. E. A. o. E. Plońska-Gościniak, Edyta, "Echocardiography in aortic diseases: EAE recommendations for clinical practice," *European Journal of Echocardiography*, vol. 11, pp. 645–658, 09 2010.

[71] D. P. Zipes, P. Libby, R. O. Bonow, D. L. Mann, G. F. Tomaselli, and E. Braunwald, "Braunwald's heart disease : a textbook of cardiovascular medicine," 2019.

[72] J. Van Puyvelde, E. Verbeken, P. Verbrugghe, P. Herijgers, and B. Meuris, "Aortic wall thickness in patients with ascending aortic aneurysm versus acute aortic dissection," *European Journal of Cardio-Thoracic Surgery*, vol. 49, pp. 756–762, 05 2015.

[73] A. D. Atkins, M. J. Reardon, and M. D. Atkins, "Endovascular management of the ascending aorta: State of the art," *Methodist DeBakey Cardiovascular Journal*, Mar 2023.

[74] F. Lohse, N. Lang, W. Schiller, W. Roell, O. Dewald, C.-J. Preusse, A. Welz, and C. Schmitz, "Quality of life after replacement of the ascending aorta in patients with true aneurysms," *Tex Heart Inst J*, vol. 36, no. 2, pp. 104–110, 2009.

[75] E. Buratto and I. E. Konstantinov, "Valve-sparing aortic root surgery in children and adults with congenital heart disease," *The Journal of Thoracic and Cardiovascular Surgery*, vol. 162, pp. 955–962, Sep 2021.

[76] M. S. Olufsen, "Structured tree outflow condition for blood flow in larger systemic arteries," *American Journal of Physiology-Heart and Circulatory Physiology*, vol. 276, no. 1, pp. H257–H268, 1999. PMID: 9887040.

[77] S. Pirola, Z. Cheng, O. Jarral, D. O'Regan, J. Pepper, T. Athanasiou, and X. Xu, "On the choice of outlet boundary conditions for patient-specific analysis of aortic flow using computational fluid dynamics," *Journal of Biomechanics*, vol. 60, pp. 15–21, July 2017.

[78] F. Pappalardo, J. Wilkinson, F. Busquet, A. Bril, M. Palmer, B. Walker, C. Curreli, G. Russo, T. Marchal, E. Toschi, R. Alessandrello, V. Costignola, I. Klingmann, M. Contin, B. Staumont, M. Woiczinski, C. Kaddick, V. D. Salvatore, A. Aldieri, L. Geris, and M. Viceconti, "Toward a regulatory pathway for the use of in silico trials in the CE marking of medical devices," *IEEE Journal of Biomedical and Health Informatics*, vol. 26, pp. 5282–5286, Nov. 2022.

[79] A. , "V&V 40–2018, assessing credibility of computational modeling through verification and validation: Application to medical devices."

[80] M. Andersson and M. Karlsson, "Characterization of anisotropic turbulence behavior in pulsatile blood flow," *Biomechanics and Modeling in Mechanobiology*, vol. 20, pp. 491–506, Apr. 2021.

[81] M. Andersson, T. Ebbers, and M. Karlsson, "Characterization and estimation of turbulence-related wall shear stress in patient-specific pulsatile blood flow," *Journal of Biomechanics*, vol. 85, pp. 108–117, 2019.

[82] L. Xu, L. Yin, Y. Liu, and F. Liang, "A computational study on the influence of aortic valve disease on hemodynamics in dilated aorta," *Mathematical Biosciences and Engineering*, vol. 17, no. 1, pp. 606–626, 2020.

[83] K. Capellini, E. Gasparotti, U. Cella, E. Costa, B. M. Fanni, C. Groth, S. Porziani, M. E. Biancolini, and S. Celi, "A novel formulation for the study of the ascending aortic fluid dynamics with in vivo data," *Medical Engineering & Physics*, p. S1350453320301387, Sept. 2020.

[84] J. Lantz, R. Gårdhagen, and M. Karlsson, "Quantifying turbulent wall shear stress in a subject specific human aorta using large eddy simulation," *Medical Engineering & Physics*, vol. 34, no. 8, pp. 1139–1148, 2012.

[85] A. N. Beris, J. S. Horner, S. Jariwala, M. J. Armstrong, and N. J. Wagner, "Recent advances in blood rheology: a review," *Soft Matter*, vol. 17, pp. 10591–10613, 2021.

[86] J. E. Hall, *Guyton and Hall Textbook of Medical Physiology.* Saunders, twelfth ed., 2010.

[87] S. Lynch, N. Nama, and C. A. Figueroa, "Effects of non-Newtonian viscosity on arterial and venous flow and transport," *Scientific Reports*, vol. 12, p. 20568, Nov. 2022.

[88] F. De Vita, M. D. de Tullio, and R. Verzicco, "Numerical simulation of the non-Newtonian blood flow through a mechanical aortic valve," *Theoretical and Computational Fluid Dynamics*, vol. 30, pp. 129–138, Apr. 2016.

[89] S. van Wyk, L. Prahl Wittberg, K. V. Bulusu, L. Fuchs, and M. W. Plesniak, "Non-Newtonian perspectives on pulsatile blood-analog flows in a 180° curved artery model," *Physics of Fluids*, vol. 27, p. 071901, July 2015.

[90] D. Biswas, D. M. Casey, D. C. Crowder, D. A. Steinman, Y. H. Yun, and F. Loth, "Characterization of Transition to Turbulence for Blood in a Straight Pipe Under Steady Flow Conditions," *Journal of Biomechanical Engineering*, vol. 138, 06 2016. 071001.

[91] M. O. Khan, K. Valen-Sendstad, and D. A. Steinman, "Direct Numerical Simulation of Laminar-Turbulent Transition in a Non-Axisymmetric Stenosis Model for Newtonian vs. Shear-Thinning Non-Newtonian Rheologies," *Flow, Turbulence and Combustion*, vol. 102, pp. 43–72, Jan. 2019.

[92] S. A. Bahrani and C. Nouar, "Intermittency in the transition to turbulence for a shear-thinning fluid in hagen-poiseuille flow," *Journal of Applied Fluid Mechanics*, vol. 7, no. 1, pp. 1–6, 2014.

[93] S. Nadeem, S. Akhtar, A. Saleem, N. Akkurt, H. Ali Ghazwani, and S. M. Eldin, "Numerical computations of blood flow through stenosed arteries via cfd tool openfoam," *Alexandria Engineering Journal*, vol. 69, pp. 613–637, 2023.

[94] S. Akhtar, Z. Hussain, S. Nadeem, I. M. R. Najjar, and A. Sadoun, "Cfd analysis on blood flow inside a symmetric stenosed artery: Physiology of a coronary artery disease," *Science Progress*, vol. 106, no. 2, p. 00368504231180092, 2023. PMID: 37292014.

[95] C. Binter, A. Gotschy, S. H. Sündermann, M. Frank, F. C. Tanner, T. F. Lüscher, R. Manka, and S. Kozerke, "Turbulent Kinetic Energy Assessed by Multipoint 4-Dimensional Flow Magnetic Resonance Imaging Provides Additional Information Relative to Echocardiography for the Determination of Aortic Stenosis Severity," *Circulation: Cardiovascular Imaging*, vol. 10, p. e005486, June 2017.

[96] P. Dyverfeldt, M. D. Hope, E. E. Tseng, and D. Saloner, "Magnetic Resonance Measurement of Turbulent Kinetic Energy for the Estimation of Irreversible Pressure Loss in Aortic Stenosis," *JACC: Cardiovascular Imaging*, vol. 6, pp. 64–71, Jan. 2013.

[97] E. L. Manchester, S. Pirola, M. Y. Salmasi, D. P. O'Regan, T. Athanasiou, and X. Y. Xu, "Evaluation of Computational Methodologies for Accurate Prediction of Wall Shear Stress and Turbulence Parameters in a Patient-Specific Aorta," *Frontiers in Bioengineering and Biotechnology*, vol. 10, p. 836611, Mar. 2022.

[98] L. Xu, T. Yang, L. Yin, Y. Kong, Y. Vassilevski, and F. Liang, "Numerical Simulation of Blood Flow in Aorta with Dilation: A Comparisonbetween Laminar and LES Modeling Methods," *Computer Modeling in Engineering & Sciences*, vol. 124, no. 2, pp. 509–526, 2020.

[99] S. Bozzi, D. Dominissini, A. Redaelli, and G. Passoni, "The effect of turbulence modelling on the assessment of platelet activation," *Journal of Biomechanics*, vol. 128, p. 110704, Nov. 2021.

[100] L. P. Parker, A. Svensson Marcial, T. B. Brismar, L. M. Broman, and L. Prahl Wittberg, "Computational Fluid Dynamics of the Right Atrium: A Comparison of Modeling Approaches in a Range of Flow Conditions," *Journal of Engineering and Science in Medical Diagnostics and Therapy*, vol. 5, p. 031108, Aug. 2022.

[101] S. Karimi, M. Dabagh, P. Vasava, M. Dadvar, B. Dabir, and P. Jalali, "Effect of rheological models on the hemodynamics within human aorta: Cfd study on ct image-based geometry," *Journal of Non-Newtonian Fluid Mechanics*, vol. 207, pp. 42–52, 2014.

[102] N. S. Kelly, H. S. Gill, A. N. Cookson, and K. H. Fraser, "Influence of Shear-Thinning Blood Rheology on the Laminar-Turbulent Transition over a Backward Facing Step," *Fluids*, vol. 5, p. 57, Apr. 2020.

[103] L. Geronzi, P. Haigron, A. Martinez, K. Yan, M. Rochette, A. Bel-Brunon, J. Porterie, S. Lin, D. M. Marin-Castrillon, A. Lalande, *et al.*, "Assessment of shape-based features ability to predict the ascending aortic aneurysm growth," *Frontiers in Physiology*, vol. 14, p. 378, 2023.

[104] L. Antiga, D. Steinman, S. Manini, and R. Izzo, "VMTK, the Vascular Modeling Toolkit." http://www.vmtk.org/, 2004–2018.

[105] L. Geronzi, E. Gasparotti, K. Capellini, U. Cella, C. Groth, S. Porziani, A. Chiappa, S. Celi, and M. E. Biancolini, "High fidelity fluid-structure interaction by radial basis functions mesh adaption of moving walls: A workflow applied to an aortic valve," *Journal of Computational Science*, vol. 51, p. 101327, 2021.

[106] M. J. M. M. Hoeijmakers, V. Morgenthaler, M. C. M. Rutten, and F. N. van de Vosse, "Scale-Resolving Simulations of Steady and Pulsatile Flow Through Healthy and Stenotic Heart Valves," *Journal of Biomechanical Engineering*, vol. 144, 11 2021. 031010.

[107] L. J. De Chant, "The venerable 1/7th power law turbulent velocity profile: A classical nonlinear boundary value problem solution and its relationship to stochastic processes," *Appl. Math. Comput.*, vol. 161, p. 463–474, feb 2005.

[108] P. van Ooij, E. S. Farag, C. P. S. Blanken, A. J. Nederveen, M. Groenink, R. N. Planken, and S. M. Boekholdt, "Fully quantitative mapping of abnormal aortic velocity and wall shear stress direction in patients with bicuspid aortic valves and repaired coarctation using 4D flow cardiovascular magnetic resonance," *Journal of Cardiovascular Magnetic Resonance*, vol. 23, p. 9, Dec. 2021.

[109] J. Garcia, R. L. van der Palen, E. Bollache, K. Jarvis, M. J. Rose, A. J. Barker, J. D. Collins, J. C. Carr, J. Robinson, C. K. Rigsby, and M. Markl, "Distribution of Blood Flow Velocity in the normal aorta: Effect of age and gender," *Journal of Magnetic Resonance Imaging*, vol. 47, pp. 487–498, Feb. 2018.

[110] C. E. Richards, A. E. Parker, A. Alfuhied, G. P. McCann, and A. Singh, "The role of 4-dimensional flow in the assessment of bicuspid aortic valve and its valvulo-aortopathies," *The British Journal of Radiology*, vol. 95, p. 20220123, Nov. 2022.

[111] J. Alastruey, T. Passerini, L. Formaggia, and J. Peiró, "Physical determining factors of the arterial pulse waveform: Theoretical analysis and calculation using the 1-D formulation," *Journal of Engineering Mathematics*, vol. 77, pp. 19–37, Dec. 2012.

[112] J. Feher, *Multiscale, Multiphysics and Reduced Order Modelling Techniques for Hemodynamics*. Ph.d. thesis, Politecnico di Milano, Dec. 2019.

[113] D. K. Lilly, "A proposed modification of the germano subgrid-scale closure method," *Physics of Fluids A: Fluid Dynamics*, vol. 4, no. 3, pp. 633–635, 1992.

[114] Y. I. Cho and K. R. Kensey, "Effects of the non-Newtonian viscosity of blood on flows in a diseased arterial vessel. Part 1: Steady flows," *Biorheology*, vol. 28, pp. 241–262, June 1991.

[115] B. M. Johnston, P. R. Johnston, S. Corney, and D. Kilpatrick, "Non-newtonian blood flow in human right coronary arteries: Steady state simulations," *Journal of Biomechanics*, vol. 37, no. 5, pp. 709–720, 2004.

[116] J. C. Weddell, J. Kwack, P. I. Imoukhuede, and A. Masud, "Hemodynamic Analysis in an Idealized Artery Tree: Differences in Wall Shear Stress between Newtonian and Non-Newtonian Blood Models," *PLOS ONE*, vol. 10, p. e0124575, Apr. 2015.

[117] M. Iasiello, K. Vafai, A. Andreozzi, and N. Bianco, "Analysis of non-Newtonian effects on Low-Density Lipoprotein accumulation in an artery," *Journal of Biomechanics*, vol. 49, pp. 1437–1446, June 2016.

[118] A. Arzani, "Accounting for residence-time in blood rheology models: Do we really need non-newtonian blood flow modelling in large arteries?," *Journal of The Royal Society Interface*, vol. 15, no. 146, p. 20180486, 2018.

[119] U. Morbiducci, R. Ponzini, D. Gallo, C. Bignardi, and G. Rizzo, "Inflow boundary conditions for image-based computational hemodynamics: Impact of idealized versus measured velocity profiles in the human aorta," *Journal of Biomechanics*, vol. 46, no. 1, pp. 102–109, 2013.

[120] V. Mendez, M. Di Giuseppe, and S. Pasta, "Comparison of hemodynamic and structural indices of ascending thoracic aortic aneurysm as predicted by 2-way FSI, CFD rigid wall simulation and patient-specific displacement-based FEA," *Computers in Biology and Medicine*, vol. 100, pp. 221–229, Sept. 2018.

[121] J. A. Rizzo, M. A. Coady, and J. A. Elefteriades, "Procedures for estimating growth rates in thoracic aortic aneurysms," *Journal of Clinical Epidemiology*, vol. 51, pp. 747–754, Sep 1998.

[122] Y. Hirose, S. Hamada, and M. Takamiya, "Predicting the growth of aortic aneurysms: A comparison of linear vs exponential models," *Angiology*, vol. 46, no. 5, pp. 413–419, 1995. PMID: 7741325.

[123] B. P. Adriaans, M. J. F. G. Ramaekers, S. Heuts, H. J. G. M. Crijns, S. C. A. M. Bekkers, J. J. M. Westenberg, H. J. Lamb, J. E. Wildberger, and S. Schalla, "Determining the optimal interval for imaging surveillance of ascending aortic aneurysms," *Netherlands Heart Journal*, vol. 29, pp. 623–631, Dec. 2021.

[124] A. Gulati, J. Leach, Z. Wang, Y. Xuan, M. D. Hope, L. Ge, and E. E. Tseng, "Ascending thoracic aortic aneurysm growth is minimal at sizes that do not meet criteria for surgical repair," *Structural Heart*, vol. 5, no. sup1, pp. 63–63, 2021.

[125] D. Detaint, H. I. Michelena, V. T. Nkomo, A. Vahanian, G. Jondeau, and M. E. Sarano, "Aortic dilatation patterns and rates in adults with bicuspid aortic valves: a comparative study with marfan syndrome and degenerative aortopathy," *Heart*, vol. 100, no. 2, pp. 126–134, 2014.

[126] R. S. Bonser, D. Pagano, M. E. Lewis, S. J. Rooney, P. Guest, P. Davies, and I. Shimada, "Clinical and patho-anatomical factors affecting expansion of thoracic aortic aneurysms," *Heart*, vol. 84, no. 3, pp. 277–283, 2000.

[127] G. Koullias, R. Modak, M. Tranquilli, D. P. Korkolis, P. Barash, and J. A. Elefteriades, "Mechanical deterioration underlies malignant behavior of aneurysmal human ascending aorta," *The Journal of Thoracic and Cardiovascular Surgery*, vol. 130, no. 3, pp. 677.e1–677.e9, 2005.

[128] C. Martin, W. Sun, T. Pham, and J. Elefteriades, "Predictive biomechanical analysis of ascending aortic aneurysm rupture potential," *Acta Biomaterialia*, vol. 9, pp. 9392–9400, Dec. 2013.

[129] M. J. Levesque and R. M. Nerem, "The Elongation and Orientation of Cultured Endothelial Cells in Response to Shear Stress," *Journal of Biomechanical Engineering*, vol. 107, pp. 341–347, 11 1985.

[130] J. Zhou, Y.-S. Li, and S. Chien, "Shear stress–initiated signaling and its regulation of endothelial function," *Arteriosclerosis, Thrombosis, and Vascular Biology*, vol. 34, no. 10, pp. 2191–2198, 2014.

[131] J. E. Wagenseil, "Bio-chemo-mechanics of thoracic aortic aneurysms," *Current Opinion in Biomedical Engineering*, vol. 5, pp. 50–57, 2018. Futures of Biomedical Engineering: Cardiovascular Bioengineering and Vascular Biomechanics.

[132] D. G. Guzzardi, A. J. Barker, P. van Ooij, S. C. Malaisrie, J. J. Puthumana, D. D. Belke, H. E. Mewhort, D. A. Svystonyuk, S. Kang, S. Verma, J. Collins, J. Carr, R. O. Bonow, M. Markl, J. D. Thomas, P. M. McCarthy, and P. W. Fedak, "Valve-Related Hemodynamics Mediate Human Bicuspid Aortopathy," *Journal of the American College of Cardiology*, vol. 66, pp. 892–900, Aug. 2015.

[133] P. M. den Reijer, D. Sallee, P. van der Velden, E. R. Zaaijer, W. J. Parks, S. Ramamurthy, T. Q. Robbie, G. Donati, C. Lamphier, R. P. Beekman, and M. E. Brummer, "Hemodynamic predictors of aortic dilatation in bicuspid aortic valve by velocity-encoded cardiovascular magnetic resonance," *Journal of Cardiovascular Magnetic Resonance*, vol. 12, p. 4, Jan 2010.

[134] K. Suwa, O. A. Rahman, E. Bollache, M. J. Rose, A. A. Rahsepar, J. C. Carr, J. D. Collins, A. J. Barker, and M. Markl, "Effect of aortic valve disease on 3d hemodynamics in patients with aortic dilation and trileaflet aortic valve morphology," *Journal of Magnetic Resonance Imaging*, vol. 51, no. 2, pp. 481–491, 2020.

[135] G. De Nisco, P. Tasso, K. Calò, V. Mazzi, D. Gallo, F. Condemi, S. Farzaneh, S. Avril, and U. Morbiducci, "Deciphering ascending thoracic aortic aneurysm hemodynamics in relation to biomechanical properties," *Medical Engineering & Physics*, vol. 82, pp. 119–129, 2020.

[136] P. Youssefi, A. Gomez, T. He, L. Anderson, N. Bunce, R. Sharma, C. A. Figueroa, and M. Jahangiri, "Patient-specific computational fluid dynamics—assessment of aortic hemodynamics in a spectrum of aortic valve pathologies," *The Journal of Thoracic and Cardiovascular Surgery*, vol. 153, no. 1, pp. 8–20.e3, 2017.

[137] T. Korpela, S. P. Kauhanen, E. Kariniemi, P. Saari, T. Liimatainen, P. Jaakkola, R. Vanninen, and M. Hedman, "Flow displacement and decreased wall shear stress might be associated with the growth rate of an ascending aortic dilatation," *European Journal of Cardio-Thoracic Surgery*, vol. 61, pp. 395–402, 11 2021.

[138] S. C. S. Minderhoud, J. W. Roos-Hesselink, R. G. Chelu, L. R. Bons, A. T. van den Hoven, S.-A. Korteland, A. E. van den Bosch, R. P. J. Budde, J. J. Wentzel, and A. Hirsch, "Wall shear stress angle is associated with aortic growth in bicuspid aortic valve patients," *European Heart Journal - Cardiovascular Imaging*, vol. 23, pp. 1680–1689, 01 2022.

[139] J. I. Cotella, T. Miyoshi, V. Mor-Avi, K. Addetia, M. Schreckenberg, D. Sun, J. A. Slivnick, M. Blankenhagen, N. Hitschrich, V. Amuthan, R. Citro, M. Daimon, P. Gutiérrez-Fajardo, R. Kasliwal, J. N. Kirkpatrick, M. J. Monaghan, D. Muraru, K. O. Ogunyankin, S. W. Park, A. C. Tude Rodrigues, R. Ronderos, A. Sadeghpour, G. Scalia, M. Takeuchi, W. Tsang, E. S. Tucay, M. Zhang, A. D. Prado, F. M. Asch, and R. M. Lang, "Normative values of the aortic valve area and Doppler measurements using two-dimensional transthoracic echocardiography: results from the Multicentre World Alliance of Societies of Echocardiography Study," *European Heart Journal - Cardiovascular Imaging*, vol. 24, pp. 415–423, 11 2022.

[140] R. Kikinis, S. D. Pieper, and K. G. Vosburgh, *3D Slicer: A Platform for Subject-Specific Image Analysis, Visualization, and Clinical Support*, pp. 277–289. New York, NY: Springer New York, 2014.

[141] V. Mazzi, D. Gallo, K. Calò, M. Najafi, M. O. Khan, G. De Nisco, D. A. Steinman, and U. Morbiducci, "A eulerian method to analyze wall shear stress fixed points and manifolds in cardiovascular flows," *Biomechanics and Modeling in Mechanobiology*, vol. 19, pp. 1403–1423, Oct 2020.

[142] U. Morbiducci, V. Mazzi, M. Domanin, G. De Nisco, C. Vergara, D. A. Steinman, and D. Gallo, "Wall shear stress topological skeleton independently predicts long-term restenosis after carotid bifurcation endarterectomy," *Annals of Biomedical Engineering*, vol. 48, pp. 2936–2949, Dec 2020.

[143] V. Mazzi, U. Morbiducci, K. Calò, G. De Nisco, M. Lodi Rizzini, E. Torta, G. C. A. Caridi, C. Chiastra, and D. Gallo, "Wall shear stress topological skeleton analysis in cardiovascular flows: Methods and applications," *Mathematics*, vol. 9, no. 7, 2021.

[144] O. Rahman, M. Scott, E. Bollache, K. Suwa, J. Collins, J. Carr, P. Fedak, P. McCarthy, C. Malaisrie, A. J. Barker, and M. Markl, "Interval changes in aortic peak velocity and wall shear stress in patients with bicuspid aortic valve disease," *The International Journal of Cardiovascular Imaging*, vol. 35, pp. 1925–1934, Oct 2019.

[145] A. Arzani and S. C. Shadden, "Wall shear stress fixed points in cardiovascular fluid mechanics," *Journal of Biomechanics*, vol. 73, pp. 145–152, 2018.

[146] C. Wang, B. M. Baker, C. S. Chen, and M. A. Schwartz, "Endothelial cell sensing of flow direction," *Arteriosclerosis, Thrombosis, and Vascular Biology*, vol. 33, no. 9, pp. 2130–2136, 2013.

[147] J.-J. Chiu and S. Chien, "Effects of disturbed flow on vascular endothelium: Pathophysiological basis and clinical perspectives," *Physiological Reviews*, vol. 91, no. 1, pp. 327–387, 2011. PMID: 21248169.

[148] K. Capellini, E. Vignali, E. Costa, E. Gasparotti, M. E. Biancolini, L. Landini, V. Positano, and S. Celi, "Computational Fluid Dynamic Study for aTAA Hemodynamics: An Integrated Image-Based and Radial Basis Functions Mesh Morphing Approach," *Journal of Biomechanical Engineering*, vol. 140, 08 2018. 111007.

[149] P. Reymond, P. Crosetto, S. Deparis, A. Quarteroni, and N. Stergiopulos, "Physiological simulation of blood flow in the aorta: Comparison of hemodynamic indices as predicted by 3-d fsi, 3-d rigid wall and 1-d models," *Medical Engineering & Physics*, vol. 35, no. 6, pp. 784–791, 2013.

[150] A. G. Brown, Y. Shi, A. Marzo, C. Staicu, I. Valverde, P. Beerbaum, P. V. Lawford, and D. R. Hose, "Accuracy vs. computational time: Translating aortic simulations to the clinic," *Journal of Biomechanics*, vol. 45, no. 3, pp. 516–523, 2012.

[151] M. Nowak, B. Melka, M. Rojczyk, M. Gracka, A. J. Nowak, A. Golda, W. P. Adamczyk, B. Isaac, R. A. Białecki, and Z. Ostrowski, "The protocol for using elastic wall model in modeling blood flow within human artery," *European Journal of Mechanics - B/Fluids*, vol. 77, pp. 273–280, 2019.

[152] S. Chandra, S. S. Raut, A. Jana, R. W. Biederman, M. Doyle, S. C. Muluk, and E. A. Finol, "Fluid-Structure Interaction Modeling of Abdominal Aortic Aneurysms: The Impact of Patient-Specific Inflow Conditions and Fluid/Solid Coupling," *Journal of Biomechanical Engineering*, vol. 135, p. 081001, 06 2013.

[153] X. Wang and X. Li, "Computational simulation of aortic aneurysm using fsi method: Influence of blood viscosity on aneurismal dynamic behaviors," *Computers in Biology and Medicine*, vol. 41, no. 9, pp. 812–821, 2011.

[154] B. Wolters, M. Rutten, G. Schurink, U. Kose, J. de Hart, and F. van de Vosse, "A patient-specific computational model of fluid–structure interaction in abdominal aortic aneurysms," *Medical Engineering & Physics*, vol. 27, no. 10, pp. 871–883, 2005. Advances in the finite element modelling of soft tissue deformation.

[155] M. Xenos, N. Labropoulos, S. Rambhia, Y. Alemu, S. Einav, A. Tassiopoulos, N. Sakalihasan, and D. Bluestein, "Progression of abdominal aortic aneurysm towards rupture: Refining clinical risk assessment using a fully coupled fluid–structure interaction method," *Annals of Biomedical Engineering*, vol. 43, pp. 139–153, Jan 2015.

[156] M. Alimohammadi, J. M. Sherwood, M. Karimpour, O. Agu, S. Balabani, and V. Díaz-Zuccarini, "Aortic dissection simulation models for clinical support: Fluid-structure interaction vs. rigid wall models," *BioMedical Engineering OnLine*, vol. 14, no. 34, 2015.

[157] M. Bonfanti, S. Balabani, M. Alimohammadi, O. Agu, S. Homer-Vanniasinkam, and V. Díaz-Zuccarini, "A simplified method to account for wall motion in patient-specific blood flow simulations of aortic dissection: Comparison with fluid-structure interaction," *Medical Engineering & Physics*, vol. 58, pp. 72–79, 2018.

[158] J. Sigüenza, D. Pott, S. Mendez, S. J. Sonntag, T. A. Kaufmann, U. Steinseifer, and F. Nicoud, "Fluid-structure interaction of a pulsatile flow with an aortic valve model: A combined experimental and numerical study," *International Journal for Numerical Methods in Biomedical Engineering*, vol. 34, no. 4, p. e2945, 2018. e2945 cnm.2945.

[159] P. Moireau, N. Xiao, M. Astorino, C. A. Figueroa, D. Chapelle, C. A. Taylor, and J.-F. Gerbeau, "External tissue support and fluid–structure simulation in blood flows," *Biomechanics and Modeling in Mechanobiology*, vol. 11, pp. 1–18, Jan 2012.

[160] J. Gindre, A. Bel-Brunon, A. Kaladji, A. Duménil, M. Rochette, A. Lucas, P. Haigron, and A. Combescure, "Finite element simulation of the insertion of guidewires during an evar procedure: example of a complex patient case, a first step toward patient-specific parameterized models," *International Journal for Numerical Methods in Biomedical Engineering*, vol. 31, no. 7, p. e02716, 2015. e02716 CNM-Feb-15-0028.

[161] J. Gindre, A. Bel-Brunon, M. Rochette, A. Lucas, A. Kaladji, P. Haigron, and A. Combescure, "Patient-specific finite-element simulation of the insertion of guidewire during an evar procedure: Guidewire position prediction validation on 28 cases," *IEEE Transactions on Biomedical Engineering*, vol. 64, no. 5, pp. 1057–1066, 2017.

[162] S. Z. Pagoulatou, M. Ferraro, B. Trachet, V. Bikia, G. Rovas, L. A. Crowe, J.-P. Vallée, D. Adamopoulos, and N. Stergiopulos, "The effect of the elongation of the proximal aorta on the estimation of the aortic wall distensibility," *Biomechanics and Modeling in Mechanobiology*, vol. 20, pp. 107–119, Feb 2021.

[163] A. Hardikar, R. Harle, and T. H. Marwick, "Aortic thickness: A forgotten paradigm in risk stratification of aortic disease," *Aorta (Stamford)*, vol. 8, pp. 132–140, Dec. 2020.

[164] S. Lin, M. C. Morgant, D. M. Marín-Castrillón, P. M. Walker, L. S. Aho Glélé, A. Boucher, B. Presles, O. Bouchot, and A. Lalande, "Aortic local biomechanical properties in ascending aortic aneurysms," *Acta Biomaterialia*, vol. 149, pp. 40–50, 2022.

[165] D. Craiem, A. F. Pascaner, M. E. Casciaro, U. Gencer, J. Alcibar, G. Soulat, and E. Mousseaux, "Automatic correction of background phase offset in 4d-flow of great vessels and of the heart in mri using a third-order surface model," *Magnetic Resonance Materials in Physics, Biology and Medicine*, vol. 32, pp. 629–642, Dec 2019.

[166] A. Barrera-Naranjo, D. M. Marin-Castrillon, T. Decourselle, S. Lin, S. Leclerc, M.-C. Morgant, C. Bernard, S. De Oliveira, A. Boucher, B. Presles, O. Bouchot, J.-J. Christophe, and A. Lalande, "Segmentation of 4d flow mri: Comparison between 3d deep learning and velocity-based level sets," *Journal of Imaging*, vol. 9, no. 6, 2023.

[167] J. E. Solem, M. Persson, and A. Heyden, "Velocity based segmentation in phase contrast mri images," in *Medical Image Computing and Computer-Assisted Intervention – MICCAI 2004* (C. Barillot, D. R. Haynor, and P. Hellier, eds.), (Berlin, Heidelberg), pp. 459–466, Springer Berlin Heidelberg, 2004.

[168] I. Amidror, "Scattered data interpolation methods for electronic imaging systems: a survey," *Journal of Electronic Imaging*, vol. 11, no. 2, pp. 157–76, 2002.

[169] W. K. Laskey, H. G. Parker, V. A. Ferrari, W. G. Kussmaul, and A. Noordergraaf, "Estimation of total systemic arterial compliance in humans," *Journal of Applied Physiology*, vol. 69, no. 1, pp. 112–119, 1990. PMID: 2394640.

[170] J. Alastruey, T. Passerini, L. Formaggia, and J. Peiró, "Physical determining factors of the arterial pulse waveform: theoretical analysis and calculation using the 1-d formulation," *Journal of Engineering Mathematics*, vol. 77, pp. 19–37, Dec 2012.

[171] N. Stergiopulos, D. Young, and T. Rogge, "Computer simulation of arterial flow with applications to arterial and aortic stenoses," *Journal of Biomechanics*, vol. 25, no. 12, pp. 1477–1488, 1992.

[172] N. Xiao, J. Alastruey, and C. Alberto Figueroa, "A systematic comparison between 1-d and 3-d hemodynamics in compliant arterial models," *International Journal for Numerical Methods in Biomedical Engineering*, vol. 30, no. 2, pp. 204–231, 2014.

[173] K. Khanafer, A. Duprey, M. Zainal, M. Schlicht, D. Williams, and R. Berguer, "Determination of the elastic modulus of ascending thoracic aortic aneurysm at different ranges of pressure using uniaxial tensile testing," *The Journal of Thoracic and Cardiovascular Surgery*, vol. 142, pp. 682–686, Sep 2011.

[174] W. W. Nichols, M. F. O'Rourke, and D. A. McDonald, *McDonald's blood flow in arteries : theoretical, experimental, and clinical principles*. London, New York: Hodder Arnold ; Distributed in the U.S.A. by Oxford University Press, 5th ed ed., 2005.

[175] O. H. Yeoh, "Some Forms of the Strain Energy Function for Rubber," *Rubber Chemistry and Technology*, vol. 66, pp. 754–771, 11 1993.

[176] F. Cosentino, V. Agnese, G. M. Raffa, G. Gentile, D. Bellavia, M. Zingales, M. Pilato, and S. Pasta, "On the role of material properties in ascending thoracic aortic aneurysms," *Computers in Biology and Medicine*, vol. 109, pp. 70–78, 2019.

[177] A. Polanczyk, M. Podgorski, M. Polanczyk, N. Veshkina, I. Zbicinski, L. Stefanczyk, and C. Neumayer, "A novel method for describing biomechanical properties of the aortic wall based on the three-dimensional fluid-structure interaction model," *Interactive CardioVascular and Thoracic Surgery*, vol. 28, pp. 306–315, 08 2018.

[178] P. Reymond, F. Merenda, F. Perren, D. Rüfenacht, and N. Stergiopulos, "Validation of a one-dimensional model of the systemic arterial tree," *American Journal of Physiology-Heart and Circulatory Physiology*, vol. 297, no. 1, pp. H208–H222, 2009. PMID: 19429832.

[179] A. Isebree Moens, *Die Pulscurve*. Leiden: E.J. Brill, 1878.

[180] D. J. Korteweg, "Ueber die fortpflanzungsgeschwindigkeit des schalles in elastischen röhren," *Annalen der Physik*, vol. 241, no. 12, pp. 525–542, 1878.

[181] B. E. Engelmann, R. G. Whirley, and G. L. Goudreau, "A simple shell element formulation for large-scale elastoplastic analysis," (United States), Jul 1989. Research Org.: Lawrence Livermore National Lab. (LLNL), Livermore, CA (United States).

[182] J. C. Simo and T. J. R. Hughes, "On the Variational Foundations of Assumed Strain Methods," *Journal of Applied Mechanics*, vol. 53, pp. 51–54, 03 1986.

[183] J. Bols, J. Degroote, B. Trachet, B. Verhegghe, P. Segers, and J. Vierendeels, "A computational method to assess the in vivo stresses and unloaded configuration of patient-specific blood vessels," *Journal of Computational and Applied Mathematics*, vol. 246, pp. 10–17, 2013. Fifth International Conference on Advanced COmputational Methods in ENgineering (ACOMEN 2011).

[184] S. Q. Liu and Y. C. Fung, "Zero-Stress States of Arteries," *Journal of Biomechanical Engineering*, vol. 110, pp. 82–84, 02 1988.

[185] I. Vesely, A. Lozon, and E. Talman, "Is zero-pressure fixation of bioprosthetic valves truly stress free?," *The Journal of Thoracic and Cardiovascular Surgery*, vol. 106, no. 2, pp. 288–298, 1993.

[186] M. K. Rausch, M. Genet, and J. D. Humphrey, "An augmented iterative method for identifying a stress-free reference configuration in image-based biomechanical modeling," *Journal of Biomechanics*, vol. 58, pp. 227–231, 2017.

[187] F. Del Pin, *The meshless finite element method applied to a lagrangian particle formulation of fluid flows*. PhD thesis, 2003. Universidad del Litoral.

[188] C. Farhat, M. Lesoinne, and P. Le Tallec, "Load and motion transfer algorithms for fluid/structure interaction problems with non-matching discrete interfaces: Momentum and energy conservation, optimal discretization and application to aeroelasticity," *Computer Methods in Applied Mechanics and Engineering*, vol. 157, no. 1, pp. 95–114, 1998.

[189] M. Neumann, S. Tiyyagura, W. Wall, and E. Ramm, "Robustness and efficiency aspects for computational fluid structure interaction," in *Computational Science and High Performance Computing II* (E. Krause, Y. Shokin, M. Resch, and N. Shokina, eds.), (Berlin, Heidelberg), pp. 99–114, Springer Berlin Heidelberg, 2006.

[190] C. Felippa and K. Park, "Staggered transient analysis procedures for coupled mechanical systems: Formulation," *Computer Methods in Applied Mechanics and Engineering*, vol. 24, no. 1, pp. 61–111, 1980.

[191] P. Causin, J. Gerbeau, and F. Nobile, "Added-mass effect in the design of partitioned algorithms for fluid–structure problems," *Computer Methods in Applied Mechanics and Engineering*, vol. 194, no. 42, pp. 4506–4527, 2005.

[192] S. Rodolfo Idelsohn, F. Del Pin, and R. Rossi, *Avoiding instabilities caused by added mass effects in fluid-structure interaction problems*, p. 165–220. John Wiley & Sons, 2010.

[193] Y. G. Stergiou, A. G. Kanaris, A. A. Mouza, and S. V. Paras, "Fluid-structure interaction in abdominal aortic aneurysms: Effect of haematocrit," *Fluids*, vol. 4, no. 1, 2019.